MEASUREMENT OF ASPHERICAL SURFACES USING A TEST PLATE AND COMPUTER GENERATED HOLOGRAMS

by

Feenix YuanFeng Pan

A Dissertation Submitted to the Faculty of the

COMMITTEE ON OPTICAL SCIENCES (GRADUATE)

In Partial Fulfillment of the Requirements
For the Degree of

DOCTOR OF PHILOSOPHY

In the Graduate College

THE UNIVERSITY OF ARIZONA

2002

UMI Number: 3073249

ProQuest Information and Learning Company
300 North Zeeb Road
P.O. Box 1346
Ann Arbor, MI 48106-1346

THE UNIVERSITY OF ARIZONA ®
GRADUATE COLLEGE

As members of the Final Examination Committee, we certify that we have read the dissertation prepared by Feenix Y. Pan

entitled Measurement of Aspherical Surfaces Using a Test Plate and Computer Generated Holograms

and recommend that it be accepted as fulfilling the dissertation requirement for the Degree of Doctor of Philosophy

James H. Burge	Oct 21, 2002 Date
James C. Wyant	Oct. 21, 2002 Date
Roland V. Shack	10/21/02 Date
	Date
	Date

Final approval and acceptance of this dissertation is contingent upon the candidate's submission of the final copy of the dissertation to the Graduate College.

I hereby certify that I have read this dissertation prepared under my direction and recommend that it be accepted as fulfilling the dissertation requirement.

Dissertation Director, James H. Burge — Nov. 19, 2002 Date

STATEMENT BY AUTHOR

This dissertation has been submitted in partial fulfillment of requirements for an advanced degree at The University of Arizona and is deposited in the University Library to be made available to borrowers under rules of the Library.

Brief quotations from this dissertation are allowable without special permission, provided that accurate acknowledgment of source is made. Requests for permission for extended quotation from or reproduction of this manuscript in whole or in part may be granted by the copyright holder.

SIGNED: 

ACKNOWLEDGEMENTS

First, I wish to thank my advisors Prof. Jim Burge and Prof. James Wyant for the privilege of working with them over the past four years. They took me under their wings and taught me what they know about the field of optical testing. Prof. Burge trusted me with the method he invented and let me run with it. Together, their advice, feedback, and support made this project possible.

I would like to express my deep gratitude to Prof. Roland Shack. Prof. Shack not only served on my defense committee, but also is a friend and mentor -- both professionally and personally. From him I learned to trust and honor my inner child so I too can be free.

Also, I would like to thank Rayleigh Optics for their generous donation of hardware for my experiments and Prof. Alexander Poleshchuk from the Russian Academy of Science for donating the CGH for my experiment. Finally, I would like to thank the department administrative assistants, my co-workers, and friends for making me laugh when the project went into hibernation.

On a personally note, I want to thank my parents for bringing my brother and I to the United States. Most importantly, I want to thank my beloved husband for his faith in me. Without his support, encouragement, and constant companionship, this project would never have been possible. You are the sunshine of my life. From you, I gained the courage to challenge life and to stand tall and strong in the face of adversaries. From you, I learned to love and trust unconditionally. You made me whole.

DEDICATION

To my beloved husband
Eugene
Whose unconditional love, faith and support made me whole.

To our beautiful children
Alexa and Byron
Whose eyes I gazed upon and felt the meaning of perfection.

TABLE OF CONTENTS

TABLE OF CONTENTS--CONTINUED

TABLE OF CONTENTS--CONTINUED

LIST OF FIGURES

LIST OF FIGURES--CONTINUED

LIST OF FIGURES--CONTINUED

LIST OF FIGURES--CONTINUED

LIST OF FIGURES--CONTINUED

LIST OF FIGURES--CONTINUED

LIST OF FIGURES--CONTINUED

APPENDICES

LIST OF TABLES

LIST OF TABLES--CONTINUED

APPENDICES

ABSTRACT

A major paradigm shift in the design of large telescopes is currently in progress. In order to increase the size of a telescope primary mirror, current designs use mirrors that are comprised of multiple segments instead of one monolithic piece. While this approach allows for larger primary mirrors than the monolithic approach, new challenges arise. One of the primary challenges is to accurately, rapidly, and cost-effectively test the multiple asphere segments.

This dissertation provides a thorough design analysis and experimental validation on a novel method, proposed by Burge and Anderson, for measuring off-axis aspherical surfaces using test plate and computer-generated holograms. This new method is optimal for measuring segments of aspheric primary mirrors, and can be applied to any aspheric surface, convex or concave. It interferometrically compares the aspheric surface with a nearly matching spherical reference surface and uses CGH to compensate the aspherical departure. Like other Fizeau-type interferometric tests, high accuracy is achieved economically since the spherical reference is the only surface that directly affects the measurement. This technique is optimal for testing primary mirror segments where all the different off-axis pieces of the asphere can be measured with a single test plate, replacing only the smaller hologram. The most important property of this test for segmented mirrors is the fine control of the curvature provided by using a reference plate in close proximity to the aspherical surface being measured. This allows all the segments

to be separately manufactured, assumes that they will fit together to form a single aspheric surface.

In this dissertation, I examine, optimize, and validate this novel method, making it readily available for future telescope designers/manufacturers. First, the quantitative analysis on how segmentation tightens the testing requirements during fabrication and alignment provides valuable information in determining essential telescope parameters such as segment size, F/#, fabrication and alignment specifications. Secondly, the detailed optimization processes show how the test system can be designed and built to achieve high accuracy with maximum cost effectiveness. Lastly, the experimental data successfully validate the test and the method of design and analysis.

CHAPTER 1

INTRODUCTION

1.1 BACKGROUND

Advancements in instruments used for scientific research bring major advances in science. This is especially the case in observational astronomy, where majority of its scientific research is based on the amount of light collected by an instrument -- the telescope. More information can be extracted if more light is collected.

The promise of obtaining more light, thus more information, from very faint objects is one of the principal motivations for building larger telescopes. The light-gathering power of optical telescopes increased steadily since Galileo's, but up until 1948 when the famous 5-m Hale Telescope at Palomar Mountain was completed[1] (Figure 1-1). Then in the 1980's, new approaches to large mirror fabrication emerged, and one result is the world first and largest segmented telescope. The twin W. M. Keck 10-m telescopes each has a f/1.75 10-m primary that is made up of 36 pieces of 2-m hexagonal segments (Figure 1-2). The W. M. Keck observatory is located in Mauna Kea (Hawaii) and was completed in 1992[2] (Keck 1) and 1996 (Keck 2)[3].

Segmentation solved one of the two major problems facing ground-based telescopes, i.e. the ability to gather more light. The other technology hurdle was image degradation due to air turbulence. In the past, this turbulence limited image angular size

to 0.5 arc second regardless of telescope size. The Hubble Space Telescope (HST) achieves 0.1-arc second image resolution with a 2-meter primary mirror because it orbits

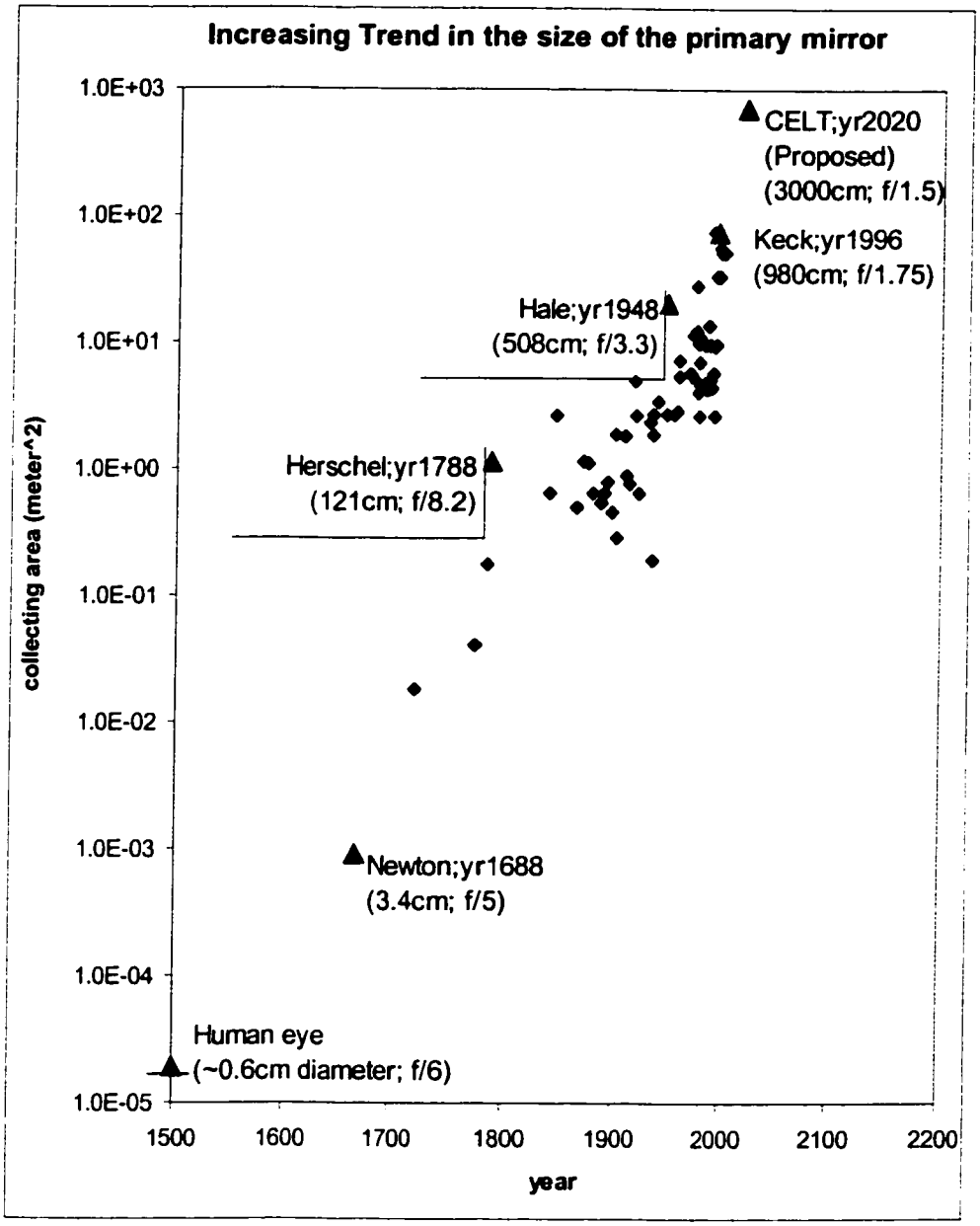

Figure 1-1. Increasing Trend in the size of the primary mirror. (Data for this figure are compiled from references [4], [5,6,7])

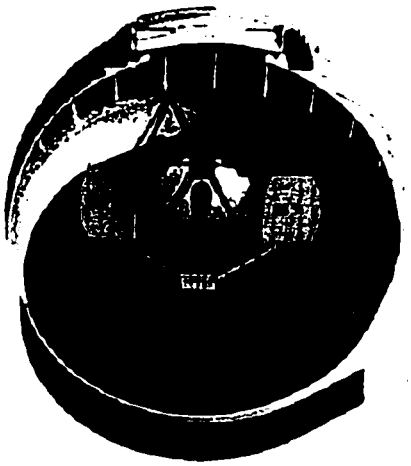

Figure 1-2*. One of the Keck telescopes as it is situated inside the dome. A mosaic of mirror segments is pieced together to form a larger continuous primary mirror for this telescope.

*ILLUSTRATION BY TOM CONNELL/WILDLIFE ART LTD.
FROM THE READER'S DIGEST "ATLAS OF THE UNIVERSE"

outside of the atmospheric layer. Air turbulences have been preventing ground-based telescopes from reaching the diffraction-limited image size set by the fundamental wave-behavior of light.

Fortunately in recent years, application of a new emerging technology, adaptive optics (AO) where atmospheric blurring is corrected real-time, allows ground-based telescopes to achieve diffraction limited image size. The diffraction-limit is determined by the diameter (D) of the telescope and the wavelength (λ) of the light used. At the diffraction limit, the angular resolution is proportional to λ/D. With the help of AO, ground-based telescopes can now compete and compliment space-based telescopes in performance. For instance, the Keck telescopes complimented with AO and 16-fold increase in collecting area, have achieved a sharp 0.025 arc second angular resolution[8], a factor of 4 improvement compared to the Hubble Space Telescope's 0.1 arc second angular resolution.

Since the atmosphere absorbs heavily in certain wavelength range, there will always be a strong case for designing, launching and maintaining a space telescope. However, with recent advancements in telescope fabrication and adaptive optics discussed above, ground-based telescopes remain competitive with their performance. In addition, for the cost reason alone, ground-based telescopes will have larger primary mirrors that have more light-gather power than space-based telescopes for the foreseeable future[9]. For example, in the last 1-2 years, there has been an ambitious proposal for building a 100-m ground-based telescope[10].

On one hand, segmenting large primary mirrors into smaller mosaics of pieces makes fabricating, testing and transporting these giant mirrors (up to 100-m) feasible. On the other hand, segmentation brings new technical difficulties and challenges to different aspects of constructing and operating these telescopes. In optical testing, segmentation tightens the requirements on measurement and alignment accuracies of each mirror segments.

1.2 MOTIVATION FOR CURRENT WORK

The demands for measuring segments from large telescopes are unique. In addition to requiring accurate, low noise measurements, the test for segmented optics must meet the following requirements:

1. The relative radii of curvatures (ROC) need to be matched to an interferometric tolerance. When this requirement is not met, residual local power from segments degrades overall telescope performance significantly.

2. The mirror segments must be positioned accurately. This is because primaries get faster and larger, the aspherical departure of the segments (especially the outer segments) increases. If segments are not oriented and/or positioned correctly, their aspherical departure can no longer match the parent mirror. This can degrade the overall telescope performance considerably.

3. The measurement time for testing individual segments must be minimized. With primary mirrors getting larger, the number of segments increases drastically. For some current primary designs, a fabrication-testing rate of 1 segment per 24 hours is demanded.

Traditional asphere tests fail to address these issues unique to the segmented mirrors. The first telescope using the segmented mirrors, Keck Telescopes (1977-1993), has 36 pieces hexagonal segments and they were tested using time-consuming autocollimation method[8]. Using the same method to test nearly 1,100[11] pieces of 1-m segments that is proposed for the California Extremely Large Telescope (CELT) is impractical. This is because the primary mirror of CELT is 3 times larger than that of the Keck and uses 30 times more segments must be tested (Figure 1-3).

To summarize, the traditional asphere testing method fails to address unique requirements of testing segmented mirrors in several ways: (1) no built-in mechanism for establishing relative radius of curvature to interferometric tolerances, (2) no mechanism to establish accurate axis location for each segment, and (3) no efficiency in testing large quantities of segments due to lack of built-in alignment accuracy.

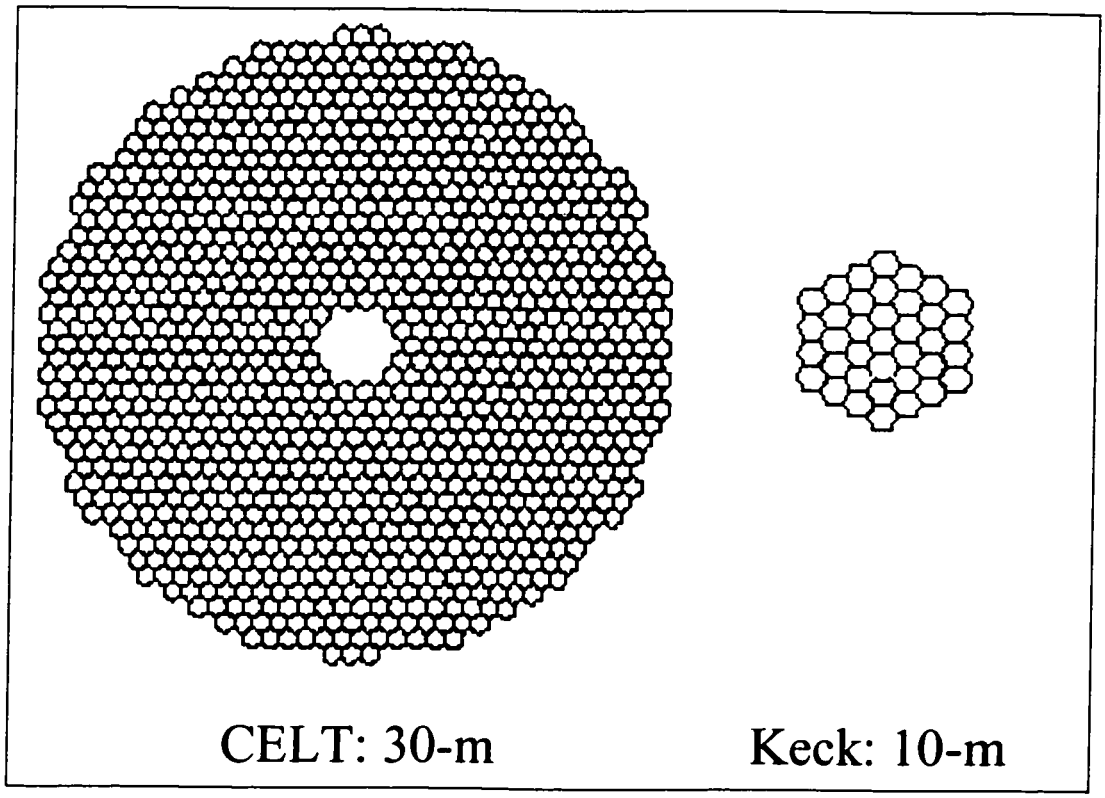

Figure 1-3 Geometry of California Extremely Large Telescope (CELT) primary mirror (f/1.5). The Keck mirror (f/1.75) geometry is shown to scale for comparison.

1.3 TOPIC OF RESEARCH

A new method, specifically designed to test large quantities of mirror segments in an accurate and efficient way is the topic of this dissertation. This new method, pioneered by J. Burge and D. Anderson[12,13], compares concave mirror segments to a matching-in-size convex spherical reference surface of a test plate. Small CGHs (approximately 30mm in diameter) are used to compensate aspherical departure of the segment from the reference surface. The reference surface is chosen to be spherical so it can be very cost effectively manufactured to high accuracy. Since all segments are compared to the same

reference surface located in close proximity to the segmented mirrors, this test provides excellent matching of radii of curvatures. Test of different segments is made by replacing only the CGH and making no other alignment after the initial alignment. Position of mirror segments are accurately registered using fiducial marks on the hologram that are projected on the test plate. More specifically, this new method has the following significant advantages:

1. High accuracy –achieves $\lambda/100$ RMS or better.
2. Low cost – requires only one highly accurate spherical reference surface to test all segments.
3. Simple to implement –needs minimal vibration/noise suppression due to its near-common path configuration
4. Excellent radius matching –can achieve < 0.010μm PV power in surface.
5. Accurate axis location –achieves high accuracy in absolute segment placement.

1.4 DISSERTATION CONTENTS

This dissertation presents a comprehensive analysis of the novel measurement method. In this dissertation, I first quantify how segmentation tightens testing requirements through series of simulation and theoretical calculations. Next I present a thorough investigation on the new method of testing aspherical segments where topics include: design trade-offs, optimization, experimental validation, and detailed error analysis. The objective of this work is fourfold. First, scrutinize the effect of segmentation on telescope performances. Second investigate design trade-offs and streamline the

optimization process. Both theory of operation and process of optimization are documented. Third validate this new method by providing experiment results so comparison can be made to traditional methods. Last, illustrate, through a case study, how to use this method to design a test system for measuring segmented mirror telescope (including error analysis).

This dissertation begins with an explanation on how segmentation tightens the testing requirements in Chapter 2. Segmented mirrors are sensitive to errors in the rigid body position of the mirror segments and to other errors that easily compensated for monolithic optics. This chapter mathematically quantifies how different fabrication and alignment errors degrade the telescope performance. This provides a strong motivation for introduction of the new method investigated by the author.

The theory of operation for the new method of testing aspherical mirror segments is documented in Chapter 3. The first part of this chapter provides a short summary on disadvantage of traditional aspherical testing methods in measuring the segmented mirrors. The second half of this chapter describes designs of each of the optical subsystems. Details such as advantages of this new method are also discussed.

Since one of the most import aspects of this new method is its inherent efficiency in testing large quantities of aspherical mirror segments, chapter 4 is devoted to the optimization of this method. This chapter documents the complete optimization process for designing and optimizing a test system to measure off-axis aspherical mirror segments.

Experimental data supporting the accuracy of this test is documented in Chapter 5 where a laboratory demonstration of the test method was performed. In this experiment, the CGH test method is used to measure a 30-cm spherical surface with known quality and the measurement result agreed with a conventional method to 3.7nm, within the error budget of 3.9nm for the test.

Chapter 6 gives a detailed case study that for testing a F/1.0 30-m parabolic primary mirror with 618 hexagonal 1-m segments using this new method. The design of this test system follows steps laid out in chapters 3 and 4. Tolerance analysis for this case study is the subject of Chapter 7. Even though the results obtained in this chapter pertain to a specific test system design, the process itself stays the same and can be applied to other test systems. Finally, Chapter 8 summarizes the results of this work and provides suggestions for future applications.

CHAPTER 2

SEGMENTATION TIGHTENS TESTING REQUIREMENTS

Segmented mirrors are sensitive to unique fabrication and alignment errors that are easily compensated for monolithic optics. Positioning errors such as piston and tilt, both are easily adjusted by shifting the location of the image plane for monolithic optics, can not be easily adjusted for segmented optics. This is because, with segmented mirrors, each segment may have a different piston and/or tilt error compared to other segments. As a result, these once benign alignment errors now lead to image degradation compared to the ideal diffraction limited case for the segmented optics.

In addition, segmented optics is sensitive to fabrication errors that are easily compensated for monolithic mirrors. For instance, radius of curvature error degrades the system performance in segmented mirrors whereas, in a monolithic mirror, a simple re-location of image plane compensates such error. Also, if aspherical profiles of segments are themselves erroneous (either caused by fabrication error or misalignment with respect to segments' mechanic features), higher order aberration results.

This chapter quantifies how these unique fabrication and alignment errors degrade the system performance of a segmented telescope. Organization of this chapter is as follows. Sections 2.1 gives definitions and an overview of five types of fabrication and

alignment errors unique to segmented optics. In Section 2.2 mathematical expressions on how these errors degrade the overall system performances are given.

2.1 FIVE ERROR SOURCES UNIQUE TO SEGMENTED MIRRORS

Five error sources unique to segmented mirrors are: matching of piston (or phasing) error, tilt (or pointing) error, power or (radius of curvature), translation (or segment) positioning, and rotation (or segment orientation). In this section, we first give definition for each error and then give corresponding mathematical expressions of the performance degradation.

To visualize how each type of the errors affects the overall phase wavefront of the parent mirror, two simulated plots[†] are provided: (a) phase map of the parent mirror and (b) interferogram of corresponding wavefront. Phase maps and the corresponding interferograms are produced using Monte Carlo calculation by following these steps:

Generate n Gaussian distributed random values α_i ($i=1, 2, ..., n$), where n is number of the segments in the primary.

Specify wavefront error, Δw_i, for each segment i ($i=1, 2, ..., n$). Pupil dependence of Δw_i varies as the type of the error that is being simulated. Magnitude of Δw_i is α_i generated in step 1.

[†] Collaborated with Mr. Y. Wang
Department of Information Engineering
ShiJiaZhuang University of Economics
ShiJiaZhuang, China

Generate the full aperture wavefront of the parent mirror, ΔW, which is the sum of all Δw_i, i.e.,

$$\Delta W = \sum_{i=1}^{n} \Delta w_i \qquad [2.1]$$

Compute the corresponding interferogram using equation [2.2]

$$I(x_p, y_p) = 0.5 + 0.5\left(\cos(\frac{2\pi}{\lambda}\Delta W)\right), \qquad [2.2]$$

where ΔW is found in equation [2.1].

2.1.1 Phasing or piston error

Phasing error has been well studied[14,15,16,17,18,19] and its importance is readily appreciated. To achieve diffraction-limited performance, a segmented mirror telescope must be phased, that is the piston errors between segments must be reduced to a small fraction of wavelength. This enables individual images from each segment be superimposed coherently. A poorly phased telescope can only achieve resolution limit set by the size of the segment not the full parent aperture.

We quantify the effect of piston error as a wavefront error across the segment given by:

$$\Delta w_i(x,y) = 2\,\alpha_i \qquad [2.3]$$

where,

$\Delta w_i(x,y)$: wavefront error of the ith segment in the pupil coordinates (x,y)

α_i: ith segment's random piston error at the segment surface, measured in waves

Piston error is illustrated below where α_i's are selected from a random Gaussian distribution with zero mean and standard deviation of σ. Figure 2-1 shows how random piston error affects the full aperture wavefronts. Figures Figure 2-2 and Figure 2-3

depict the interferograms of the wavefront corresponding to RMS piston error with σ =0.05 λ and 0.15 λ respectively.

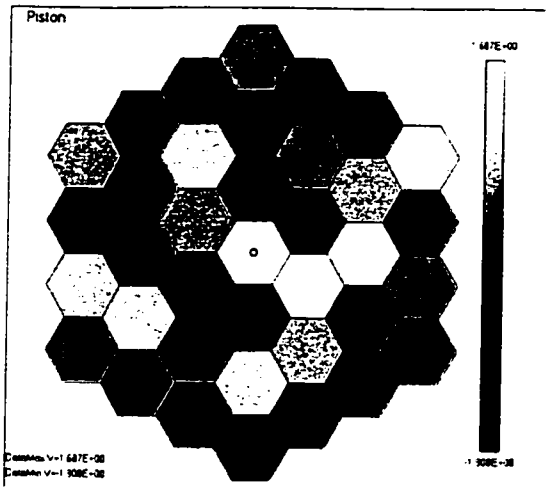

Figure 2-1. Phase map of the full aperture. Standard deviation of the piston error is σ=0.15 λ.

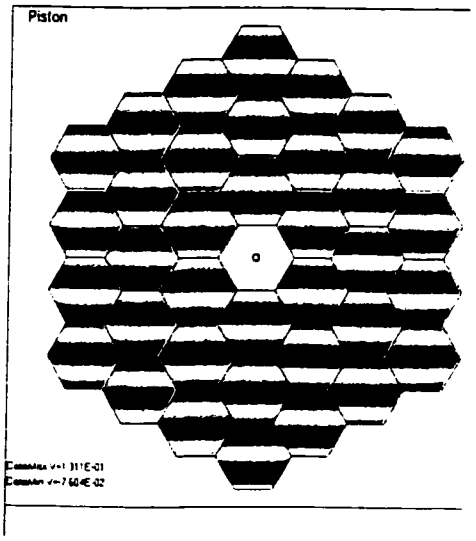

Figure 2-2. Interferogram of the primary when RMS piston error is σ=0.05 λ.

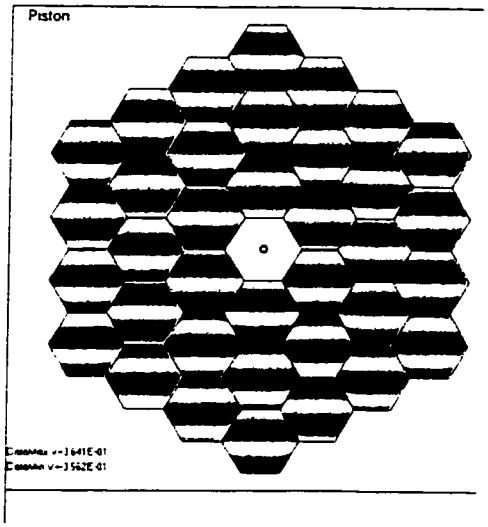

Figure 2-3. Interferogram of the primary when RMS piston error is σ=0.15 λ.

2.1.2 Tilt error

The individual segments must be matched in their tilt. We quantify the effect of tilt error as a wavefront error across the segment given by:

$$\Delta W_i = 2\,[\beta_i (x/a_0) + \gamma_i (y/a_0)]\,, \qquad [2.4]$$

where,

$\Delta W_i(x,y)$: wavefront error of the ith segment, in pupil coordinates (x,y)

a_0: segment radius

β_i, γ_i: random x-tilt and y-tilt errors, at the segment surface, for the ith segment

Tilt error is illustrated below where β_i's and γ_i's are selected from two independent random Gaussian distributions with zero mean and same standard deviation $\sigma_\beta=\sigma_\gamma=\sigma$. Figure 2-4 shows how random tilt errors affect the full aperture wavefronts for a RMS tilt errors of $\sigma_x=\sigma_y=0.15\ \lambda$. Figure 2-5 and Figure 2-6 depict the interferograms of the wavefront corresponding to $\sigma_x=\sigma_y=0.05\ \lambda$ and 0.15λ respectively.

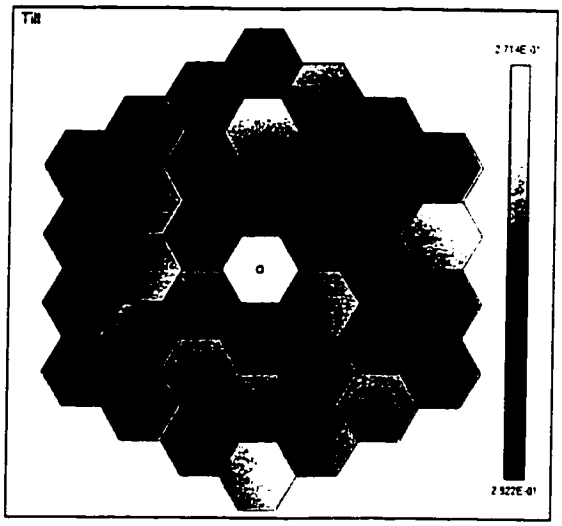

Figure 2-4. Phase map of the full aperture when random tilt error is present. Standard deviation of the piston error is $\sigma=0.15\ \lambda$.

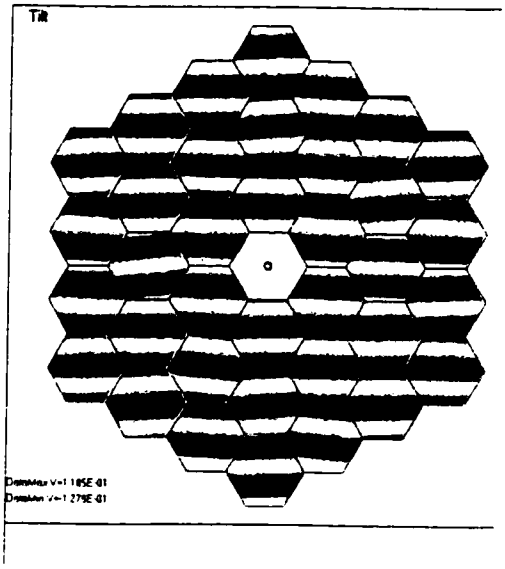

Figure 2-5. Interferogram of the primary mirror when RMS tilt errors are $\sigma_\beta=\sigma_\gamma=0.05\ \lambda$.

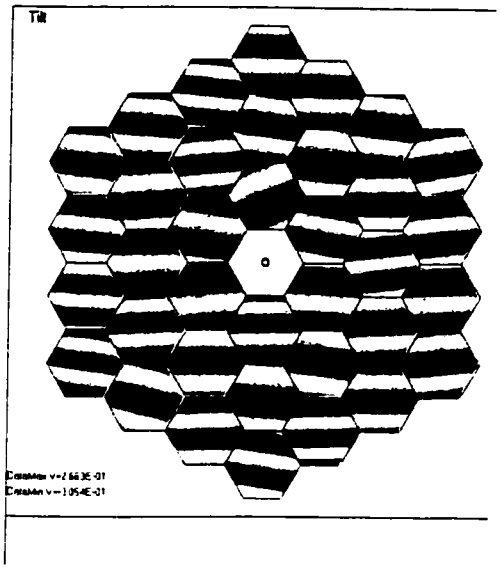

Figure 2-6. Interferogram of the primary mirror when RMS tilt errors are $\sigma_\beta=\sigma_\gamma=0.15\ \lambda$.

2.1.3 Unmatched relative radius of curvature (ROC)

Radius of curvature must also be matched in all the segments. The radius of curvature (ROC) error varies as the square of radial position in segment. We quantify the effect of tilt error as a wavefront error across the segment given by:

$$\Delta W_i = 2S_i\,(a/a_0)^2 \qquad [2.5]$$

where,

$\Delta W_i(a.\theta)$: wavefront error of the ith segment, in pupil coordinates (ρ, θ)
S_i: random sag error for the ith segment
a_0: segment half-diameter

Sag error is illustrated below, where the magnitude of the error in each segment, S_i, are generated through a Gaussian random variable with zero mean and standard deviation of

σ. Figure 2-7 shows how random sag error with RMS $\sigma = 0.15\ \lambda$ affects the full aperture wavefronts. Figure 2-8 and Figure 2-9 depict interferograms of the wavefront corresponding to RMS sag errors of $\sigma = 0.05\lambda$ and 0.15λ respectively.

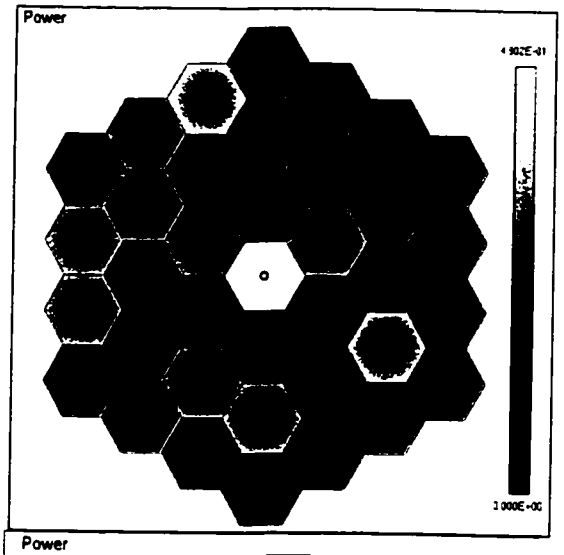

Figure 2-7 Phase map of the full aperture. Standard deviation of the sag error is $\sigma = 0.15\ \lambda$.

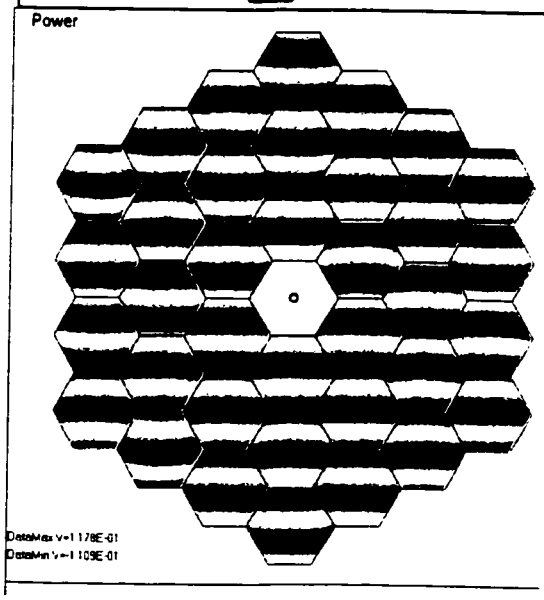

Figure 2-8. Interferogram of the primary mirror when RMS tilt errors are $\sigma = 0.05\ \lambda$.

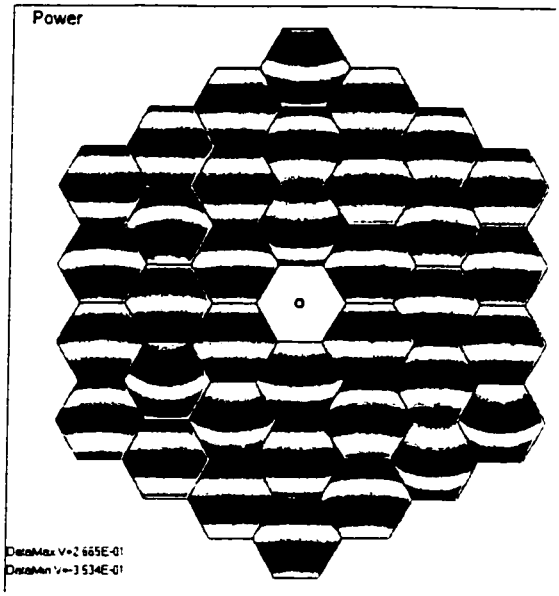

Figure 2-9 Interferogram of the primary mirror when RMS tilt errors are $\sigma = 0.15\ \lambda$.

2.1.4 Segment positioning or rotation error

Three types of in plane position errors of segment are rotation, radial translation, and tangential translation (Figure 2-10). Rotational and translation errors or misalignment refer to clocking and radial shift of the segment. These displacements introduce lower order wavefront error, whereas, due to symmetry, the tangential displacement of the segment does not. Unlike previous three errors, the effect of rotation and radial translation errors depend on the segment size and on the parameters of the parent mirror.

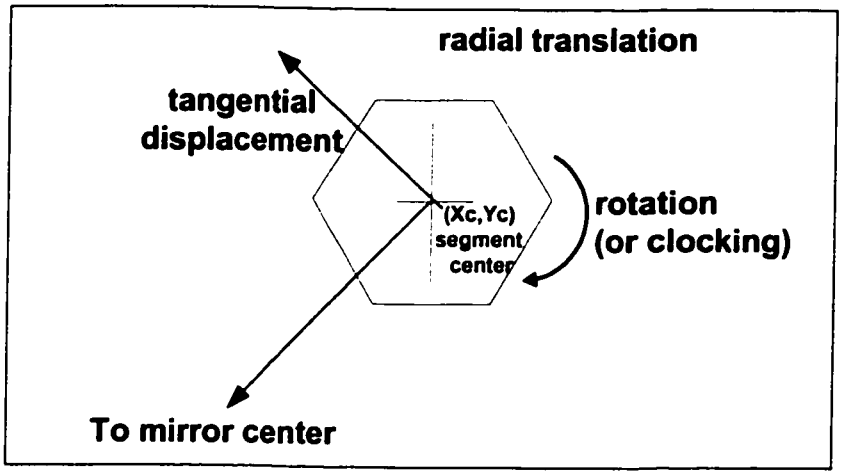

Figure 2-10. Three in-plane displacement errors are: rotation, radial displacement, and tangential displacement. Due to symmetry, only the first two types introduce lower order aberrations.

To model the rotation and translation errors, we have to first find the aspherical departure, $A_i(a,\theta)$, of the segments in the local segment coordinates (a, θ) and then use Eqn.[2.6] to calculate the induced wavefront error due to these displacements.

$$\Delta w_i = \frac{\partial A_i}{\partial b}(\Delta b)_i,$$

$$\Delta w_i = \frac{\partial A_i}{\partial \theta}(\Delta \theta)_i \qquad [2.6]$$

where,

$A_i(a,\theta)$: aspherical departure of the ith segment, in local segment coordinates (a, θ)

Δb_i: random radial translation error of the ith segment

$\Delta \theta_i$: random rotation error of the ith segment

To find the aspheric departure in the local segment coordinates, we start by using the simple aspheric departure equation for the parent mirror:

$$S(r) := a_4 \cdot r^4 + a_6 \cdot r^6 + a_8 \cdot r^8 + a_{10} \cdot r^{10} + ... \qquad [2.7]$$

where,

$$a_4 := \frac{K}{8 \cdot R^3} + A1$$

$$a_6 := 3 \cdot \frac{\left[(K+1)^2 - 1\right]}{48 \cdot R^5} + A2$$

$$a_8 := 15 \cdot \frac{\left[(K+1)^3 - 1\right]}{384 \cdot R^7} + A3$$

$$a_{10} := 105 \cdot \frac{\left[(K+1)^4 - 1\right]}{3840 \cdot R^9} + A4$$

(r,φ): global radial coordinate of the parent mirror

A1, A2,A3 and A4: higher order aspheric polynomial deformation terms (all zero for simple parabolic primary).

Next, the global radius coordinate (r, ϕ) of the parent mirror is connected to the local coordinates (a, θ) of the segments. This is depicted in Figure 2-11 and the equation [2.8] connects these two coordinate systems.

$$X_g = b\cos(\phi_c) + a\cos(\theta)$$
$$Y_g = b\cos(\phi_c) + a\cos(\theta) \qquad [2.8]$$

where the meaning of each variable is explained in Table 2-1.

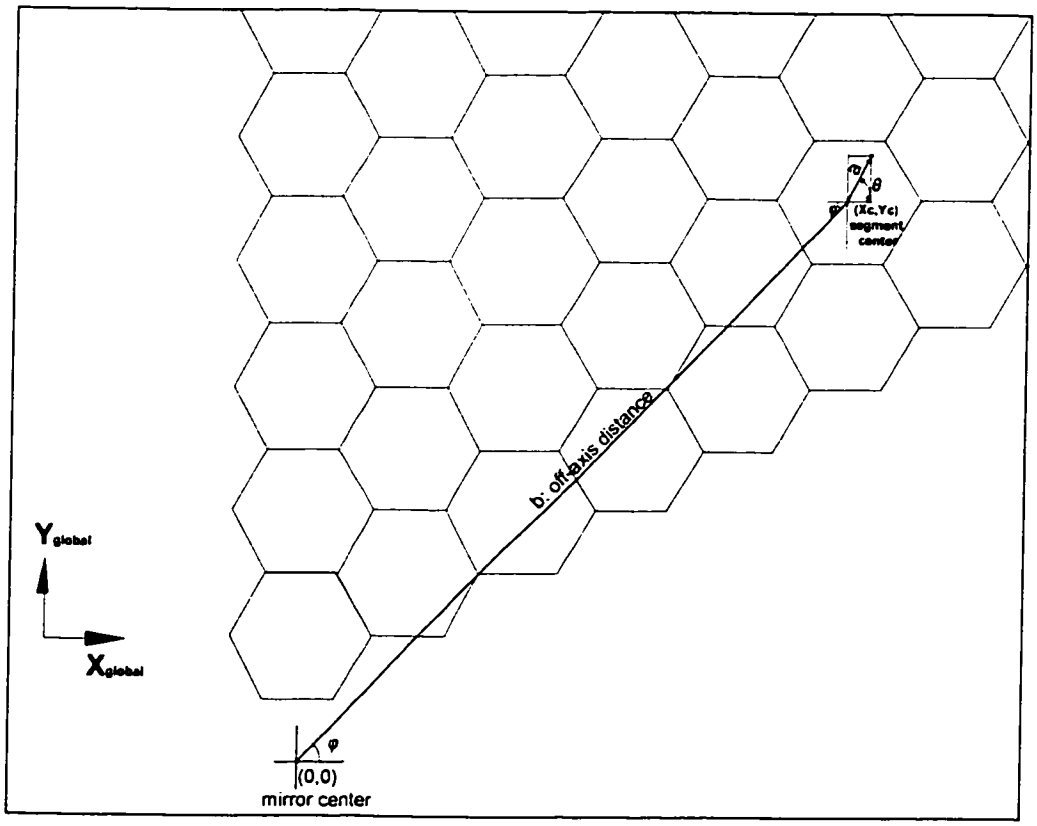

Figure 2-11 Global coordinate system (r,ϕ) is related to the local segment coordinate system (a, θ) through equation [2.8]

Finally, we substitute equation [2.8] into [2.7] and gather appropriate terms together according to their dependence on the pupil coordinates (a,θ), we have aspherical departures in each segment that are similar to third order Seidel aberrations (Table 2-2):

Table 2-1. Definitions of the variables in Eqn. [2.8]

Variable name		Meaning	Coordinate system
(X_g, Y_g) or (b,ϕ)		Location of segment center	global
$X_G = b\cos(\phi)$ $Y_G = b\sin(\chi)$	$b^2 = X_g^2 + Y_g^2$ $\phi = \tan^{-1}(Y_g / X_g)$		
(x_l, y_l) or (a, θ)		Location of an arbitrary point in the segment	local
$x_l = a\cos(\theta)$ $y_l = a\sin(\theta)$	$a^2 = x_l^2 + y_l^2$ $\phi = \tan^{-1}(y_l / x_l)$		

Table 2-2 Aspherical departure in individual segment

Spherical aberration like term:

$$C_{40}(a) := \left(\frac{K}{8 \cdot R^3}\right) \cdot a^4$$

Coma like terms:

$$C_{31}(a,\theta) := \left(4 \cdot b \cdot \frac{K}{8 \cdot R^3}\right) \cdot a^3 \cdot \cos(\theta)$$

Astigmatism like term:

$$C_{22}(a,\theta) := \left(2 \cdot b^2 \cdot \frac{K}{8 \cdot R^3}\right) \cdot a^2 \cdot \cos(2 \cdot \theta)$$

Trefoil term:

$$C_{33}(a,\theta) := \left[2 \cdot b^3 \cdot \frac{\left[(K+1)^2 - 1\right]}{16 \cdot R^5}\right] \cdot a^3 \cdot \cos(3 \cdot \theta)$$

Quadfoil term:

$$C_{44}(a,\theta) := \left[10 \cdot b^4 \cdot \frac{\left[(K+1)^3 - 1\right]}{128 \cdot R^7}\right] \cdot a^4 \cdot \cos(4 \cdot \theta)$$

where,

(a,θ): local coordinates of the segments

k: conic constant of the primary mirror

R: radius of curvature of the parent mirror

b: off-axis distance of the segment as depicted in Figure 2-11.

Using Table 2-2, we can now generate the wavefront for individual segments when rotation error is present:

$$\Delta w_i = \left[\frac{\partial}{\partial \theta}\left(C_{40(a,\theta)} + C_{31(a,\theta)} + C_{22(a,\theta)} + C_{33(a,\theta)} + C_{44(a,\theta)}\right)\right](\Delta\theta)_i, \qquad [2.9]$$

where,

$\Delta\theta_i$: magnitude of rotation error for the i^{th} segment (measured in radian).

Rotation error is illustrated below where $\Delta\theta_i$'s are drawn from a Gaussian distribution with zero mean and standard deviation of σ. Simulation of the full aperture phase map is shown in Figure 2-12 where σ=0.15 mrad for the case of an f/1 10-m primary with 1.8-m segments (size of diameters). Figure 2-13 through Figure 2-15 depict interferograms corresponding to rms rotation error of σ=0.015-mrad and 0.15-mrad respectively.

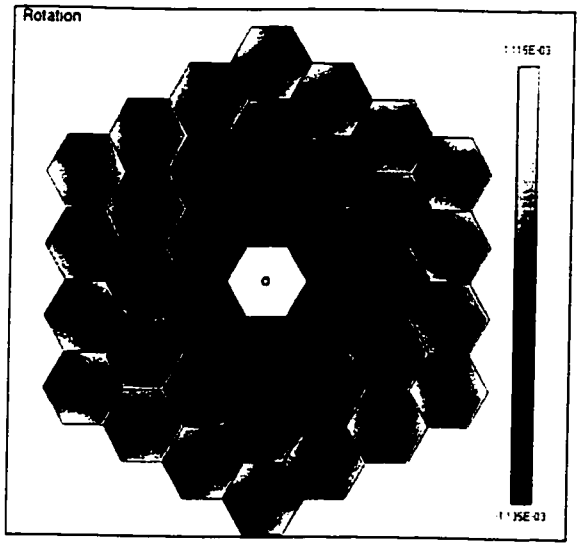

Figure 2-12. Phase map of the full aperture when random rotation error is present (σ=0.15mrad). Parent mirror is an F/1 10-m paraboloid consists of 36 1.8-m hexagonal segments.

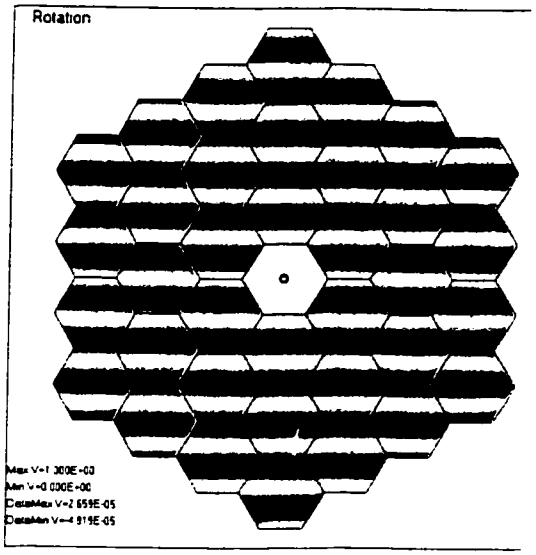

Figure 2-13. Interferogram of the primary mirror when RMS tilt errors are σ=0.015mrad

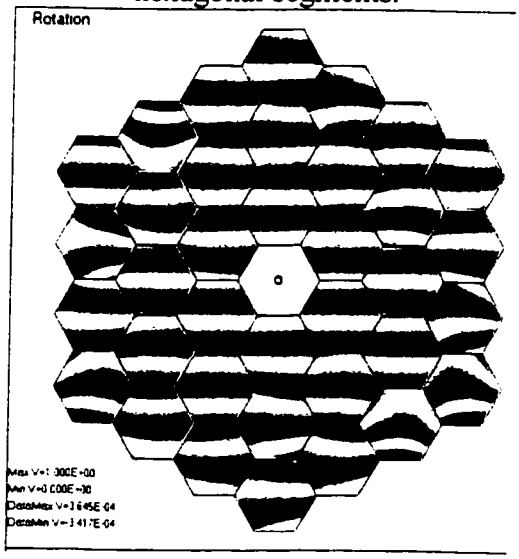

Figure 2-14 Interferogram of the primary mirror when RMS tilt errors are σ=0.15mrad.

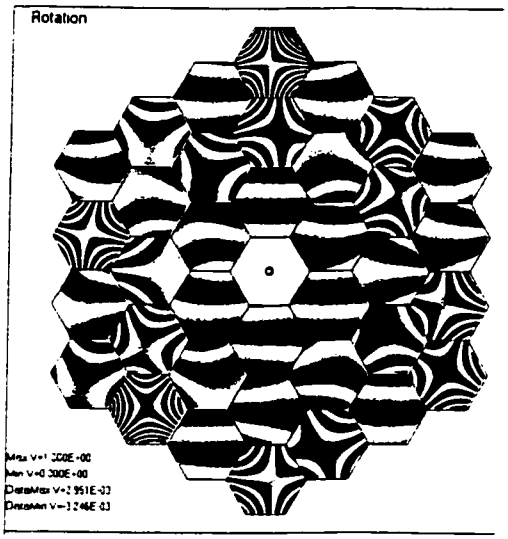

Figure 2-15. Interferogram of the primary mirror when RMS tilt errors areσ=1.5 mrad.

2.1.5 Segment location or radial translation error

When segments are misaligned in the radial direction, lower order aberration ,coma like in this case, are present. We quantify the effect of this radial translation error as a wavefront error across the segment given by Eqn.[2.10] where we took derivative with respect to b_i, the off-axis distance of any segment:

$$\Delta w_i(a,\theta) = \left[\frac{\partial}{\partial b_i}\left(C_{40(a,\theta,b_i)} + C_{31(a,\theta,b_i)} + C_{22(a,\theta,b_i)} + C_{33(a,\theta,b_i)} + C_{44(a,\theta,b_i)}\right)\right](\Delta b)_i, \quad [2.10]$$

where

$\Delta w_i(a,\theta)$: wavefront error of the ith segment when radial translation error is present

(a,θ): local coordinates of the segments

b_i: off-axis distance of the ith segment as depicted in Figure 2-11

Δb_i magnitude of the radial translation error for the ith segment

Radial translation error is illustrated below where Δb_i (measured in radian) is drawn from a Gaussian distribution with standard deviation of σ. Simulation of the full aperture phase map is shown in Figure 2-16 where σ=0.15-mm for an F/1.0 10-m primary with segment diameter of 1.8-m. Figure 2-17 through Figure 2-19.depict interferograms corresponding to rms translation error of σ=0.015-mm, 0.15-mm and 1.5-mm respectively. Much like the results for the rotation case, the results depend on the size of the segment .

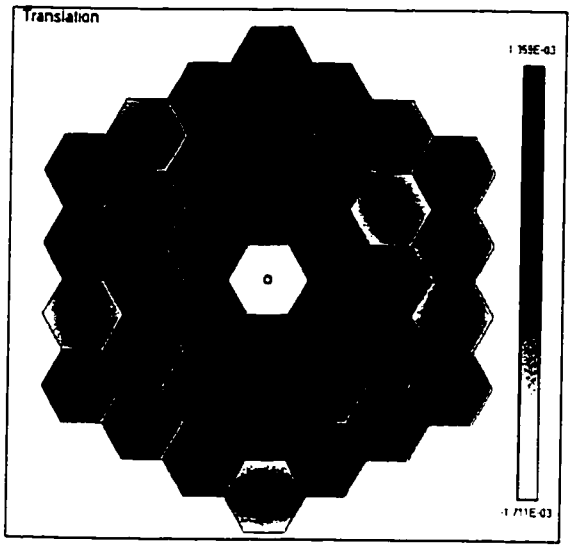

Figure 2-16. Phase map of the full aperture when random translation error is present. Standard deviation of the error is 1.5-mm. (Parent mirror is a F/1 30-m paraboloid consists of 36 1.8-m hexagonal segments).

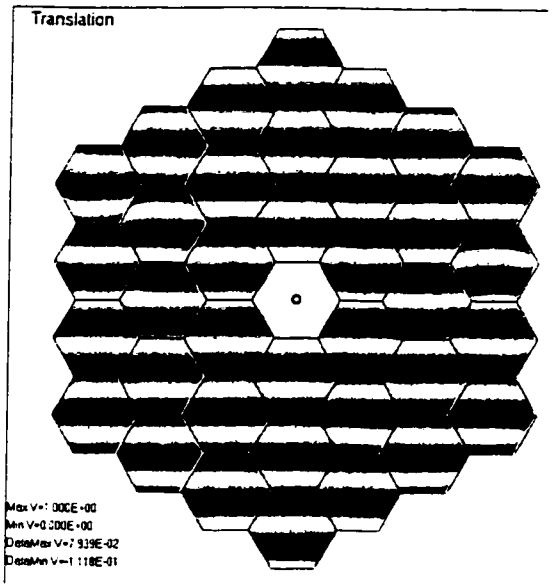

Figure 2-17 Interferogram of the primary mirror when RMS translation error has σ=0.05 mm.

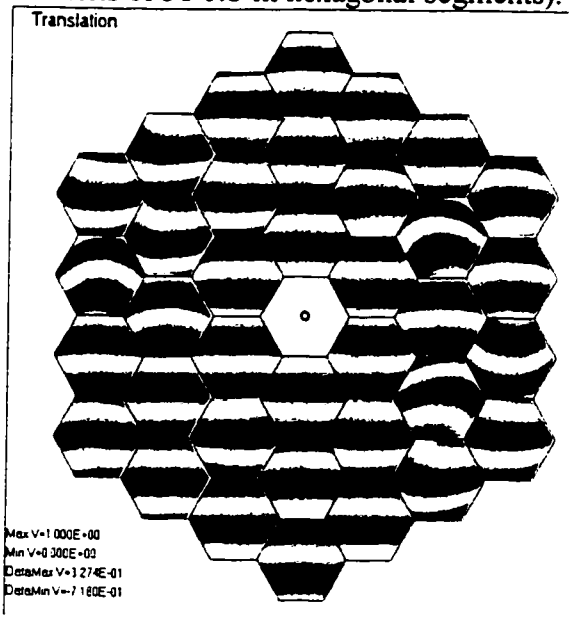

Figure 2-18 Interferogram of the primary mirror when RMS translation error has σ=0.27mm .

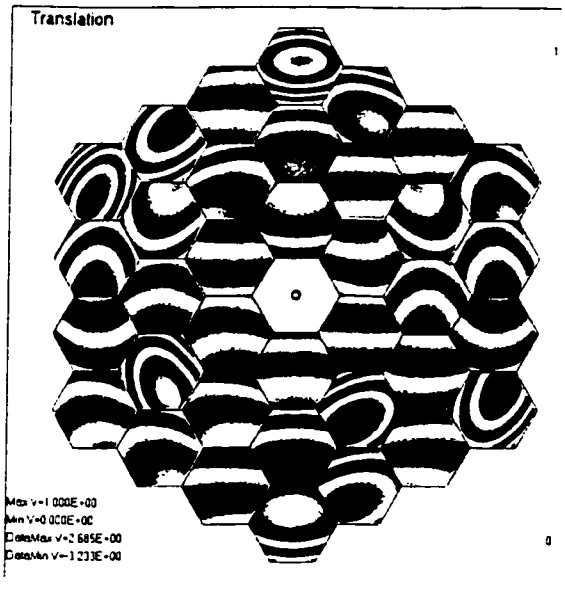

Figure 2-19. Interferogram of the primary mirror when RMS translation error has σ=1.5 mm .

2.2 HOW ERRORS DEGRADE THE TELESCOPE PERFORMANCE

Five fabrication and alignment errors unique to segmented optics affect the system performance. In this section, we quantify how Strehl ration (SR) varies as a function of these errors. Strehl ratio (SR) is defined as the ratio of the intensity at the Gaussian image point in the presence of aberration, divided by the intensity obtained without aberration. The SR is an excellent figure of merit for near diffraction-limited systems such as space telescopes or ground-based telescope with adaptive optics. For seeing limited telescopes, we use the RMS wavefront error σ_W instead. Mathematically, SR can be calculated by[20]

$$SR = \frac{1}{\pi^2}\left|\int_0^{2\pi}\int_0^1 e^{i2\pi\Delta W(\rho,\theta)}\,\rho d\rho\, d\theta\right|^2, \qquad [2.11]$$

where, ΔW, measured in units of waves, is the wavefront aberration relative to the reference sphere for the diffraction focus.

For small RMS wavefront errors, where SR>0.1, Eqn. [2.11] can be approximated by Eqn.[2.12], and we use this approximation to quantify how fabrication and alignment errors affect the SR of the system.

$$SR \approx e^{-(2\pi)^2\left(\overline{\Delta W^2}-\left[\overline{\Delta W}\right]^2\right)} \qquad [2.12]$$

Before applying Eqn. [2.12] to segmented optics, we must realize that for our case, ΔW is the sum of the wavefront from each segment from the primary mirror

(Eqn.[2.1]). From here, applying mathematical definitions of 1st and 2nd moments of ΔW (Eqns. [2.13] and [2.14]), we found a general expression (Eqn.[2.16]) to calculate Strehl Ratio for segmented optics (Appendix A).

$$\overline{\Delta W^2} \overset{def}{=} \frac{\iint [\Delta W]^2 dA}{\iint dA}, \text{ (dA is integrated over the primary mirror)} \quad [2.13]$$

$$\overline{\Delta W} \overset{def}{=} \frac{\iint [\Delta W] dA}{\iint dA}, \text{ (dA is integrated over the primary mirror)} \quad [2.14]$$

$$\sigma_w^2 = \overline{\Delta W^2} - \left[\overline{\Delta W}\right]^2 \quad [2.15]$$

$$SR \approx e^{-(2\pi\sigma_w)^2}$$

$$= EXP\left[-(2\pi)^2\left[\frac{\sum_{i=1}^{N}\iint (\Delta w_i)^2 da_i}{\sum_{i=1}^{N}\iint da_i} - \left[\frac{\sum_{i=1}^{N}\iint (\Delta w_i) da_i}{\sum_{i=1}^{N}\iint da_i}\right]^2\right]\right], \quad [2.16]$$

where da_i is integrated over the segments.

Using Eqn. [2.16], it is possible to calculate how SR changes as a function of five types of error discussed earlier. Eqn. [2.16] is cumbersome for any practical use since it is based on Monte Carol numerical calculation, so we carried Eqn. [2.16] further and developed closed forms for each of the five errors. The detailed derivations are included in Appendix A and results are reported in Table 2-3. To verify these closed forms, we plotted SR for each types of error using first the Monte Carlo method and then the close forms and results are in excellent agreement. Table 2-4. Few points are noted:

(1) The SR analysis on phasing is in excellent agreement with previously established closed analytical expression calculated by Chanan[14] (Eqn. [2.17]). As

N, the number of segments gets large, $SR \xrightarrow{\text{large N}} e^{-(2\pi \cdot 2\sigma_p)^2}$ which is the same as Eqn.[2.28] in Table 2-4.

$$SR = \frac{1+(N-1)e^{2^2(2\pi)^2\sigma_p^2}}{N}, \qquad [2.17]$$

where

N: total number of segments
σ_p: RMS piston error at the segment surface.

(2). Piston error is more detrimental compared to tilt and ROC mismatch as shown by Eqns. [2.28], [2.29] and [2.30] where SR is calculated as a function of RMS these three errors. Figure 2-20 through

Figure 2-22 shows that SR degrades with a faster curvature with piston error than with other two errors.

(3). The translation and rotation errors have a higher dependency on segment size (quadratic dependence) than on F/# of the primary. This can be observed from Figure 2-25 through Figure 2-28 where plots were generated for the following three scenarios (a) through (c):

	F/ 0.6	F/1.0
segment diameter a=2-m	(a) M=13 rings	(b) M=9 rings
a=1-m		(c) M=17 rings

Table 2-3. RMS wavefront as a function of alignment/fabrication errors

Error	Monte Carlo Numerical Results	Closed form
Piston error	$\sigma_{WF}^2 = 4\left(\frac{\sum_i (\alpha_i)^2}{N} + \left[\frac{\sum_i (\alpha_i)}{N}\right]^2\right)$ [2.18]	$\sigma^2_{WF} = 4\,\sigma^2_p$, [2.19]
	where α_i's are drawn from the Gaussian distribution with zero mean and standard deviation of σ_p	where σ_p : rms piston error at the mirror surface
Tilt error	$\sigma_{WF}^2 = \sum_i \frac{(\beta_i)^2}{N} + \frac{(\gamma_i)^2}{N}$, [2.20]	$\sigma^2_{WF} = 2\,\sigma^2_{tilt}$, [2.21]
	where β_i and γ_i are independently drawn from two Gaussian distributions each with 1/e width of σ_{tilt}	where σ_{titl} : rms tilt error at the mirror surface
Relative radius of curvature (ROC) mismatch	$\sigma_{WF}^2 = \frac{4}{3}\left(\frac{\sum_i (s_i)^2}{N}\right)$, [2.22]	$\sigma^2_{WF} = 4/3\,\sigma^2_s$, [2.23]
	where s_i's are drawn from the Gaussian distribution with 1/e width of σ_s	where σ_s: rms sag error at the mirror surface

Table 2-3. RMS wavefront as a function of alignment/fabrication errors (cont)

Error	Monte Carlo Numerical Results	Closed form
Translation error	$\sigma_{WF}^2 = \frac{2}{3}\left(\frac{ka_0^2}{2R^3}\right)^2\left(\frac{\sum_i(\Delta b_i)^2}{N}(b_i)^2\right)$, [2.24]	$\sigma_{WF}^2 = \frac{3}{4}\left(\frac{k^2M^2(M+1)^2}{N}\right)\left(\frac{a_0}{R}\right)^6\sigma_{\Delta b}^2$ [2.25]
	where k: conic constant R: radius of curvature; a_0: segment radius b_i :segment center distance from the parent mirror's optical axis. Δb_i: tranlation error for the ith segment. Drawn from the Gaussian distribution with 1/e width of $\sigma_{\Delta b}$ (RMS translation error).	where M: total number of rings N: total number of segments K: conic constant R: primary mirror radius of curvature $\sigma_{\Delta b}$ is the rms translation error at the mirror surface
Rotation error	$\sigma_{WF}^2 = \frac{16}{6}\left(\frac{\sum_i(\Delta\theta_i)^2}{N}\left(\frac{ka_0^2}{4R^3}b_i\right)^2\right)$ [2.26]	$\sigma_{WF}^2 = 9\left(\frac{\sigma_{\Delta w}^2}{N}\right)\left(\frac{a_0}{R}\right)^6(ka_0)^2\sigma_{\Delta w}^2\sum_{j=1}^{M}j^5$ [2.27]
	where k: conic constant R: radius of curvature; a_0: segment radius b_i :segment center distance from the parent mirror's optical axis. $\Delta\theta_i$: rotation error for the ith segment. Drawn from the Gaussian distribution with 1/e width of $\sigma_{\Delta\theta}$ (RMS rotation error).	where M: total number of rings N: total number of segments K: conic constant R: primary mirror radius of curvature $\sigma_{\Delta\theta}$:the rms rotation error at the mirror surface

Table 2-4. Strehl Ratio for five types of alignment/fabrication errors.

PISTON ERROR

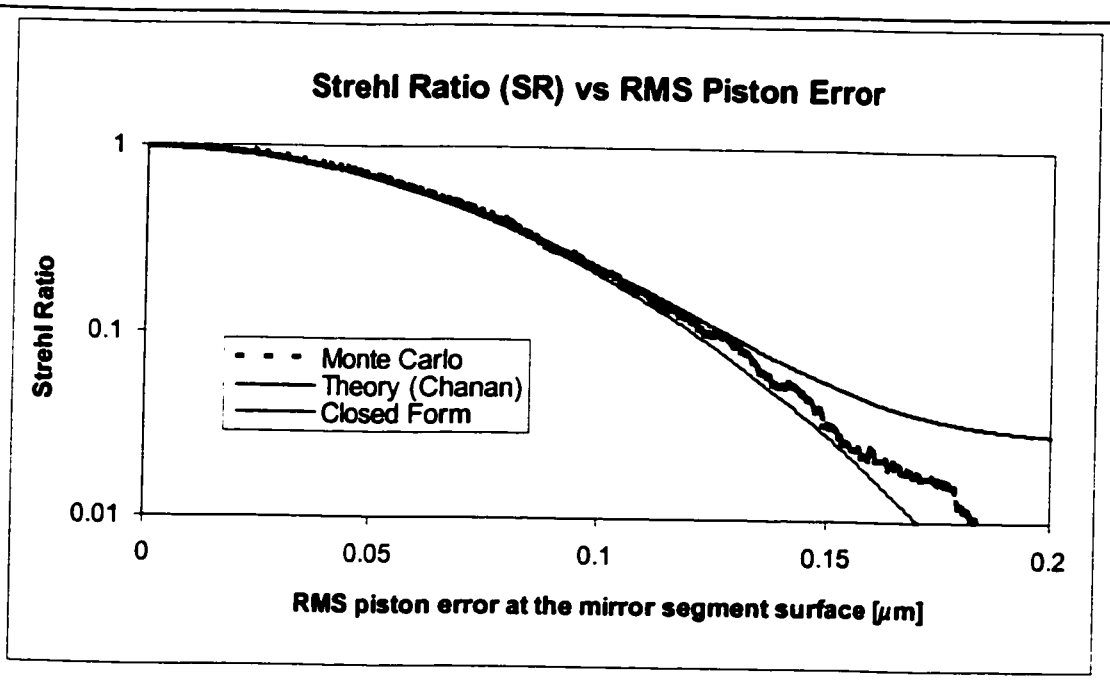

Figure 2-20. Strehl Ratio as a function of RMS piston error at the mirror surface. Solid smooth line is plotted using Eqn. [2.28] and the rippled line is using Monte Carlo calculation described in this chapter.

$$SR \approx e^{-(2\pi \cdot 2\sigma_{piston})^2} \qquad [2.28]$$

Table 2-4 (cont.) Strehl Ratio for five types of alignment/fabrication errors.

Tilt error

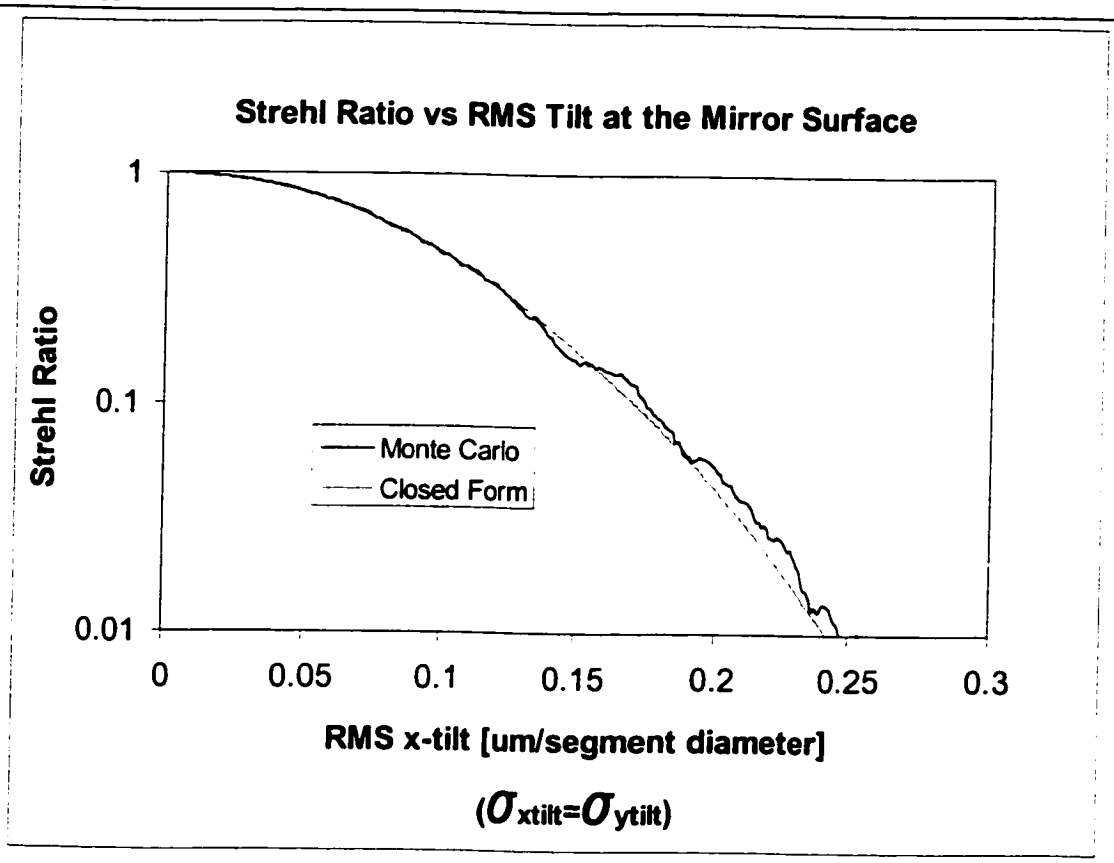

Figure 2-21 Strehl Ratio as a function of RMS tilt error at the mirror surface. Solid smooth line is plotted using Eqn. [2.29] and the rippled line is using Monte Carlo calculation described in this chapter.

$$SR \approx e^{-(2\pi \cdot \sqrt{2}\sigma_{tilt})^2} \qquad [2.29]$$

Table 2-4 (cont.) Strehl Ratio for five types of alignment/fabrication errors.

ROC error

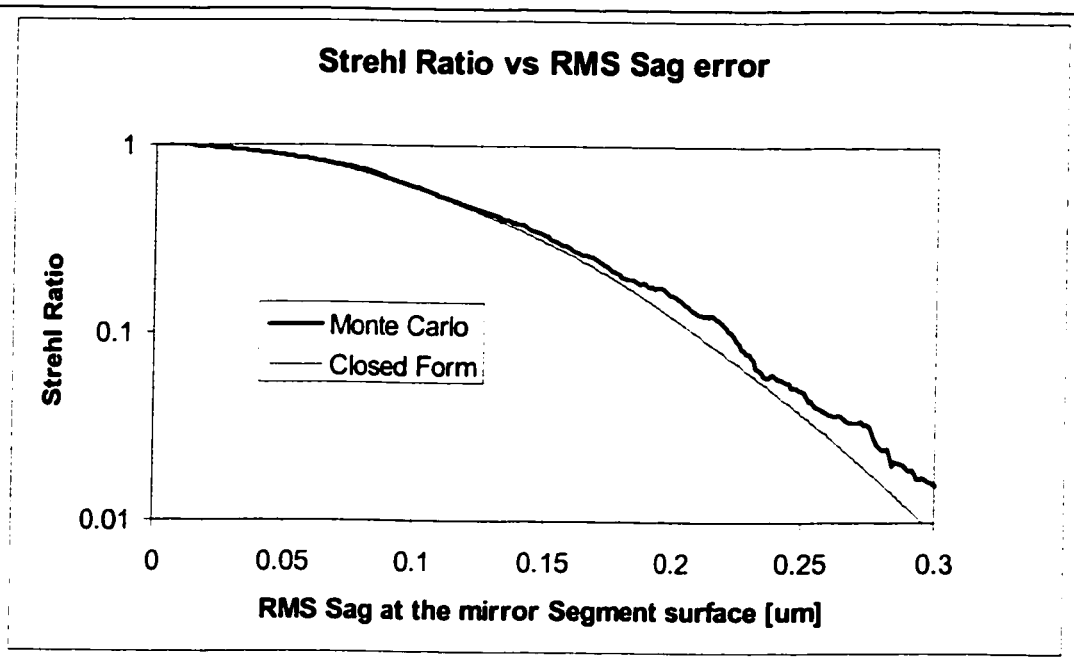

Figure 2-22. Strehl Ratio as a function of RMS relative radius of curvature (ROC) mismatch at the mirror surface. Solid smooth line is plotted using Eqn. [2.30]and the rippled line is using Monte Carlo calculation described in this chapter.

$$SR = e^{-\left(2\pi \cdot \sqrt{\frac{4}{3}}\sigma_{sag}\right)^2} \qquad [2.30]$$

Table 2-4 (cont.) Strehl Ratio for five types of alignment/fabrication errors.

Translation Error

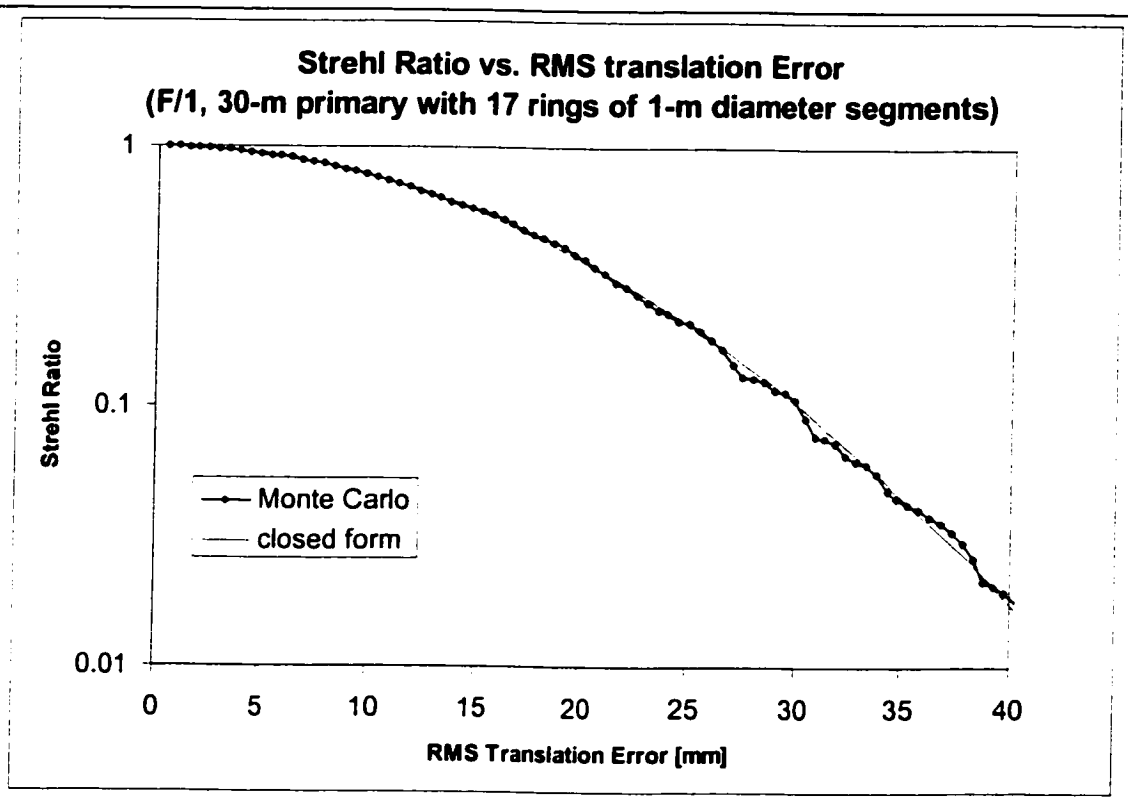

Figure 2-23. Strehl Ratio as a function of RMS translation error. Solid smooth line is plotted using Eqn. [2.31] and the rippled line is using Monte Carlo calculation described in this chapter.

$$SR = EXP\left[-\left(\frac{2\pi}{\lambda}\right)^2 \frac{3}{4}\left(\frac{k^2M^2(M+1)^2}{N}\right)\left(\frac{a}{R}\right)^6 \sigma_{\Delta\delta}^2\right] \qquad [2.31]$$

Table 2-4 (cont.) Strehl Ratio for five types of alignment/fabrication errors.

Rotation Error

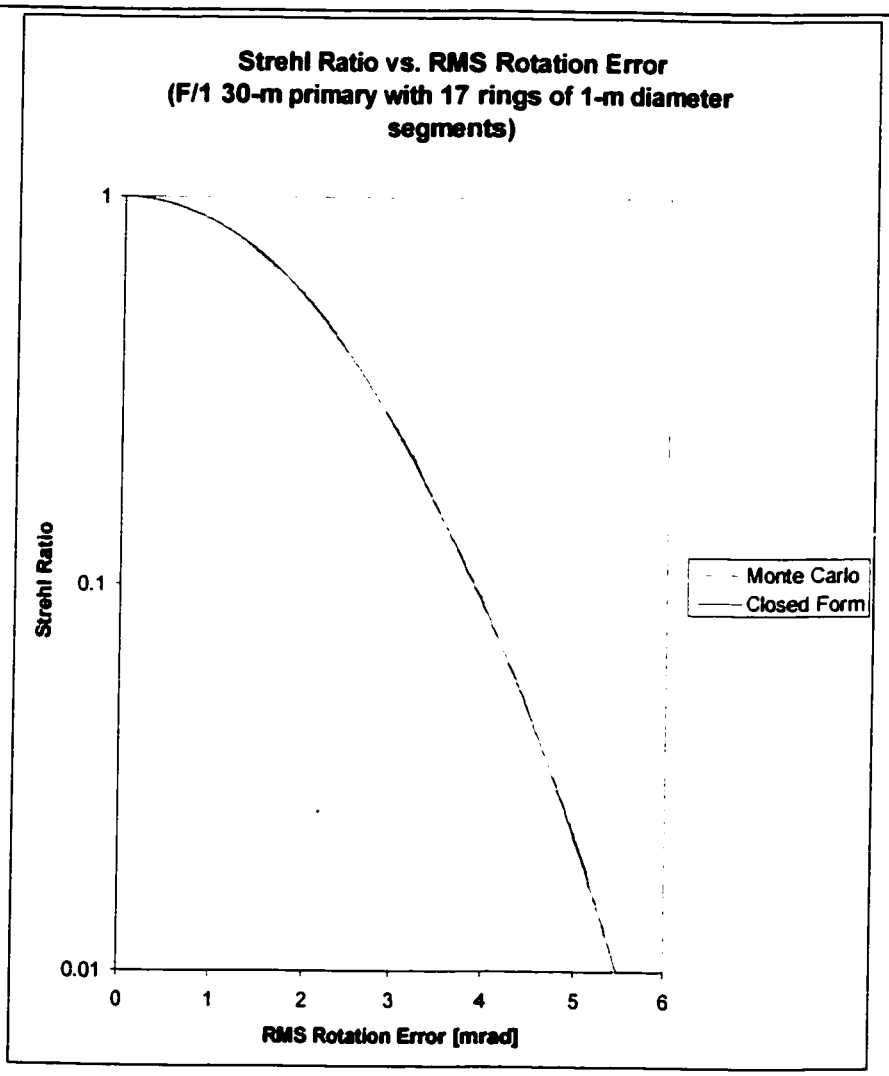

Figure 2-24. Strehl Ratio as a function of RMS relative radius of curvature (ROC) mismatch at the mirror surface. Solid smooth line is plotted using Eqn. [2.32] and the rippled line is using Monte Carlo calculation described in this chapter.

$$SR = EXP\left[-\left(\frac{2\pi}{\lambda}\right)^2 9\left(\frac{\sigma_{\Delta\omega}^2}{N}\right)\left(\frac{a}{R}\right)^6 (ka)^2 \sigma_{\Delta\omega}^2 \sum_{j=1}^{M} j^5\right] \qquad [2.32]$$

Table 2-5. Comparison of Translation and rotation tolerances as function of primary mirror F/# and segment diameter

Translation Error

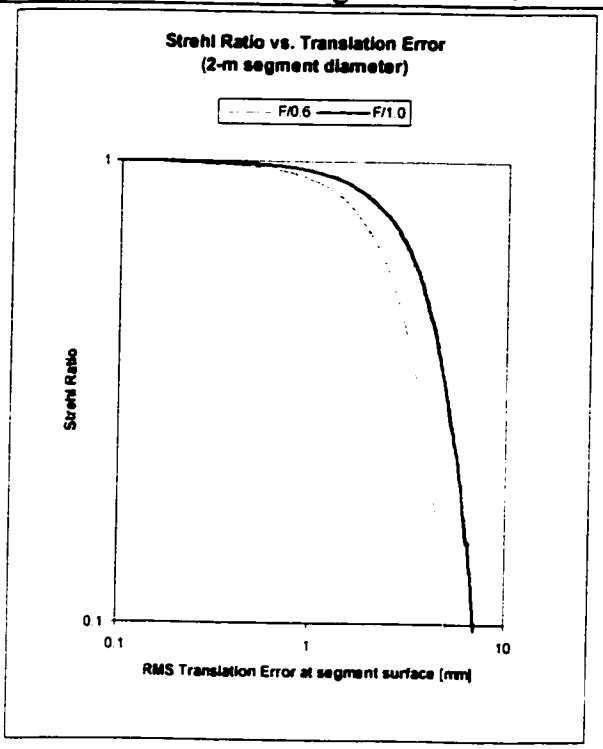

Figure 2-25. Strehl Ratio as a function of RMS translation error (F/1 and F/0.6 primary mirrors).

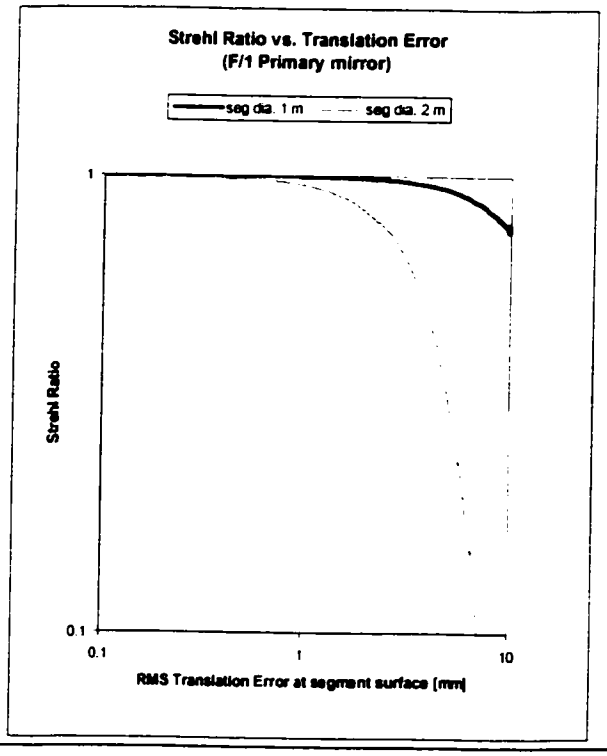

Figure 2-26. Strehl Ratio as a function of RMS translation error (1-m and 2-m segments).

Rotation Error

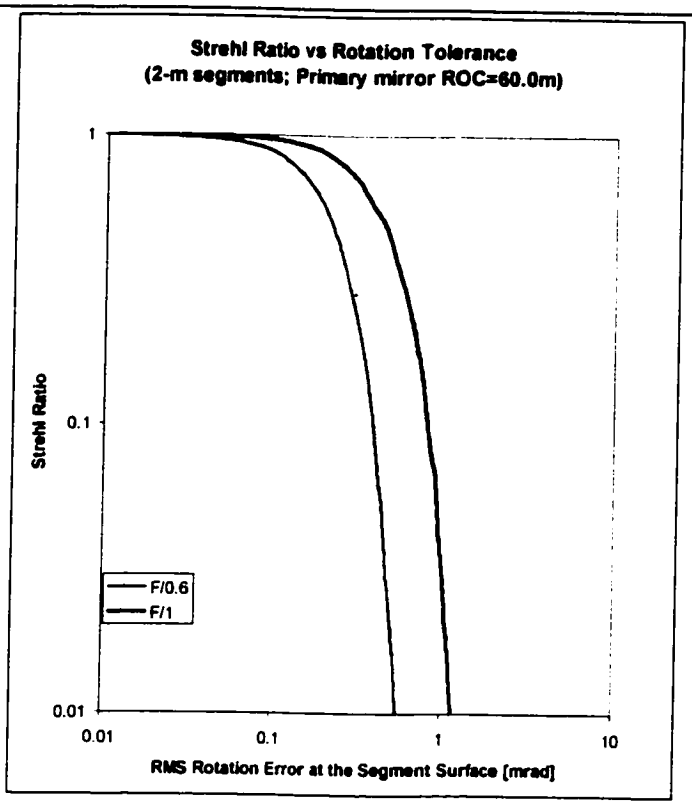

Figure 2-27. Strehl Ratio as a function of RMS rotation error (F/1 and F/0.6 primary mirrors).

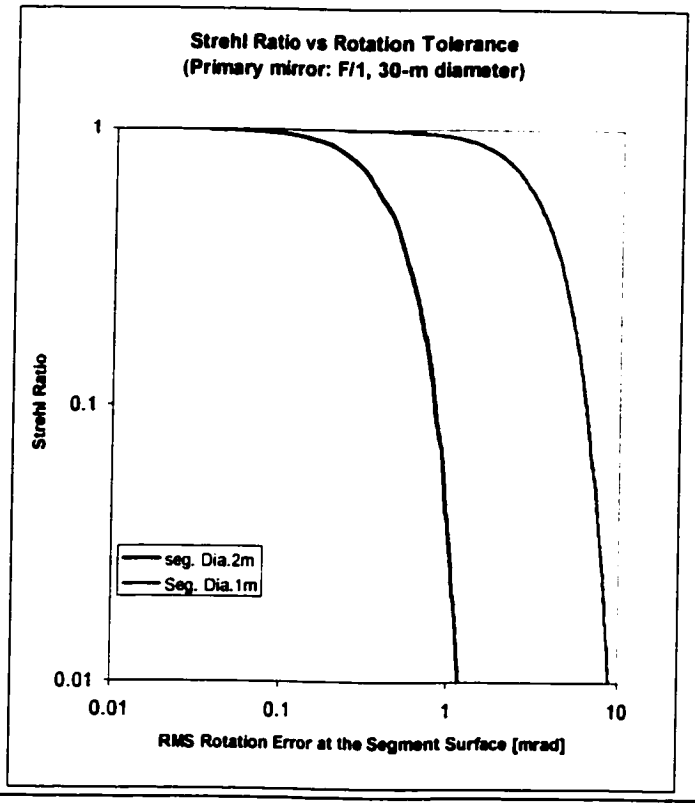

Figure 2-28. Strehl Ratio as a function of RMS translation error (1-m and 2-m segments).

CHAPTER 3

A NEW METHOD FOR MEASURING OFF-AXIS ASPHERIC MIRROR SEGMENTS

This chapter describes a new method of using a test plate as a reference combined with computer-generated holograms (CGH) to measure off-axis aspheric surfaces. This new method allows fast and accurate figure measurement of the optical surface, ensures excellent relative radius-of-curvature matching, and gives absolute x and y positions of the aspheric surface. Subsections of this chapter include: theory of operation (Section 3.1), an overview of the system design (Section 3.2), advantages of this new method (Section 3.3), and a brief summary of other known methods at the time this dissertation is written (Section 3.4).

3.1 THEORY OF OPERATION

The test compares a concave segment to the convex spherical reference surface of a test plate. The size of the test plate matches that of the segment under test. The CGH is used to compensate for the aspheric departure of the segment from the spherical reference surface. The test plate reference surface is chosen to be spherical, since spherical surfaces are cost effective to manufacture to high accuracy. Figure 3-1 illustrates how this method works:

- A Laser beam is first expanded to uniformly illuminate the CGH.

- The CGH is imaged onto the test surface by the projection lens.
- Two CGH diffraction orders, 0^{th} and 1^{st}, are selected by placing the object stop at the focal plane of the projection lens (Table 3-1).
- The reference beam originates as the 0^{th} diffraction order from the CGH, reflects off the reference side of the test plate, and then reaches the charge-coupled device (CCD).

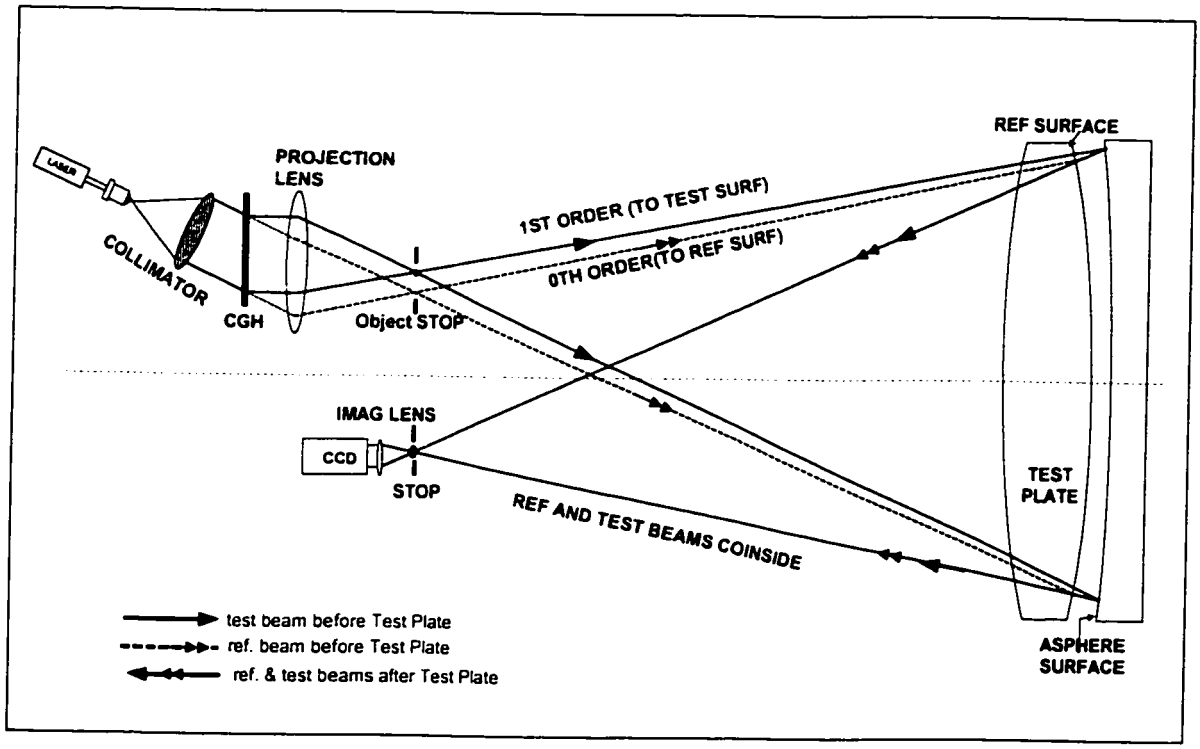

Figure 3-1. The test compares a concave segment to a convex spherical reference surface of the test plate whose size matches to that of the mirror segment. A CGH is used to compensate aspherical departure of the segment from the spherical reference surface.

- The test beam originates from the 1st order of the CGH. It has a pre-distorted wavefront that matches the shape of the aspheric mirror segment under test. After reflecting off the test surface, it too reaches the CCD.
- The reference and test beams are combined at the reference surface and travel together to the CCD imager. The resulting interference fringes sensed by the CCD array measure the shape error of the mirror segment.
- Translating the test plate by using three piezo-electric transducers (PZTs) allows phase shifting interferometry.
- The Image stop is placed at the front focal plane of the image lens to select appropriate orders (Figure 3-2).

Order from CGH	Reflected from	Final destination
Zero order	Test plate ⟹	**Reference beam**
	Segment	Blocked at the image stop
First order	Segment ⟹	**Test beam**
	Test plate	
All other orders	----------	Blocked at the stop following the projection lens

Table 3-1. Order selection at the object stop. The 0th order reflecting off the spherical reference surface becomes the reference beam, and the 1st order reflecting off the test surface becomes the test beam.

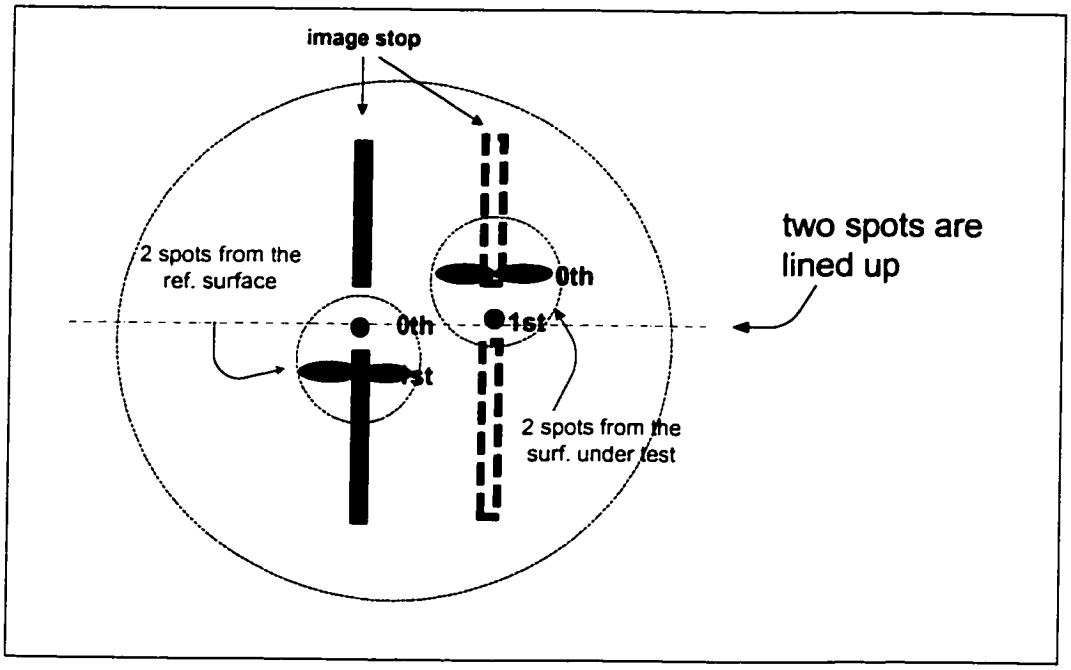

Figure 3-2. Order selection at the image stop: The 0^{th} order reflected off the test surface and the 1^{st} order reflected off the reference surface are blocked by the image stop. The two remaining orders are superimposed to produce the interferogram.

3.2 SYSTEM DESIGN OVERVIEW

From the system design point of view, the test setup (Figure 3-1) consists four parts: (i) CGH, (ii) the projection sub system, (iii) the test plate, and (iv) the imaging sub system. The sequence under which the test is designed is

1. Specification of the test plate (Section 3.2.1)
2. Design of the projection sub system (Section 3.2.2).
3. Design of the imaging system (3.2.3).
4. Generation of CGH (3.2.4).

This section summarizes the functionality of each component in the order given above.

3.2.1 Specification of the test plate

The test plate is the largest and thus most expensive component of this test. It provides reflected wavefront from its convex surface as a reference wavefront and transmits test wavefront. Its size matches that of the mirror segments. Depending on its size, the thickness of the test plate is chosen so it can be supported mechanically. For a 1-m test plate, this means a thickness of ~100-mm is desired. One side of the test plate (reference side) provides a convex reference surface with surface slope less than 0.01 wv/cm. The other side (back side or illumination side) of the test plate controls the viewing distance, measured from the object stop to the test plate (Figure 3-1). Each side of the test plate is carefully optimized to achieve maximum performance with minimum cost (Chapter 4: System optimization).

From the system point of view, fabrication cost of the test plate can be reduced if the tolerance on the illumination surface slope is relaxed. This can be accomplished if the input beam (traveling to) and output beam (traveling from) the test plate is located coaxially (Figure 3-4). This is because the two input beams experience a small lateral shear at the illumination surface of the test plate before they are recombined into the output beam (Figure 3-3). After the reference of the test plate, both input beams are completely common path. The amount of wavefront error due to this lateral shear can be reduced if coaxial setup is used. A sample case study developed in Chapter 7 shows that, to stay within pre-allocated 0.002 λ wavefront error, illumination surface slope of

0.02λ/cm is needed for the non-coaxial setup, compared to 1.6λ/cm if coaxial setup is used instead.

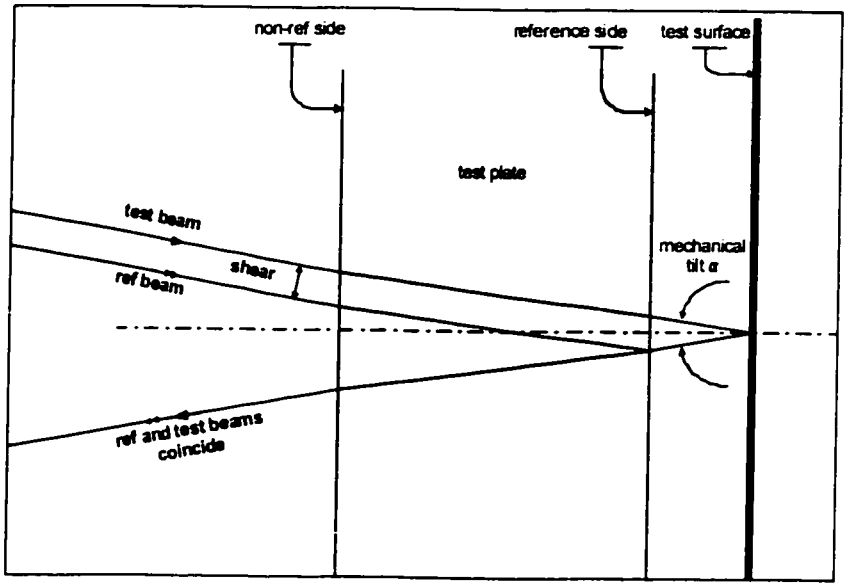

Figure 3-3. A non-coaxial setup increases the effective shear of the input beams, and tightens the illumination surface slope requirement of the test plate. This leads to higher cost.

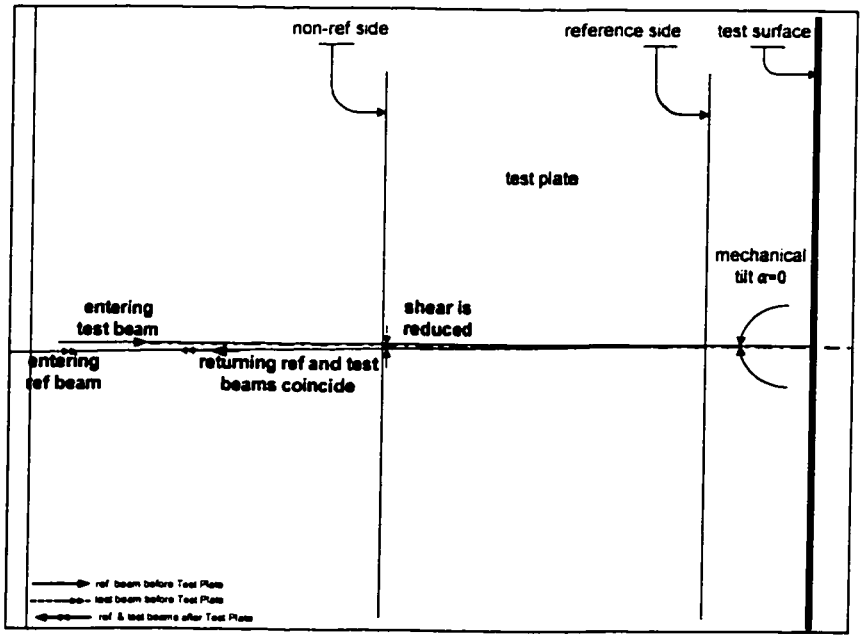

Figure 3-4. A coaxial setup reduces the effective shear of the input beams. This reduces the illumination surface slope requirement, making the test plate less expensive.

3.2.2 Design of the projection sub system

The projection system creates images of CGH pattern on the test segment. It is designed to be telecentric in the object space where CGH is located. This is so the CGH can be illuminated with collimated light, thus easing the manufacturing difficulties in requiring a specific wavefront for illumination. By placing an aperture stop at the focal plane of the projection system (Figure 3-1), only two diffraction orders (0^{th} and 1^{st}) from the CGH are allowed to pass through.

The performance of the projection system is critical to this test since accurate compensation of the aspheric departure of the segments requires the CGH to be projected onto the test surface. To achieve test accuracy 10-nm RMS wavefront for the entire system, a typical error budget for the projection system is then 5.7-nm RMS wavefront error (each of the three major error sources is budgeted 10-nm/$\sqrt{3}$ or 5.7-nm). More detailed analysis on this is found in Chapter 6 (Case study, Part II: Tolerance analysis).

The projection system can be designed in reverse – imaging the test mirror onto the CGH (Figure 3-5). Three basic constraints on these lenses are (i) the image scale, (ii) the effective entrance pupil size, and (iii) image space telecentricity. The complexity of the project system can be simplified if the effective entrance pupil size is reduced. This can be achieved if the 1^{st} diffraction order of the CGH is centered on the axis of the projection system (Figure 3-6). Analysis in Chapter 5 (Case study, Part A: System design) shows that by aligning the aberrated 1^{st} order on the axis of the projection system, the stop size of the projection system can be reduced by ~20%.

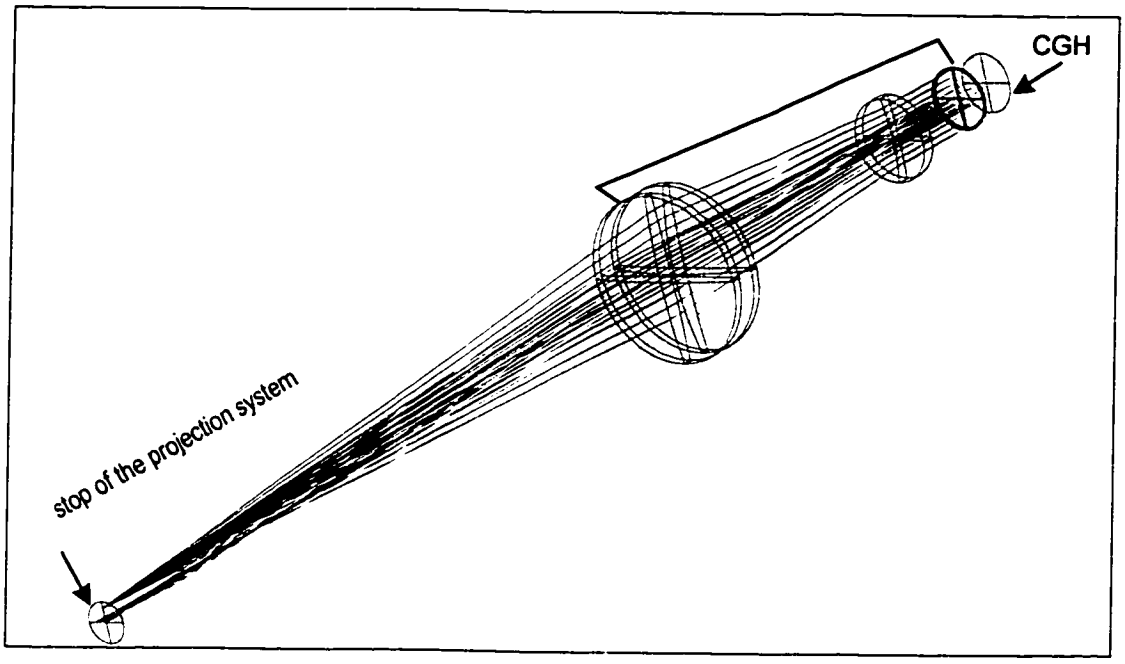

Figure 3-5. Stop location of the projection system.

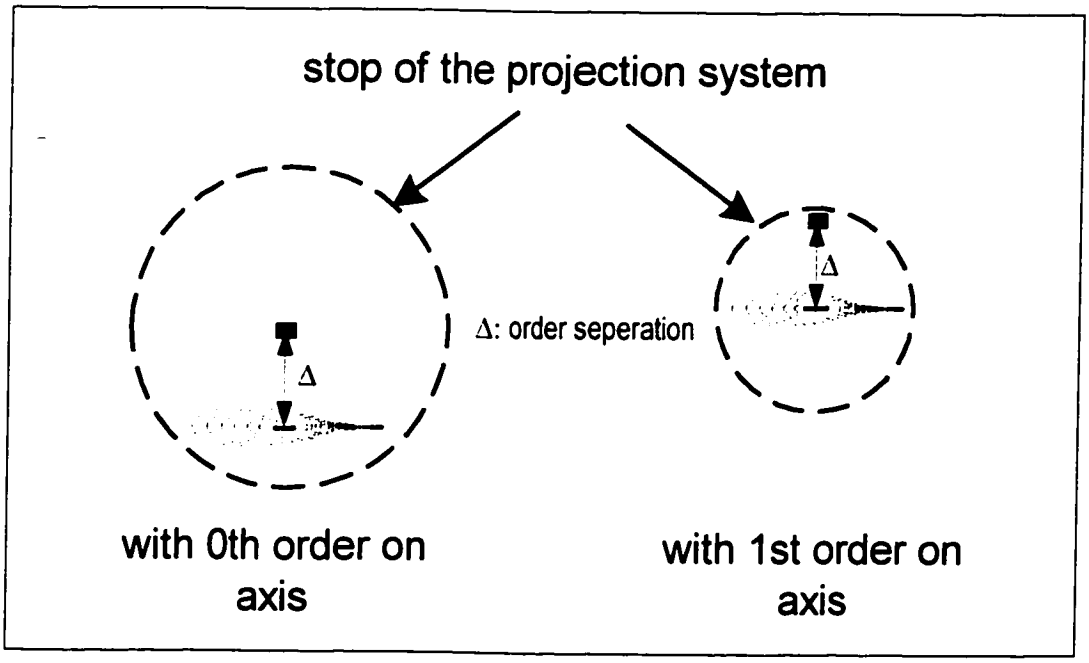

Figure 3-6. Locating the 1st order on-axis reduces the projection system stop size and eases the design complexity of the projection system.

3.2.3 Design of the imaging sub system

The imaging system creates a good image of the test part onto the CCD where the interferogram can be captured and then analyzed to obtain a surface map of the segment under test. Basic design constrains of this system includes: (i) magnification suitable to image a large test segment (~1 meter depending on the segment design) onto a small CCD (~6m x 8 mm), (ii) small distortion (less than 1%) for accurate transfer of the interferogram to CCD, and (iii) telecentricity in the CCD- plane so image size does not change when CCD is not at the correct position.

The imaging system is designed to accommodate spherical aberration in the system introduced by the illumination surface. The design example showcased in Chapter 5 illustrates this point in details.

3.2.4 Generation of CGHs

This test uses CGHs to correct the aspherical departure of the mirror segments from the the spherical reference surface. CGHs can be specified as phase functions using Zernike polynomials. The coefficients of the polynomials are then directly imported to CGH manufacturers (like Diffraction International)[21]. The hologram pre-distorts the test beam, making it match the reference beam. Neither the reference nor the test beam needs to be perfect – just perfectly matched. The two-step process of generating CGHs is detailed in Chapter 5. The holograms are designed to be amplitude gratings with 50% duty cycle. This puts 25% and 10% of input optical power into the 0^{th} and 1^{st} diffraction orders respectively [22].For measuring bare glass segments (4% reflection efficiency), good

contrasted fringes of visibility 90% are achieved, and for measuring aluminized mirror segments (95% reflection efficiency), 58% contrast is reached[23]. Both numbers are well within acceptable range.

3.3 ADVANTAGES OF THE NEW METHOD

This new method is optimal for testing many off-axis segments of an aspheric primary mirror for the following reasons:

1. It produces excellent relative radius-of-curvature (ROC) matching:

   During the test, all concave aspheric segments are tested against the same convex spherical reference surface.

2. It reduces individual segment testing time:

   By simply replacing the CGH, a single test setup can be optimized to accommodate measurement of all the different segments that make a complete aspherical primary mirror.

3. It is cost effective:

   Both reference and test beams coincide at the CGH, so that the CGH can be written on a standard lithography substrate, and the near common-path configuration allows the test plate to be made from a non-precision transmission grade glass.

4. It achieves a high degree of measurement accuracy:

Phase-shifting interferometry (PSI) is employed. Also this method has a near common-path configuration, so the test is relatively insensitive to vibration and noise.

5. It gives accurate registration of the aspheric surface:

   The position and orientation of the off-axis optical surface are aligned using fiducial marks etched on the CGH substrate.

3.4 SUMMARY OF OTHER KNOWN METHODS

Aside from the common autocollimation test, the center of curvature test with a null lens and the CGH test in a Twyman-Green setup, there are two other new interferometric methods proposed by Sommargren[24-5] for testing mildly aspheric segments from CELT (f/1.5 30-m primary with 1-m 1,080 segments). Both of them use a phase-shifting diffraction interferometer. In one setup (Figure 3-7) the segment is measured in the

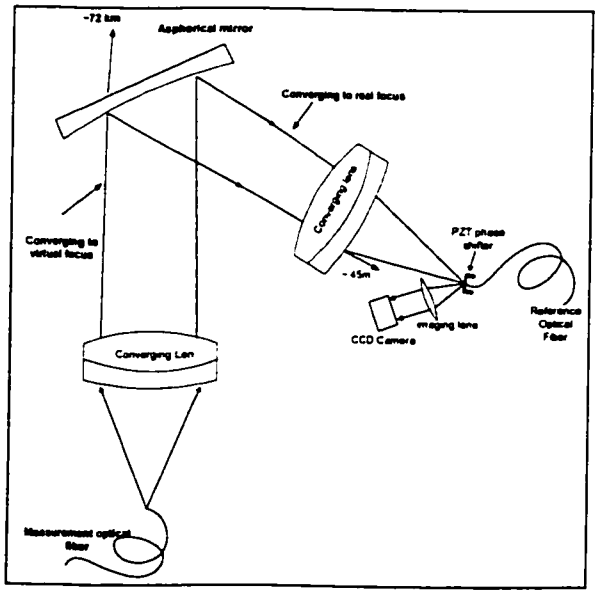

Figure 3-7. Configuration for measuring an aspheric mirror segments as it is functionally used in a f/1 30-m primary (k=-1.0002)

configuration that will be used in the telescope, so the test geometry itself is used to cancel any asphericity seen by the interferometer. Two identical converging lenses are used to reduce the size of the test setup. The wavefront reflected from the aspheric mirror segments is brought to focus at the real image point by the second converging lens where it is reflected, phase shifted, and combined with the diffracted wavefront from the reference fiber. Advantage of this method is its cost effectiveness due to a relative small amount of optics involved.

The second approach of testing off-axis aspherical segments using point-diffraction interferometry is shown in Figure 3-8. Here a variable tilt lens is design and used to create a matching for the dominating astigmatism found in the segments so a

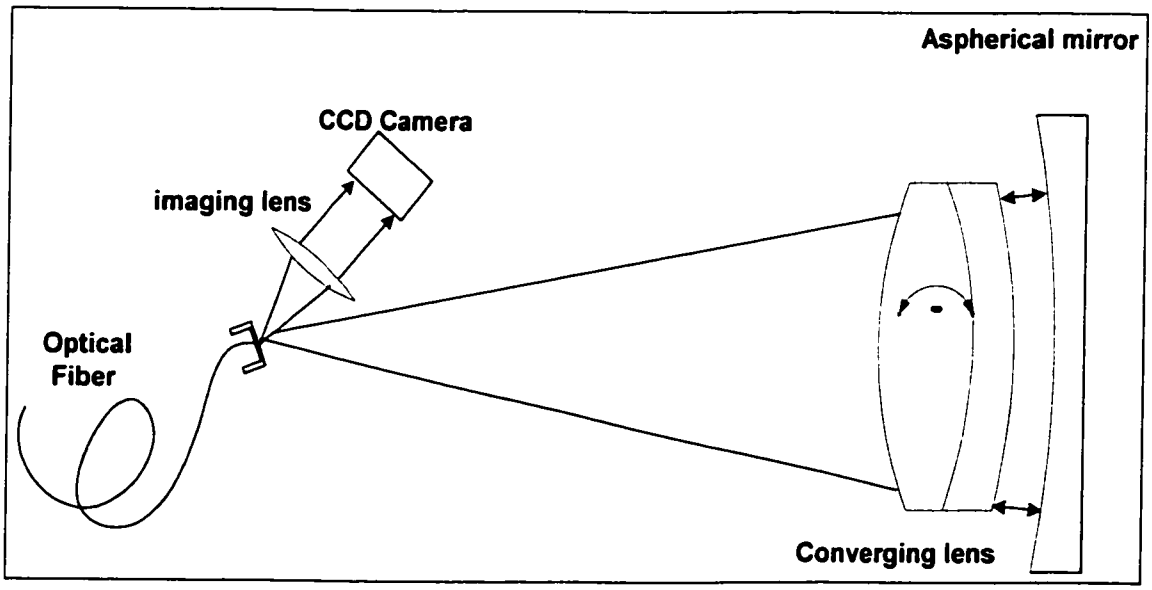

Figure 3-8. Configuration for measuring an aspheric mirror segments using a phase-shifting diffraction interferometer with a variable tilt lens. The tilt is varied to match the astigmatism of the segment, producing a near-null interference pattern.

near-null interference pattern can be produced. Sommargren[4] reported that in a ray-traced simulation for testing CELT segments (F/1.5 30-m primary with 1,080 1-m segments), the lens-induced astigmatism and coma cancel those terms in the segment-reflected wavefront and the remaining aberration from the furthest-out segments is small enough that they can be measured with the phase-shifting interferometer. A tilt angle of 2.45 degrees, controlled to accuracy of 0.006 degrees, is required for this cancellation.

The advantages of both configurations are their cost effectiveness. However, for the first setup, to test a 30-m primary mirror, conjugate points of the segment surface are at f1=72km and f2=45m, so this configuration has a large optical path difference between the reference and the test beam, thus is very sensitive to non-ideal environmental vibrations. For the second configuration ,the results are highly sensitive to the test geometry and the spacing between the converging lens and mirror has to be adjusted to accommodate the range of the segment radii of curvatures. In addition, this distance has to be controlled to very high accuracy to ensure good radius of curvature matching.

CHAPTER 4

SYSTEM OPTIMIZATION

Optimization of the system allows the designer to achieve high testing efficiency and excellent measurement accuracy. When the system is properly optimized, a single test plate with its projection and imaging systems can be aligned once to test all segments by inserting different CGHs. During the optimization process, optical elements are carefully chosen so the test achieves high measurement accuracy and is cost effective.

From the system point of view, three independent variables must be optimized are: (i) test plate reference surface radius of curvatures (ROC), (ii) illumination system, and (iii) system magnification factor M. The system magnification factor M is defined as the size of the test segment over the size of the CGH. Optimization of each is discussed in detail below.

4.1 REFERENCE SURFACE OPTIMIZATION

The system design starts with selecting an optimal reference ROC. A well-optimized reference surface allows this test to be cost effective so that all segments can be tested with a single test plate. The test plate provides a convex spherical reference surface. The reference surface is chosen to be spherical so it can be manufactured to high accuracy more cost effectively compared its aspherical counterparts.

The reference surface is held closely to the mirror segment with a small air gap in between the two surfaces. Controlling the air gap to an accuracy of ~25μm permits relative radius of curvature amongst different segments to be matched to better than 1 part in 10^5 as calculated in Chapter 6 (Case study. Part B – Tolerance Analysis). This technique has been previously implemented at the University of Arizona [25].

In order to understand optimization of the reference ROC, we first show how choice of reference ROC affects the test accuracy. Then we illustrate how to select the optimal ROC that minimizes the test sensitive to errors.

4.1.1 Choice of the reference surface ROC affects test accuracy

Test accuracy depends on the slope variation compensated by computer-generated hologram, and choice of reference surface ROC changes this slope variation. If a segment is compared to a reference surface with a poorly chosen ROC, large optical path differences (OPD) between the two surfaces results. This, in turn, leads to a large slope difference between the two surfaces that must be compensated by the CGH, so test accuracy suffers as the result.

One requirement of using CGH to compensate the slope variations is that enough tilt carrier fringes must be added to separate different diffraction orders. The minimum amount of tilt must be three times the maximum slope variation[26] (Figure 4-1).

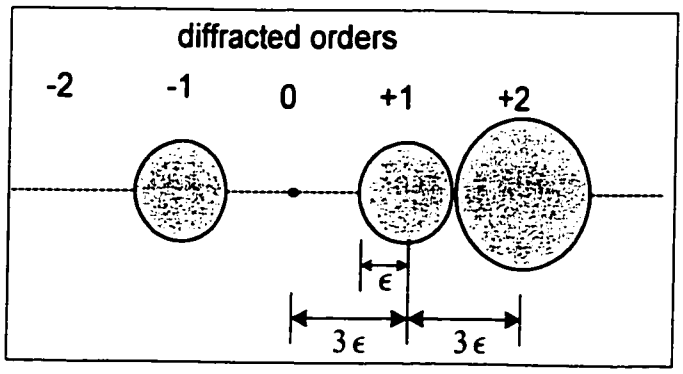

Figure 4-1. Minimum CGH tilt minimum tilt needed for order separation is 3ε, where ε is the slope variation (measured in rad)

Clearly, large slope variation (result of a poorly chosen ROC) requires more tilt fringes to separate diffraction orders. Figure 4-2 shows that when slope errors are different along x- and y- directions, the smaller valued slope error (ε_x in this illustration) must be chosen for calculation of the CGH tilt carrier fringes, so test sensitivity to CGH fabrication error is minimized. Figure 4-3 depicts that without proper tilt fringes in the CGH, diffraction orders overlap. This is compared to Figure 4-4 where fully separated orders are illustrated when proper tilt fringes are added. In Figure 4-5, we show that if tilt fringes are added along the direction where larger slope error exists, fringe density is much higher and making the test more sensitive to hologram fabrication errors.

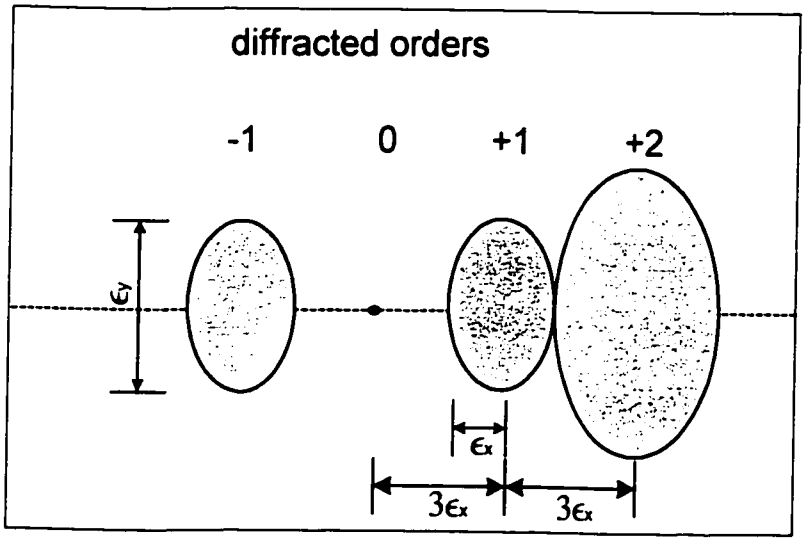

Figure 4-2. When slope error is different along x- and y- directions, the smaller slope error (ε_x in this case) is chosen for calculation of the CGH tilt carrier fringes.

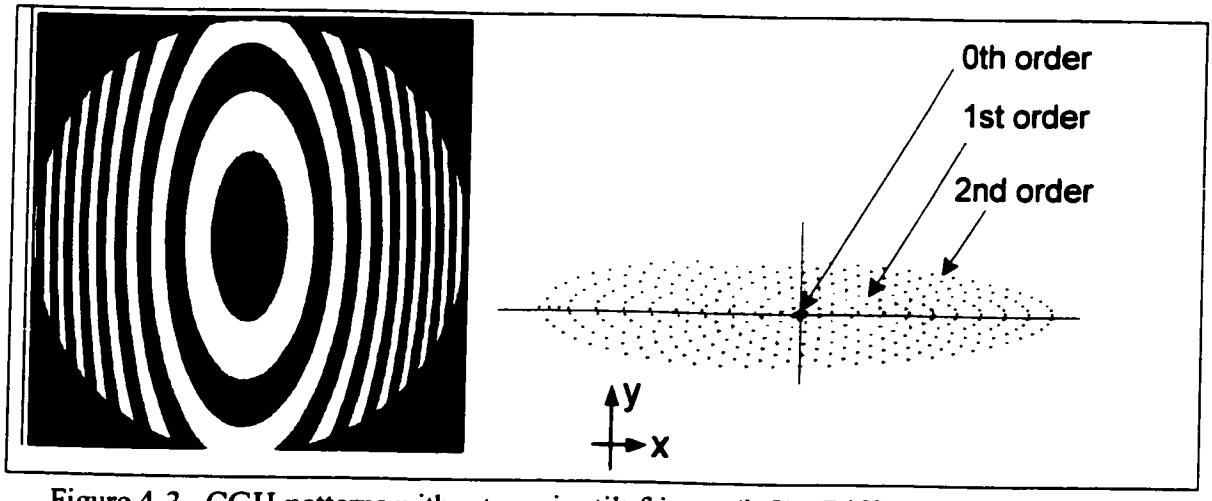

Figure 4-3. CGH patterns without carrier tilt fringes (left). Diffraction orders are not separated (right).

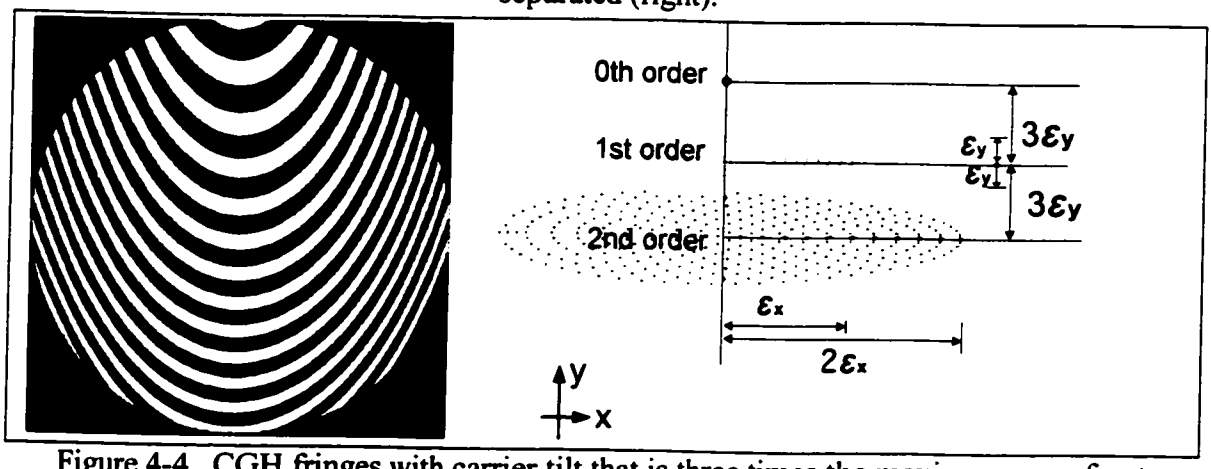

Figure 4-4. CGH fringes with carrier tilt that is three times the maximum wavefront slope of the aberrated wave (left). Diffraction orders are separated in this case (right). Tilt is along y-direction to improve test accuracy.

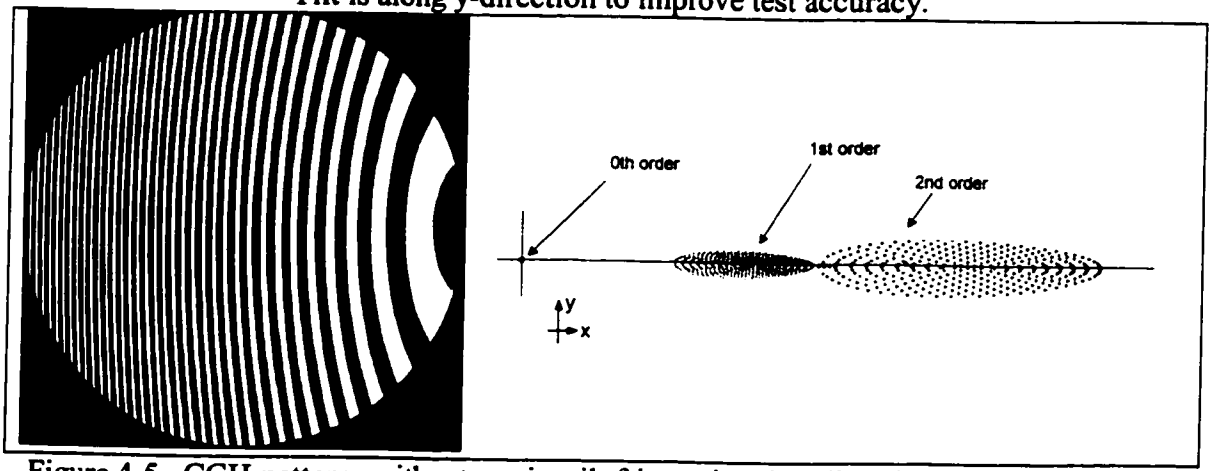

Figure 4-5. CGH patterns without carrier tilt fringes in other direction (left). Diffraction orders are separated in another direction (right).

For the same size CGH, more tilt fringes means CGH patterns are more closely spaced. This reduces the test accuracy since tightly spaced patterns are more sensitive to CGH fabrication errors. Since tilt carrier fringes is the dominating feature on a CGH, testing accuracy depends on the carrier frequency. Figure 4-6 depicts the reduction in the measurement accuracy when the CGH line spacing is narrowed for the case of 0.125μm accuracy in fabricating the hologram. Widen the fringe spacing by increasing the CGH size does reduce the sensitive to fabrication error, but also leads to the undesirable increase in the CGH fabrication cost. Hence, to achieve a high-test accuracy without increasing cost, slope variation between the reference and test surface must be minimized so the CGH tilt carrier fringes can be kept as sparse as possible.

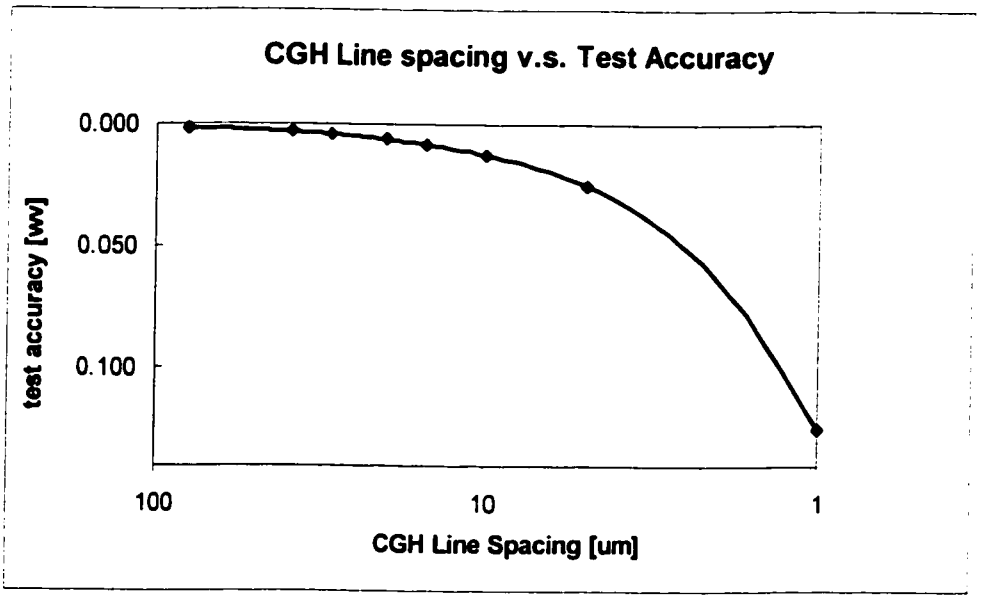

Figure 4-6. Test accuracy degrades with the decreasing spacing for the case of fabrication error 0.125μm.

4.1.2 Choosing the optimal reference surface ROC

Different selections of reference ROC change the slope variations of the aberrated wavefronts, and this in turn, affect the system sensitivity to errors. The optimal reference surface ROC is selected so that a single test plate can be used for measuring all of the segments and minimizing the system sensitivity to errors. Burge[27] theorized that the optimal reference ROC is where the slope error of the farthest off-axis segment is matched to that of the nearest off-axis segment.

To locate the optimal ROC so that a single test plate can be used to test all segments, we developed a computer program that numerically calculate how changes in the reference ROC value affect the slope variations of different segments. The results from this algorithm are shown in Figure 4-7, Figure 4-8 and Figure 4-9. In the first two figures, four segments' slope variations along both x- (Figure 4-7) and y-direction (Figure 4-8) are plotted as a function of possible reference ROCs. S1 and S14 have the nearest and furthest off-axis distances respectively. Selecting the optimal reference ROC can be visualized in Figure 4-9. In this illustration, we plotted slope variations of the same four segments at four different ROC values (lines A, B, C and D from Figure 4-7 and Figure 4-8). ROC values at lines B and C in Figure 4-9 are of interests: On line B, we see that y-slope variations are matched for the nearest segment (S1) and the furthest segment (S14). On line C, we see the same but now along x-direction. Since test sensitivity to CGH fabrication error is less for smaller slope error, the matched y-direction slope error is used to locate the optimal reference ROC.

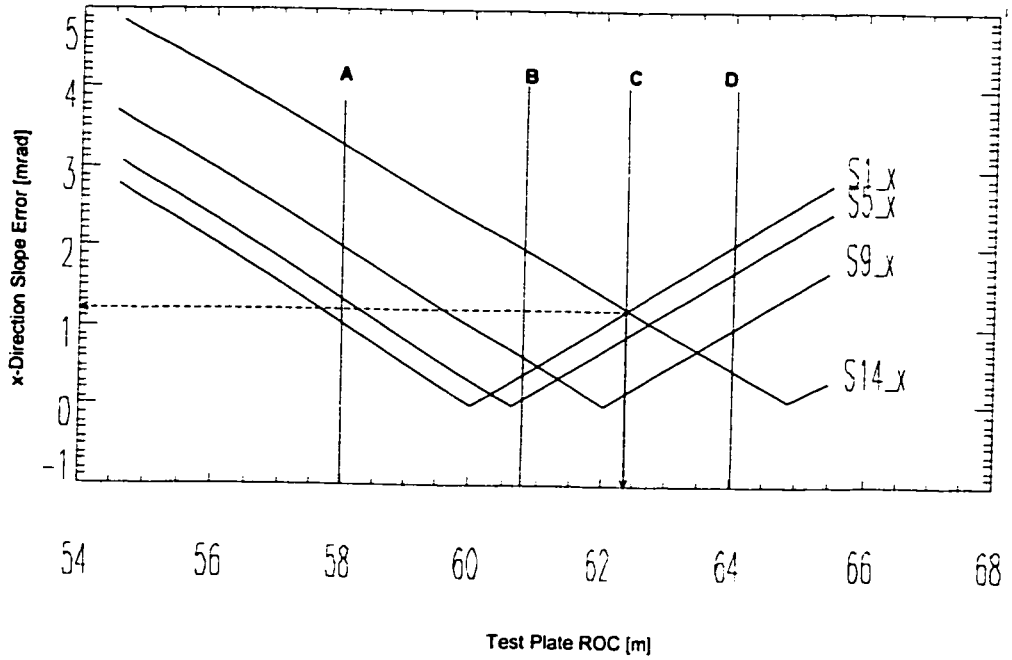

Figure 4-7. x-direction slope variations of 4 segments as a function of different reference radius of curvatures (ROCs). S1 is the nearest off-axis segment and S14 is the furthest segment.

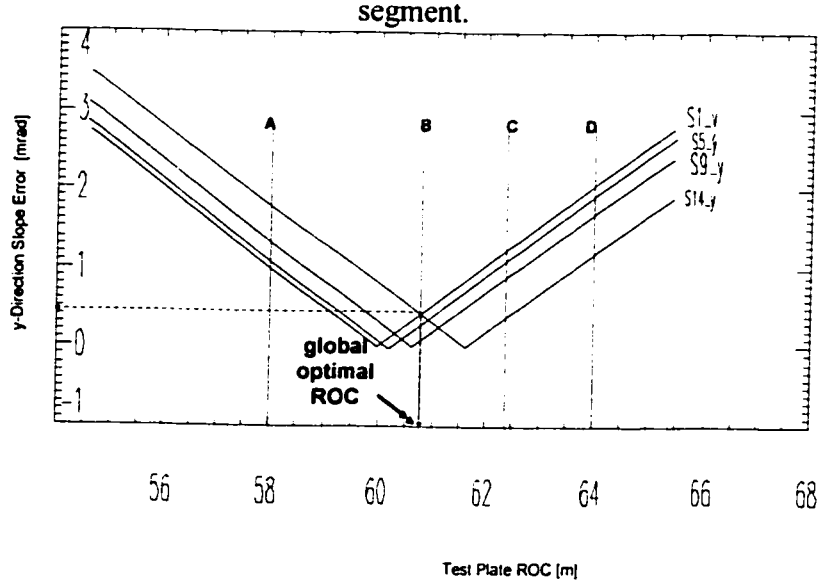

Figure 4-8. y-direction slope variations of 4 segments as a function of different reference radius of curvatures (ROCs). S1 is the nearest off-axis segment and S14 is the furthest segment.

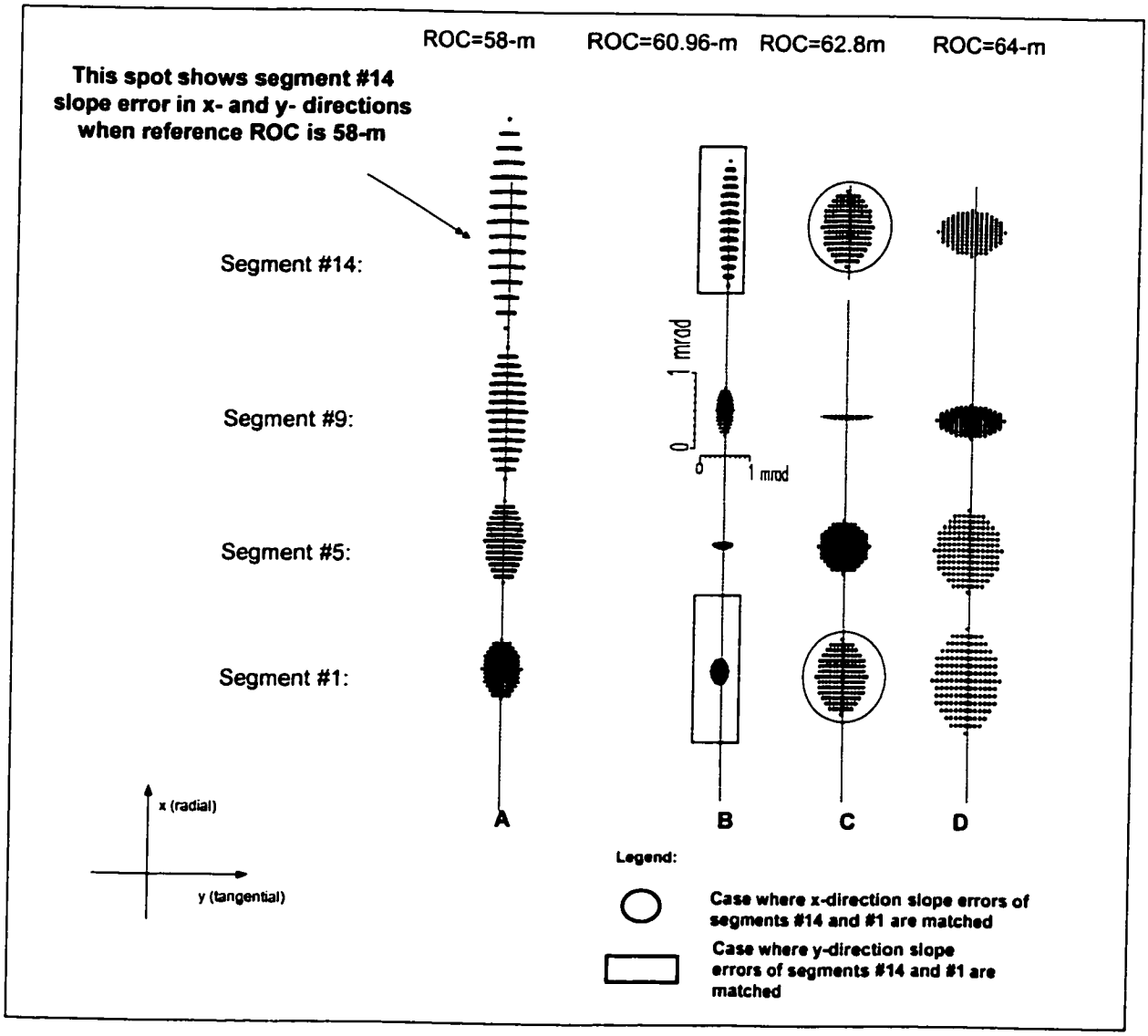

Figure 4-9. The optimal system reference ROC is where is where the slope error of the farthest off-axis segment (S14) is matched to that of the nearest off-axis segment (S1). Smaller valued y-directional slope error is used to locate the optimal ROC so test sensitivity to CGH fabrication error is reduced.

To summarize, the optimal reference ROC can be found by using Figure 4-7 and Figure 4-8 by the following steps:

1. Locate the points where curve S14 intersects S1 in both Figure 4-7 and Figure 4-8.
2. Compare which of the two intersection points has a smaller slope error.
3. Chose the reference ROC corresponds to the smaller slope error and this is the optimal reference ROC.

This process is summarized in Figure 4-10. In this figure, there are two points where slope variations of S14 (farthest out segment) matches to that of S1 (closest segment):

e_x = 1.003 mrad when reference ROC=62.820-m

e_y = 0.344 mrad when reference ROC=60.955-m

Since e_y = 0.344 mrad is smaller than e_x = 1.003 mrad, the optimal reference ROC has the value of 60.955-m.

The above calculation proves that one can indeed simply match the slope from the inner most and the outer most segments to find the optimum reference radius of curvature.

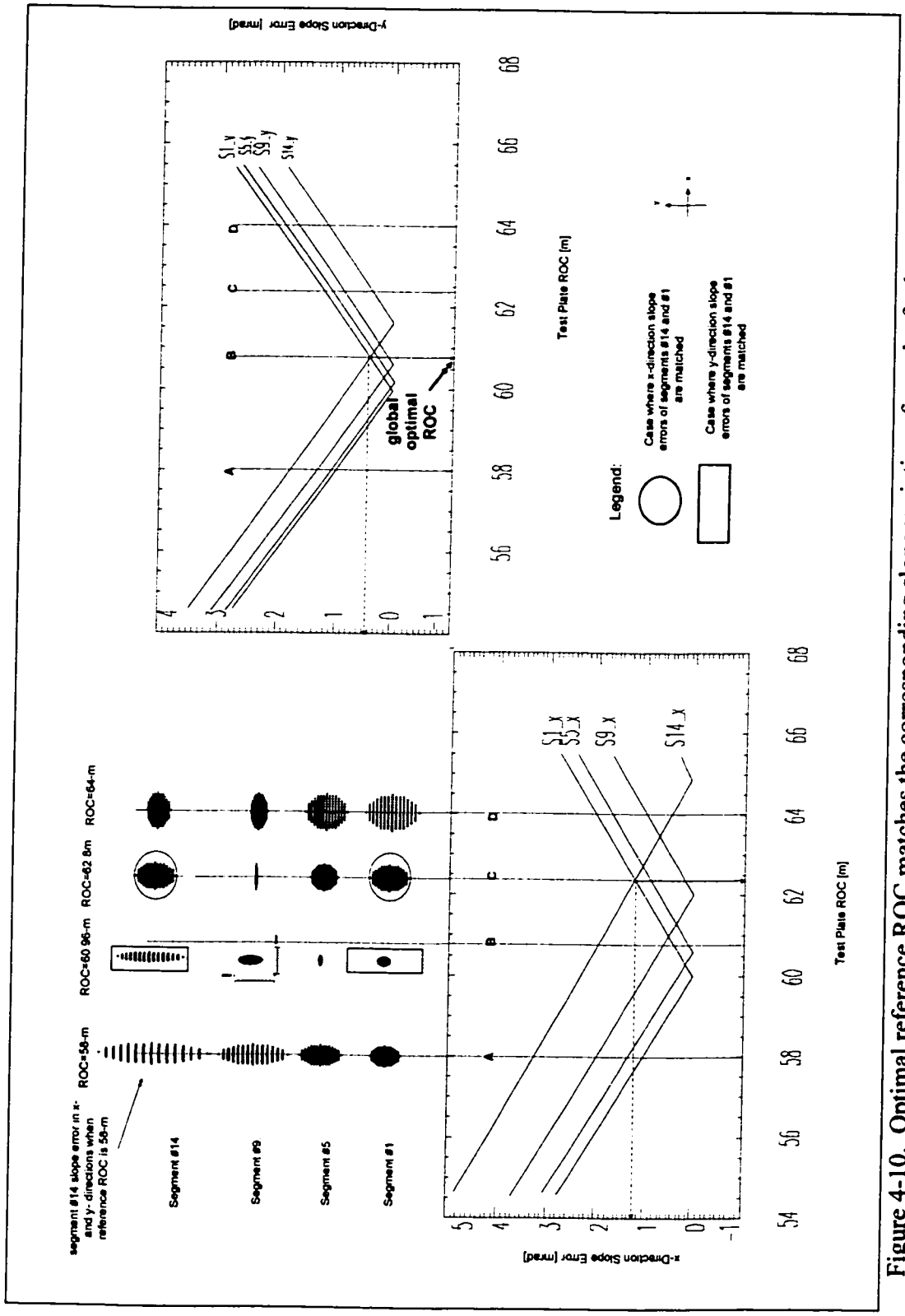

Figure 4-10. Optimal reference ROC matches the corresponding slope variations from the farthest out segment (S14 here) and the nearest segment (S1 here). When slope variations are different along x- and y-directions, smaller of the two should be chosen.

4.2 OPTIMIZATION OF THE ILLUMINATION SYSTEM

After optimization of the reference surface ROC, the second component that must be optimized is the illumination system. The illumination system must force all input rays to hit the mirror segment under test at normal incidence. Various detailed designs are well documented elsewhere [28-11]. In designing the illumination system for this test, our main objective is to make the test cost effective, so we designed the entire illumination system using only the test plate's backside, i.e., the non-reference surface.

The illumination surface of the test plate was designed in reverse order. We started by creating a wavefront that matches the aspheric surface (Figure 4-11). This is accomplished by modeling a fictitiously high refractive index to the right of the test surface. The thickness of the test plate is chosen appropriately, so it can be supported to

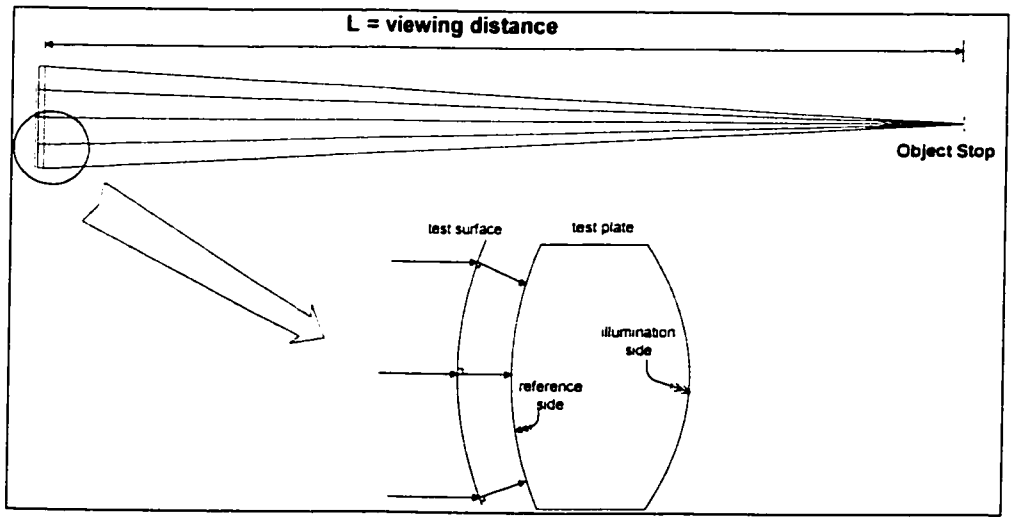

Figure 4-11 The illumination surface of the test plate was designed in reverse order. Collimate light to the left of the segment is forced to leave the test surface at normal incidence. This is accomplished by modeling a fictitiously high refractive index to the right of the test surface.

maintain required surface slopes. Next, the illumination surface is chosen to be spherical, not aspherical in shape, so the test plate fabrication cost can be reduced.

To complete the design of the illumination system using only the backside of the test plate, the only design parameter must be chosen is the ROC of the illumination surface. A smaller ROC shortens the viewing distance, measured from the test plate to the object stop, and makes the test setup shorter. However, small ROCs introduce higher spherical aberration (SA) into the system. SA blurs all focused spots at the image stop and too much SA makes the order separation at the image stop difficult. Figure 4-12 through Figure 4-14 depict this point. Figure 4-12 shows that at the object stop, only two diffraction orders are allowed to pass and others are blocked.

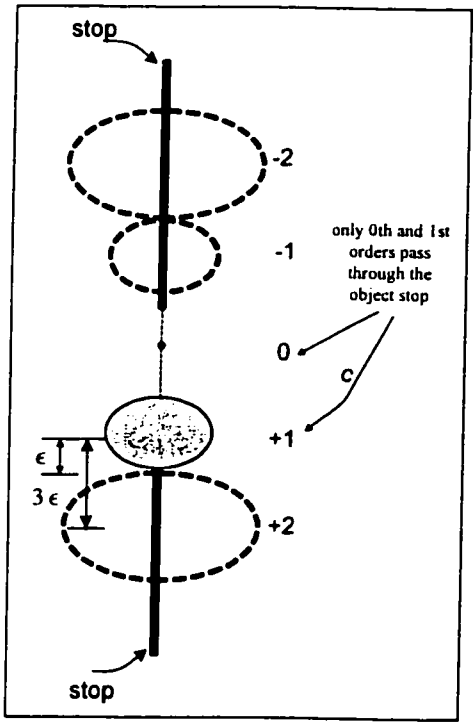

Figure 4-12 At the object stop, only 0^{th} and 1^{st} orders are passed through

In the absence of SA (Figure 4-13), two diffraction orders passed through the object stop are lined up for interference. When significant amount of SA is present (Figure 4-13), separation of orders becoming increasing difficult.

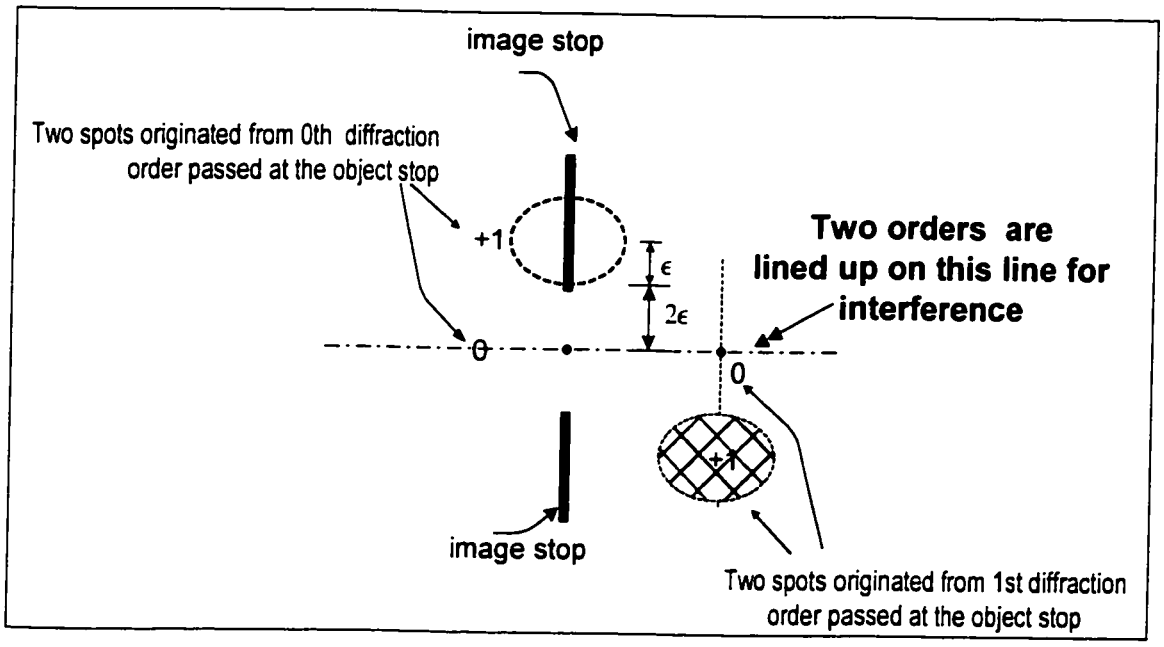

Figure 4-13 At the image stop, when spherical aberration (SA) is absent, appropriate orders a lined up for interference

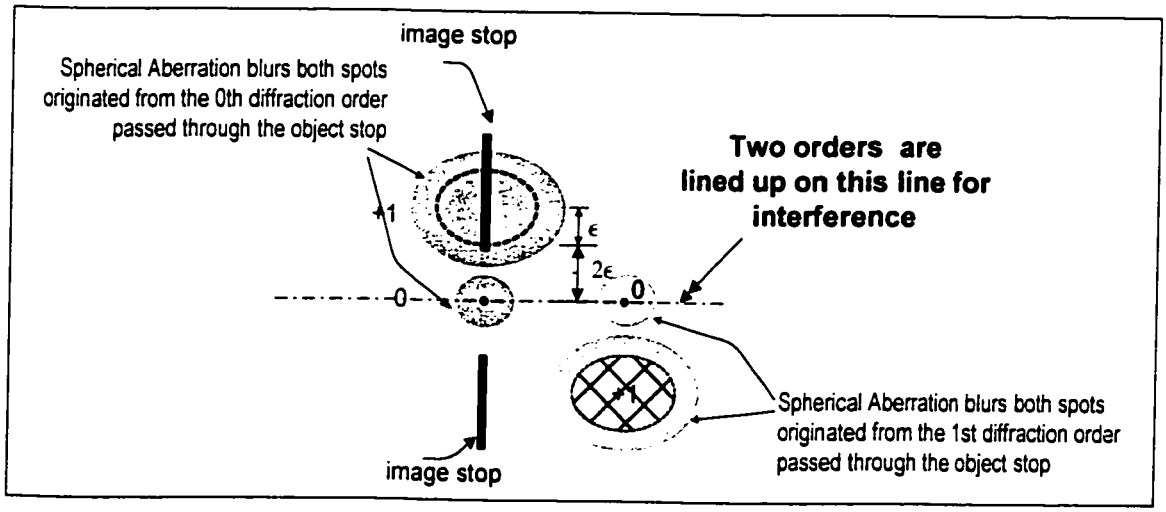

Figure 4-14 At the image stop, when spherical aberration (SA) is present, appropriate orders that are lined up for interference are blurred.

Figure 4-15 shows that the theoretical maximum amount of blur the system can allow is when the blurred 0^{th} order overlaps the blurred 1^{st} order. From here we conclude that the maximum amount of SA the system can tolerate is one third of the separation distance between 0^{th} and 1^{st} orders. At this limit, there is no room for other effects and all tolerances become very tight and thus only half of the theoretic maximum should be taken when designing the illumination system.

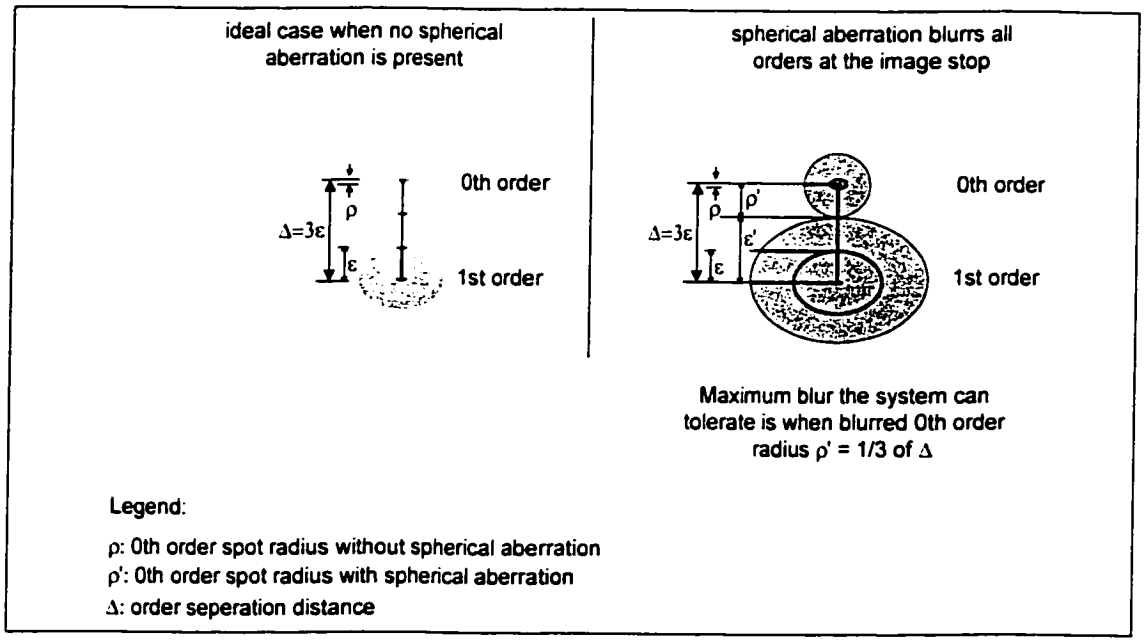

Figure 4-15. Maximum blur the system can tolerate is 1/3 of the order separation distance.

At this point, we have all the tools to locate the optimal illumination ROC. We know that (1) spherical illumination surface is the most cost effective illumination system we can design for this test, (2) the illumination system is designed in reverse order (Figure 4-11), and (3) spherical illumination surface introduce spherical aberration into

the system, and blurs all diffraction orders at the image stop (Figure 4-14); and (4) the maximum spot size blur the system can tolerate is 33% of the order separation distance. Figure 4-16 illustrates that using a spherical surface, the viewing distance must be kept comparative long whereas the choice of using aspherical surface is costly.

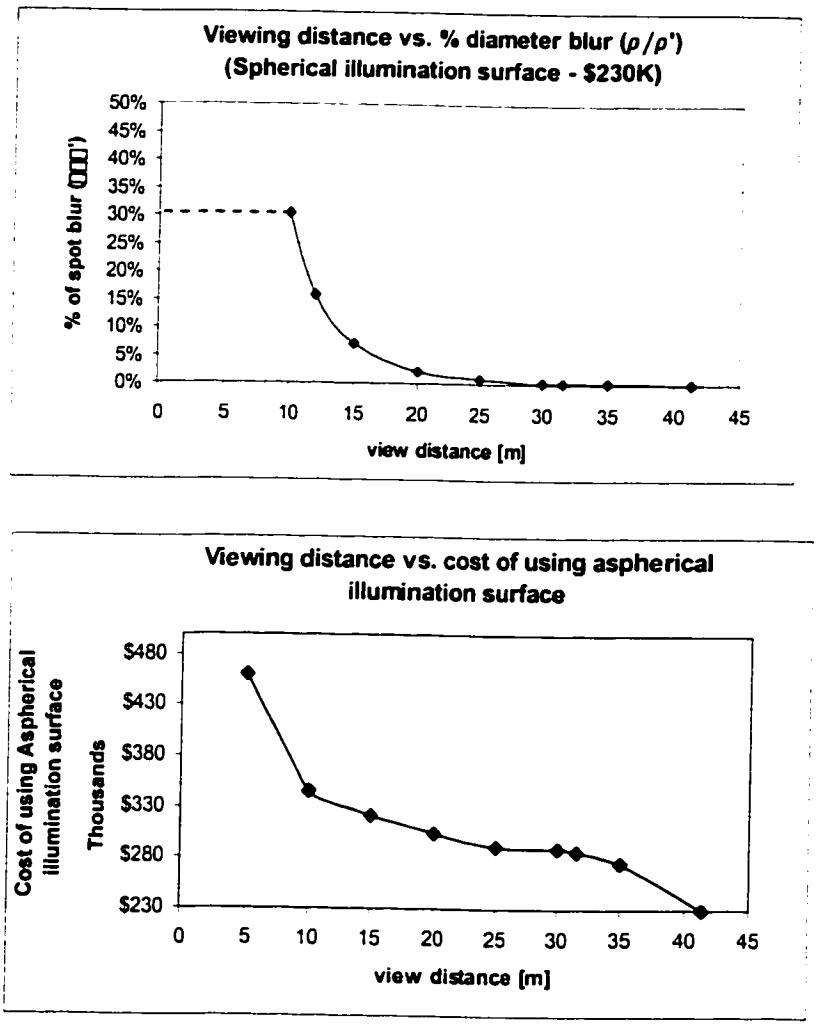

Figure 4-16. Cost and performance comparison of spherical (top) and aspherical (bottom) illumination surfaces. Whereas using spherical illumination surface, it is not possible to have test setup length less than 12-m, aspherical illumination surface proves to be quite costly.

4.3 OPTIMIZATION OF SYSTEM MAGNIFICATION M

The last parameter that must be optimized for the system design is the system magnification M. System magnification is tied to the optimum reference radius of curvature that minimized the system slope variation. At the optical space where the test plate and the test surface locate, the net slope difference can be fictitiously characterized using fringes – one dark line per one wave of optical path difference. Since the hologram and the test plate are conjugate pairs, the fictitious interferogram at the test plate is demagnified M times into the hologram itself.

The optimum System magnification M is defined in Eqn. [2.33] as the ratio of segment size over CGH size, or since the CGH and the segment are image conjugates, M can also be defined in its equivalent form in equation[2.34]. This alternate definition is easier to work with and is adopted throughout this section.

$$M \triangleq \frac{\text{segment diameter}}{\text{CGH diameter}} \qquad [2.33]$$

$$M = \frac{\Lambda}{s} \equiv \frac{\text{fringe spacing at the test surface}}{\text{CGH line spacing}} \qquad [2.34]$$

Optimization of the system magnification M is based on balancing test accuracy with cost. Choice of magnification M changes the CGH pattern spacing, and this affects the test sensitivity to CGH fabrication error. Wider CGH line spacing improves the test accuracy but increases the accumulative cost of CGHs because it enlarges the CGH size (Figure 4-17).

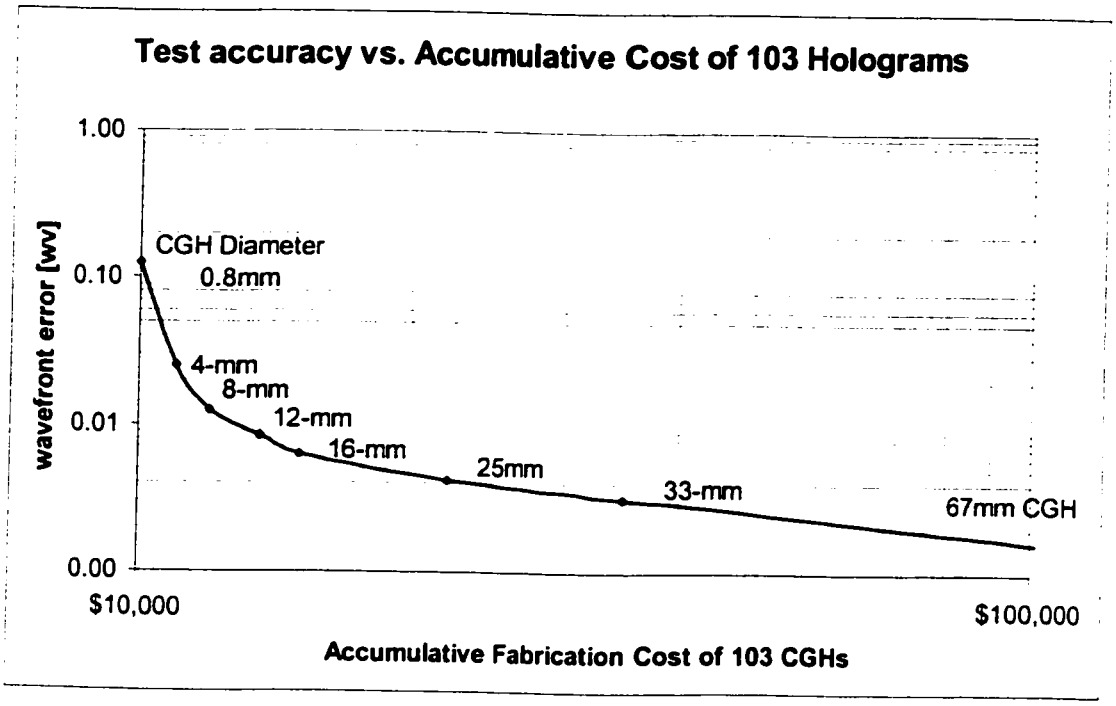

Figure 4-17 Test accuracy is increased if wider CGH line spacing is used, but this increases the accumulative CGH cost.

Traditionally, in testing monolithic optical elements using CGH, CGH size is not minimized to its theoretical limit. This is because, to make a hologram of 30-mm or of 70-mm in diameter, the associated cost is still one substrate on which the CGH is written. This is not the case in testing multiple segments using multiple CGHs. To allow more CGHs fit on the same substrate, CGH pattern spacing must be kept at minimum where pre-allocated error budget is satisfied. For example, if we allocate 2.5-nm surface error for CGH fabrication error, the minimum pattern spacing should be set to 15μm (Eqn. [2.35]), assuming laser light with λ of 632-nm is used during the test and CGHs are made with standard accuracy of ±0.125μm.

$$s = \frac{0.125\mu m}{2.6nm}\left(\frac{\lambda}{2}\right) \qquad [2.35]$$

To determine the system magnification M using Eqn. [2.34], we also need to determine the fringe spacing Λ at the test plate. Eqn. [2.36] allows us to find Λ using minimum amount of tilt needed for order separation, ε_{system}, obtained earlier in optimize the reference ROC (Section 4.1.2).

$$\Lambda = \frac{\lambda}{\sin(\varepsilon_{system})} \qquad [2.36]$$

CHAPTER 5

EXPERIMENTAL VALIDATION AND ERROR ANALYSIS

We devised a laboratory demonstration to compare this method with an established method, so we can validate the new method of testing off-axis aspherical segments using computer-generated holograms and a test plate. The goals set out for the demonstration have all been met. These are summarized below:

Goal	Final Result
verify design process	interferograms with excellent fringe contrast were obtained (Table 5-1)
verify isolation of diffraction orders	
verify fringe contrast	
verify phase shifting interferometer	
verify error analysis	modeled to be 0.0125 λ RMS wavefront measured to be 0.0116λ RMS wavefront

This chapter first documents the laboratory demonstration in Section 5.1 and discusses the fabrication of the hologram 5.2. Section 5.3 reports the experimental results. The tolerance analysis in Section 5.4 shows that errors between the two measurement methods agree very well. Section 5.5 shows that repeatability of the setup is excellent and finally Sections 5.6 and 5.7 list important lessons learned through this experiment.

5.1 OPTICAL CONFIGURATION

In this demonstration, a plano-convex test plate was used to measure a concave sphere of known surface quality. A computer-generated hologram was designed and used in the same manner as the asphere test, but the pattern corresponded to testing of a sphere. Since it was used in the same manner as testing of an asphere, the dominating feature on the CGH was large tilt carrier pattern. Therefore, testing of sphere changes very little in the validation of the test and its sensitivity since large tilt carrier always dominates the hologram sensitivity. The system that we used to validate the computer models for the test design and the error analysis included the following:

- Matching 30-cm test plate and test sphere Figure 5-3.
- A hologram (Figure 5-6) of 20-cm in diameter consists of chrome patterns written onto flat glass substrates.
- An off-the-shelf bi-convex lens with F=200-mm (as the projection system).
- An off-the-shelf plano-concave lens F=50.2-mm (as imaging system).

To improve the test accuracy, phase shifting was implemented. This was accomplished by translating the test sphere with respect to the test plate using three piezo-electric transducers (PZTs) on the back of the test surface (Figure 5-4). Figure 5-1 depicts the schematics of the system and Figure 5-2 shows photography of the actual setup.

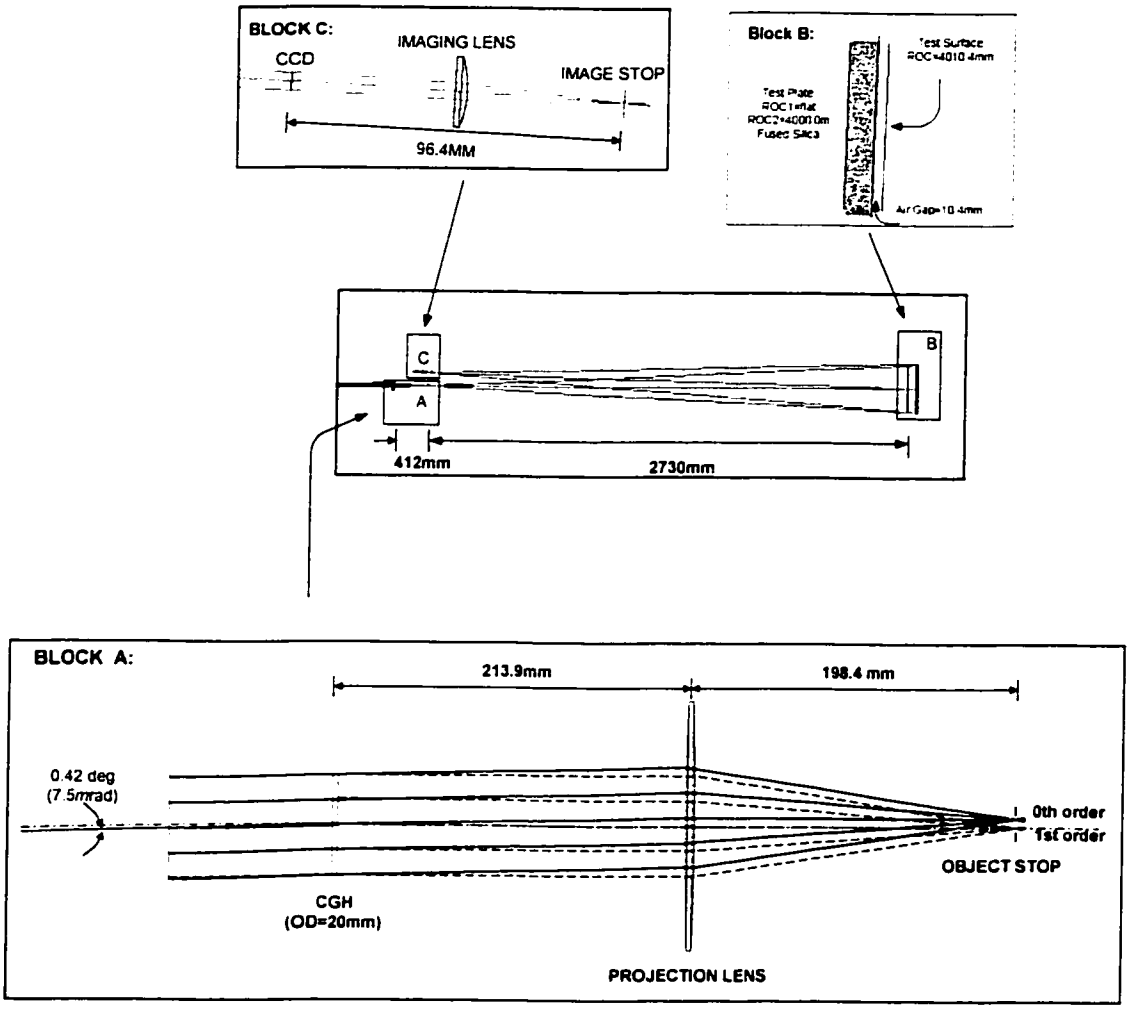

Figure 5-1. Schematics of the laboratory setup. The projection system (Block A) is 2,730-mm away from the test plate (Block B). Imaging system (Block C) is located 165-mm away from the projection system. The collimated light illuminates the CGH at 0.42 degrees off the axis defined by the centers of the CGH and the projection lens. This setup is used to validate testing of aspheres using a test plate and CGH.

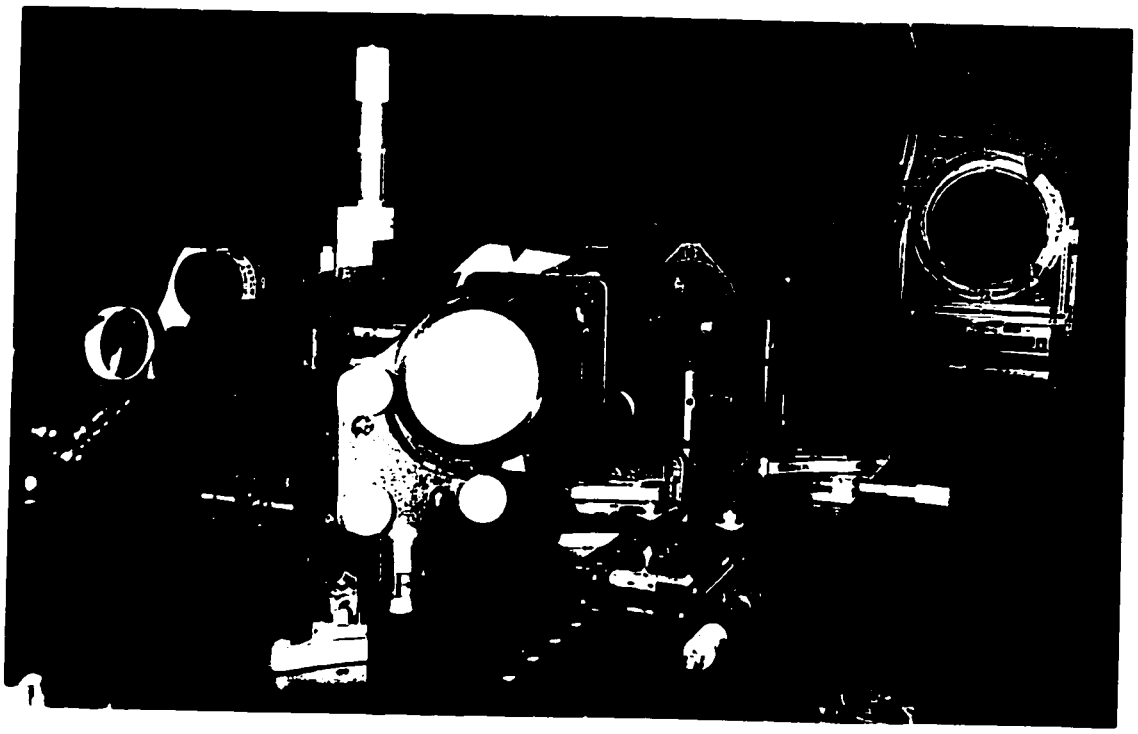

Figure 5-2. The entire laboratory setup fits on a 4-m floating table.

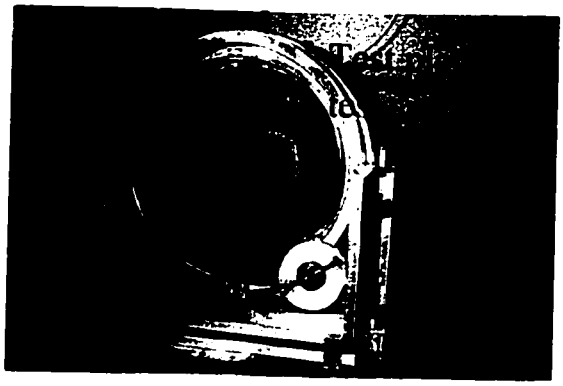

Figure 5-3. Matching 30-cm (12") test plate and test sphere. The test plate (foreground) is plano-convex and the test sphere (behind the test plate) is convex in shape.

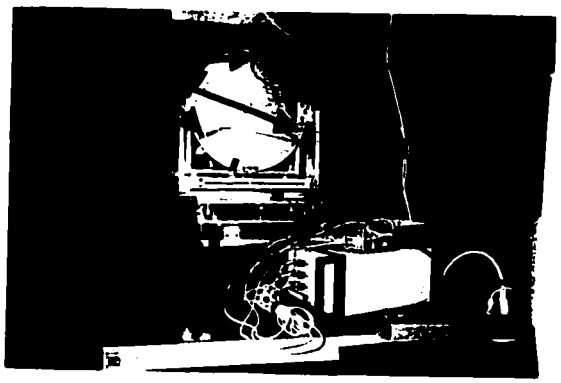

Figure 5-4. Three piezo-electrical transducers (PZTs) are positioned on the back of the test sphere for phasing shifting.

Using the setup shown in Figure 5-2and employing the phase shifting interferometry (PSI), series of five fringes (Table 5-1) are captured on CCD and processed to obtain a surface map of the segment (Figure 5-5)

The software used for such processing is Durango (Diffraction International Inc.) and phase calibration is done automatically. A sample of five-frame phase-shifted interferograms (Table 5-1) are captured by Pulnix TM741E CCD and then digitized.

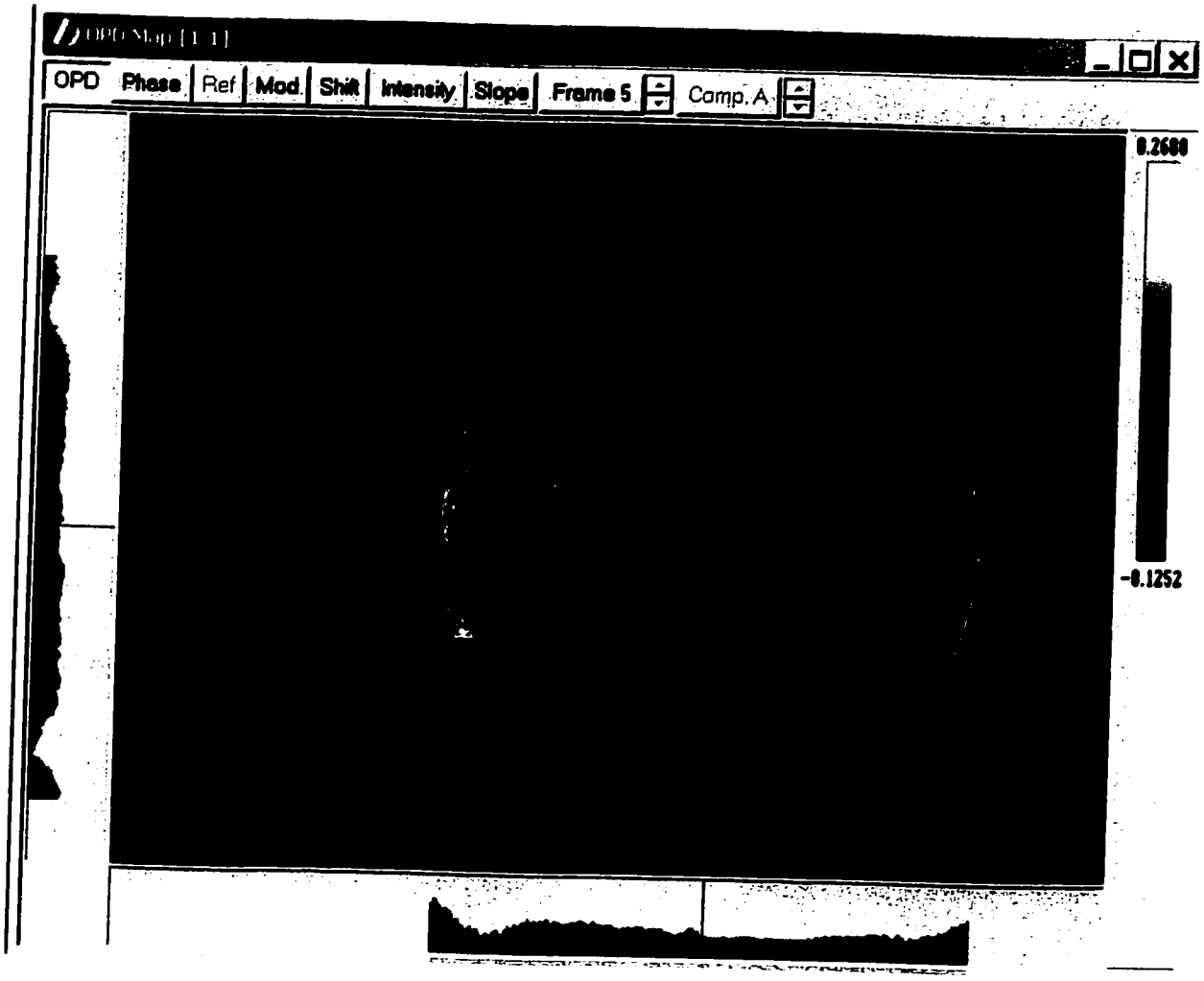

Figure 5-5. A surface map of the test sphere. PV=0.3932λ, RMS=0.0425λ.

Table 5-1. The five frames are used to compute a surface map of the test sphere. The fifth frame also verifies that the phase shifting is correctly stepped every 90 degrees.

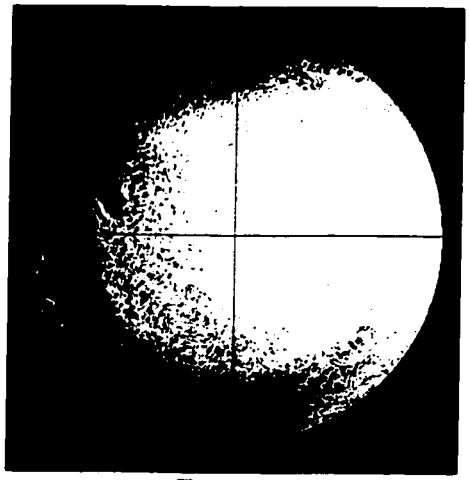

Frame 1

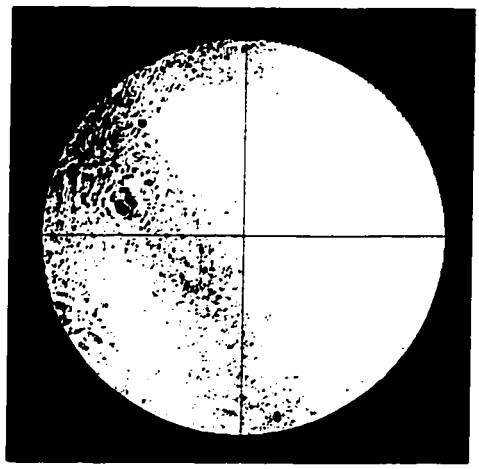

Frame 2

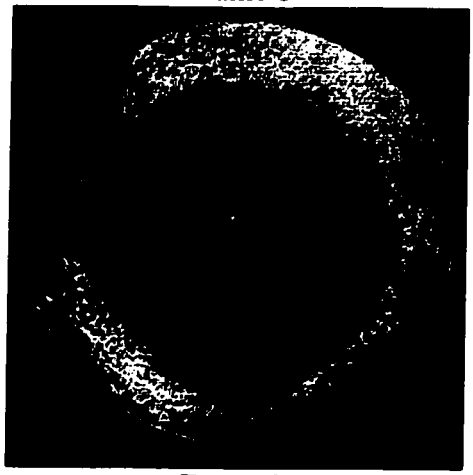

Frame 3

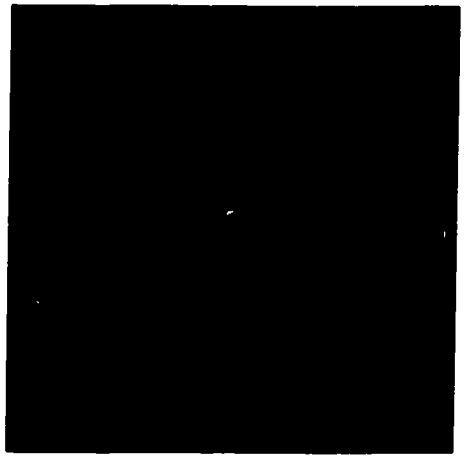

Frame 4

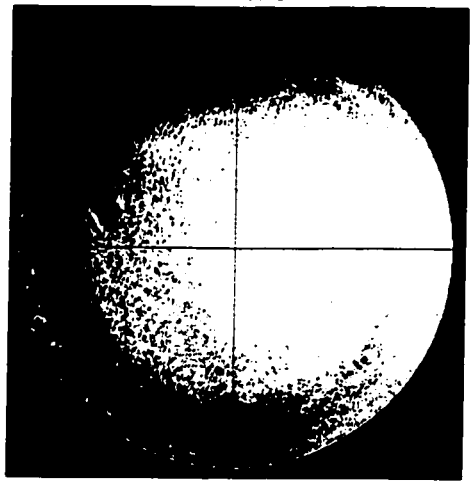

Frame 5
(identical to Frame 1 as expected when the phase is correctly stepped).

5.2 CGH FABRICATION

The sample CGH used for the test is shown in Figure 5-6 ("magnified" 10x or every line represents 10λ of optical path difference) and Table 5-3 lists the corresponding Zernike used to generate the CGH. As expected, the dominating feature of the CGH is large tilt carrier fringes (126λ). This ensures us that the test accuracy can be gauged accurately since large tilt fringes dominate the test sensitivity to CGH fabrication errors.

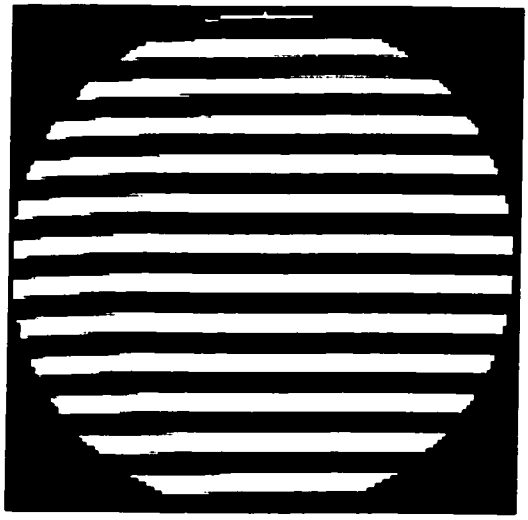

Figure 5-6. The sample CGH (plotted here with very fringe equals to 10λ optical path differnce) used to validate the new test method. Here, a 30-cm convex sphere with known surface quality was tested using CGH and a 30-cm test plate. The CGH was design and used in the same manner as testing of an asphere. The dominating feature on the CGH is large tilt carrier fringes (126λ across the 20mm hologram) so test sensitive is the same as that of testing an asphere.

Zernike definitions used in Zemax for defining the phase function are included in Table 6-11. Fabrication of the hologram was generously denoted by Prof. Alexander Poleshchuk of the Russian Academe of Science. To interface with Prof. Poleshchuk's hologram writing machine (run by Vadim Cherkashin), we first developed an algorithm to sample and translate the continuous phase function Φ(x,y) into a binary function according to the logic presented in Figure 5-7.

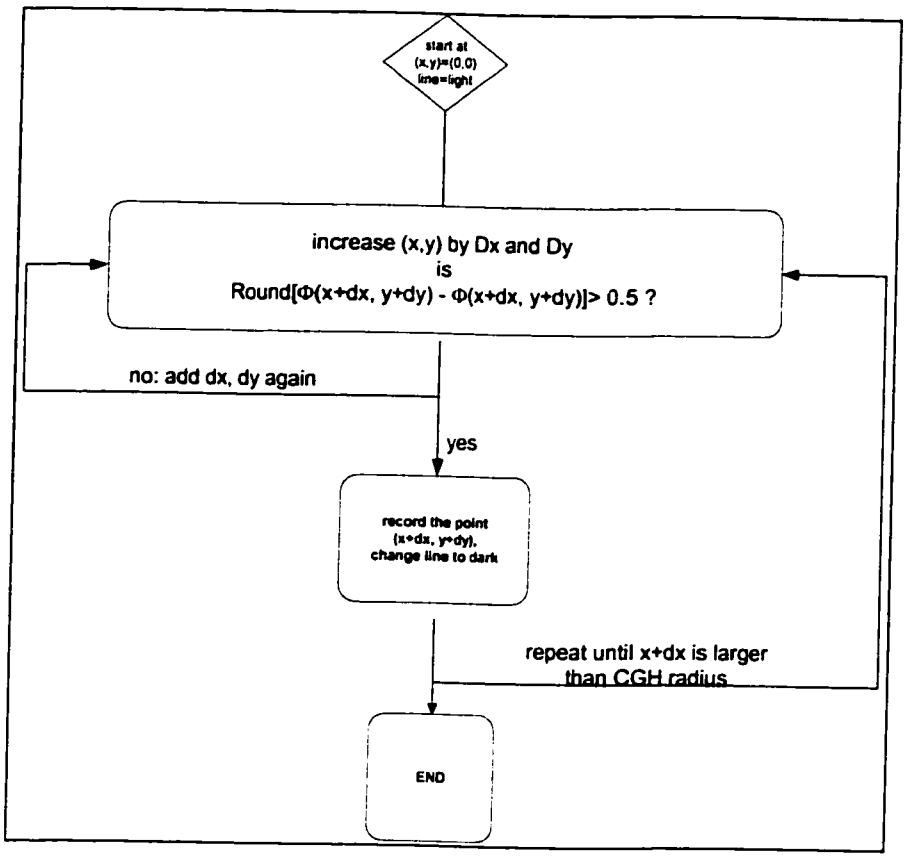

Figure 5-7. Logic used to binize the continuous phase function.

To verify the phase function developed in the algorithm, phase value of the hologram was separately checked using a customized Zemax macro (Appendix C). The result from two completely different programs are in excellent agreement (Table 5-2).

Table 5-2. Hologram phase is verified using two uncorrelated methods.

from c-code			from Zemax macro (Appendix C)	
x	y	phase(x,y)	(x,y)	phase (x,y)
-5.00	0.00	0.008186	(-5.0000, 0.0000)	0.008186
-5.00	-5.00	63.17134	(-5.0000, -5.0000)	63.17134
0.00	10.00	-126.5189	(0.0000, 10.0000)	-126.5189
10.00	0.00	-0.062185	(10.000, 0.0000)	-0.062185

Table 5-3. Zernike representation of the CGH shown in Figure 5-6. All units are in waves.

MAX TERM OF ZERN USED IS 37	
NORMAL RADIUS IS 10.00	Zernike #19 = -0.0000000006
Zernike # 1 = 0.0000000000	Zernike #20 = 0.0000002654
Zernike # 2 = 0.0000000012	Zernike #21 = -0.0000004684
Zernike # 3 = -126.4012057689	Zernike #22 = 0.0000000003
Zernike # 4 = -0.0315276745	Zernike #23 = -0.0000000008
Zernike # 5 = -0.0305603901	Zernike #24 = -0.0000004168
Zernike # 6 = 0.0000000028	Zernike #25 = 0.0000000142
Zernike # 7 = -0.0000000015	Zernike #26 = -0.0000000018
Zernike # 8 = -0.1166768359	Zernike #27 = -0.0000000002
Zernike # 9 = 0.0000319112	Zernike #28 = 0.0000000008
Zernike #10 = -0.0000000002	Zernike #29 = 0.0000000017
Zernike #11 = 0.0000802366	Zernike #30 = 0.0000000002
Zernike #12 = -0.0001320164	Zernike #31 = 0.0000000012
Zernike #13 = 0.0000000001	Zernike #32 = 0.0000000004
Zernike #14 = -0.0000000014	Zernike #33 = 0.0000000000
Zernike #15 = -0.0002013990	Zernike #34 = -0.0000000004
Zernike #16 = 0.0000031107	Zernike #35 = 0.0000000015
Zernike #17 = 0.0000000788	Zernike #36 = 0.0000000017
Zernike #18 = 0.0000000002	Zernike #37 = 0.0000000170

Table 5-4. Zernike definitions used in Zemax.

Z 1	1	Z 19	(5p^2 - 4) p^3 * COS (3A)
Z 2	(p) * COS (A)	Z 20	(5p^2 - 4) p^3 * SIN (3A)
Z 3	(p) * SIN (A)	Z 21	(15p^4 - 20p^2 + 6) p^2 * COS (2A)
Z 4	(2p^2 - 1)	Z 22	(15p^4 - 20p^2 + 6) p^2 * SIN (2A)
Z 5	(p^2) * COS (2A)	Z 23	(35p^6 - 60p^4 + 30p^2 - 4) p * COS (A)
Z 6	(p^2) * SIN (2A)	Z 24	(35p^6 - 60p^4 + 30p^2 - 4) p * SIN (A)
Z 7	(3p^2 - 2) p * COS (A)	Z 25	(70p^8 - 140p^6 + 90p^4 - 20p^2 + 1)
Z 8	(3p^2 - 2) p * SIN (A)	Z 26	(p^5) * COS (5A)
Z 9	(6p^4 - 6p^2 + 1)	Z 27	(p^5) * SIN (5A)
Z 10	(p^3) * COS (3A)	Z 28	(6p^2 - 5) p^4 * COS (4A)
Z 11	(p^3) * SIN (3A)	Z 29	(6p^2 - 5) p^4 * SIN (4A)
Z 12	(4p^2-3) p^2 * COS (2A)	Z 30	(21p^4 - 30p^2 + 10) p^3 * COS (3A)
Z 13	(4p^2-3) p^2 * SIN (2A)	Z 31	(21p^4 - 30p^2 + 10) p^3 * SIN (3A)
Z 14	(1Op^4 - 12p^2 + 3) p * COS (A)	Z 32	(56p^6 - 1(A)
Z 15	(1Op^4 - 12p^2 + 3) p * SIN (A)	Z 33	(56p^6 - 1(A)
Z 16	(20p^6 - 30p^4 + 12p^2 - 1)	Z 34	(126 p^8 - * COS (A)
Z 17	(p^4) * COS (4A)	Z 35	(126 p^8 - * SIN (A)
Z 18	(p^4) * SIN (4A)	Z 36	(252p^10 - 2 - 1)
		Z 37	(924p^12 - 420p^4 - 42p^2 + 1)

5.3 EXPERIMENTAL RESULTS

In this experiment, we designed a system for the CGH test and devised a traditional method to measure the same test surface in the same setup without using the hologram. The new method uses both 1^{st} and 0^{th} diffraction orders whereas the traditional method is equivalent to use only the 0^{th} order. We then procured the hologram to the design, and built the setup in the laboratory. The actual setup departs from the design slightly in that we did not illuminate the hologram off-axis as depicted in Figure 5-1 (0.42 degrees off-axis in the design). Instead of purchasing another hologram, we modeled the laboratory setup in a computer simulation and backed out the residual effect. This section describes these steps and reports how well the two methods agree.

5.3.1 Raw experimental data

The test sphere was measured using the new proposed method and a traditional method. For the traditional method, we used only the 0^{th} order of the CGH in the same test setup (which is equivalent to not using CGH). Table 5-5 shows the results from these two methods. Note that the results shown in Table 5-5 are average of many measurements. This is because individual measurements of the test have smaller random errors that are caused by the environmental and/or electronic noises. Since these noises are small in amplitude and are assumed to be uncorrelated, average of measurements reduce the effect of these noise on the measurement to a negligible level according to Eqn. [2.37].

$$\overline{N} = \frac{1}{\sqrt{M}}[n_i], \qquad [2.37]$$

where

N: final noise in the averaged measurement result

M: number of measurements

n_i: individual noise in the ith measurement.

Table 5-5. Raw measurement data from two methods (surface maps)

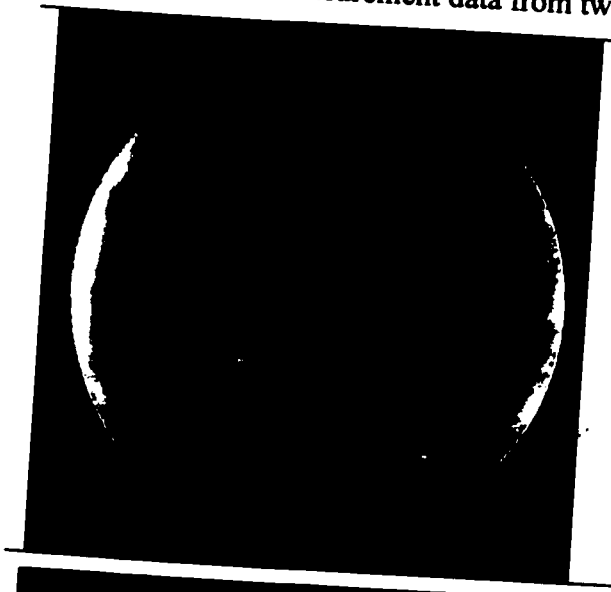	**Proposed method:** Includes the known errors from the as-built system. RMS=0.0369 λ (wavefront) (Average of 146 measurements)
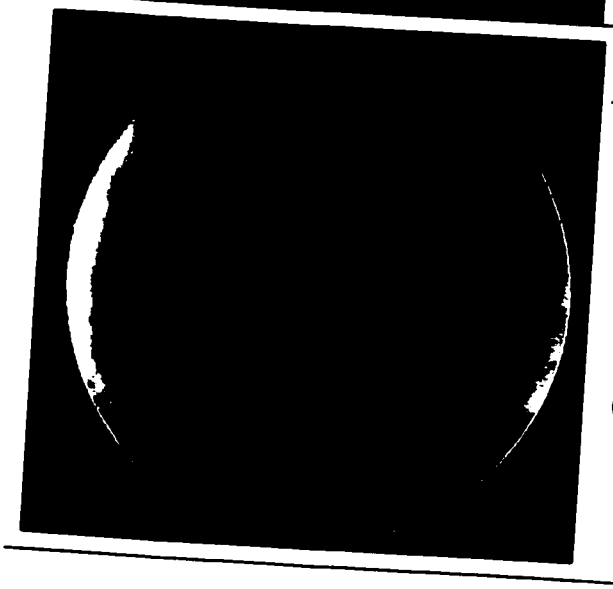	**Traditional method:** Includes the known errors from the as-built system. RMS=0.0490 λ (wavefront) (Average of 156 measurements)

To estimate the noise present in the measurement for each method, two measurement data were randomly chosen and were subtracted from their respective average. Figure 5-8 and Figure 5-9 show that, for the new and traditional methods, the individual random noise presented in the single measurement is 0.0069λ and 0.0099λ respectively (i=23 for this example). Since N= 146 and 134 for these two cases, the average noise in the final measurements are 0.00057λ and 0.00085λ respectively.

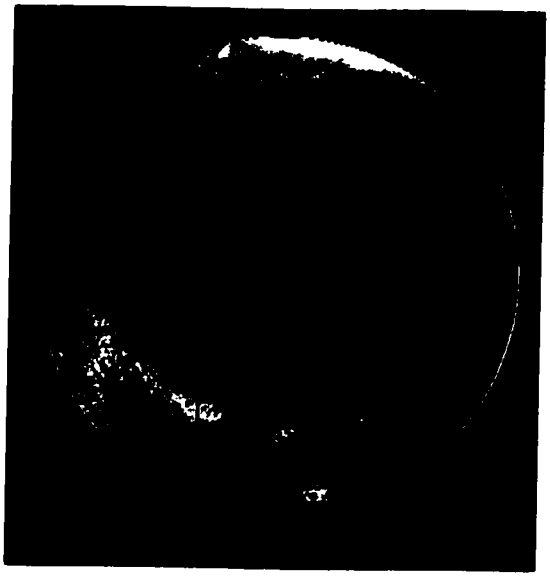

Figure 5-8. Typical individual noise in the measurement using traditional method has RMS=0.0099 λ. The average noise is reduced to 0.00085λ after average of 136 measurements.

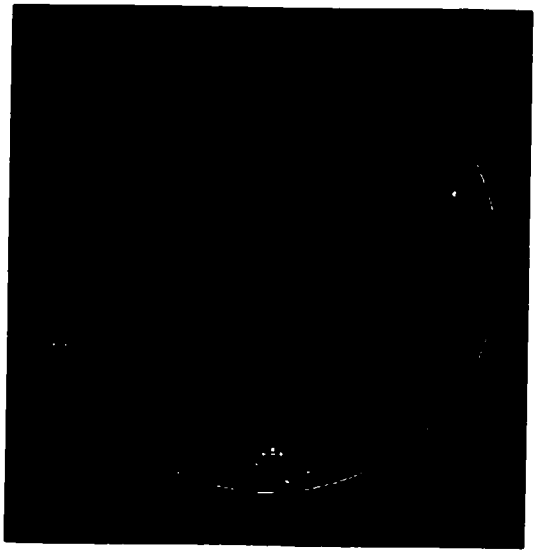

Figure 5-9. Typical individual noise in the measurement using the new method has RMS=0.0069 λ. The average noise is reduced to 0.00057λ after average of 146 measurements.

5.3.2 Simulated System Errors

Computer models were developed, for both the new and traditional methods, to simulate the induced system errors when the CGH was illuminated on-axis, not as designed 0.42-degree off-axis illumination. Instead of taking the CGH out, it was kept in place for the measurement of traditional method so the system alignment is not disturbed. This means that when the CGH is not illuminated as it was designed, the traditional method also incurs induced system error, as the location of the 0^{th} order is now different. Table 5-6 shows the simulated errors that are induced by on-axis illumination. Note that the induced errors are mostly lower order astigmatism and coma.

5.3.3 Comparison of Corrected Data

Subtracting the induced errors (Table 5-6) out from the measurement data (Table 5-5), we now have the corrected data, shown in Table 5-6. Two methods result in a net measurement difference of 0.0116λ RMS wavefront. This result matches the predicted 0.0124 λ RMS wavefront detailed in Section 5.4 (Error Analysis). This validates the computer model used for the tolerance analysis very well. In addition, tolerance analysis shows that instead of using an off-the-shelf BK7 lens as the projection system, the measurement accuracy can be improved to 0.0056λ RMS-wavefront if the quality of the projection lens can be improved from λ/4 peak-to-valley (PV) surface to λ/8 PV surface. One last noteworthy point is that this experiment validation only serves as 'proof-of-

Table 5-6. Simulated System Errors induced by on-axis illumination.

traditional method (uses 0^{th} order only)		new proposed method (uses 1^{st} and 0^{th} orders)	
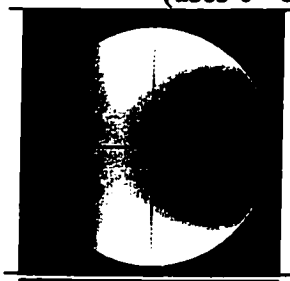	RMS = 0.0086λ	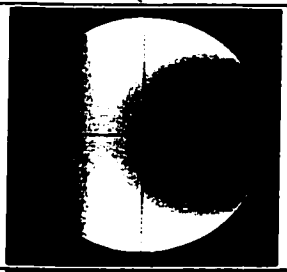	RMS = 0.0161λ
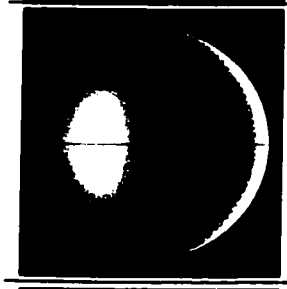	COMA COMPONENT: RMS = 0.0040λ z8 = 0.011λ	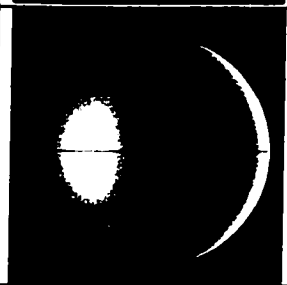	COMA COMPONENT: RMS = 0.0079λ z8 = 0.0224λ
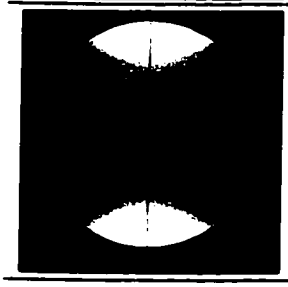	ASTIGMATISM COMPONENT: RMS = 0.0077λ z4 = -0.0188λ	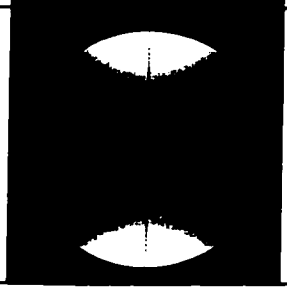	ASTIGMATISM COMPONENT: RMS = 0.0140λ z4=-0.0344λ

concept' and was completed without the aid of alignment fiducial marks that were to be etched on the CGH. As discussed earlier in Chapter 5 and Chapter 6, fiducial marks allows for accurate registration of the CGH with respect to position of the surface under test. In the absence of these marks, the only aberration we could visually remove from the interferogram is the defocus (by nulling out the interferogram). The result shown in Figure 5-11 predicts that if residual coma and astigmatism can be taken out, the net measurement accuracy would on the order of 0.0069λ RMS wavefront.

Table 5-7. Comparison of corrected measurement data.

	before correction (wavefront)	after correction (wavefront)
traditional method	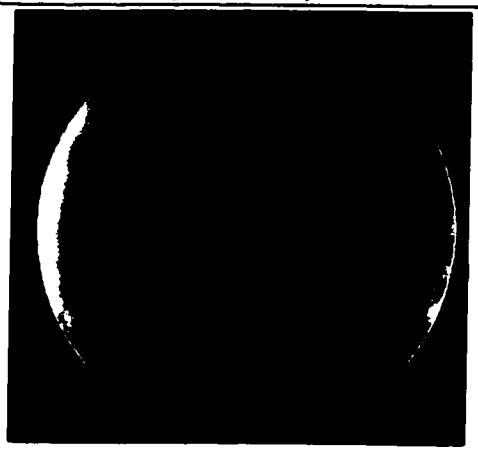	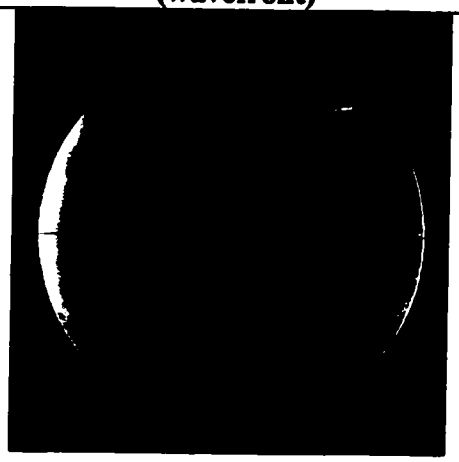
	0.0490λ rms	0.0554λ rms
new method	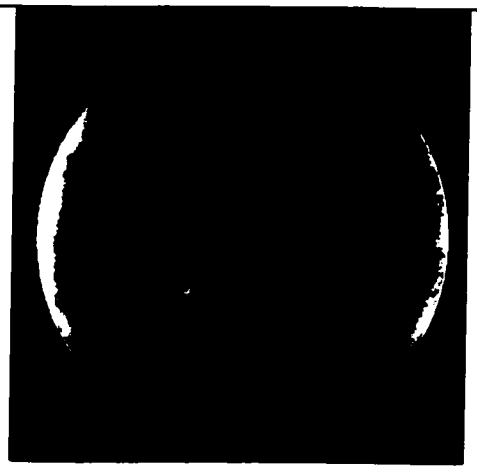	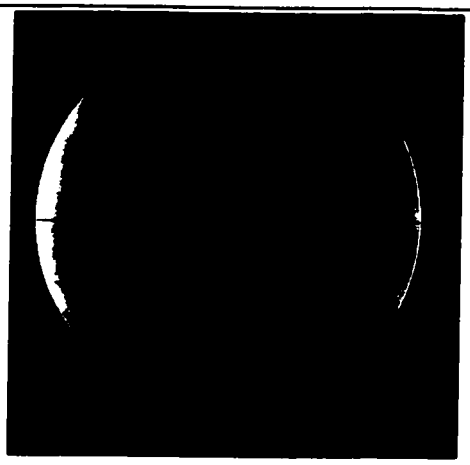
	0.0386λ rms	0.0489λ rms
difference		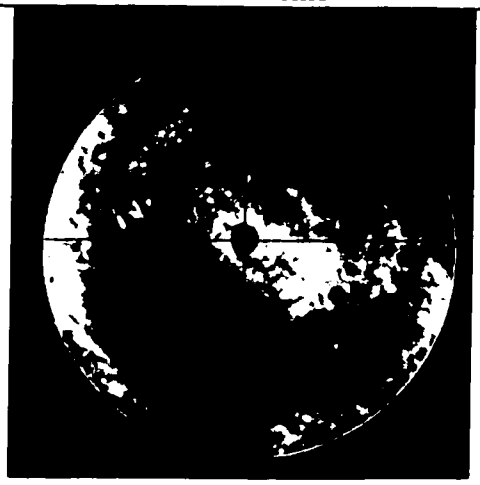
		0.0116λ rms

Figure 5-10. Measurement difference when alignment marks are not used for the proposed method.

RMS wavefront error = 0.0116λ

Figure 5-11. Measurement difference (same as above) when lower order coma and astigmatism are taken out.

RMS wavefront error = 0.0069λ

5.4 TOLERANCE ANALYSIS

Tolerance analysis, error budget, and error analysis all address the same thing: how good do the optical components and alignment accuracies have to be to meet the desired test accuracy. There are really two types of error in the tolerance analysis: imperfections in manufacturing of the optical components and inability to put these components at the precise location. The first type, caused by small variations in the thickness, refractive index, curvature of an element may be, in theory, compensated by either changing the lens spacing or by pre-coding these errors in the CGH – provided that the errors are measured very accurately beforehand. The second type, caused by the inability to know

precisely where these elements are, is more difficult to correct. This type of error is the 'expected error' of the experiment since it gives us the uncertainty of the measurement itself.

The tolerance analysis for this experiment consists both manufacturing and measurement uncertainty. It is created in a two-step process: First, small perturbations were introduced to the components and positioning of these components, one at a time. Second, a dummy Zernike phase surface was added at the CCD to fully correct the reference beam. Since the reference and the test beams coincide at the CCD, the net error induced by the perturbation in the first step shows up in the test beam only. Following these two steps, containing all the perturbations and their induced effects are tabulated. To simulate the removal of the defocus in the actual experiment, net error shown in the test beam were fitted to the lower four Zernike terms first and only the residual fitted error was recorded. This is equivalent to removing tilt and power terms.

Table 5-8. Tolerance analysis of the laboratory setup

parameter	value	Tol.	units	tilt and focus are removed	
				λ/4 optics	λ/8 optics
Laser Beam					
Collimation	-	1	λ	0.000687	0.000687
Beam alignment*	-	0.002	deg	0.000119	0.000119
CGH					
Decenter in x	-	0.1	mm	0.0017	0.0017
Decenter in y	-	0.1	mm	0.0017	0.0017
Tilt in x	-	0.1	deg	0.0000	0.0000
Tilt in y	-	0.1	deg	0.0000	0.0000
Rotation	-	0.1	deg	0.0003	0.0003
CGH - L1 spacing	213.93	1	mm	0.000001	0.000001
LENS 1					
R1	206.335	0.1	mm	0.0001	0.0001
Thickness	6.15	0.1	mm	0.0000	0.0000
R2	- 206.26	0.1	mm	0.0001	0.0001
Index	BK7	0.00001	-	0.0001	0.0001
Surface 1	Surf PV	0.25 or 0.125	λ	0.0076	0.0020
Surface 2	Surf PV	0.25 or 0.125	λ	0.0077	0.0020
Inhomogeneity	PV	2.00E-06	-	0.0020	0.0020
Decenter in x	-	0.1	mm	0.0017	0.0017
Decenter in y	-	0.1	mm	0.0017	0.0017
Tilt in x	-	0.1	mm	0.0009	0.0009
Tilt in y	-	0.1	mm	0.0009	0.0009
Wedge	-	8.73E-04	rad	0.0022	0.0022
L1 - TP spacing	2908.38	1	mm	0.0001	0.0001
Test Plate (TP)					
R1	14222.5	2,000	m	0.0000	0.0000
Thickness	51.5366	0.0127	mm	0.0000	0.0000
R2	3998.4172	0.1	mm	0.0003	0.0003
Index	F Silica	0.0001	-	0.0000	0.0000
Surface 1	Surf PV	0.125	λ	0.0038	0.0011
Wedge	-	7.27E-04	rad	0.0001	0.0001
RSS (WF)	-	-	λ	**0.0124**	**0.0056**

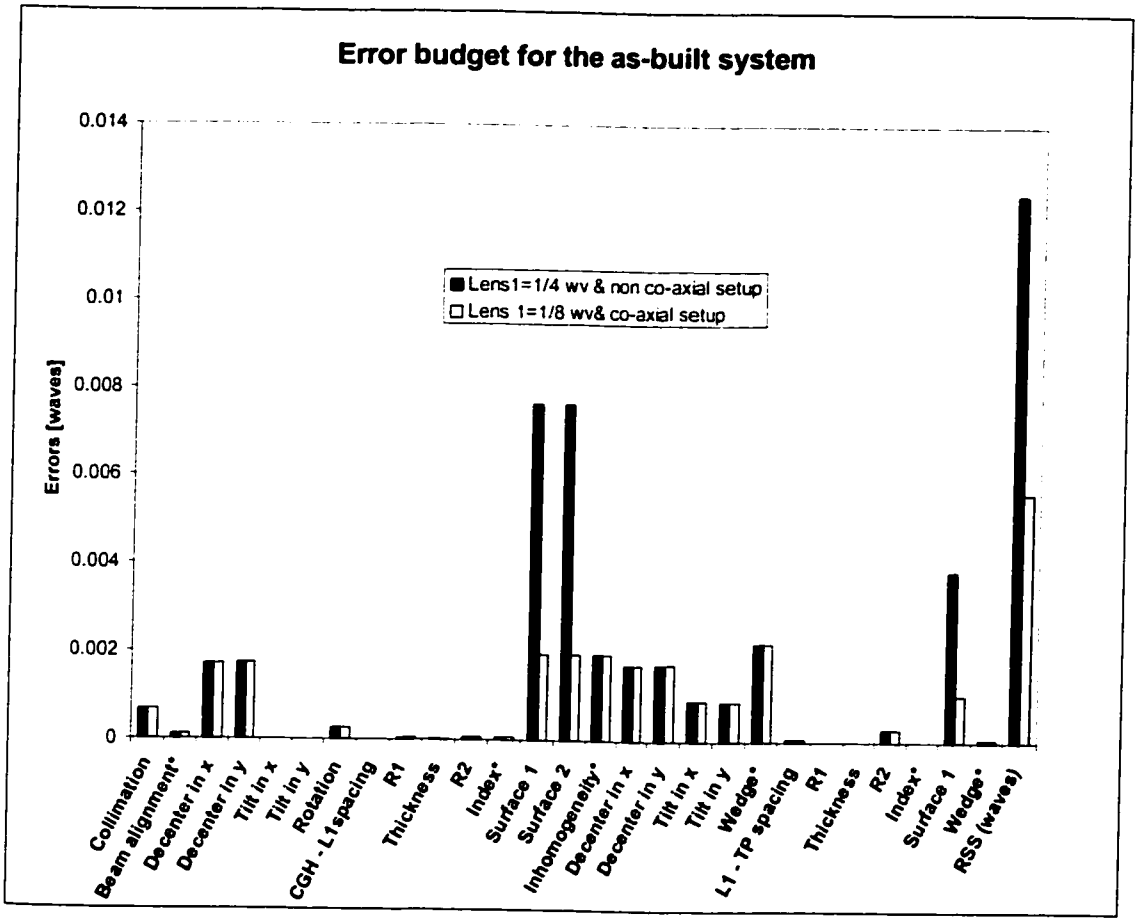

Figure 5-12. Error budget comparison for the CGH test. By using a better projection lens (lens 1) and utilizing the co-axial setup, the test accuracy can be improved dramatically.

5.5 INTERFEROMETER REPEATABILITY

The repeatability of a test is one of the important performance gauge as it show how accurately does one measurement matches to the next one. The repeatability is calculated by subtracting two consecutive measurements. For each of the measurements, tilt and focus are optimized to minimize the number of fringes across the CCD (i.e. the most

fluffed-out fringes). Figure 5-13 shows the result of subtracting two consecutive measurements. It shows that the RMS noise is approximately 0.009λ (wavefront).

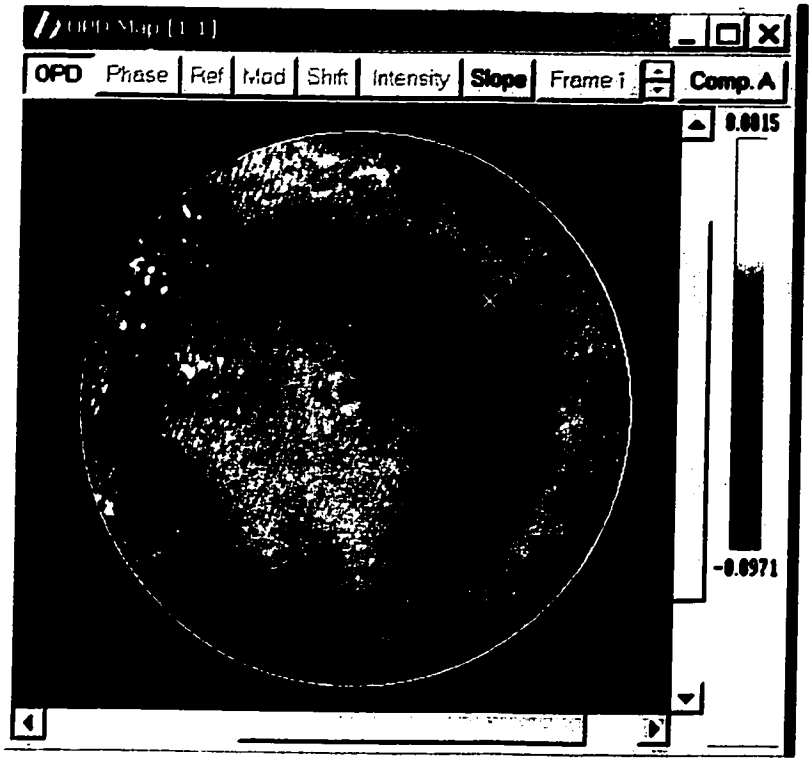

Figure 5-13. Subtraction of two consecutive measurements shows the root-mean-square (RMS) test repeatability is 0.009λ (wavefront).

5.6 LESSONS LEARNED

One important lesson learned form this experiment is that co-axial setup is an very effective way to improve the test accuracy. From Table 5-8 and Figure 5-12 we see that three dominating errors are from the surface irregularities of the projection lens and from the surface slope of the illumination surface of the test plate. The first two (from the same lens) are relatively inexpensive to correct, as the size of the projection lens is only

slightly larger than the CGH, or roughly ~20mm to 35mm for most cases. The last one, the wavefront error caused by the surface slope of the test plate (illumination side), appears to be very expensive to improve because its size has to match the test segment, which is 30-cm in this experiment and up to 2-meters other cases. A closer examination reveals that there is a very inexpensive way to reduce this last error. As discussed in Chapter 3 (Figures 3-3 and 3-4), having the input beam (traveling to) and output beam (traveling from) of the test plate co-axial can greatly reduce this last error without imposing the tightened surface slope tolerance.

In this test setup, the test plate is tilted 1.6° with respect to the optical axis defined by the LASER and the projection lens. This was done so that the imaging system can be spatially separated from the projection system. This 1.6° causes reference and test beams to have a induced lateral shear of 910μm on the illumination surface. Using similar method shown in Section 6.2.3, this shear leads to ~0.006 λ wavefront error, which agrees with ZEMAX simulated $\Delta w = 0.0039\ \lambda$. Figure 5-3 shows the amount of induced shear (Δx) approximately increases linearly with the amount of tilt (angle α). When $\alpha=0$, the system has the smallest shear Δx, which is can be calculated using Eqn. [2.38].

$$\Delta x_{min} = \Delta t_{test\ plate} \times \sin^{-1}\left(\frac{\varepsilon_{order\ separation}}{n_{test\ plate}}\right), \qquad [2.38]$$

where

Δt: center thickness of the test plate

n: refractive index of the test plate

ε: minimum tilt needed for the order separation (optimized in Chapter 4)

For this particular laboratory setup, by using co-axial setup, shear between the reference and test beams can be reduced from 910μm to 14μm, thus reducing the wavefront error from 0.003λ to 0.00006λ. Therefore, instead of tightening the surface slope requirement, which is expensive, it is cost effective to reduce the amount of shear (Δx). Figure 5-14 illustrates just how much shear is introduced when co-axial setup is not used. Note also that by inserting a pellicle beam splitter, the projection system can be spatially separate from the image system.

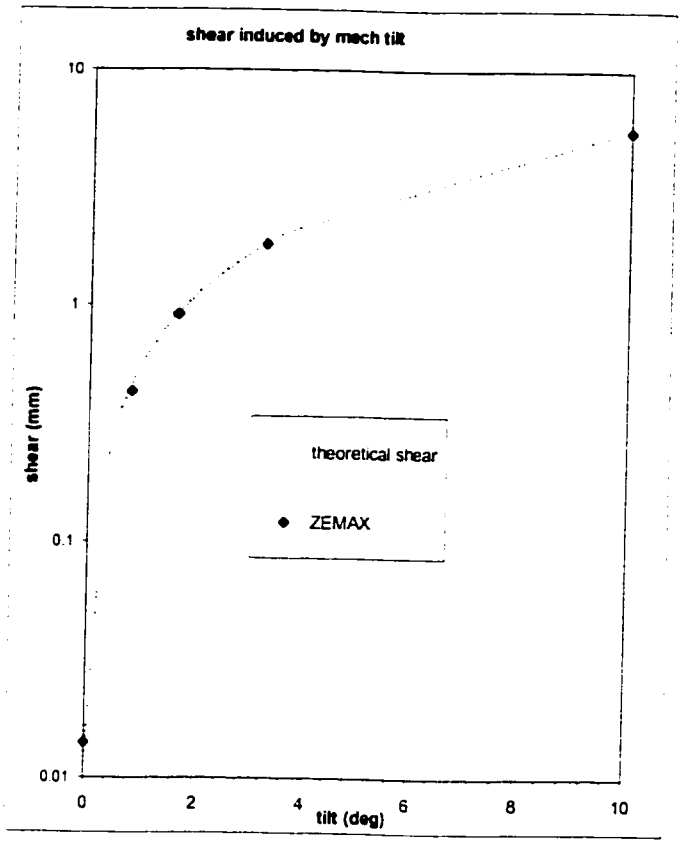

Figure 5-14 Shear and wavefront error linearly depend on the mechanical tilt angle

5.7 SUMMARY

The demonstration was highly successful as a proof that the test, the method of design and analysis are valid. In addition, we learned many things that can be applied for subsequent test system. These are summarized in Figure 5-9.

Table 5-9. Lessons learned from this experiment

optics: • Used the co-axial setup for the next phase of this experiment. • establish the optical axis early on in setting up the experiment and always check to see if it is making sense. • have the setup drawn up in scale BEFORE starting to setup • when mounting anything (lens, CGH, mirrors etc.), ask 'can I adjust it later without moving other pieces?' and 'can I measure the distances between the optics easily later on?' Electronics: • for this particular setup, a pre-existing trim box is used to provide three different level of amplifications to the three PZT drivers. The trim-box seems to be quick sensitive to slightest adjustment and maybe to temperature variation too. A less sensitive circuitry might improve the measurement repeatability. • If piezo-electric transducers (PZT) has to be used for phase shifting, make sure there is a resister connected to it or it burns out very quickly.

The next logic step to carry this experiment one step further is to use the same setup to test an off-axis asphere (currently in progress to be manufactured at the time of writing this dissertation). Testing the asphere will require the alignment fiducials be fabricated on the CGH as discussed earlier.

CHAPTER 6

CASE STUDY-- PART A: SYSTEM DESIGN

This chapter showcases the application of the optimization process discussed previously in Chapter 4. The prime goal of this chapter is to establish the design processes from which similar test systems can be designed and analyzed in the future. The organization of this chapter is as follows. Section 6.1 gives an overview of the properties of the primary mirror under this study. Section 6.2 applies theory developed in Chapters 3 and 4 for optimally selecting three system parameters. System (Sections 6.3 & 6.4) and CGH designs (Section 6.5) are detailed as well. Specification of CGHs are listed in Section 6.6. Finally, fringe contrast are discussed in Section 6.7.

6.1 PROPERTIES OF GSMT PRIMARY MIRROR AND ITS SEGMENTS

GSMT, Giant Segmented Mirror Telescope (Figure 6-1), is a telescope currently being studied by the National Optical Astronomical Observatory (NOAO[1]). It a 30-m parabolic F/1 primary mirror with 618 hexagonal segments, each with 1.33-m in point-to-point dimension. Out of the 618 segments, six representative segments were chosen for the optimization of the system parameters. Locations of these six segments are of particular interests, since the first system parameter, reference surface ROC is optimized based on the information contained in these locations.

[1] NOAO is operated by the Association of Universities for Research in Astronomy under cooperative agreement with National Science Foundation)

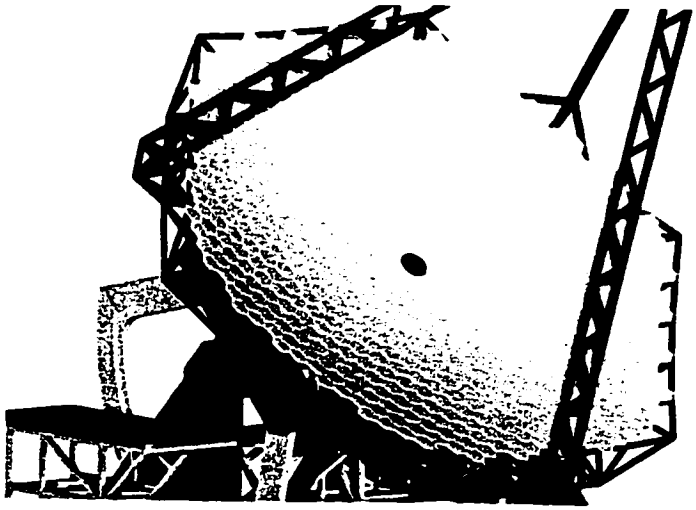

Figure 6-1. The GSMT, Giant Segmented Mirror Telescope, is a telescope currently being studied by the National Optical Astronomical Observatory (NOAO). It a 30-m parabolic F/1 primary mirror with 618 hexagonal segments, each with 1.33-m in point-to-point dimension.

The primary mirror is pieced together with 618 hexagonal segments, each with a 1.330-m point-to-point in dimension (Figure 6-2 and Figure 6-3). This primary mirror may enter the fabrication/testing stages in the next 5-10 years.

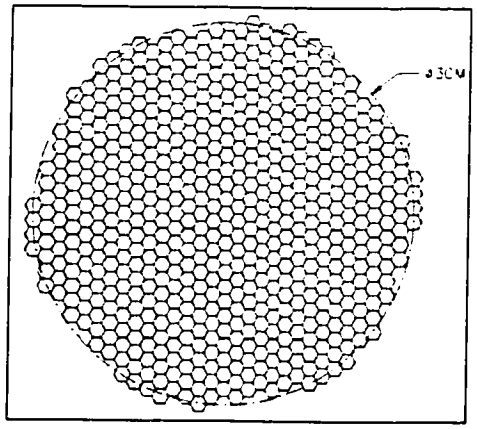

Figure 6-2. The primary mirror is a 30-m F/1.0 parabolic with 618 hexagonal segments.

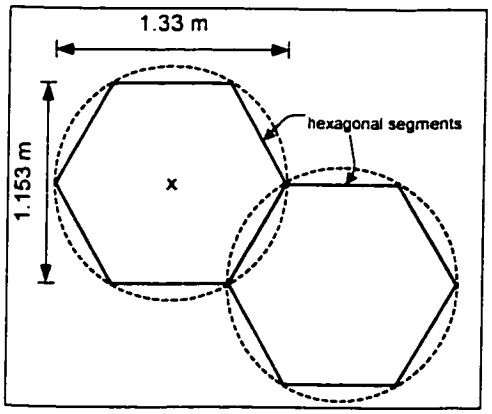

Figure 6-3. Configuration of the segments. Each segment has a 1.330-m point-to-point in dimension (right).

The parent optical surface (Figure 6-2) is a paraboloid of revolution specified by vertex radius of curvature (ROC) and conic constant K (ROC= 60.0m and K= -1.000). The individual segments are defined by their off-axis distance and by the size and orientation of the hexagonal part. The nominal segment dimensions are 1.153 meters across flats, 1.33 meters point to point, and 50 mm thick. A 3% deviation in size varies from the center of the aperture to the edge. The gap between segments is nominally 3 mm. The bevels on the edges are nominally 1 mm wide[29]. The test is designed to go outside of the hexagonal clear aperture by 5-mm in every direction. In addition, to simplify the optical design, all tests are designed over a circular region 1340-mm in diameter. The final CGH design will be stopped down to the correct hexagonal shape.

The point design has 618 segments and the total projected area of the 618 segments is 711 square meters. Since the hexagonal pattern of the segments has six-fold symmetry, the total number of optically unique segments is equal to the total number of segments divided by six, which equals 103 pieces (Figure 6-4). Also shown in Figure 6-4 is the location of six segments (#1, #4, #8, #10, and #13) chosen out of those 103 pieces for this study. Here segment #13 has the furthest off-axis distance and segment #1 has the least.

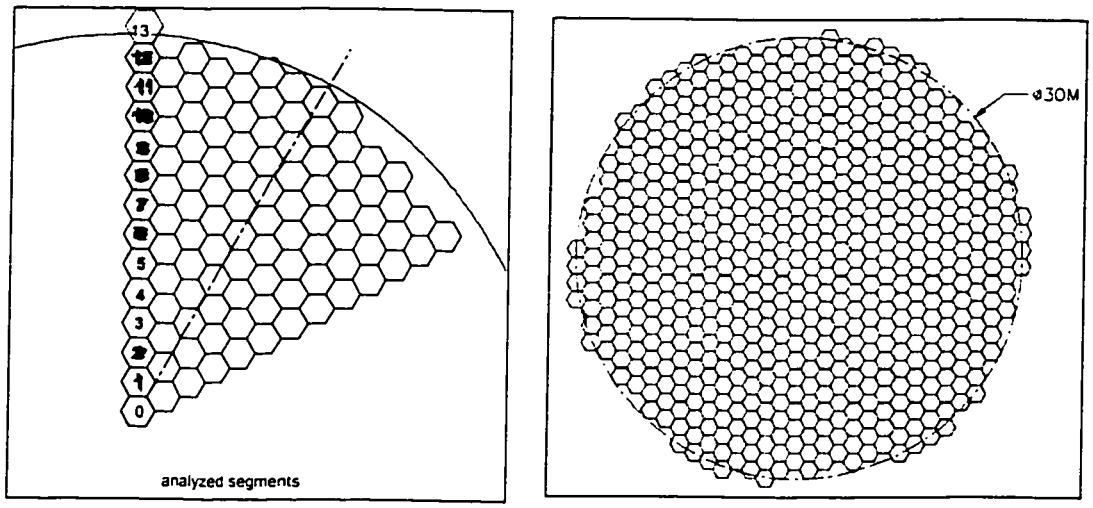

Figure 6-4 1/6 of segments (left) of the primary mirror (right) are optically unique. Also shown is the location of six segments under study (filled in yellow)

The dominating aberration in the far off-axis segments is astigmatism. Figure 6-5 illustrates the aspherical departure in the segments (#1 through # 13) labeled in Figure 6-4. Formulae used to generate Figure 6-5 are included in Table 6-1

Table 6-1. Magnitude of the dominating Seidel wavefront aberration coefficients presented in off-axis segments. Notation: a=segment radius, b=off-axis distance, k=conic constant and R= parent mirror radius of curvature

POWER	ASTIGMATISM	COMA	SPHERICAL ABERRATION
$\frac{Ka^2b^2}{2R^3}$	$\frac{Ka^2b^2}{4R^3}$	$\frac{Ka^3b}{2R^3}$	$\frac{Ka^4}{8R^3}$

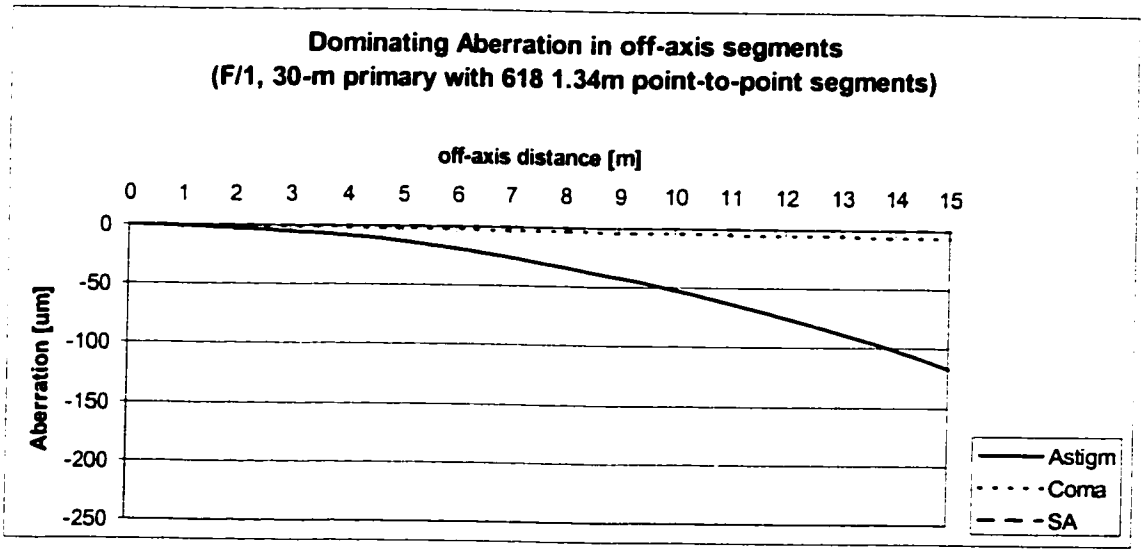

Figure 6-5. Aberrations presented in off-axis segments as a function of off-axis distance. This plot is generated using formulae in Table 6-1.

6.2 OPTIMALLY SELECTING THREE SYSTEM PARAMETERS

As discussed earlier, three system parameters must be chosen for the system design and they are: radius of curvature (ROC) of the reference surface, illumination system, and system magnification M. Once the system parameters are optimally chosen, the two sub systems, the projection and imaging systems, can then be designed accordingly. This completes the 1st order system design. Generation of CGHs needed for testing different segments can be carried out after completion of the 1st order system design.

It is important to understand the tradeoffs that were made early in the system design process so basic parameters pertaining to the system do not have to be altered, otherwise the system has to be re-designed from scratch. The following three subsections detail the design trade-offs for each of the three system parameters.

6.2.1 Optimization of reference ROC

Determination of the reference ROC is detailed in Section 4.1 and summarized here: (1) selection of this ROC value changes the slope of the aberrated wavefront, (2) changes in wavefront slope affect the test accuracy. Higher wavefront slope requires denser CGH tilt carrier fringes for order separation and this makes the test more sensitive to CGH fabrication error; (3) Optimal reference ROC is where wavefront slope of the nearest off-axis segment equal to that of the furthest off-axis segment. When slope errors different in x- and y-direction, smaller of the two should be used for the system design.

An IDL algorithm (Appendix B) was developed to calculate how choice of reference surface changes the wavefront slopes for the two extreme segments that have closest and furthest off-axis distances. The results from that program are then plotted in Figure 6-6 (x-direction slope error) and Figure 6-7 (y-direction slope error). We are interested in where two curves intersect in Figure 6-6 and Figure 6-7. Figure 6-8 shows the corresponding spot diagrams. From Chapter 4, these two intersections represent where slope errors from the two extreme segments are matched. By choosing the smaller slope error among the two, we obtain the optimal reference surface ROC. From where the numerical values of these two intersection points are listed, we conclude that the optimal ROC is 60.955m , corresponding to a system slope variation of 0.351 mrad.

Table 6-2. Numerical values of the intersection points in Figure 6-6 and Figure 6-7.

	slope variation	corresponding ROC value
x-direction	e_x=0.962 mrad	ROC=62.7104m
y-direction	e_y=0.351 mrad	ROC=60.9203m

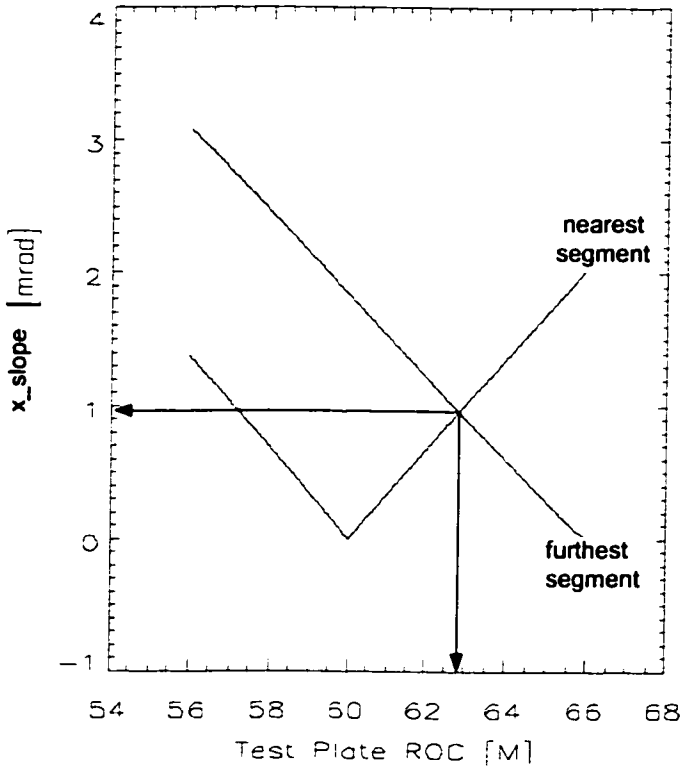

Figure 6-6. Slope variations along x-directions for the nearest segment #1 and the furthest segment #14, as a function of reference surface ROCs. Two curves cross at the point (e_x=0.962 mrad, ROC=62.7104m). Corresponding spot diagram is shown in Figure 6-8.

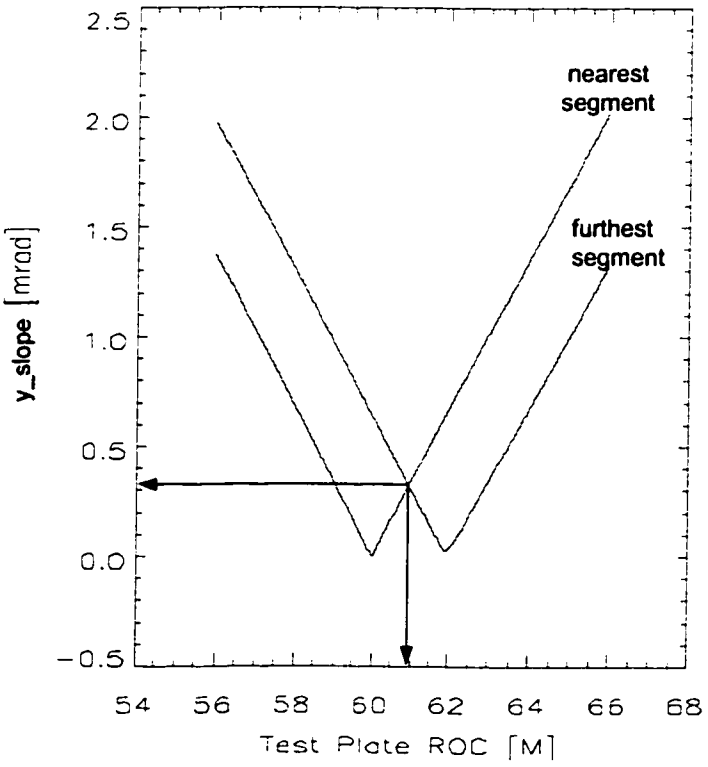

Figure 6-7. Slope variations along the y-direction for segments #1 and #14 as a function of reference surface ROCs. Two curves cross at the point (e_y=0.351 mrad, ROC=60.9203m). To minimize test sensitive to CGH fabrication errors, this plot is used for the system design. Optimal reference ROC of the system is 60.9m corresponds to slope variation of 0.351 mrad.

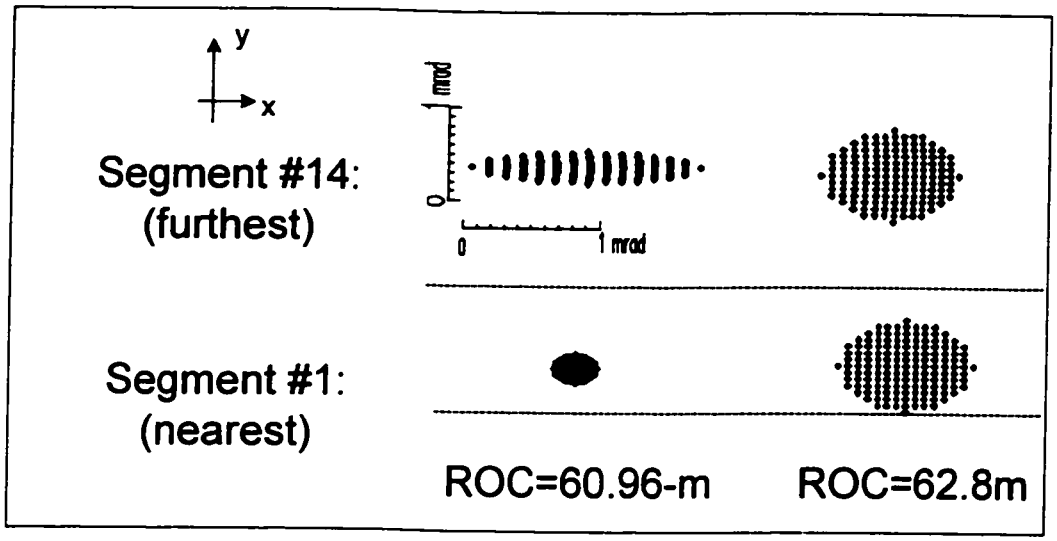

Figure 6-8. Spot diagrams for the closest and furthest segments when reference radius of curvature (ROC) is 60.96m and 62.8m. Two segments y-slope matches for ROC of 60.96m and x-slopes match at ROC of 62.8m, but x-slope has smaller value and is thus used to determine the system parameter reference ROC.

6.2.2 Optimization of the illumination system

After selection of the reference ROC, we need to optimize the second system parameter, the illumination system. As previously discussed in Chapter 4 (System design and optimization), the principal consideration for this optimization is cost. The least expensive illumination system one can design for this test is to use the non-reference side (a.k.a. the illumination side) of the test plate as the illumination system. Moreover, by making this surface spherical instead of aspherical, the cost of the test can be further reduced. A spherical surface is characterized by one parameter – its ROC, so to design the least expensive illumination system for this test is reduced to specify an optimal illumination surface ROC.

Choice of illumination surface ROC affects the amount of SA introduced to the system. SA blurs all diffraction orders at the image stop, and from Section 4.2 of Chapter 4 (System Optimization), we learned that the maximum blur the system can tolerate is a 33% increase in the size of the 0^{th} order, compared to the case when spherical aberration is absent.

To obtain the optimal illumination ROC for this system, Table 6-3 was tabulated to find out how SA affects the spot size as illumination ROC is changed. In this table, the free variable is the viewing distance, measured from the object stop to the test plate. The test setup length is dominated by this viewing distance. Our goal is to keep the test setup as short as possible to fit in a typical 10-15m testing tower and without addition of folding flats. In this table, additional information such as cost comparison between using spherical illumination surface and aspherical illumination surface is also included. The results from Table 6-3 are plotted in Figure 6-9.

Using this table and optimization criteria stated earlier, optimal illumination ROC was chosen. Entries of this table are generated following these steps:

STEP 1: In ZEMAX, setup a 'backward' testing system, where test plate is imaged onto the CGH as shown in Figure 6-10. ZEMAX prescription of this step can be found in Appendix D. The backward setup may be counter-intuitive at first, but a closer look reveals its rationale. The purpose of illumination system is to force light enter the

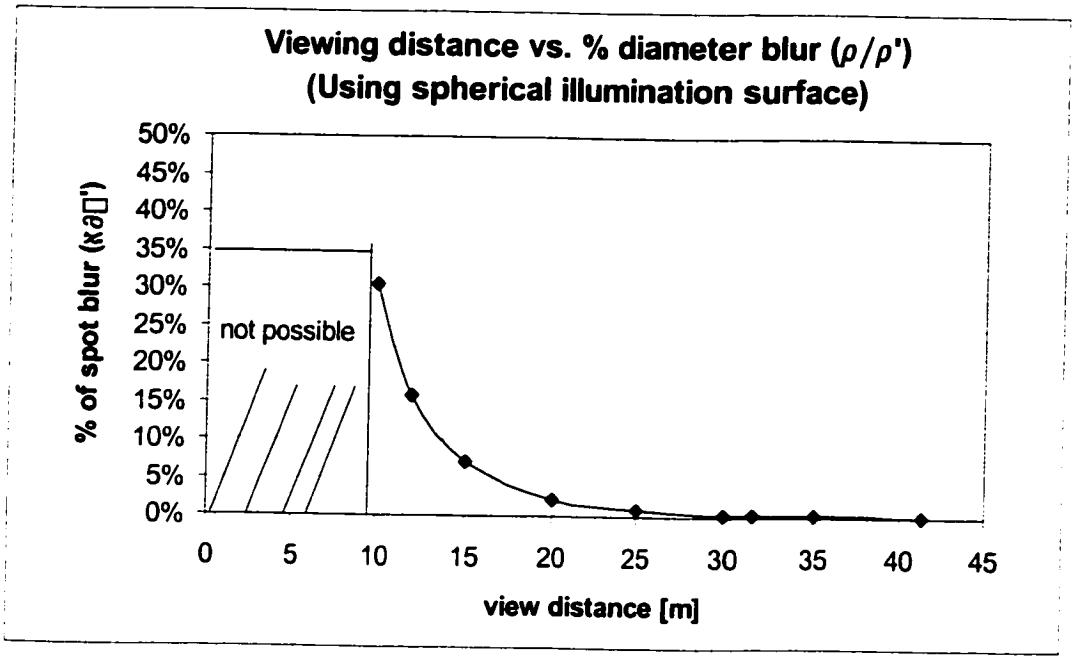

Figure 6-9. By changing radius of curvature (ROC) of the illumination surface, viewing distance (measured from the object stop to the test plate) is changed. Shorter viewing distance is achieved at the cost of higher spherical aberration (SA) which blurs the size of diffraction orders at the image stop.

Desired L [mm]	Required illumination ROC to achieve L	Percentage of blur introduced by SA with spherical illumination surface (ρ/ρ')	Cost of test plate with aspherical illumination surface
4.13E+04	*1.00E+08*	*0.01%*	*$230,000*
3.50E+04	*1.04E+05*	*0.12%*	*$276,000*
3.00E+04	*5.00E+04*	*0.36%*	*$287,500*
2.50E+04	*2.89E+04*	*0.94%*	*$299,000*
2.00E+04	*1.77E+04*	*2.63%*	*$303,600*
1.50E+04	*1.08E+04*	*8.55%*	*$322,000*
1.00E+04	*6.08E+03*	*37.64%*	*$345,000*
5.00E+03	*2.70E+03*	*384.3%* ***(not realizable)***	*$460,000*

Table 6-3. Choice of illumination ROC changes the viewing distance, measured from the object stop to the test plate (listed here as "desired test length [mm]". The cost of test plate (1340mm in diameter) with spherical illumination surface is fix at $230,000.

test segment perpendicularly, so the return beam re-trace itself upon reflection. By setting the system backward, ZEMAX can easily be tricked into accomplish this if we set the refractive index (n') of the space lay between the segment and reference surface fictitiously high. Using Snell's law (Eqn. [6.39]), if n' is fictitiously large, sin(θ') = 0 or output beam is normal to the segment surface.

$$\frac{n}{n'} = \frac{\sin(\theta)}{\sin(\theta')} \qquad [6.39]$$

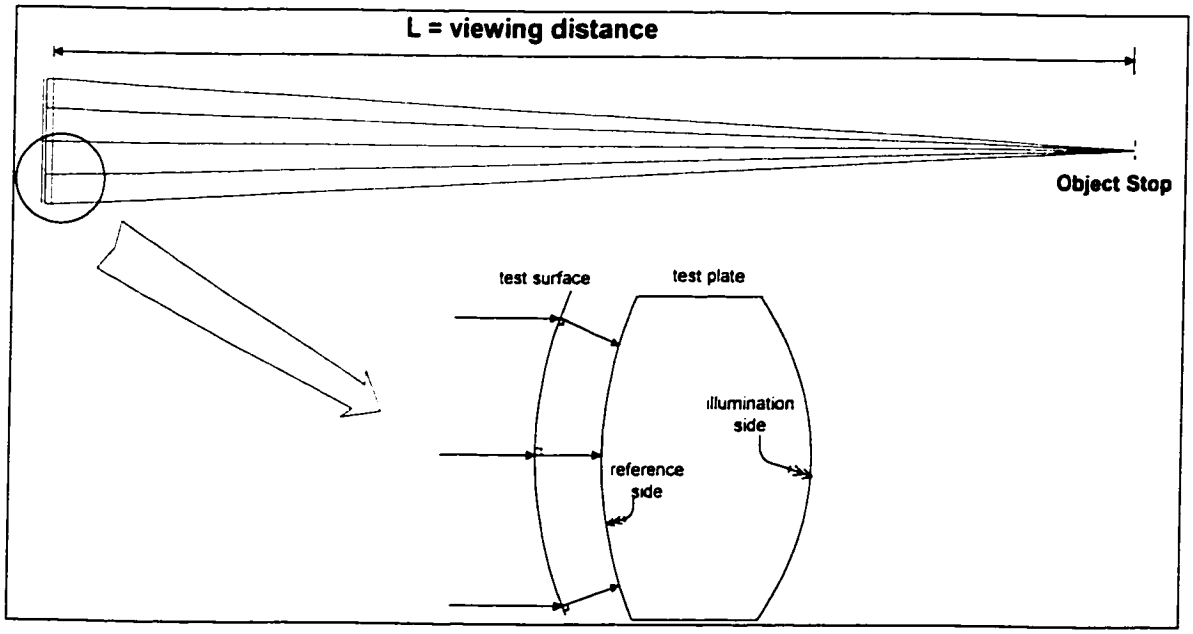

Figure 6-10. A 'backward' test system layout is used to design the illumination system. Collimated light to the left of the test surface is forced to leave the test surface at normal angle by setting the refractive index of the space to the right of the test surface fictitiously high (Eqn. [6.39]). This backward setup is also used to determine the amount of SA introduced to the system when illumination side ROC is changed.

STEP 2: After setting up the backward system in ZEMAX, a viewing distance is specified. For this particular system, we chose viewing distance of 5, 10, 12, 15, 20, 25, 30 and 35 meters. In addition, we included two special cases: (1) illumination surface is

flat (this leads to a viewing distance of 41.3m), and (2) illumination surface has same ROC as the reference ROC (this leads to a viewing distance of 31.53 meters).

STEP 3: Setup illumination surface as a spherical surface; optimize the backward system setup in step 1 for smallest RMS radius spot at the image plane. This gives us ρ', the radius of the blurred 0^{th} diffraction order. The blurred 0^{th} order radius ρ' should be smaller than a third of order separation distance Δ. Δ is calculated using Eqn. [6.40] and $\alpha_{\text{tilt at test plate}}$ is the system slope variation of 0.351 mrad found earlier.

$$\Delta = \left[\alpha_{\text{tilt at the test plate}}\right] \text{x} \left[\text{viewing distance}\right] \qquad [6.40]$$

STEP 4: For each of the viewing distances listed above, set the illumination surface aspherical with four aspherical terms. The backward test system is optimized for the smallest RMS radius spot at the image plane. This enabled us to find ρ, the radius of the 0^{th} order diffraction without SA present in the system. Four aspherical terms can be used to calculate sag added by the aspherical terms so fabrication cost can be estimated. Not surprising, we found that for the shortest viewing distance of 5m,

Using Table 6-3, we see that without using aspherical illumination surface, the shortest viewing distance that offers an acceptable performance of ρ'/Δ=15% is 12.0 meters. This is the illumination ROC we chose for the design of this test system. Last note about the illumination surface is that its surface slope can be quite rough (2.0λ/cm) yet still introduce no more than 0.003 λ of wavefront error to the test accuracy. A detailed discussion can be found in Chapter 7 (Case Study. Part B: Tolerance Analysis).

6.2.3 Optimization of system magnification M

The last system parameter must be optimized in the system magnification M. As discussed earlier in Chapter 4, the main tradeoff in this optimization is test accuracy verses the accumulative fabrication cost of 103 CGHs. Figure 6-11 summarized this design process.

We allocated surface error of 2.6-nm to CGH fabrication error. With the standard CGH fabrication error of ±0.125 μm, we find this corresponds to a minimum CGH line spacing of 15μm (Eqn. [2.41]).

$$\text{surface measurement error} = \left[\frac{0.125\mu\text{m}}{\text{CGH line spacing}}\right] \times \left[\frac{\lambda}{2}\right] \qquad [2.41]$$

To fit more CGHs onto on a standard 6'x6' substrate, thus reducing the cost of fabricating 103 CGHs, the size of the CGHs are kept at their minimum. This is accomplished by keeping the CGH line spacing at the minimum, where CGH fabrication inaccuracy would not exceed the pre-allocated error budget. Since this minimum CGH line spacing is Λ=15um, the corresponding optimal system magnification M is then 40.0x, found by substituting 1.053mrad for α, the tilt at the test plate in Eqn.[2.42]. Note, α is merely the tilt needed for order separation and is equal to three times the system slope variation of 0.351-mrad obtained when the reference surface ROC was optimized.

$$M = \frac{\lambda}{\sin(\alpha)\Lambda} \qquad [2.42]$$

To summarized, system magnification of 40.0x was chosen to meet the required test

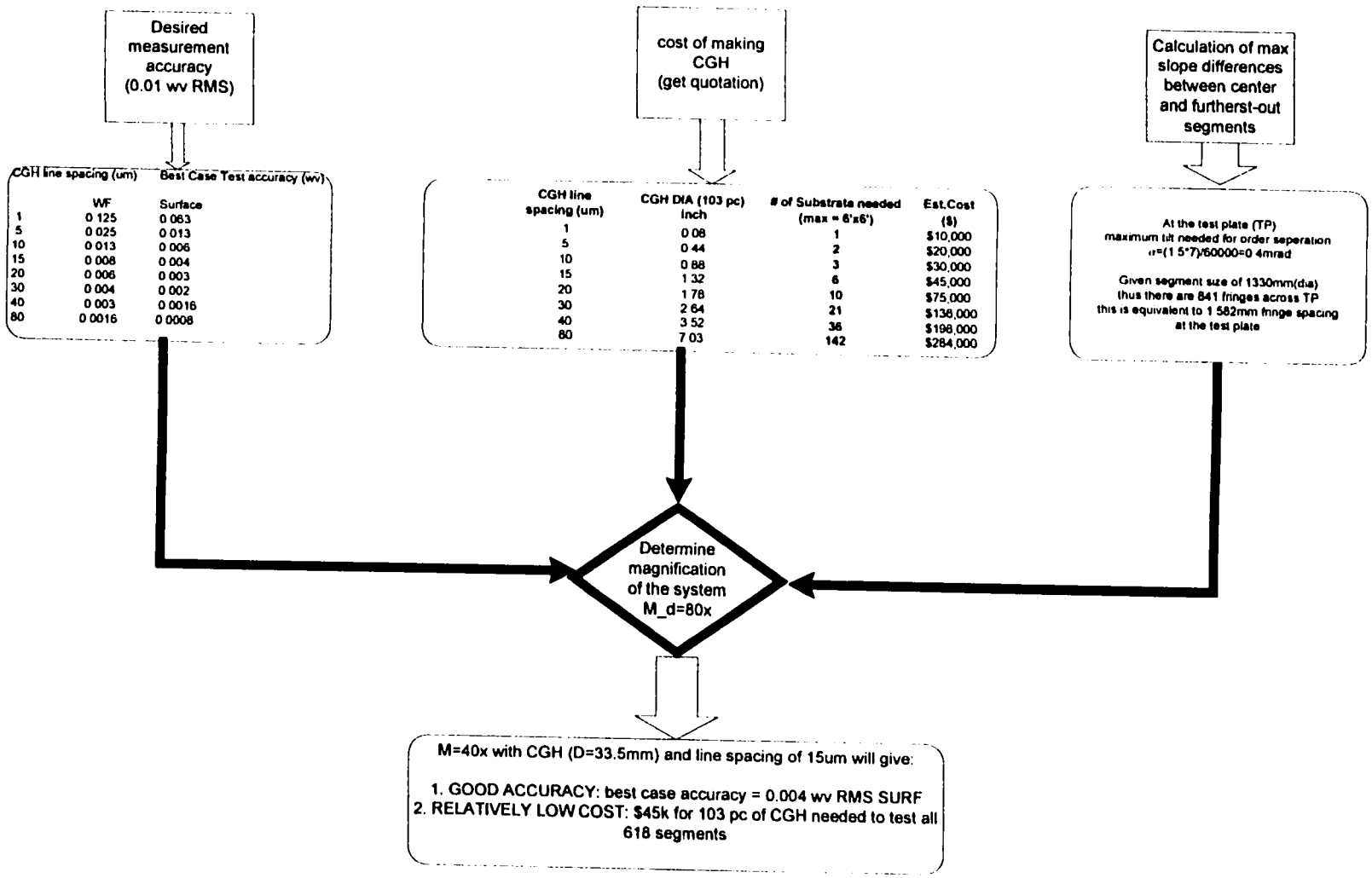

Figure 6-11 . Flow process of optically choosing the system magnification M.

accuracy of 5 nm RMS surface uncertainty (2.6nm is allocated to hologram fabrication error). This allows for all 103 holograms to fit on six standard 6"x6" substrates. Each hologram is 33.5mm in diameter and estimated total cost of $45,000.

6.3 PROJECTION AND IMAGING SUB SYSTEM DESIGNS

Once the three system parameters are optimally selected, we can construct the projection and imaging systems, two sub systems must be designed so CGHs, used to test the mirror segments, can be generated.

The primary function of the projection system is two fold. First, it creates a good spherical wavefront serving as the origin of the reference beam. Secondly, it creates a good image of CGH patterns at the test segment. It is to be designed telecentric at the CGH, so collimated light can be used to illuminate the CGH.

The imaging system creates a good image of the test segment onto a charge coupled device (CCD) array. It is designed to be telecentric at the CCD, so misplacement of CCD does not change the image size so much that it can not be observed on the output monitor connected to the CCD.

6.3.1 Design of the projection system

The projection system consists of lenses (two in this case) and an aperture stop so only two diffraction orders from the hologram (0th and 1st order) are transmitted. These lenses are critical to this test because accurate compensation for the aspheric departure of the segments requires the holograms to be projected to the test surface. For example, if the projected CGH pattern on the test part were distorted by 1um, this would introduce

0.0016 λ wavefront errors into the test measurement (since 1μm/(40.0x15μm) waves =0.0016 waves).

The projection system was actually designed in reverse order, i.e., they were designed to image the test mirror onto the CGH. Figure 6-12shows how the projection system fits in the test system as a whole and Figure 6-13 shows how it was designed backward. A similar system, based on which this projection system is designed, was obtained from J. H. Burge[30] and was used as a starting point.

The basic constrains of the projection system are: (1) magnification M of 40.x, (2) good wavefront quality and, if possible, telecentricity in the image space where CGH would be located. These constrains are to serve the following purposes: (1) image a 1340-mm test segment onto a 33.5-mm CGH, (2) create a near aberration free image, and (3) allow the CGH to be illuminated with collimated light, and ease the manufacturing difficulties in requiring a specific wavefront for illumination.

To ease the design of the projection system, we need to reduce the stop size of the projection system. This is accomplished by placing the 1st diffraction order, instead of the 0th diffraction order, to the center of the projection system. Figure 6-14 depicts this point. In this figure, the 1st order spot size at the stop is of elongated along one direction (approximate size is 39-mm by 8-mm). The order separation distance D is 13-mm. By locating the 1st order on the axis of the projection system, the stop of the projection system is reduced from 22.2-mm (radius) to 19.5-mm. This is equivalent to a 13% reduction in the stop size. Since the difficulty of designing the projection system

approximately varies as fourth power of the aperture size, a reduction of 13% in aperture size eases the design complexity greatly.

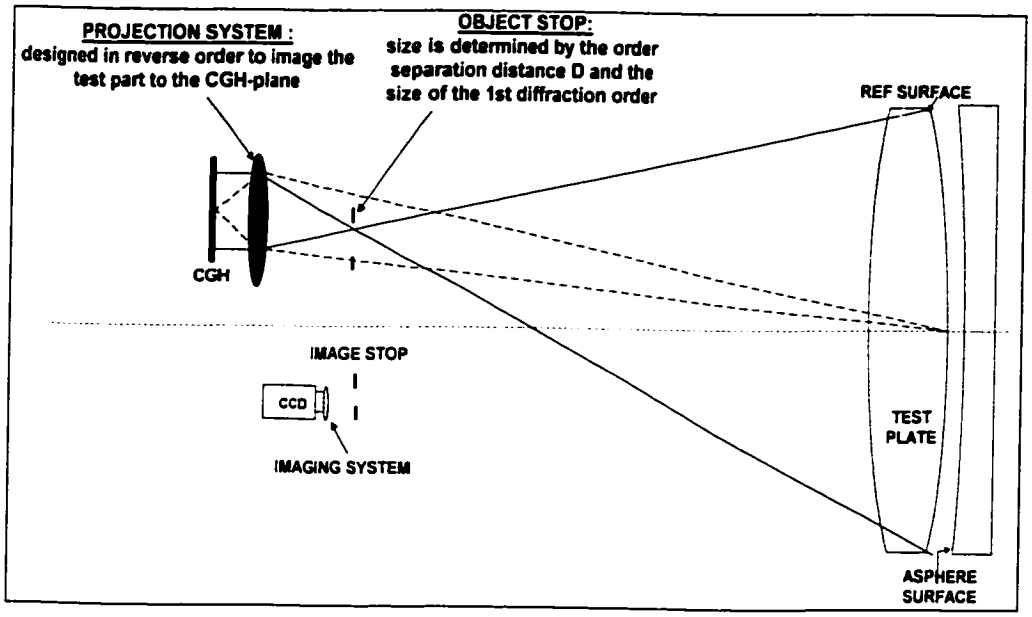

Figure 6-12. Location of the projection system as a part of the test system. The projection system is designed in reverse order (Figure 6-13)

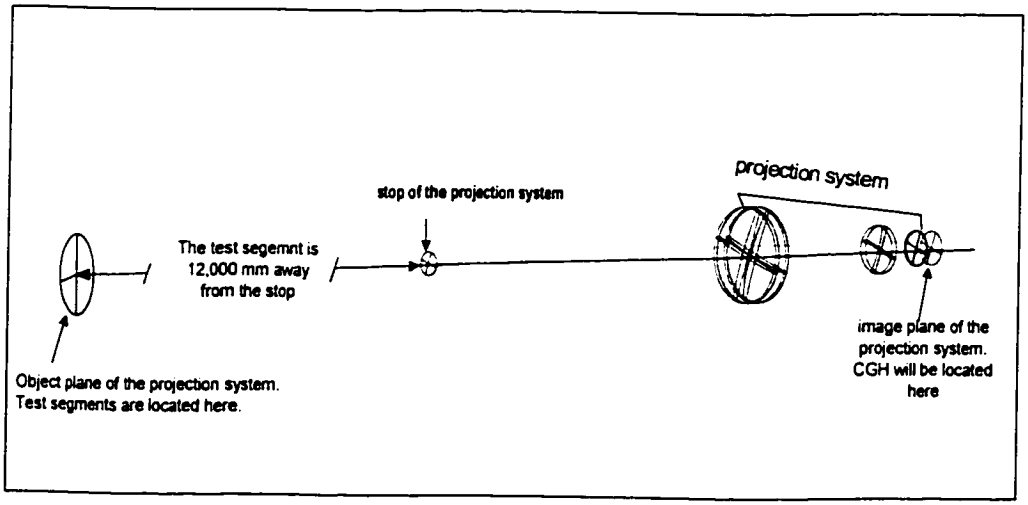

Figure 6-13. Effective entrance pupil of the projection system is located 12 meters away from the test segment.

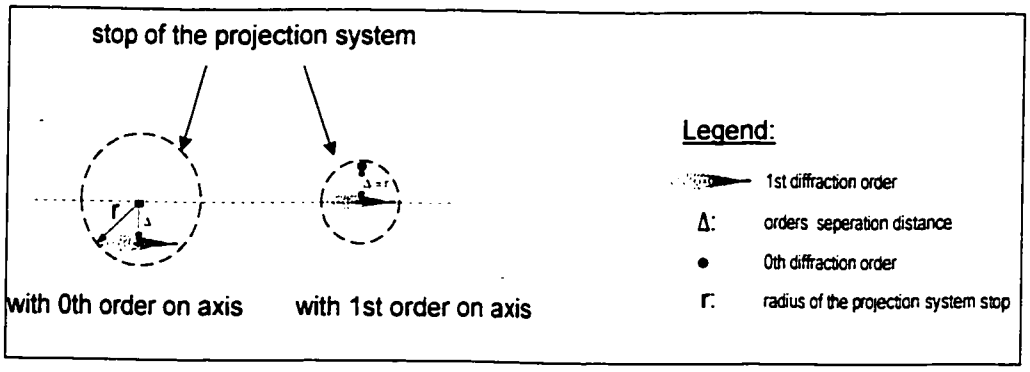

Figure 6-14. Reducing the stop size by deliberately placing the 1st order on-axis in the stop.

The prescription of the actual projection system designed for this case study is shown in Table 6-4 and to-scale drawings are shown in Figure 6-15. Unlike the large test plate, the reference and test beams are separated after CGH and do not travel through the projection system together. This means that the surface figure and internal quality of the projection optics is very important.

Table 6-4. Prescription of the designed projection system. All units are mm

Surf		Comment	Radius	Thickness	Glass	Diameter	Conic
OBJ	collimated light	1=REF; 2=TEST	Infinity	150000		1340	0
1			Infinity	0		13	0
STO		STOP	Infinity	265.7911		13	0
3	lens 1		-482.7981	20	BK7	15.39688	0
4			-243.2402	794.7636		15.73171	0
5	lens 2	ROJECTION LENS	-11.95199	20	BK7	9.474923	0
6			-20.04327	899.4453		14.99338	0
IMA			Infinity			33.54743	0

Figure 6-16 through Figure 6-19 show that the system has excellent performance: (1) wavefront variation across the entire pupil is less than 0.012 λ; (2) distortion is less than 0.2%. Although this over designed for the test since in reality, CGH can be designed to correct any non-ideal behavior in the projection optics, a well-designed

projection optics can ensure that good image of the alignment mark is produced; (3) at full field of (+/- 750mm object height), wavefront aberration is less than +/- 0.05 waves, and (4) transverse ray aberration less than +/1 5μm at full field.

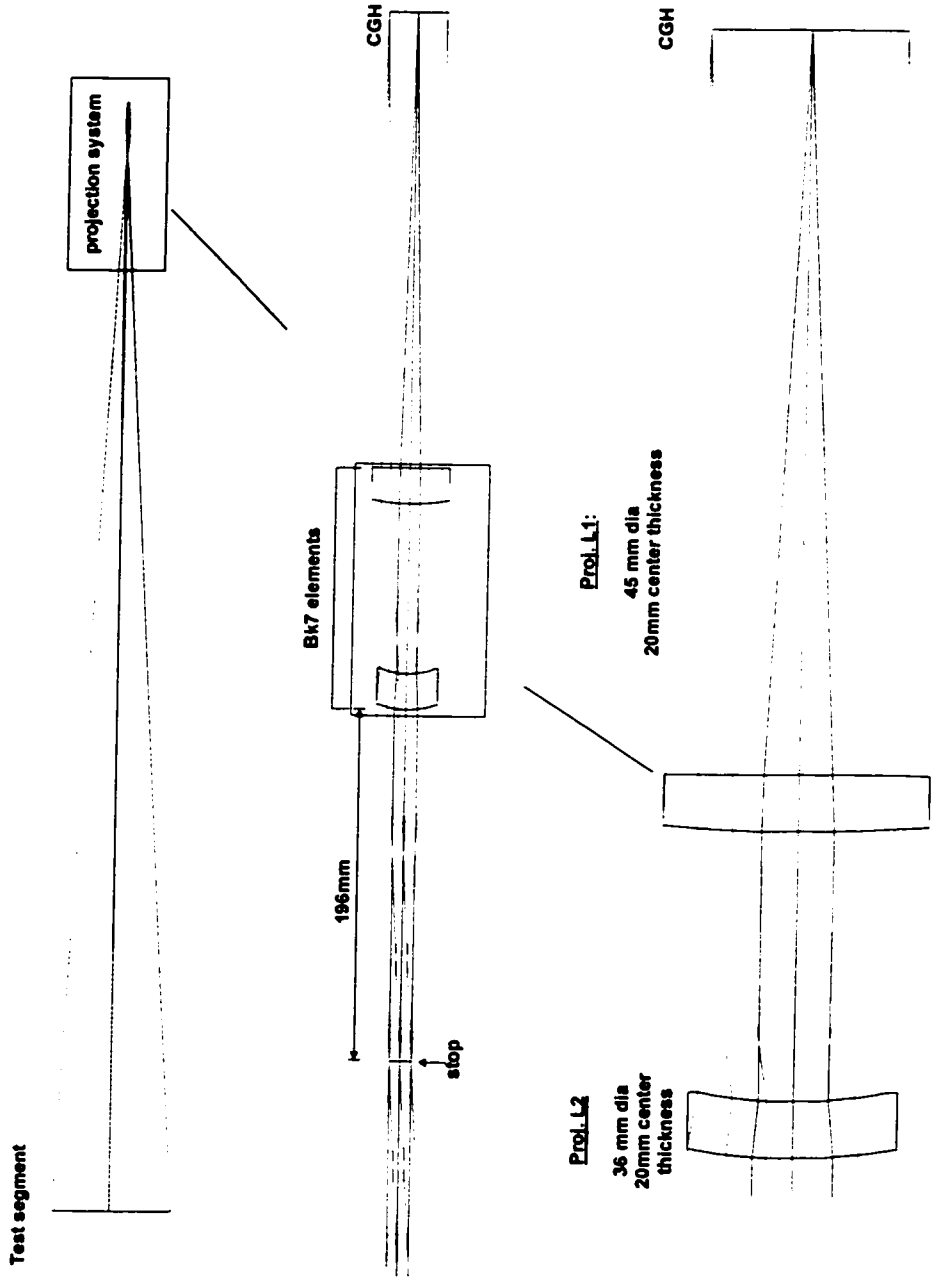

Figure 6-15 Layout of the projection system (to scale). The system is designed in reverse order: imaging the test plate on to the CGH.

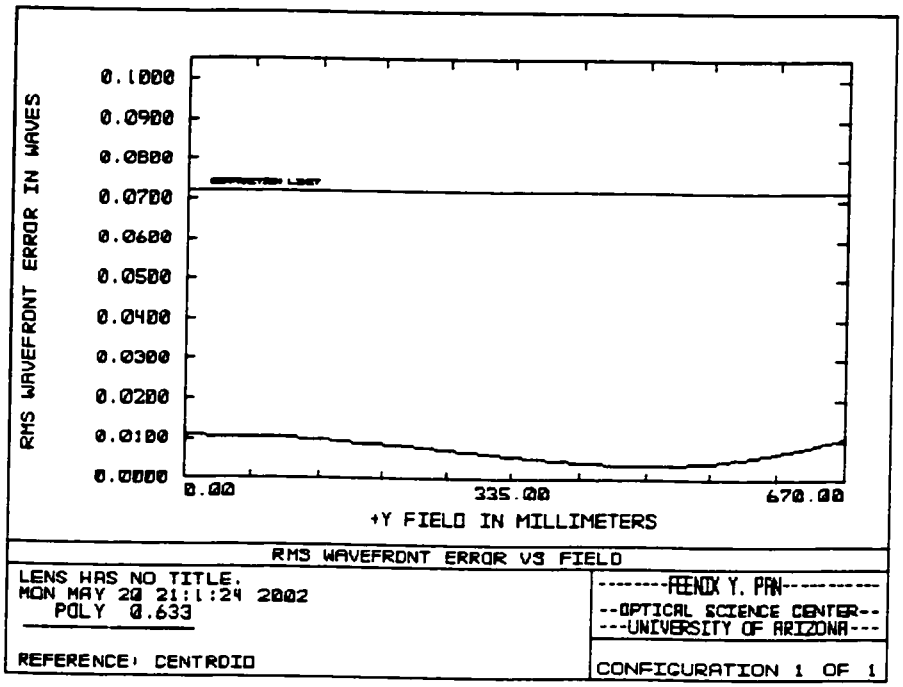

Figure 6-16. Wavefront variation across the entire projection system pupil is less than 0.012 waves.

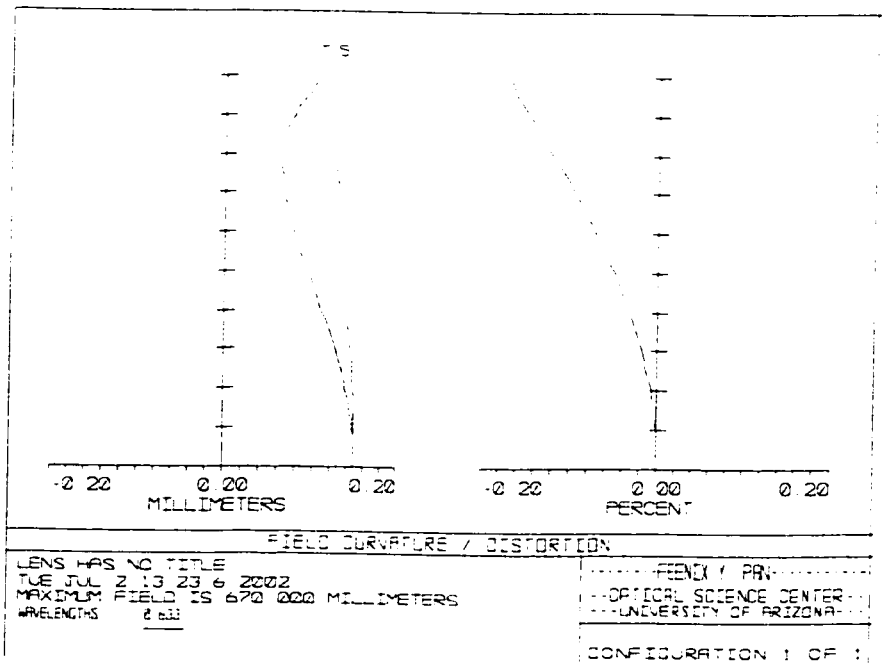

Figure 6-17. Distortion of the projection system is less than 0.2%

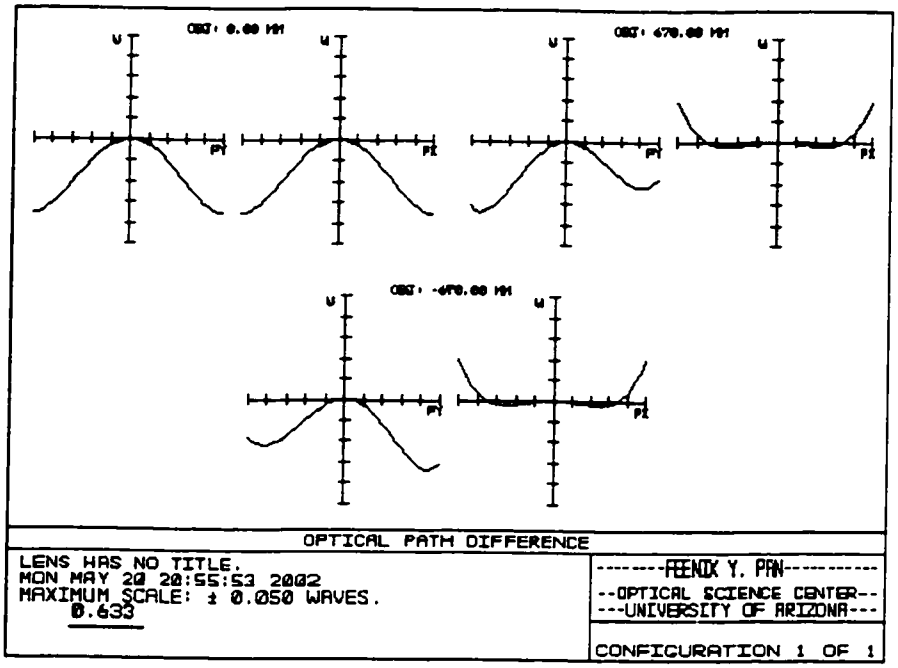

Figure 6-18. at full field of (+/- 750-mm object height), wavefront aberration is less than +/- 0.05 waves

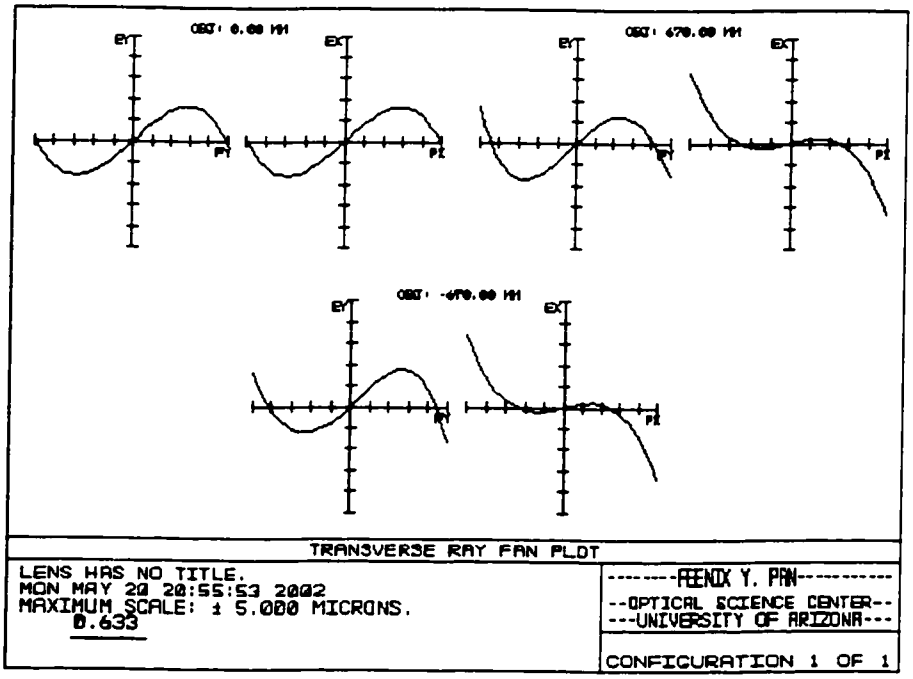

Figure 6-19. Transverse ray aberration less than +/1 5-um at full field.

To aid the alignment of the segment with respect to the CGH (therefore the entire test system), six alignment fiducials are fabricated on the CGH substrate outside the CGH patterns (Figure 6-20). Since the projection system is also used to project these alignment marks to the test segment, the projection system must produce a diffraction-limited image at the edge of the field. Aberrations in the projection system would limit the ability to determine the centroid of the projected alignment fiducial marks.

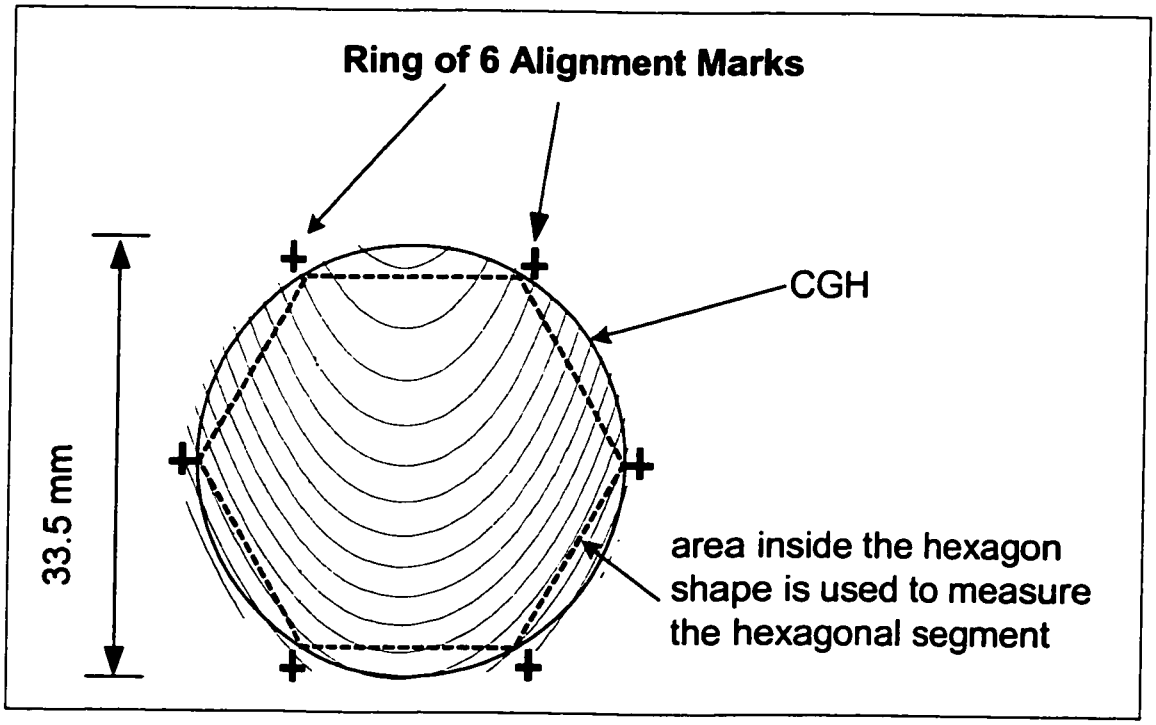

Figure 6-20. CGH (33.5 mm OD) with a ring of 6 alignment marks fabricated on the same substrate. The hologram is magnified 100x, i.e. one contour line is 100λ of optical path difference (OPD).

6.3.2 Design of the imaging system

The imaging system is the last of the two sub systems that must be designed before the CGH can be generated for testing of aspherical mirror segments. The imaging system

images the test segment onto the CCD array, so the interferogram can be analyzed to obtain surface map of the segment under test. Unlike through the projection system, the test and reference beams travel through the imaging system together. For this reason, the imaging system was initially designed only for the reference beam. This does not change for the different segments because the CGHs are designed to compensate the aspherical departure, thus making the test and reference beams identical.

Basic requirements for designing the imaging system are: (1) magnification of 1/286. This is to ensure the test segment of 1340-mm in diameter can be imaged to a standard 2/3" format CCD (8mm x 6mm) (imager size is approximated to 5mm x 5mm); (2 telecentricity in the CCD plane. This allows the image size stay unchanged even when the CCD is not at the correct position.

In addition to specification of its magnification, specification of its stop size is required to design the imaging system. To determine this stop size, we need to realize that when the imaging system is used as a part of the test system, the stop of the imaging system corresponds to the image stop (Figure 6-21). This means that the stop size of the imaging system is determined by the beam spot size returned from the test plate (or test segment since the reference and test beams are identical at this point). The beam spot size is blurred by the spherical aberration introduced by the illumination surface of the test plate. From earlier analysis on optimizing the test plate illumination surface we know that the best focus, including the spherical aberration (SA), is at 12,036 mm from the test plate. Assuming the nominal fabrication errors of the test plate, including index inhomogeneity, are 0.1 mrad/pass (or 0.2 mrad in wavefront). This corresponds to 2.4

mm image blur. Adding another 2.0mm image blur due to the SA presented in the system, we set the stop size at 5.0 mm in diameter.

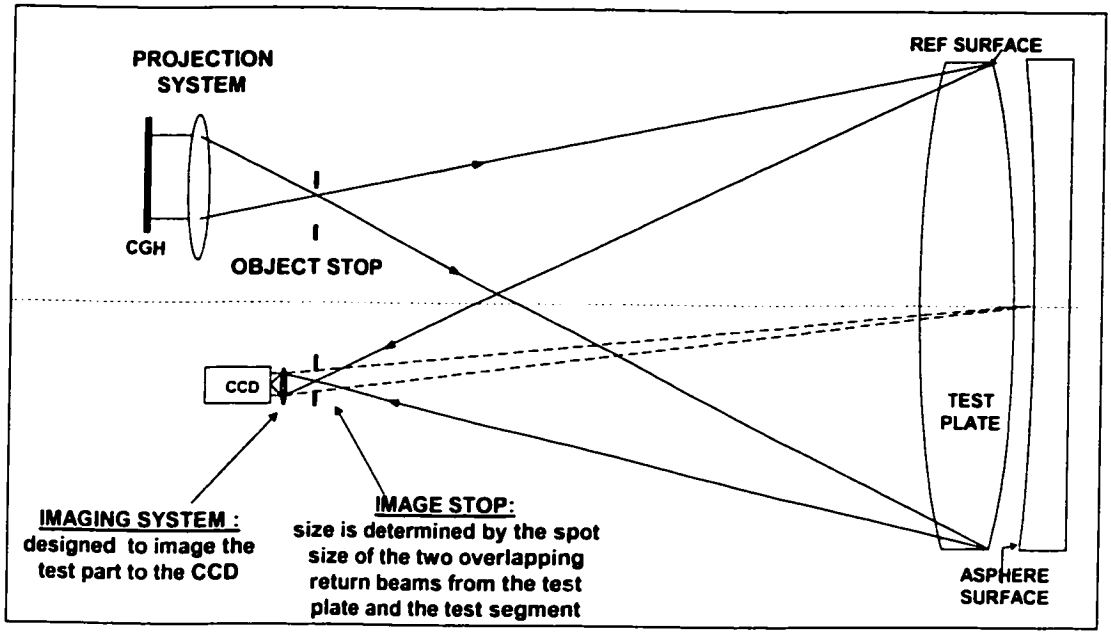

Figure 6-21. Location of the imaging system as it fits to the test system. Specification of the image stop size is required for the designing of the imaging system.

The prescription of the designed imaging system is shown in Table 6-5 and Figure 6-22 shows its schematics. The imaging lenses are designed and analyzed assuming the worst case of system errors up to ± 0.2 mrad. These system errors define the pupil function for the imaging lenses so the pupil is sized to be 6 mm. In reality, most of the light will go through the central 1 mm of this lens so the imaging performance will be much better than described here. Although this design and analysis assumes the worst case, the performance is excellent and the optical system is still quite simple.

Performance of the imaging system is excellent: (1) wavefront aberration less than ±0.5λ at the full filed of +/- 740-mm object height, (2) less than 0.1% distortion.

Table 6-5. Prescription of the designed imaging system.

	R (mm)	T (mm)	Glass	DIA (mm)
stop		-10		7.6
lens1	74.97262	3.5	BK7	20
	-36.85109	31.36836		20
lens2	31.40183	3.5	BK7	12
	-218.2646	10		12
CCD	Infinity			5.0

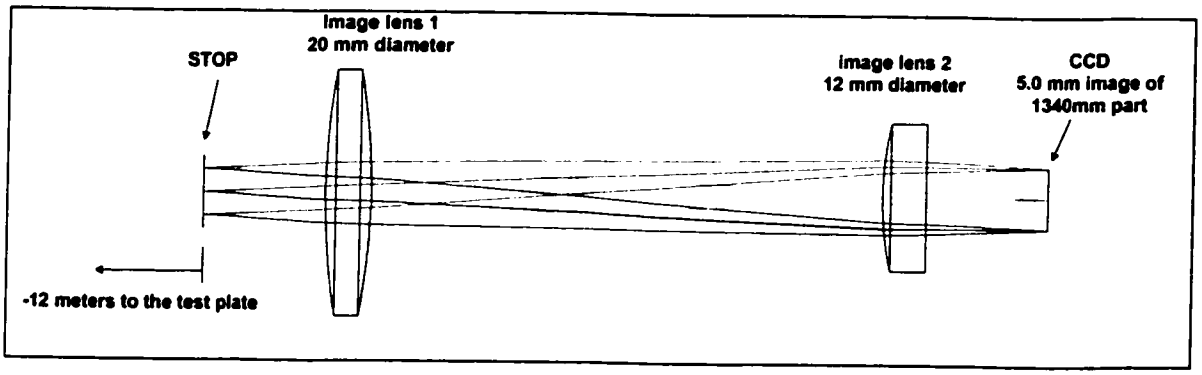

Figure 6-22. Schematics of the imaging system (overall length is 68mm)

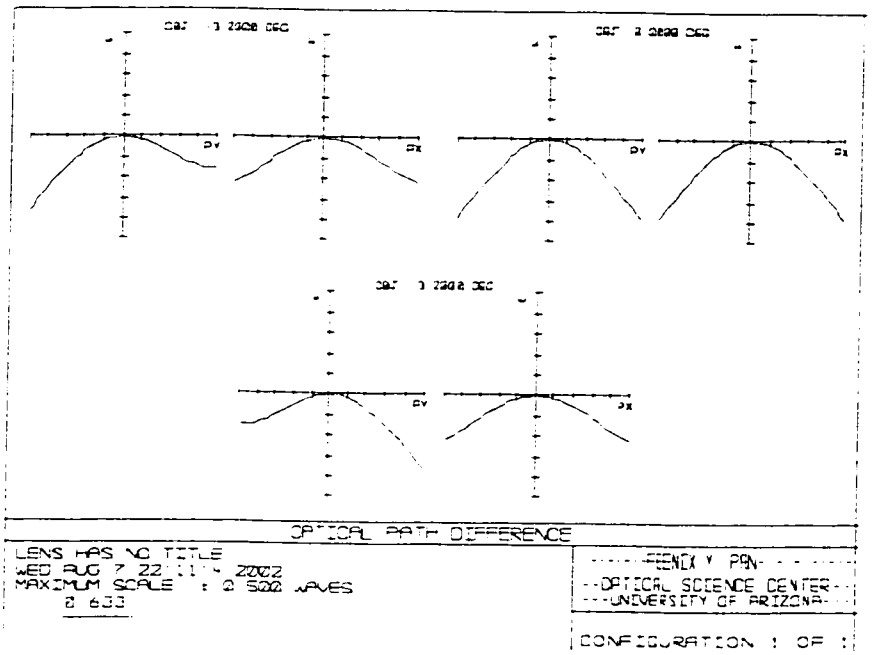

Figure 6-23. Wavefront aberration of the designed imaging system is less than +/- 0.5 λ.

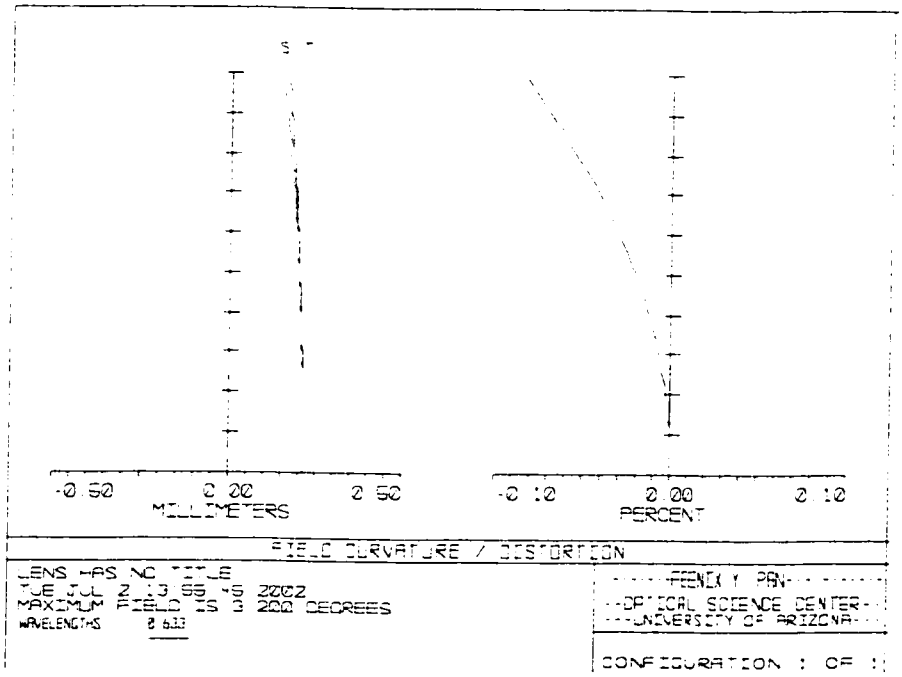

Figure 6-24. The designed imaging system has less than 0.2% distortion.

6.4 SUMMARY OF THE OPTICAL SYSTEM DESIGN

Table 6-6. Summary of the optical system

Component	Function	Brief description
Computer generated holograms	• Provide wavefront correction for aspheric departure of mirror segments • Use sufficient tilt to separate 1st and 0^{th} diffraction orders • Different CGHs for different segments	• 33.5-mm diameter, chrome patterns on 3-mm fused silica substrates. • Nominally 20 μm line spacing • 50% duty cycle (line width = half of period).
Projection optics	• Project an image of the CGH onto test segment • Pass only 0th and 1st diffraction orders Same system and alignment for all tests	• 0.6-m long, with 2 BK7 elements • Lens diameter -- 36 cm and 46 cm respectively. • 300mm EFL, magnifies CGH40.0 times. • Corrected for 33.5mm CGH over 40mm pupil. • Telecentric at CGH
Test plate	• Provide reflected wavefront from convex surface as a reference. • Transmit test wavefront • Minimize viewing distance	• ROC (ref side) = -6.09553E+004mm • RCO(non-ref side)= 7.79186E+003mm • Made of Zerodur • 1.340 meter diameter;. • 10 cm center thickness • Located 12.0 m from projection and imaging systems
Imaging optics	• Create a good image of the test part onto a CCD array. • Pass only the reference and test beams – block others	• 58 mm long with 2 BK7 elements, 20 and 12 mm diameters each. • Creates 5.0-mm image of 1880-mm part. This fits standard 2/3" format CCD's. • Accommodates 6-mm stop, allowing system slope errors of ±0.2 mrad. • Allows 1000 resolution elements across interferogram. • Telecentric at CCD • Distortion of image 0.1% or < 1 mm at segment.

6.5 OPTICAL SYSTEM SIMULATION AND CGH DESIGN

System design of this test ties together optimization of the test plate and two subsystem designs (projection and imaging systems). Each of these is detailed in previous sections. The purpose of this section is two fold: (1) supply a complete how-to roadmap for setting up the system in a computer simulation program like ZEMAX, and (2) present final CGHs obtained for testing six representative segments chosen earlier (Figure 6-4).

6.5.1 Setting up the optical system in ZEMAX

The optical system summarized in Section 6.4 is simulated in a computer-modeling program ZEMAX (chosen only for its availability at the time this work was performed). Even though the steps described in this section pertains to the ZEMAX environment, the process of setting up the optical system in any other program stays the same. The ZEMAX code used to simulate the optical system is shown in Table 6-7. Several important points are highlighted:

1. Multi-configuration was used to create the two interference beams. This is accomplished by setting the reference surface as a mirror in configuration 1, and by setting the test segment as a mirror in configuration 2 (line #15 and #20).
2. The collimated light is set 2.413 degrees off the optical axis which coincides with the mechanical axis defined by the center of the test plate and the center of the LASER. CGH is used to locate the 1^{st} diffraction order on-axis, thus reducing the size of the projection aperture (discussed in Section 6.3.1). The numerical value

of 2.413 degree is obtained through Eqn.[2.43], where the system magnification M is 40.0x and $\alpha_{tilt\_at\_test\_plate}$ is 1.053-mrad calculated in Section 6.2.1).

$$\alpha_{tilt\_at\_CGH}^{'} = M \times \alpha_{tilt\_at\_testplate} \qquad [2.43]$$

3. The Projection and imaging sub systems are entered. The projection system is entered backward from its prescription shown in Table 6-4, since it was designed in the reverse order (Section 6.3.1).
4. Two distances were adjusted sequentially so first CGH and test plate, then test plate and CCD, are conjugate pairs. This was done in two steps. First, the distance from the CGH to the projection system (thickness=259.9157 from line 6) was adjusted so CGH is conjugated to the test plate. Secondly, the distance from the last image lens to the CCD is adjusted so the test plate is conjugated to the CCD (line #29: thickness = -10.33864; negative for return beam direction).
5. Segment location is defined with respect to the parent mirror. This was done in three steps (lines #18 through #20 in Table 6-7): (i) sag of +1878.983-mm, (ii) off-axis (Δx) of +15015.922-mm and (iii) rotation of 14.05 degrees (Section 6.6 discusses how this number is calculated).

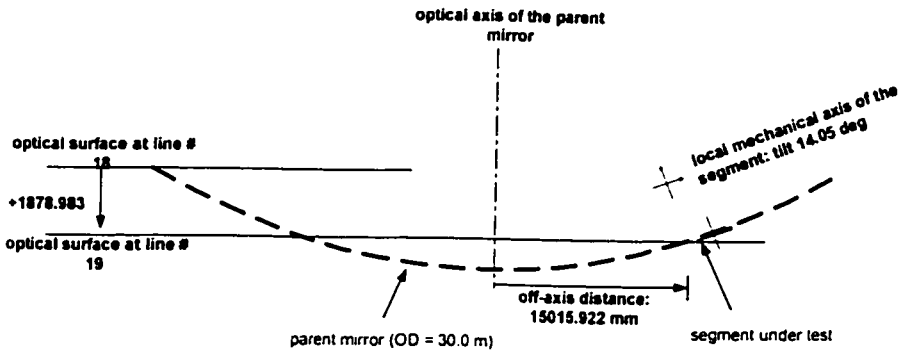

Figure 6-25. Definition of an off-axis segment with respect to the parent mirror.

Table 6-7. ZAMAX codes used to simulate the optical system summarized in Table 6-6

Surf	Type		Comment	Radius	Thickness	Glass	Diameter	Conic	(comment)	Dx	Dy	tilt @ x	tilt @y	tilt @ z	order
OBJ	STANDARD			Infinity	Infinity		0.0	0							
1	STANDARD			Infinity	50		34.0	0							
2	COORDBRK		FOR ORDER SEPERATION	-	0		-	-							
3	STANDARD			Infinity	0		34.0	0							
4	STANDARD		1=REF; 2=TEST	Infinity	0		34.0	0							
5	STANDARD		CGH SUBSTRATE	Infinity	3	SILICA	34.0	0							
6	SZERNPHA		CGH ZERN PHASE	Infinity	259.9157		33.5	0							
7	STANDARD		PROJECTION LENS	Infinity	20	BK7	70.0	0							
8	STANDARD			-126.6618	94.98618		70.0	0							
9	STANDARD			-41.21586	20	BK7	64.0	0							
10	STANDARD			-49.20629	196.0715		64.0	0							
11	STANDARD		OBJ STOP	Infinity	0		27.0	0							
12	STANDARD		TO TP	Infinity	12000		40.0	0							
13	COORDBRK	→	MOVE TP	-	0		-	-							
14	STANDARD		TP: NON-REF SIDE	7791.868	100	SILICA	1357.7	0							
15	STANDARD		TP: REF SIDE	-60955.39	0		1359.3	0							
16	STANDARD		GET TO OUTSIDE OF TP	-60955.39	0		0.0	0							
17	STANDARD		AIR GAP OF 5 MM	-60955.39	5		0.0	0							
18	STANDARD		SEGMENT POSITION	Infinity	1878.983		0.0	0							
19	COORDBRK	→	SEGMENT LOCATION	-	0		-	-		15015.92		-0.03024	14.05055		1
20	STANDARD		PARENT MIRROR	-60000	0		30000.0	-1							
21	COORDBRK	→	UN: SEGMENT LOCATION	-	0		-	-		15015.92		-0.03024	14.05055		0
22	STANDARD		2X SEGMENT POSITION	Infinity	-1878.983		0.0	0 ←	returning beam						
23	STANDARD		2X AIR GAP	-60000	-5		0.0	0							
24	STANDARD		2X TP REF SIDE	-60955.39	-100	SILICA	1359.3	0							
25	STANDARD		2X TP NON-REF SIDE	7791.868	0		1359.3	0 ←							
26	COORDBRK	→	UNMOVE TP	-	-12000		-	-							
27	STANDARD		IMAGE STOP	Infinity	-10		0.7	0							
28	STANDARD		IMAGE SYSTEM	-63.07848	-3.5	BK7	20.0	0							
29	STANDARD			56.7993	-41.1354		20.0	0							
30	STANDARD			-28.28116	-3.5	BK7	12.0	0							
31	STANDARD			637.614	-10.33864		12.0	0							
STO	STANDARD		CCD	Infinity	0		5.0	0							
33	SZERNPHA		DUMMY ZERN: null ref. beam	Infinity	0		5.0	0							
34	PARAXIAL			-	-1000		5.0	-							
IMA	STANDARD			Infinity			5.0	0							

6.5.2 Design of computer-generated holograms

After the ZEMAX model is completed (Table 6-7), the last task at hand is to generate the CGHs for testing off-axis segments. The holograms are specified as phase function using Zernike polynomials. Coefficients of these polynomials can be directly given to CGH manufacturers for fabrication.

The basic idea behind this is that the CGH is generated to *match* the reference wavefront – either wavefront has to be perfect just perfectly matched. To ease the design of the CGHs, ZEMAX was manipulated to create a perfect reference wavefront so net error between the test and reference beams equals to that from the test beam alone. This was accomplished by adding a dummy Zernike surface, after the CCD (line #33 in Table 6-7). Coefficients from this dummy Zernike surface are optimized to null the reference beam. After creating a perfect reference beam, a second set of Zernike coefficients corresponding to the CGH itself was optimized to create a perfect test beam. This second set of Zernike coefficients is what is needed to test aspherical segments. This process is repeated for the five representative segments chosen for this study.

Locating segments well is important for generation of the holograms. Three parameters required to locate one segment are (i) sag, (ii) off-axis distance, and (iii) local slope with respect to the parent mirror. A computer algorithm was developed to compute these parameters for five segments (Figure 6-26) chosen for this case study. The results from the algorithm (Table 6-8) are then compared to information provided by NOAO[31]. Percentage of error using these two difference methods is tabulated in Table 6-9. They are in excellent agreement.

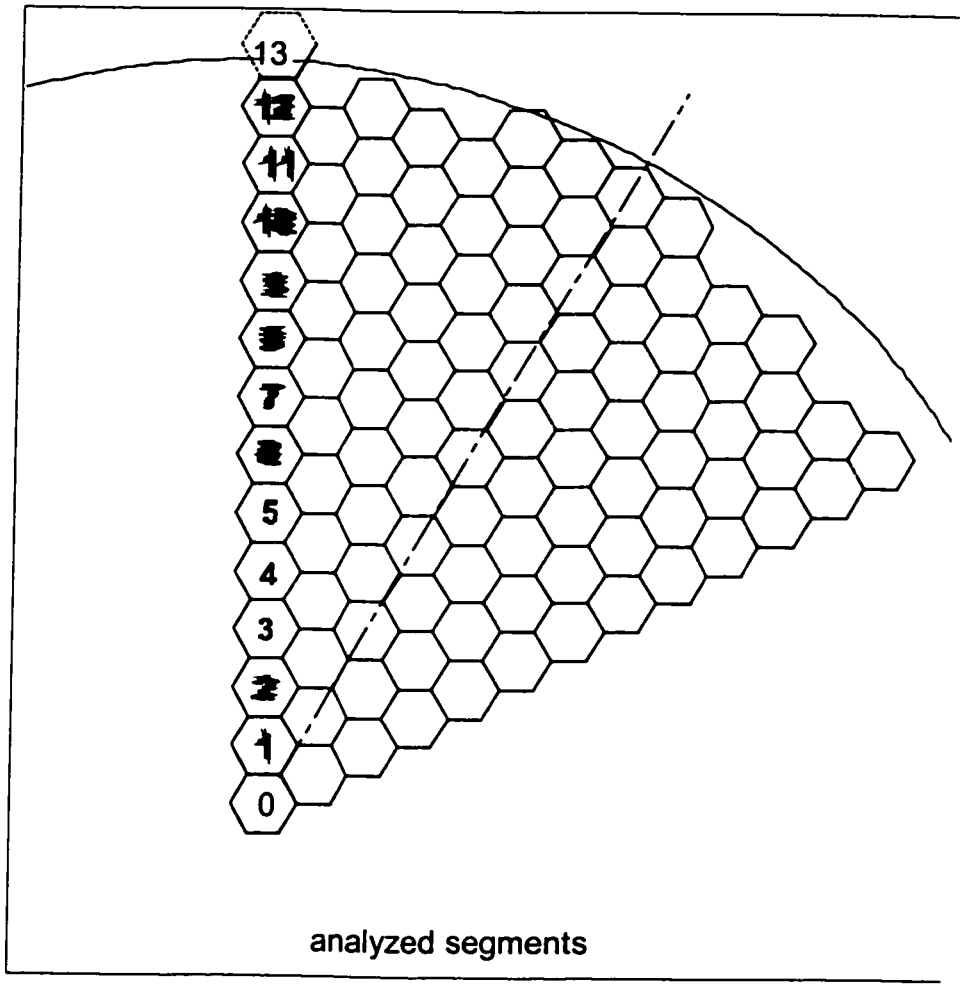

Figure 6-26 Location of the five segments under study (filled in yellow).

Table 6-8 Segment locations are computed using an IDL algorithm and results are compared to that given by a different source from NOAO[3].

		From an IDL algorithm		NOAO's data	
SEGMENT #	off_axis distance[m]	sag is[mm]	slope is[deg] .	sag is[mm]	sag is[mm]
0	0	0	0	0	0
1	1155.0709	11.11824	1.1028752	11.11824058	1.10280755
2	2310.1418	44.47296	2.2049337	44.47295625	2.20479859
3	3465.2127	100.06416	3.3053626	100.0641289	3.30516022
4	4620.2836	177.89184	4.4033559	177.8917285	4.40308677
5	5775.3545	277.956	5.4981185	277.9557136	5.49778325
6	6930.4254	400.25664	6.5888695	400.2560316	6.58846876
7	8085.4963	544.79375	7.674845	544.7926193	7.67437974
8	9240.5672	711.56735	8.7553018	711.5654038	8.75477299
9	10395.638	900.57743	9.8295198	900.5743031	9.82892852
10	11550.709	1111.824	10.896805	1111.819227	10.89615214
11	12705.78	1345.307	11.95649	1345.300077	11.95577782
12	13860.851	1601.0265	13.007941	1601.01675	13.00716973
*13*added	15015.922	1878.9825	14.050552	1878.969136	14.04972403

Table 6-9. Percentage Error of locating the segments using two difference methods shows that they are in excellent agreement.

% of Error Between two methods:			
	off_axis distance	sag	slope (deg)
1	0.00000%	0.00001%	0.00613%
2	0.00000%	0.00001%	0.00613%
3	0.00001%	0.00003%	0.00612%
4	0.00003%	0.00006%	0.00611%
5	0.00005%	0.00010%	0.00610%
6	0.00008%	0.00015%	0.00608%
7	0.00010%	0.00021%	0.00606%
8	0.00014%	0.00027%	0.00604%
9	0.00017%	0.00035%	0.00602%
10	0.00021%	0.00043%	0.00599%
11	0.00026%	0.00051%	0.00596%
12	0.00031%	0.00061%	0.00593%
13	0.00036%	0.00071%	0.00589%

6.6 SPECIFICATIONS OF CGHS

This section lists the following information about the CGH for the furthest out segment (others are in Appendix E):

- Location of the segment with respect to the parent mirror(Figure 6-27)
- Footprints of diffraction orders at the object stop, showing that all orders are well separated as they were designed (Figure 6-29)
- Zernike coefficients describing the hologram (Table 6-10)
- Contour map of the CGH pattern

Summary of all five holograms are provided in Table 6-12.

T13 CGH design

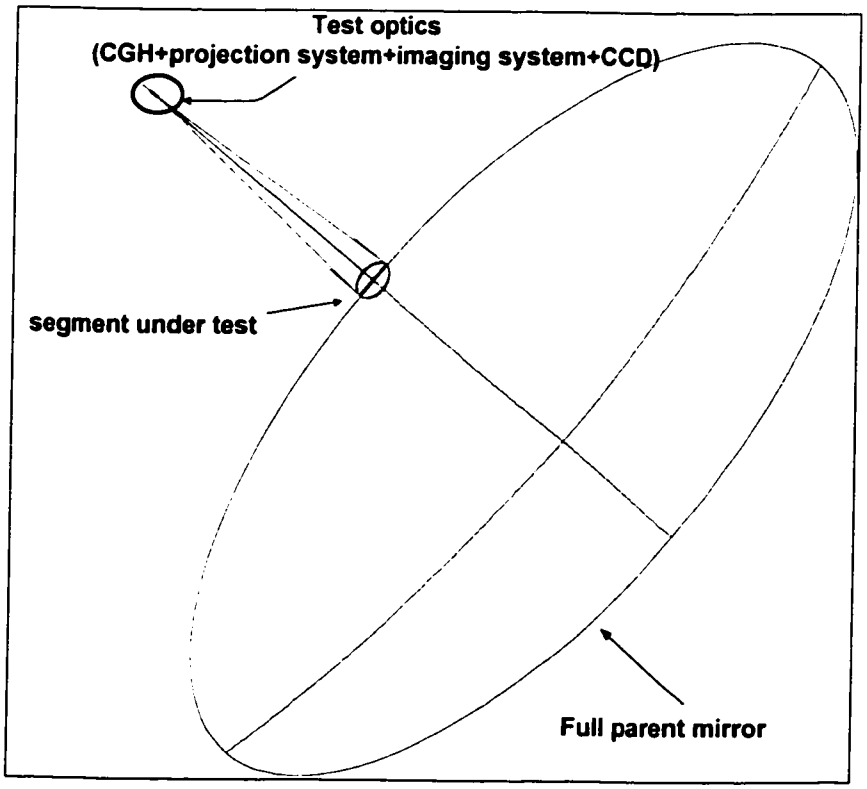

Figure 6-27 Layout of T1 test, showing parent primary, and the top-end optics (details are shown in Figure 6-28 .

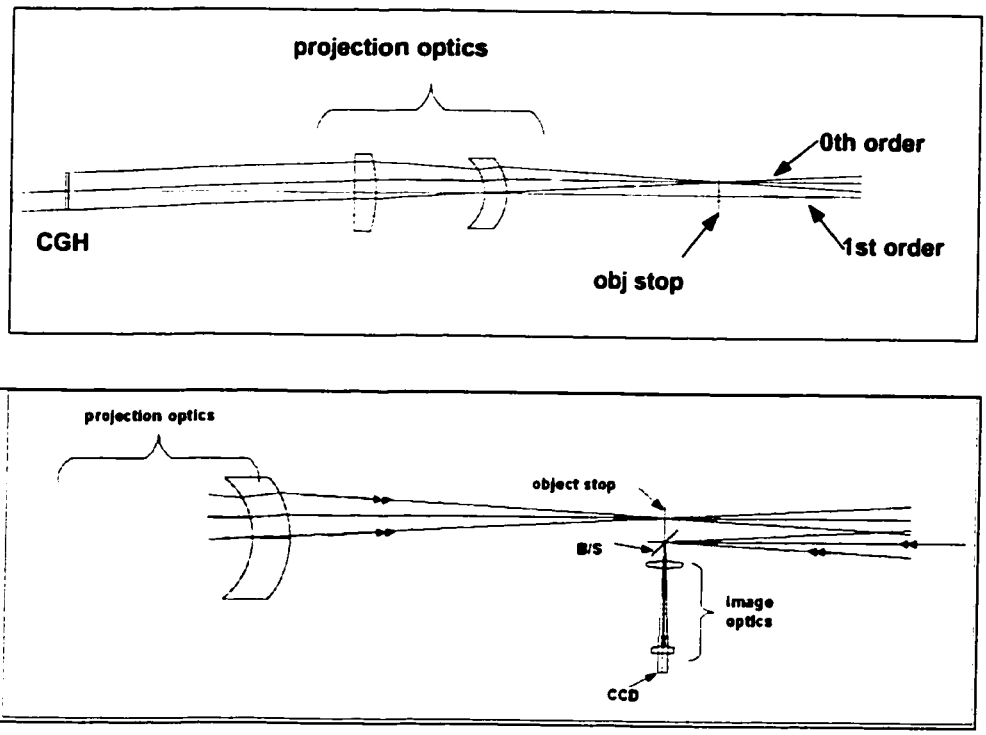

Figure 6-28. Details of the top-end optics. Top: location of CGH and the projection system. Bottom: Location of the imaging system with respect to the projection system.

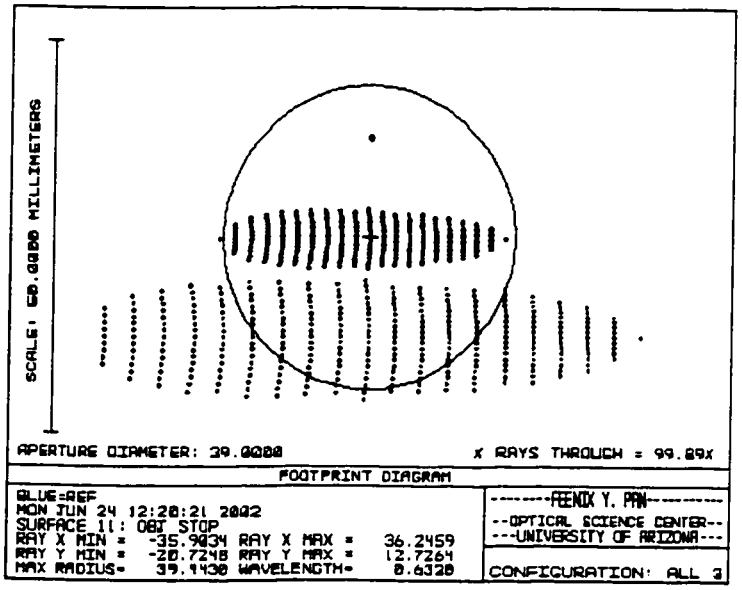

Figure 6-29 Appearance at the intermediate focus of the projection lens for the T1 hologram. The 2nd order is isolated from the 1st, but must be blocked. All orders other then 0 and 1 are blocked by the 50-mm aperture of the projection lens.

Table 6-10. The prescription for the T1 hologram is given below (definition of the Zernike phase term is in Table 6-11)

STORED IN \S13_zerns.txt
stored in\S13_zerns.txt
MAX TERM OF ZERN USED IS 37
NORMAL RADIUS IS 17.20
Zernike # 1 = 0.0000000000
Zernike # 2 = -10.3496306150
Zernike # 3 = -576.0090048576
Zernike # 4 = -156.0843108150
Zernike # 5 = -0.0184402239
Zernike # 6 = -147.3530826644
Zernike # 7 = -0.9030393963
Zernike # 8 = -3.6580486680
Zernike # 9 = 0.0026052681
Zernike #10 = 0.1724650633
Zernike #11 = -0.4563860382
Zernike #12 = -0.2569628693
Zernike #13 = 0.0001897872
Zernike #14 = 0.1024076351
Zernike #15 = 0.0006272052
Zernike #16 = -0.0045390582
Zernike #17 = -0.0010773908
Zernike #18 = 0.0108717689
Zernike #19 = 0.0024347132
Zernike #20 = 0.0053815814
Zernike #21 = 0.0012966812
Zernike #22 = -0.0019389065
Zernike #23 = 0.0000902547
Zernike #24 = 0.0017169562
Zernike #25 = 0.0001022227
Zernike #26 = 0.0000000000
Zernike #27 = 0.0000000000
Zernike #28 = 0.0000000000
Zernike #29 = 0.0000000000
Zernike #30 = 0.0000000000
Zernike #31 = 0.0000000000
Zernike #32 = 0.0000000000
Zernike #33 = 0.0000000000
Zernike #34 = 0.0000000000
Zernike #35 = 0.0000000000
Zernike #36 = 0.0000000000
Zernike #37 = 0.0000000000

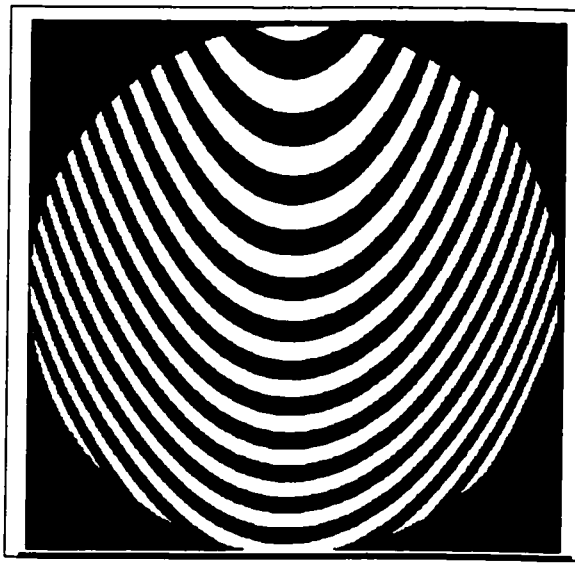

Figure 6-30. Simulated hologram T13 (Magnified 100x, i.e. every line is equal to 100λ optical path difference).

Table 6-11. Zernike definitions used in Zemax.

Z 1	1
Z 2	(p) * COS (A)
Z 3	(p) * SIN (A)
Z 4	(2p^2 - 1)
Z 5	(p^2) * COS (2A)
Z 6	(p^2) * SIN (2A)
Z 7	(3p^2 - 2) p * COS (A)
Z 8	(3p^2 - 2) p * SIN (A)
Z 9	(6p^4 - 6p^2 + 1)
Z 10	(p^3) * COS (3A)
Z 11	(p^3) * SIN (3A)
Z 12	(4p^2-3) p^2 * COS (2A)
Z 13	(4p^2-3) p^2 * SIN (2A)
Z 14	(1Op^4 - 12p^2 + 3) p * COS (A)
Z 15	(1Op^4 - 12p^2 + 3) p * SIN (A)
Z 16	(20p^6 - 30p^4 + 12p^2 - 1)
Z 17	(p^4) * COS (4A)
Z 18	(p^4) * SIN (4A)
Z 19	(5p^2 - 4) p^3 * COS (3A)
Z 20	(5p^2 - 4) p^3 * SIN (3A)
Z 21	(15p^4 - 20p^2 + 6) p^2 * COS (2A)
Z 22	(15p^4 - 20p^2 + 6) p^2 * SIN (2A)
Z 23	(35p^6 - 60p^4 + 30p^2 - 4) p * COS (A)
Z 24	(35p^6 - 60p^4 + 30p^2 - 4) p * SIN (A)
Z 25	(70p^8 - 140p^6 + 90p^4 - 20p^2 + 1)
Z 26	(p^5) * COS (5A)
Z 27	(p^5) * SIN (5A)
Z 28	(6p^2 - 5) p^4 * COS (4A)
Z 29	(6p^2 - 5) p^4 * SIN (4A)
Z 30	(21p^4 - 30p^2 + 10) p^3 * COS (3A)
Z 31	(21p^4 - 30p^2 + 10) p^3 * SIN (3A)
Z 32	(56p^6 - 1(A)
Z 33	(56p^6 - 1(A)
Z 34	(126 p^8 - * COS (A)
Z 35	(126 p^8 - * SIN (A)
Z 36	(252p^10 - 2 - 1)
Z 37	(924p^12 - 420p^4 - 42p^2 + 1)

Table 6-12. Summary of hologram designs

SEGMENT #	Pattern at focus of Projection lens	Wavefront Contour (without dominating tilt terms)(Shown at scale where 1 contour line equals 500 waves in CGH.)
T1	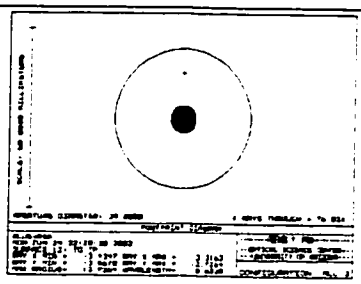	
T5	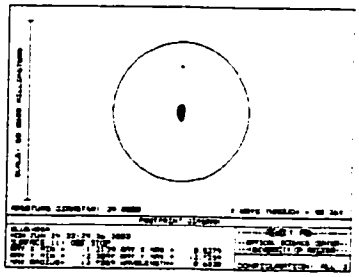	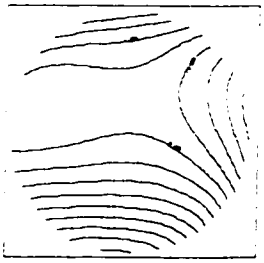
T8	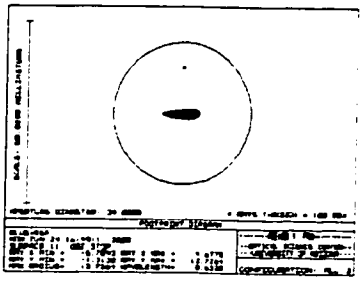	
T10	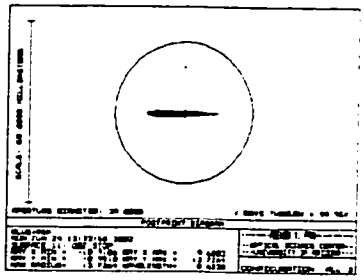	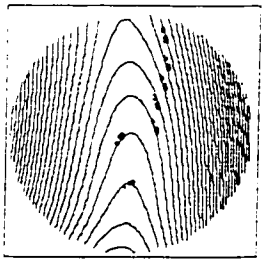
T13	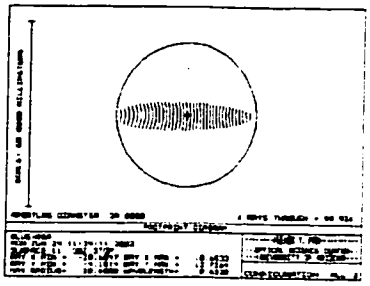	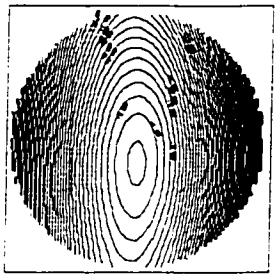

6.7 FRINGE CONTRAST

After specification of CGHs, one of the issues concerning the usage of them is how good fringes they produce. Visibility defined in Eqn. [2.44] is used to quantatively describe how well can fringes be observed. Previous analysis presented by J. Burge[30] shows that these holograms can indeed produce fairly good contrast fringes:

- The holograms are designed with 50% duty cycle. This put 25% of the incident light into the zero order and 10% into the first order.
- For measuring bare glass segments, I_{ref} = 0.01 (4% R and 25% diffraction efficiency) and I_{test} = 0.004 (4% R and 10% diffraction efficiency) and 90% contrast is achieved.
- The test can also be used to measure aluminized segments. Here I_{ref} = 0.01 and I_{test} = 0.095 (95% R and 10% diffraction efficiency) and 58% contrast is achieved. This is still adequate to allow accurate high-resolution surface measurements.

$$visibility = \frac{2\sqrt{I_{ref} I_{test}}}{I_{ref} + I_{test}} \qquad [2.44]$$

CHAPTER 7

CASE STUDY—PART B: TOLERANCE ANALYSIS

Tolerance analysis is an integral part of any testing method. It gives a quantitative answer to the question 'how good is this test?' By performing detailed tolerance analysis on a test method, systematic errors can be investigated, and only then can possible improvements be made. The error analysis presented in this chapter pertains to the system designed in the previous Chapter 6 (Case study – Part A: System Design). Even though the numerical answers obtained here is system specific, the process is not. The goal of this chapter is to establish the process from which detailed tolerance analysis can be carried out for any future designs to test similar segmented primaries presented in Chapter 6. Much of the work presented here is pioneered by J. Burge [32].

The error analysis is divided in two categories, figure errors and errors in the definition of the segment location with respect to the parent primary. Only the most difficult segment, T13 from the previous Chapter 6 is analyzed, since tolerance is most severe for this segment (Segment #13) due to its large aspherical departure. The test was designed to meet the requirement for T#13, and is over designed for all other segments.

Tolerance analysis is closely tied to system calibration since inability to back out some of the system errors inevitably resulted in the final measurement uncertainty. For this reason, Section 7.1 summarizes the calibration procedure before the figure error

analysis is dealt in Section 7.2. The low-frequency errors equivalent to misalignment of the segment are described in Section 7.3. Results of the tolerance analysis are condensed in Figure 7-1, the 'road map of tolerance analysis'.

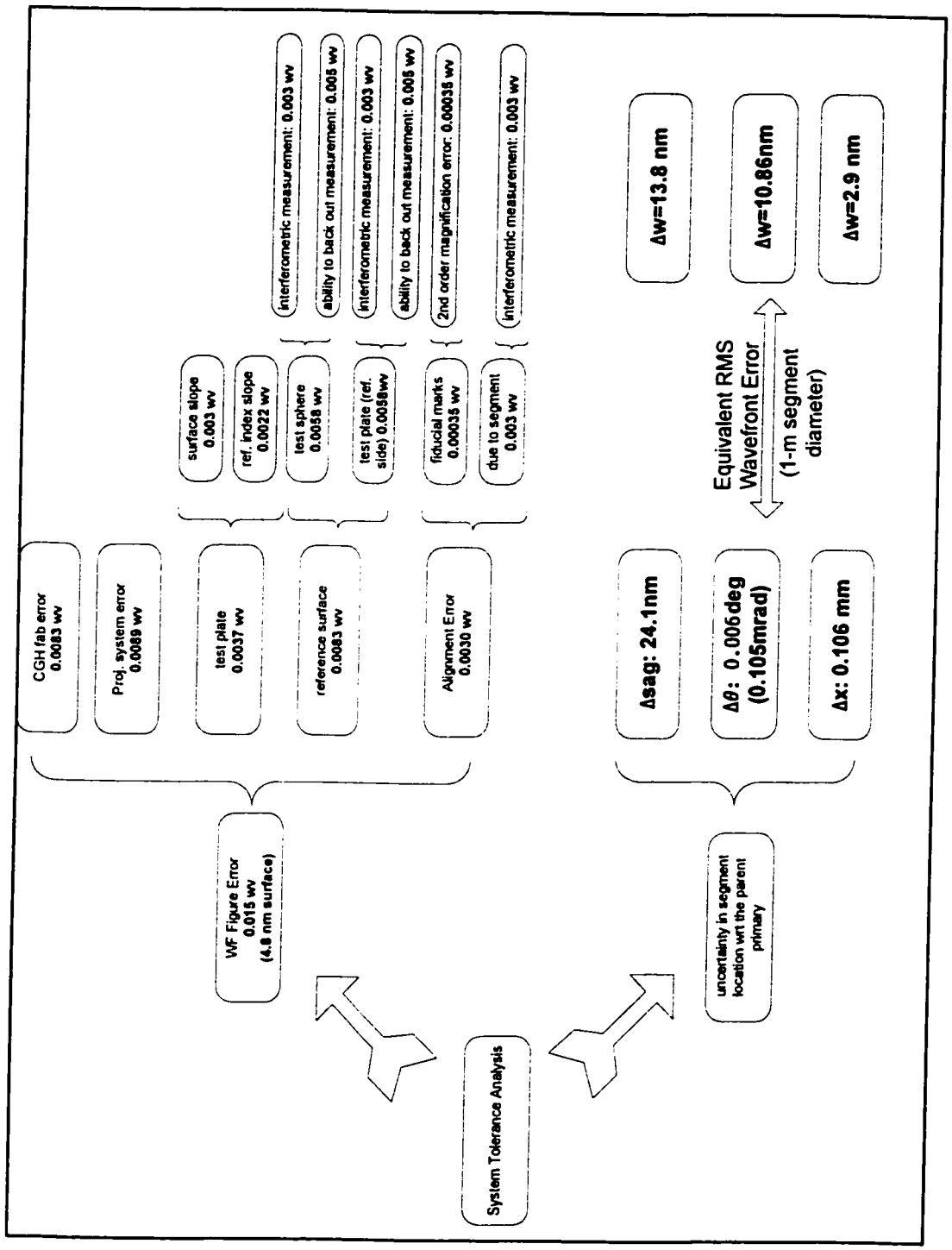

Figure 7-1 Summary of Error Analysis.

7.1 SYSTEM ALIGNMENT AND CALIBRATION

This section deals with two important topics: how to align the test system and what steps must be followed to calibrate the system. Relatively few steps are needed to align the system:

1. Move the test plate laterally and axially to align the projection system and the CGH to the reference surface. The CGH has 6 fiducial marks in a ring pattern etched outside of its clear aperture, and the reference surface will have a ring pattern scribed outside of the clear aperture.
2. Tip/tilt the test plate to the return beam light back into the CCD.
3. Place test surface behind the reference surface. Move laterally, axially and tip/tilt until all power is removed from the interferogram.

The alignment of projection and CGH to the reference surface needs to be done only once and not moved for measuring different segments. Alignment accuracy using projected fiducial marks is addressed in later section.

Calibrating the test system requires backing out errors from the reference surface and other possible systematic errors such as refractive index variation of the test plate. When a segment is measured, the result is a combination of surface figure (desired), known systematic error (can be backed out) and other errors (measurement uncertainty). This is expressed in Eqn.[7.1] below[33]. At best we can back out what we know (S_{ref}, ε_x, ε_y) and calculate what the uncertainty is (ΔS).

$$S_{total}(x,y) = S_{ref}(x,y) + \frac{\partial S}{\partial x}(x,y)\cdot\varepsilon_x(x,y) + \frac{\partial S}{\partial y}(x,y)\cdot\varepsilon_y(x,y) + \Delta S(x,y) + S_{test}(x,y) \quad [7.1]$$

where the terms are defined as:

(x,y)	absolute coordinates on segment
$S_{ref}(x,y)$	reference surface figure
$S_{test}(x,y)$	surface figure of test part
$\partial S/\partial x$, $\partial S/\partial y$	system slope from CGH in x and y directions (known from the CGH design
ε_x, ε_y	slope coupling in x and y directions.
$\Delta S(x,y)$	all other error terms
$S_{total}(x,y)$	raw surface measurement, includes all effects

The calibration is categorized into three sections:

I. Measure the reference sphere. The reference sphere is pre-measured using other interferometric method and is used to calibrate the reference of the test plate. The reference sphere has radius of curvature (ROC) a few millimeter longer than the reference ROC.

II. Measure the convex reference surface against the reference sphere (to back out $S_{ref}(x,y)$ later).

III. Backing out the possible test plate slope error due to refractive index variation using two specially designed CGHs (this is to back out ε_x, ε_y).

The calibration procedures were well developed by J. Burge[2] before the time of this writing and they are included in Appendix F for completeness.

7.2 ERROR ANALYSIS FOR FIGURE MEASUREMENT

The required surface figure measurement was specified to be 0.02λ RMS wavefront. This translates to 6.3-nm uncertainty in surface figure measurement. Our design achieves 4.8-nm uncertainty in surface figure measurement. There are five major error sources that contribute to the figure error in the measurement of a segment. These are listed below:

1. Wavefront errors from CGH or the test plate that are directly coupled into surface errors (7.2.1).
2. Errors in the projections optics, which cause a distortion when projecting the CGH image to the aspheric surface (section 7.2.2).
3. Slope errors in the system, typically from refractive index variations in the test plate, coupled with the slope differences between the two beams (section 7.2.3).
4. Inability to completely back out uncertainty in measuring the reference sphere (Sections 7.2.4).
5. Inability to completely back out the alignment error using alignment marks (Section 7.2.5).

Combined total wavefront error is summarized below in Table 7-1 and graphed in

Figure 7-2.

Table 7-1 Figure error budget for test of the T13 segment (the most difficult). Derivation for all terms is given in this section.

	Effect	Magnitude	RMS Wavefront Error [λ]	RMS Surface Figure Error [nm]
I	CGH fabrication errors	0.125 μm	0.0083	2.63
II	projection optics	Table 7-2	0.0089	2.82
	test plate inhomogeneity	±0.15 mrad	0.0003	0.94
	test plate illumination surface	2 fringes/cm	0.0030	0.70
III				
	reference surface figure	Table 7-3	0.0083	2.63
IV	segment alignment & test error	Table 7-4	0.0030	0.95
	Root Sum Squared		**0.015**	**4.76**

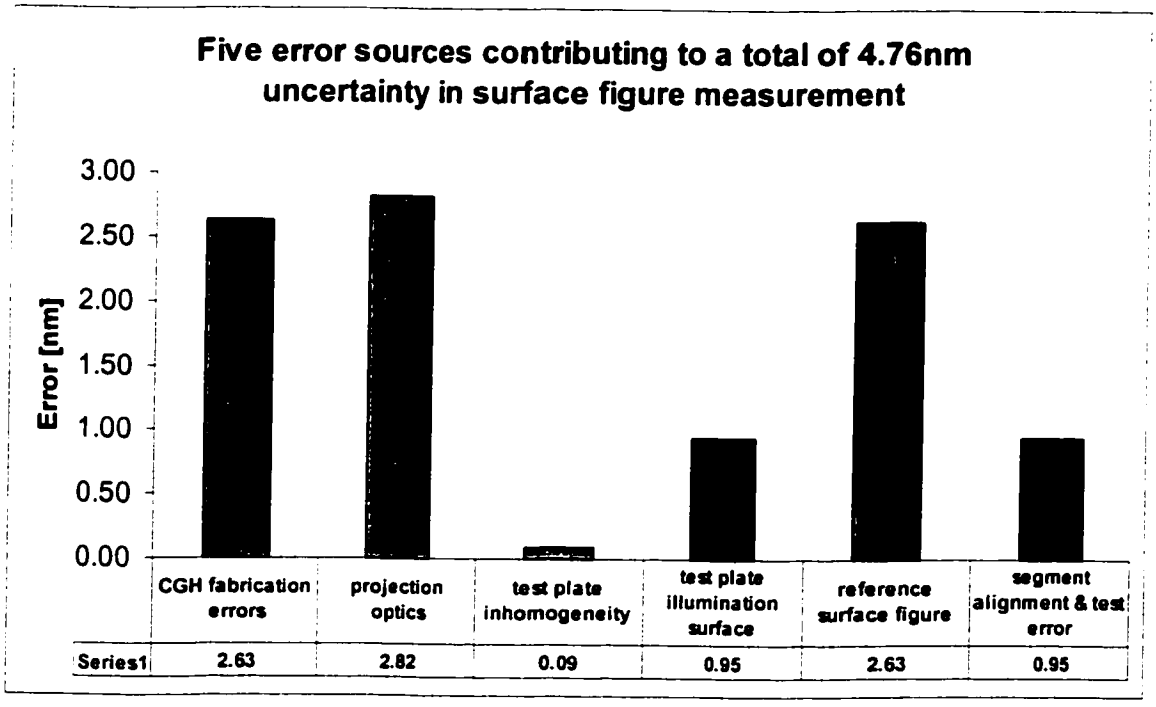

Figure 7-2. Five error sources contribute to a total of 4.76-nm uncertainty in surface figure measurement

7.2.1 Wavefront errors from CGH fabrication error

The CGH patterns have period of about 15 μm center-to-center and will be written with 50% duty cycle. These holograms can be made standard with accuracy of ±0.125 μm, which gives wavefront accuracy, in units of waves, (0.125μm/15μm) or 0.0083 λ. This corresponds to surface accuracy of 0.0042 λ or 2.6 nm. Note that since the CGH was designed to have collimated light illuminating it, and since both reference and test beam travel through it in a common path configuration, errors such substrate thickness variation or bending do not affect the test accuracy.

7.2.2 Wavefront errors from projection optics

The test and the reference beams do not travel through the projection optics together, so there is a potential wavefront error introduced into the measurement. The dominant type of error in the projection optics comes from the distortion of the CGH image at the test plate due to manufacture limitation of the projection optics. The typical line spacing is 15 μm at the CGH and the system magnification for the putting the image of the CGH onto the test plate is 40.0, so the image of the CGH at the test plate has a period of 600 μm (=15 μm x 40.0). If this image is distorted by an amount equivalent to one line, the resulting wavefront error is distorted by 1 wave. So, to keep the error to 0.01 λ, the distortion must be less then 6.0 μm over the 1340-mm image (image of CGH fills the test plate diameter).

The process to find how much the projection system contributes to the total surface figure measurement uncertainty is tedious to say the least. Each variable of each

component in the projection system was perturbed in a known amount and the resulting contribution was recorded. To get the total contribution, each individual contribution is then added together in the root-sum-square sense. The steps for simulating the effect of each parameter tolerance are given below:

1. In Zemax, introduce small amount of perturbation to the parameter of choice.

2. re-optimized the reference wavefront by changing the coefficients of a dummy aspheric function that is defined at the CCD array. This is because any perturbation in the optical system affects both the test and reference wavefronts, so by nulling the reference wave, we can then record the change in the test beam as the net change between the two beams.

3. The position of the test surface is optimized to minimize the rms wavefront in the test beam. This is accomplished by setting three position variables Δx (lateral displacement), ΔR (thickness change between the test plate and the test surface) and $\Delta\theta$ (rotation). The adjustment required for this, as well as the rms wavefront itself are then recorded.

Only the error budget for the most difficult segment, segment #13, was developed. The accuracy for the others will be better. Table 7-2 summarizes the results obtained using the above procedures.

Table 7-2 Error analysis of the projection system

PARAMETER	VALUE	TOLERANCE	UNITS	ΔR mm	Δ X mm	Δθ deg	RMS WF (λ)
LASER beam							
		1 wv	wv P-V	0.0000	0.0000	0.0000	0.0023
		0.002	deg	-0.0153	-0.0278	0.0000	0.0015
CGH							
decenter		0.01	mm	0.1847	0.0372	-0.0004	0.0009
tilt		0.005	mm	0.2041	0.0379	-0.0003	0.0009
rotation		0.002	deg	0.0040	0.0005	0.0020	0.0008
CGH - L1 spacing	259.9157	0.01	mm	-0.0882	0.0014	0.0000	0.0010
Lens1							
R1	inf	0.05	mm	0.0000	0.0000	0.0000	0.0001
center thickness	20	0.01	mm	-0.0541	0.0014	0.0000	0.0007
R2	-126.6618	0.002	mm	0.0781	0.0021	0.0000	0.0008
index		0.00001		0.01910	-0.00011	-0.00001	0.0013
surface 1	surf PV	0.125	wave	-0.0063	-0.0005	0.0000	0.0011
surface2	surf PV	0.0125	wave	-0.0166	0.0010	-0.0001	0.0009
inhomogeneity	PV	2.00E-06	-	-	-	-	0.0001
decenter		0.005	mm	-0.1028	-0.0042	0.0001	0.0012
tilt	/100mm	0.005	mm	0.0054	0.0002	-0.0001	0.0008
wedge	/100mm	0.005	mm	-0.0624	-0.0017	0.0018	0.0018
L1 - L2 spacing	94.9862	0.005	mm	-0.0476	-0.0010	0.0002	0.0008
Lens2							0.0000
R1	-41.21586	0.005	mm	0.0000	0.0031	-0.0001	0.0017
center thickness	20	0.005	mm	-0.0323	0.0068	-0.0002	0.0002
R2	-49.20629	0.005	mm	0.0197	0.0036	0.0000	0.0015
index		0.00001					0.0000
surface 1	surf PV	0.125	wave	-0.0140	0.0018	-0.0002	0.0009
surface2	surf PV	0.125	wave	-0.0001	0.0039	-0.0001	0.0013
inhomogeneity	PV	2.00E-06	-	-	-	-	0.0003
decenter		0.01	mm	0.0175	-0.0024	0.0000	0.0010
tilt	/200mm	0.01	mm	0.0087	-0.0269	0.0000	0.0024
wedge	/200mm	0.005	mm	-0.0708	-0.0023	0.0021	0.0018
Test plate							
R1	7791.8688	11.7	mm	0.0175	-0.0006	0.0000	0.0020
thickness		5	mm	0.0024	0.0000	0.0000	0.0008
wedge	/1340mm	2	mm	0.0010	0.0300	0.0020	0.0060
RSS				**0.3429**	**0.073**	**0.0040**	**0.0089**

7.2.3 Wavefront errors from the test plate

The test plate contributes to the total surface figure measurement uncertainty in four ways. They are the combined results of two slope error sources multiplied with two beam shears. The two possible slope error sources are (i) refractive index variation (Section A), and (ii) illumination surface slope (Section B). The two different net shears between the reference and the test beams are (i) due to air gap and (ii) not-completely common path configuration (both explained in Section C). This complex relation is depicted in Figure 7-3 through Figure 7-5.

Section A: test plate slope error due to refractive index varation

Some assumptions have to be made about the quality of the test plate glass. We assume that the max index change is on the order of $|\Delta n|_{max} = \pm 1E\text{-}5$, with spatial variation of 4 cycles across the test plate diameter. This leads to slope error of 0.019mrad as calculated below:

$$\Delta n = |\Delta n|_{max} \times \cos\left[\frac{2\pi \bullet 4x}{Dia_{test\ plate}}\right]$$

$$\Delta W = t_{test\ plate} \times \Delta n$$

$$\Delta\theta_{ref\ index\ error} \triangleq \frac{d(\Delta W)}{dx}$$

$$= \left[t_{test\ plate}\right] \times \left[|\Delta n|_{max}\right] \times \left[\frac{2\pi \bullet 4}{Dia_{test\ plate}}\right] \times \left[-\sin\left[\frac{2\pi \bullet 4x}{Dia_{test\ plate}}\right]\right]$$

Substituting $Dia_{test\ plate}$ =1340mm, $|\Delta n|_{max} = \pm 1E\text{-}5$ and 100mm for thickness of the test plate, we have:

$$|\Delta\theta_{\text{ref index error}}| = [100mm] \times [\pm 1\text{E-}5] \times \left[\frac{2\pi \bullet 4}{1340\text{mm}}\right]$$

or,

$$|\Delta\theta_{\text{ref index error}}| = 0.019mrad$$

Section B: test plate slope error due to illumination surface slope

The surface slope of the illumination side is specified to be on the order of 2 fringes/cm or 1λ/cm surface distortion. This gives slope error of 0.029 mrad as calculated below:

$$\Delta\theta_{\text{ref index error}} \triangleq \frac{d(\Delta W)}{dx}$$

$$\frac{\Delta W}{dx} = \frac{ds}{dx} \times (n_{\text{test plate}} - 1)$$

$$= \left[\frac{2\lambda}{\text{cm}}\right] \times [1.45 - 1]$$

$$= 0.029mrad$$

Section C: net beam shears

There are two different net beam shears we must calculate. The first one is from the not-completely common path configuration. In this case, the test plate slope error shears the reference and test beam the same amount before the air gap, but only the test beam goes through the air gap (Figure 7-5). This means that the net shear difference between the two beams comes only from the additional shear experienced by the test beam accumulated when it goes through the air gap. This shear can be easily calculated:

$$\Delta x_{\text{net}} = 2 \times t_{\text{air gap}} \times \varepsilon_{\text{order separation}} \text{ (obtained earlier from Chapter 6)}$$

$$= 2 \times 5mm \times 1.053mrad$$

$$= 10um$$

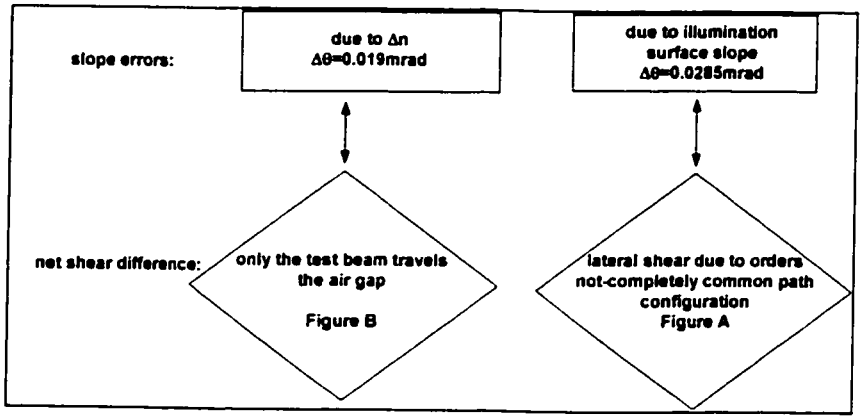

Figure 7-3 slope errors and beam shears contribute to uncertainty in surface figure measurement.

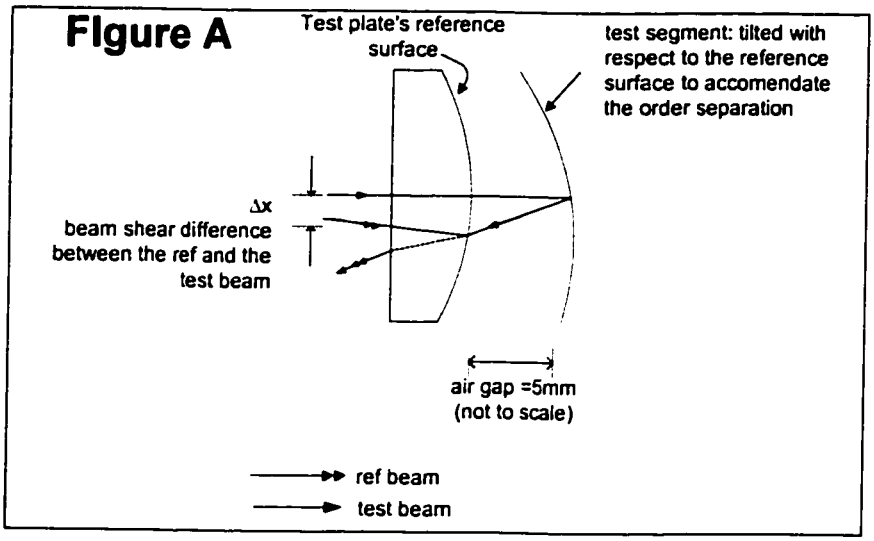

Figure 7-4. Beam shear due to order separation.

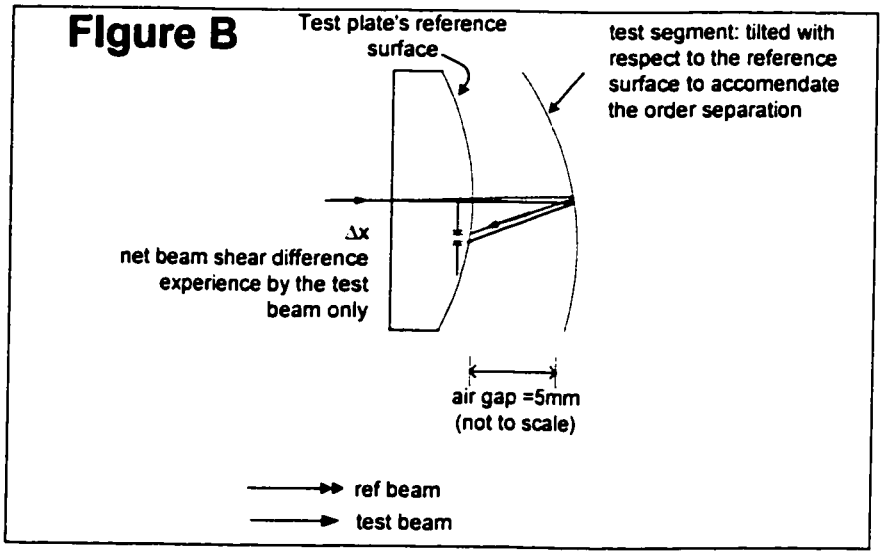

Figure 7-5. Beam shear due to not-completely common path configuration

The reference and the test beam are laterally sheared at the illumination side of the test plate due to order separation (Figure 7-4). The amount of shear is proportional to the tilt need for order separation:

$$\Delta x = \left[\Delta t_{\text{test plate}}\right] \times \left[\frac{\varepsilon_{\text{order speration}}}{n_{\text{test plate}}}\right]$$
$$= 100\text{mm} \times \frac{1.053\text{mrad}}{1.45}$$
$$= 72.6\mu m (ZEMAX :\sim 53um)$$

Section D: combined wavefront error

Combined wavefront error can now be calculated:

$$\Delta W_{\text{beam shear}} = \sqrt{\left[\Delta\theta_{\text{ref surface error}} \times \Delta x_{\text{air gap shear}}\right]^2 + \left[\Delta\theta_{\text{slope error}} \times \Delta x_{\text{beam shear}}\right]^2}$$
$$= \sqrt{\left[0.019mrad \times 10\mu m\right]^2 + \left[0.0285mrad \times 72\mu m\right]^2}$$
$$= \sqrt{3.6\text{E-}8\ \mu\text{m}^2 + 4.2\text{E-}6\mu\text{m}^2}$$
$$= 0.003\lambda$$

7.2.4 Wavefront errors from testing the reference surface

Before the aspheric segment can be measured, the reference surface of the test plate must be calibrated using a reference sphere (RS). This sequence is depicted in Figure 7-6. Multiple errors are accumulated through this process. Start with the calibration of the reference sphere. Assuming that calibration of RS uses a direct shifting interferometer, which has approximately 0.003λ of random noise (RMS wavefront) per measurement. This level can be reduced if multiple measurements are taken and data are averaged. To

be on the safe side, we assume only one measurement was taken, so RMS wavefront uncertainty is 0.003λ. In addition to this error, there is a limit to how accurately we can remove the mapping errors from the RS measurement out of the reference surface measurement. This inability to completely backing out interferometric error introduces approximately 0.005λ RMS wavefront uncertainty if we assume RS has surface slope of 0.02λ/cm and mapping error of 2.5mm. At this point, the calibration of RS has accumulated 0.0058λ RMS wavefront errors:

	$\sqrt{[0.003\lambda]^2+[(0.01\lambda/cm)(5mm)]^2}=0.0058\lambda$
assuming,	
	0.003λ of random RMS wavefront noise measuring the reference sphere
	0.01λ/cm surface slope of the reference sphere
	5mm mapping error

Calibration of the test plate reference surface against the RS accumulates similar errors:

	$\sqrt{[0.003\lambda]^2+[(0.01\lambda/cm)(5mm)]^2}=0.0058\lambda$
assuming,	
	0.003λ of random RMS wavefront noise measuring the reference sphere
	0.01λ/cm surface slope of the test plate reference surface
	5mm mapping error

Table 7-3 summarizes the error budget for measuring figure from the test plate's reference surface and the reference sphere.

Table 7-3. Error budget for measuring figure from the test plate and reference sphere.

Effect	Surface Figure λ rms	Figure nm rms
Measurement of concave reference using interferometer	0.003	0.95
Effect of distortion backing out interferometer errors	0.005	1.58
Measurement of convex test plate	0.003	0.95
Effect of distortion backing out reference sphere errors	0.005	1.58
Root sum squared	**0.00825**	**2.61**

7.2.5 Wavefront errors from alignment errors

Two factors contributing to this error are alignment error of the test plate by using six fiducial marks and interferometric measurement error of the segment. Table 7-4 summarized the combined wavefront error.

Table 7-4 Error budget for measuring surface figure from the test plate and reference sphere.

Effect	Magnitude	Surface Figure λ rms	Figure nm rms
interferometric measurement	0.003	0.003	0.95
alignment to fiducials -- coupled through magnification effect	6 @ 0.1mm	0.0003	0.10
Root Sum Squared		**0.0030**	**0.95**

Alignment mark contributes to the total wavefront error since their limited position accuracy of 31ppm (Section 7.3.1) is coupled though the system as a magnification error. Through ZEMAX simulation, it is determined that this equivalent magnification error leads to and wavefront error of 0.0003 wv.

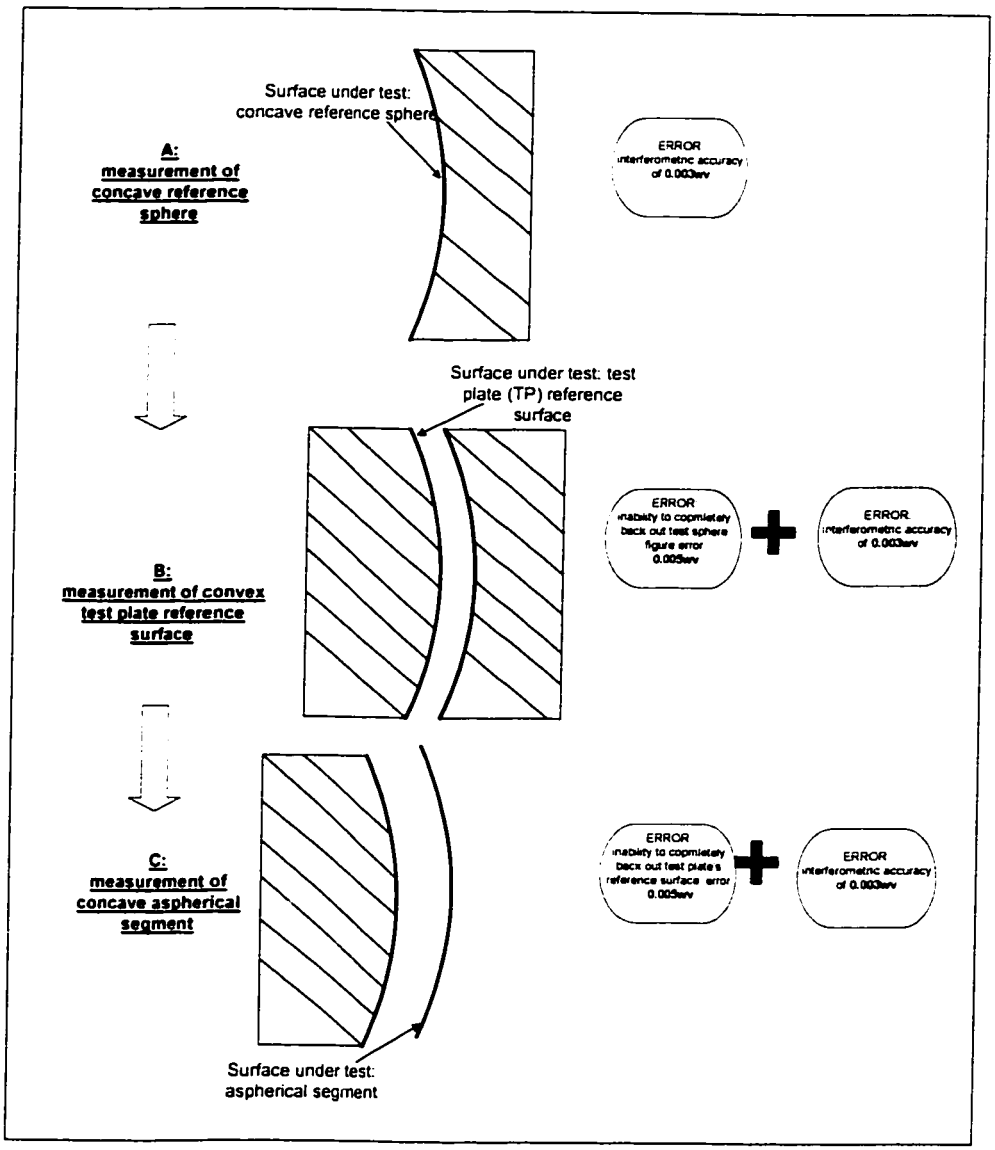

Figure 7-6 Error accumulated through calibration of reference sphere (RS) and test plate (TP) reference surface

7.3 ERROR ANALYSIS FOR DEFINING THE OPTICAL SURFACE RELATIVE TO THE PARENT MIRROR

The second part of tolerance analysis is to find out how accurately can the test define the segment position with respect to the parent primary mirror. This CGH test images 6 fiducial marks written on the CGH substrate to the test plate through the projection optics. This is used to provide accurate definition of the optical surface including radius of curvature and absolute position of off-axis segment on parent hyperboloid. Several factors limit the ability to accurately position the segment with respect to the parent mirror:

1. Imperfect projection system
2. Fabrication error on etching the fiducials
3. Misalignment to the fiducials
4. Mechanical error in transferring alignment marks

How these factors affects the segment position accuracy is the topic of this section. Organization of this section is as follows. System of fiducials is explained in section 7.3.1. Section 7.3.2 summarizes the error budget for segment position (Δx), segment rotation ($\Delta\theta$) and relative radius of curvature Δsag.

7.3.1 System of fiducials

Six alignment marks are etched in a ring pattern outside of the CGH and is imaged through the projection system onto the test segment. The alignment procedure requires the fiducials to be located to 0.1 mm. The image of the fiducial marks are 300 μm wide

(FWHM) at the test plate, so determining the center to 100 μm will not be difficult. This could be done with a simple optical loupe or with a CCD camera. Since we use 6 reference patterns and each of them will give 0.1 mm accuracy, the overall accuracy of the alignment of ring-of-fiducials to the CGH will be:

0.041 mm over diameter	since $0.1mm/\sqrt{6} = 0.041mm$
0.058 mm lateral positioning	since there are x- and y-movement, so each is allocated roughly $0.041mm \times \sqrt{2} = 0.058mm$
0.046 mrad rotation about axis	since $0.041mm/670mm = 0.061mrad$(0.0035deg)

Uncertainty in locating the six system fiducials translates into magnification error. The scale of this magnification error is 31 ppm (0.041mm/1340mm = 31E-6). The effect of this magnification error on segment position is simulated in ZEMAX following procedures described in 7.2.2 and results are listed in Table 7-5.

Table 7-5. The effect on segment position due to magnification error of 31ppm

Segment lateral shift Δx uncertainty	0.002 mm
Segment radius error Δsag uncertainty	10.54 nm
Residual wavefront error	0.0003 λ rms

Note that the segment lateral position uncertainty Δx is in addition to the 0.041 mm uncertainty from the direct effect of the fiducial alignment. There will also be a limitation to the ability to transfer the reference measured above to the segment reference

surfaces. Previous experiments have determined that this can be done to 0.05 mm, which was easily achieved with standard micrometers.

7.3.2 Segment position, orientation and relative radius of curvature relative to the parent mirror

The analysis to determine the accuracy of defining the absolute segment position and orientation is all given above. It is summarized and added for the case of segment T3, the most difficult one. The overall test accuracy is shown to be 0.106 mm for segment position and 0.105 mrad (0.006 deg) for orientation.

Table 7-6 Error budget for position and angle for the T13 segment test (the most extreme).

Effect	Magnitude	Segment position Δx [mm]	Segment rotation Δθ [Deg]
CGH fabrication errors	0.125 um	0.003	0.0002
projection optics	Table 7-2	0.073	0.0040
alignment to fiducials - coupled by scale effect	6@ 0.1 mm	0.002	1.4E-05
alignment to fiducials - direct effect	6@ 0.1 mm	0.058	0.0035
mechanical measurements	0.05 mm	0.05	0.0032
Root Sum Squared		**0.106**	**0.006**

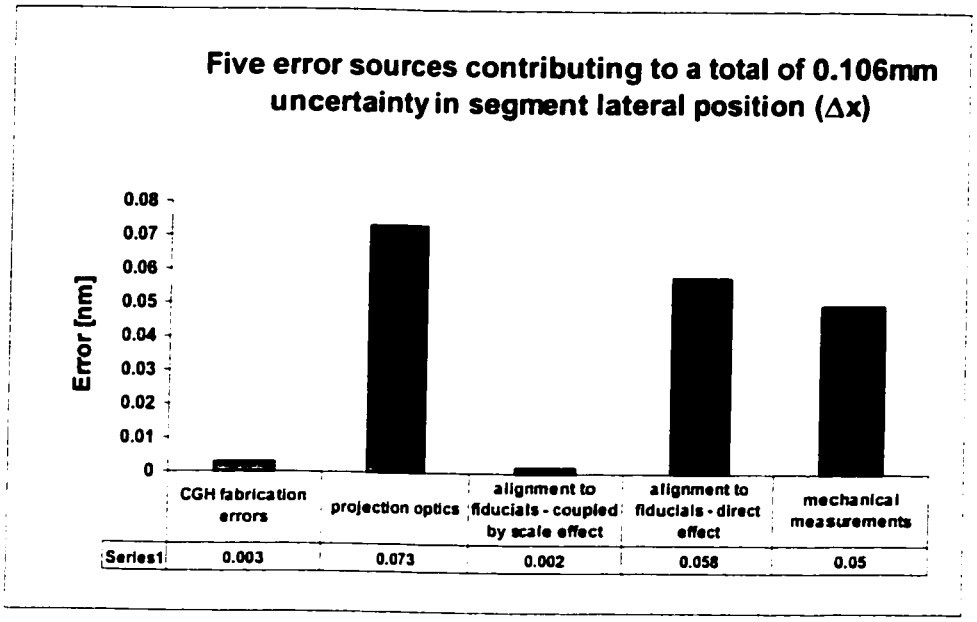

Figure 7-7. Distribution of the five contributing error sources to segment lateral position uncertainty (Δx).

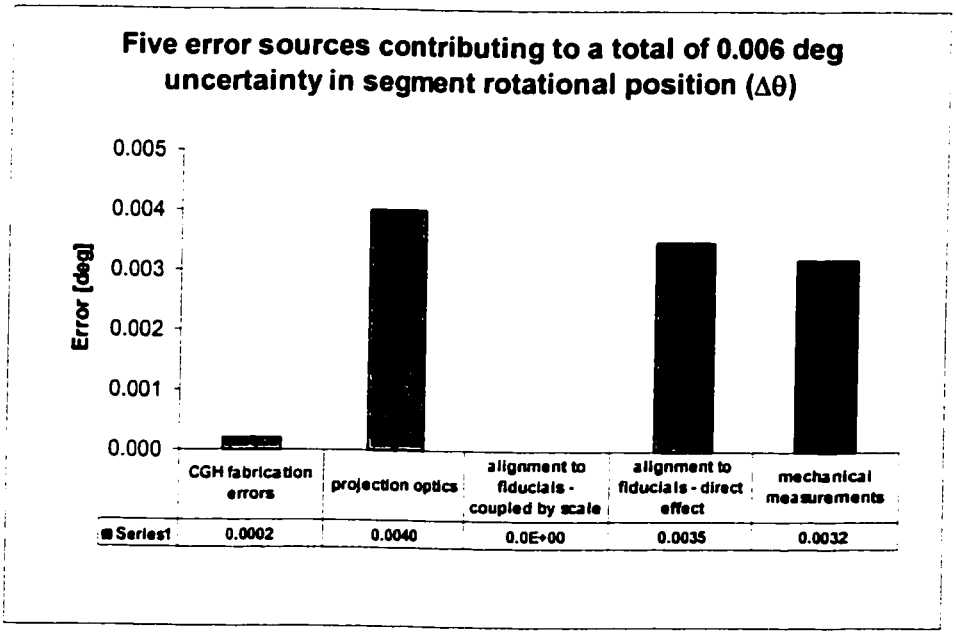

Figure 7-8. Distribution of the five contributing error sources to segment rotational position uncertainty (Δθ).

There are two specifications for radius of curvature – absolute radius and the degree of matching between segments. The overall radius of curvature will be limited by the measurement of the concave reference sphere. This analysis assumes this is known to ±2 mm. The analysis to determine the radius of curvature matching is summarized here for the case of segment T13.

Table 7-7 Error budget for radius of curvature matching for the T13 segment test (the most extreme).

Effect	Magnitude	Δsag [nm], Radius of curvature matching	ΔR [mm], Radius of curvature matching
projection optics	Table 7-2	21.38	0.34
alignment to fiducials - coupled through scale effect	6@ 0.1 mm	10.54	0.17
mechanical measurements	0.05 mm	3.12	0.05
Root Sum Squared		**24.0**	**0.39**

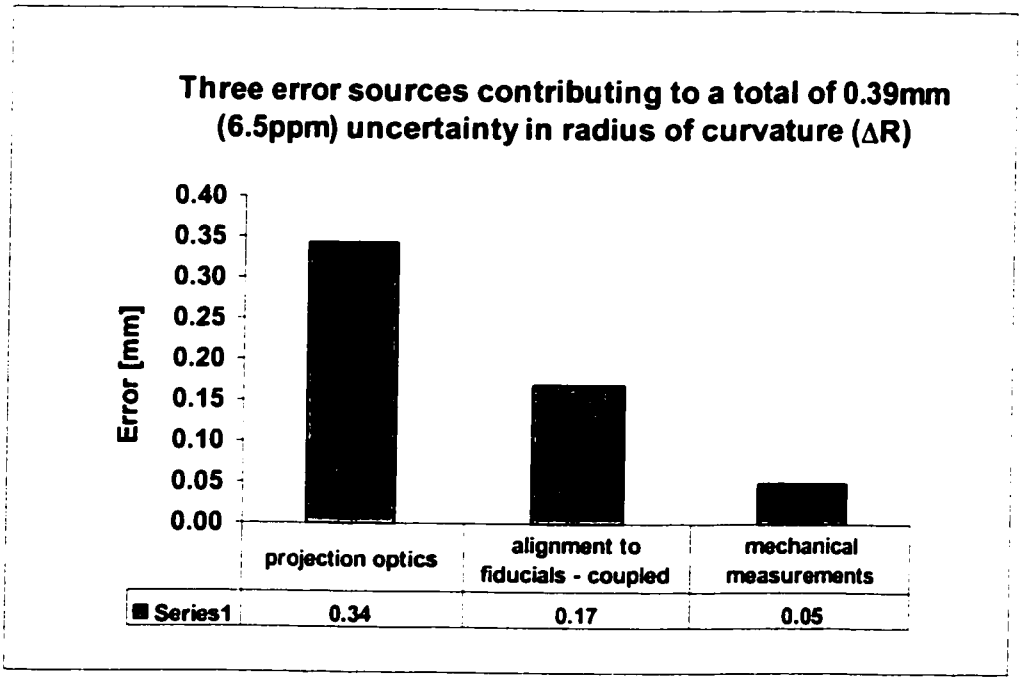

Figure 7-9. Distribution of the three contributing error sources to relative radius of curvature matching (ΔR).

CHAPTER 8

CONCLUSION

With no viable way to get closer to objects of interests, telescopes allow astronomers to study distant faint objects from our own planet. The amount of light, thus the amount of information, gathered from these distant objects is directly proportional to the size the telescope's primary mirror. The next generation of optical telescope follows the historical trend of increasing in the aperture diameter. Two recent advancements, one in mirror fabrication (using segmented optics) and one in imaging size reduction (using adaptive optics), allow ground-based telescopes to achieve improved image resolution. These innovations make the ground-telescopes competitive and desirable, both in performance and in cost effectiveness.

Presented with the increasing demand of designing/construction an ever-larger ground-telescope, developing a testing method to measure all the mirror segments becomes urgent. Pioneered by Burge and Anderson, a fast and accurate way to measure large quantities of off-axis aspherical mirror segments is to combine a test plate (for spherical reference surface) with computer-generated holograms (for aspherical departure compensation). This method matches relative radius of curvature between segments to better than 1 part in 10^5, and the requirement of one single high-quality optical surface makes this test cost effective. Built-in alignment fiducial marks allow for quick insertion of holograms to test different segments.

The work presented in this dissertation compliments, contributes to, and improves this novel aspheric testing method in several ways. First, a quantitative study on how segmentation tightens the testing tolerance provides valuable information for telescope designers on choices of essential system parameters such as the telescope segment size and F/#. From this analysis we learned that, out of the six degrees of freedom in positioning a segment, rotational and radial displacements dominate the test accuracy as the segment size increases. Secondly, systematic optimization processes presented in this work lays the foundation for future test system design using this method. Through out the optimization, accuracy and cost effectiveness was carefully considered, calculated, and balanced. Thirdly, design trade-offs, general system design rules and design pit-falls are explained and documented, making designing of a similar test system easy to follow. Lastly, experimental data provides valuable information on how the test system can be improved in the next phase. Using completely off-the-shelf components, the measurement comparison between using this novel method and traditional method shows about 0.01 λ RMS wavefront differences. Through experimental validation, a major unforeseen error source was identified. As a result, improvement can now be implemented for the next phase of test design.

FUTURE WORK

The final version of this test system would typically be housed in a 15-meter test tower. The projection system would be aligned and mounted in a barrel to standard precision. The hologram would be held in a kinematical fixture that needs to be aligned once. The

imaging optics would be aligned and mounted in a separate barrel. Once all these components are positioned correctly according to the system design, alignment fiducials etched on the hologram will be projected to the test plate. Mechanical transfer of imaged marks to appropriate local coordinates would allow accurate positioning of the mirror segment. If the segment were perfect, a featureless interferogram would be observed on the CCD where the images are captured.

The results shown in Chapter 5 (Experimental Validation) show much promise for this test method. The laboratory experiment does not utilized co-axial setup, so beam shears at the illumination surface of the test plate contributed quite significantly to the measurement error. A new CGH could be designed to implement the co-axial setup. In addition, a more carefully designed projection system could be substituted in the co-axial test setup. A significant reduction in the measurement error is expected.

After completion of the above two improvements, off-axis aspherical segment should be tested with the aid of alignment marks etched on the same CGH that is used to compensate the aspheric departure. The tolerance to error will not be must different from testing the reference sphere since CGH tilt fringes dominates the test sensitivity.

The author believes that this method will be adapted as the most common testing method for measuring large quantities of aspherical mirror segments in the next ten to twenty years when building large to extremely large ground-based telescopes becomes common practice.

APPENDIX A

RMS WAVEFRONT CALCULATION

General description of the Monte Carlo method is as follows:

1. We start with four definitions:

$$\left(\overline{\Delta W}\right)^2 \triangleq \left[\frac{\iint dA\ (\Delta W)}{\iint dA}\right]^2 \qquad [A.1]$$

where

dA: integration element over the parent mirror
ΔW(x,y): wavefront of the parent mirror
(x,y): coordinates of the parent mirror

$$\overline{\Delta W^2} \triangleq \frac{\iint dA\ (\Delta W)^2}{\iint dA} \qquad [A.2]$$

where

dA: integration element over the parent mirror
ΔW(x,y): wavefront of the parent mirror
(x,y): coordinates of the parent mirror

$$\sigma_{WF}^2 = \overline{\Delta W^2} - \left(\overline{\Delta W}\right)^2 \qquad [A.3]$$

where

σ_{WF}^2: root-mean-square (RMS) wavefront error
$\overline{\Delta W^2}$: defined in [A.1]
$\left(\overline{\Delta W}\right)^2$: defined in [A.2]

$$\Delta W = \sum_{i=1}^{N} \Delta w_i \qquad [A.4]$$

where

N: number of segments
$\Delta w_i(x,y)$: wavefront error of the ith segment
ΔW: wavefront error of the parent mirror

2. For each error, substitute the relevant expression for Δw_i into Eqns. [A.3] and [A.4]. Evaluate integrals and simplify.

3. Since all segments are identical in size,

$$\begin{aligned} A &\equiv \iint dA \\ &= N \iint da_i \\ &= N \int_0^{2\pi} d\theta \int_0^a r dr \end{aligned} \qquad [A.5]$$

where

A: total area of the primary mirror
da_i: elemental area of the segment
(r,θ): local coordinates of the segment
N: total number of segments
a: segment radium (point-to-point dimension of the hexagonal segment)

Piston Case:

$$\Delta w_i = 2\alpha_i \qquad [A.6]$$

where

α_i: piston error of the ith segment. Drawn from a zero mean Gaussian distribution with standard deviation of σ_α

$$\overline{\Delta W^2} = \frac{\sum_{i=1}^{N} \iint da_i (\Delta w_i)^2}{N\pi a^2}$$

$$= \frac{2^2 \sum_{i=1}^{N} (\alpha_i)^2 \iint r dr d\theta}{N\pi a^2}$$

$$= 2^2 \frac{\sum_{i=1}^{N} (\alpha_i)^2}{N}$$

$$\left(\overline{\Delta W}\right)^2 = \left[\frac{\sum_{i=1}^{N} \iint da_i \Delta w_i}{N\pi a^2}\right]^2$$

$$= 2^2 \left[\frac{\sum_{i=1}^{N} \alpha_i}{N}\right]^2$$

$$\sigma_{wf}^2 = 2^2 \left[\left[\frac{\sum_{i=1}^{N} (\alpha_i)^2}{N}\right] - \left[\frac{\sum_{i=1}^{N} \alpha_i}{N}\right]^2\right] \text{ (Monte Carlo)} \qquad [A.7]$$

$$\sigma_{wf}^2 = 2^2 \sigma_\alpha^2 \qquad [A.8]$$

Tilt case:

$$\Delta w_i = 2(\gamma_i \frac{x_p}{a} + \beta_i \frac{y_p}{a}) \qquad [A.9]$$

where

γ_i: x-tilt error of the ith segment. Drawn from a zero mean Gaussian distribution with standard deviation of σ_γ

β_i: y-tilt error of the ith segment. Drawn from another independent zero mean Gaussian distribution with standard deviation of $\sigma_\beta=\sigma_\gamma=\sigma$

(x_p,y_p): pupil coordinates of the ith segment

a: segment radius

$$\overline{\Delta W^2} = \frac{\sum_{i=1}^{N} \iint da_i (\Delta w_i)^2}{N\pi a^2}$$

$$= \frac{\sum_{i=1}^{N} \iint da_i \left[2\gamma_i \frac{x_p}{a} + 2\beta_i \frac{y_p}{a} \right]^2}{N\pi a^2}$$

$$= \frac{4\sum_{i=1}^{N} \left[\gamma_i^2 \iint da_i \frac{x_p^2}{a^2} + \beta_i^2 \iint da_i \frac{y_p^2}{a^2} + 2\gamma_i\beta_i \iint da_i \frac{x_p y_p}{a^2} \right]}{N\pi a^2}$$

$$= \frac{4\sum_{i=1}^{N} \left[\gamma_i^2 \int_0^a \int_0^{2\pi} r dr d\theta \frac{(r\cos\theta)^2}{a^2} + \beta_i^2 \iint da_i \frac{y_p^2}{a^2} + 2\gamma_i\beta_i \iint da_i \frac{x_p y_p}{a^2} \right]}{N\pi a^2}$$

$$= \frac{4\left[\sum_{i=1}^{N} \gamma_i^2 + \sum_{i=1}^{N} \beta_i^2 \right] \pi \left(\frac{a^2}{4} \right)}{N\pi a^2}$$

$$= \left[\frac{\sum_{i=1}^{N} \gamma_i^2}{N} + \frac{\sum_{i=1}^{N} \beta_i^2}{N} \right]$$

$= \sigma_\gamma^2 + \sigma_\beta^2$ since random variables γ and β have zero mean

$$\left(\overline{\Delta W}\right)^2 = \left[\frac{\sum_{i=1}^{N} \iint da_i \, \Delta w_i}{N\pi a^2}\right]^2$$

$$= \left[\frac{2\sum_{i=1}^{N} \iint da_i(\gamma_i x_p + \beta_i y_p)}{N\pi a^2}\right]^2$$

$$= \left[\frac{2\sum_{i=1}^{N}\left(\frac{\gamma_i}{a}\iint da_i r\cos\theta + \frac{\beta_i}{a}\iint da_i r\sin\theta\right)}{N\pi a^2}\right]^2$$

$$= 0 \text{ since } \int_0^{2\pi} d\theta\cos\theta = \int_0^{2\pi} d\theta\sin\theta = 0$$

$$\sigma_{WF}^2 = \left[\frac{\sum_{i=1}^{N}\gamma_i^2}{N} + \frac{\sum_{i=1}^{N}\beta_i^2}{N}\right] \text{ (Monte Carlo)} \qquad [A.10]$$

$$\sigma_{WF}^2 = \sigma_\gamma^2 + \sigma_\beta^2 = 2\sigma^2 \qquad [A.11]$$

ROC case:

$$\Delta w_i = 2S_i\left(\frac{r_p}{a}\right)^2 \qquad [A.12]$$

where

γ_i: sag error of the ith segment. Drawn from a zero mean Gaussian random variable with standard deviation of σ

a: segment radius

$$\overline{\Delta W^2} = \frac{\sum_{i=1}^{N}\iint da_i\,(\Delta w_i)^2}{N\pi a^2}$$

$$= \frac{\sum_{i=1}^{N}\iint da_i\left[2S_i\left(\frac{r_p}{a}\right)^2\right]^2}{N\pi a^2}$$

$$= \frac{4\sum_{i=1}^{N}S_i^2\iint da_i\,\frac{r_p^4}{a^4}}{N\pi a^2}$$

$$= \frac{4\sum_{i=1}^{N}S_i^2(2\pi)\left(\frac{a^2}{6}\right)}{N\pi a^2}$$

$$= \frac{4}{3}\left(\frac{\sum_{i=1}^{N}S_i^2}{N}\right)$$

$$\left(\overline{\Delta W}\right)^2 = \left[\frac{\sum_{i=1}^{N}\iint da_i\,\Delta w_i}{N\pi a^2}\right]^2$$

$$= \left[\frac{2\sum_{i=1}^{N}\iint da_i\left(S_i\frac{r_p}{a}\right)}{N\pi a^2}\right]^2$$

$$= \left[\frac{2\sum_{i=1}^{N}S_i\int_0^a\int_0^{2\pi} r\,dr\,d\theta\left(\frac{r_p}{a}\right)^2}{N\pi a^2}\right]^2$$

$$= \left[\frac{2\sum_{i=1}^{N}S_i\left(2\pi\frac{a^2}{4}\right)}{N\pi a^2}\right]^2$$

$= 0$ since random variable S has zero mean, i.e. $\left(\frac{\sum_{i=1}^{N}S_i}{N}\right) = 0$

$$\sigma_{WF}^2 = \frac{4}{3}\left(\frac{\sum_{i=1}^{N}S_i^2}{N}\right) \text{ (Monte Carlo)} \qquad [A.13]$$

$$\sigma_{WF}^2 = \frac{4}{3}\sigma_S^2 \qquad [A.14]$$

Translation Error:

In chapter 2, we found the expression for the aspherical departure of the off-axis segments:

$$\Delta w_i = \left[\frac{\partial}{\partial b_i}\left(C_{40(b_i,\theta)} + C_{31(b_i,\theta)} + C_{22(b_i,\theta)} + C_{33(b_i,\theta)} + C_{44(b_i,\theta)}\right)\right]\Delta b_i \qquad \text{[A.15]}$$

where

$$C_{40}(\rho) := \left(\frac{K}{8\cdot R^3}\right)\cdot\rho^4$$

$$C_{31}(\rho,\theta) := \left(4\cdot b_i\cdot\frac{K}{8\cdot R^3}\right)\cdot\rho^3\cdot\cos(\theta)$$

$$C_{22}(\rho,\theta) := \left(2\cdot b_i^2\cdot\frac{K}{8\cdot R^3}\right)\cdot\rho^2\cdot\cos(2\cdot\theta)$$

$$C_{33}(\rho,\theta) := \left[2\cdot b_i^3\cdot\frac{\left[(K+1)^2-1\right]}{16\cdot R^5}\right]\cdot\rho^3\cdot\cos(3\cdot\theta)$$

$$C_{44}(\rho,\theta) := \left[10\cdot b_i^4\cdot\frac{\left[(K+1)^3-1\right]}{128\cdot R^7}\right]\cdot\rho^4\cdot\cos(4\cdot\theta)$$

and

- Δb_i: translation error [mm] of the ith segment. Drawn from a zero-mean Gaussian random variable with standard deviation of $\sigma_{\Delta b}$.
- b_i: off-axis distance of the ith segment
- (ρ,θ): local coordinates of the segment
- R: radius of curvature of the parent mirror
- N: total number of segments
- a: radius of the segment (point-to-point dimension for a hexagonal segment)
- k: conic constant of the primary mirror

To simplify Eqn. [A.15], we first evaluate the derivative:

$$\Delta w_i = \left[\dot{C}_{40(b_i,\theta)} + \dot{C}_{31(b_i,\theta)} + \dot{C}_{22(b_i,\theta)} + \dot{C}_{33(b_i,\theta)} + \dot{C}_{44(b_i,\theta)}\right]\Delta b_i$$

where

$$\dot{C}_{40}(b_i,\theta) = 0 \qquad \text{[A.16]}$$

$$\dot{C}_{31}(b_i,\theta) = \frac{k}{2R^3}\left\{\rho^3\cos(\theta)\right\} \qquad \text{[A.17]}$$

$$\dot{C}_{22}(b_i,\theta) = \left(\frac{k}{2R^3}\right)b_i\left[\rho^2\cos(2\theta)\right] \qquad \text{[A.18]}$$

$$\begin{aligned}\dot{C}_{33}(b_i,\theta) &= \left(\frac{3}{8}\right)\left(\frac{(k+1)^2-1}{R^5}\right)b_i^2\left\{\rho^3\cos(3\theta)\right\} \\ &= \left\{\left(\frac{3}{8}\right)\left(\frac{(k+1)^2-1}{R^3}\right)b_i\left(\frac{b_i}{R^2}\right)\right\}\left\{\rho^3\cos(3\theta)\right\}\end{aligned} \qquad \text{[A.19]}$$

$$\begin{aligned}\dot{C}_{44}(b_i,\theta) &= \left(\frac{5}{16}\right)\left(\frac{(k+1)^2-1}{R^7}\right)b_i^3\left\{\rho^4\cos(4\theta)\right\} \\ &= \left\{\left(\frac{5}{16}\right)\left(\frac{(k+1)^3-1}{R^3}\right)b_i\left(\frac{b_i}{R^2}\right)^2\right\}\left\{\rho^4\cos(4\theta)\right\}\end{aligned} \qquad \text{[A.20]}$$

The following magnitude-comparisons show that the dominating term is the astigmatism-like $\dot{C}_{22}(b,\theta)$:

$\dot{C}_{31}(b,\theta)$ & $\dot{C}_{22}(b,\theta)$: $\dot{C}_{22}(b,\theta)$ dominates for any segments with off-axis distance $b_i \geq 1$m. For a primary mirror with segment size of 2-m, this means all segments and for segment size of ~ 1-m, this means for all segments but the 1st ring. The 1st ring of segments is most probably removed anyway due to the obscuration (for locating the secondary mirror).

$\dot{C}_{33}(b,\theta)$ & $\dot{C}_{22}(b,\theta)$: $\dot{C}_{22}(b,\theta)$ dominates since the magnitude of $\dot{C}_{33}(b,\theta)$ has a factor (b_i/R^2). For a 30-m f/1 primary, this amounts to ~4E-3 or $\dot{C}_{33}(b,\theta)$ is more than three magnitude smaller than $\dot{C}_{22}(b,\theta)$

$\dot{C}_{44}(b,\theta)$ & $\dot{C}_{22}(b,\theta)$: $\dot{C}_{22}(b,\theta)$ dominates since the magnitude of $\dot{C}_{44}(b,\theta)$ has a factor $(b_i/R^2)^2$. For a 30-m f/1 primary, this amounts to ~1.7E-5 or $\dot{C}_{44}(b,\theta)$ is about five magnitude smaller than $\dot{C}_{22}(b,\theta)$

Translation Error (cont.):

Following above simplification, we can now have

$$\Delta w_i = 2\Delta b_i \left(\frac{\partial c_{22,}(b_i,\theta)}{\partial \Delta b_i} \right) \rho^2 \cos 2\theta \qquad [A.21]$$

$$= 2\Delta b_i \left(\frac{k b_i a^2}{2R^3} \right) \rho^2 \cos 2\theta$$

$$\triangleq 2\Delta b_i \left(\dot{c}_{22,} \right) \rho^2 \cos 2\theta$$

where

- Δb_i: translation error [mm] of the ith segment. Drawn from a zero-mean Gaussian random variable with standard deviation of $\sigma_{\Delta b}$.
- b_i: off-axis distance of the ith segment
- (ρ,θ): local coordinates of the segment
- R: radius of curvature of the parent mirror
- N: total number of segments
- a: diameter of the segment (point-to-point dimension for a hexagonal segment)
- k: conic constant of the primary mirror

$$\overline{\Delta W^2} = \frac{\sum_{i=1}^{N} \iint da_i (\Delta w_i)^2}{N\pi a^2}$$

$$= \frac{4\sum_{i=1}^{N} \iint da_i \left[\Delta b_i \dot{c}_{22_i} \rho^2 \cos 2\theta\right]^2}{N\pi a^2}$$

$$= \frac{4\left(\sum_{i=1}^{N} [\Delta b_i]^2 \left[\dot{c}_{22_i}\right]^2\right)\left(\iint da_i \rho^4 \cos^2 2\theta\right)}{N\pi a^2}$$

$$= \frac{4\left(\sum_{i=1}^{N} [\Delta b_i]^2 \left(\frac{k b_i a^2}{2R^3}\right)^2\right)\left(\frac{\pi a^2}{6}\right)}{N\pi a^2}$$

$$= \frac{4\left(\frac{ka^2}{2R^3}\right)^2 \left(\sum_{i=1}^{N} [\Delta b_i]^2 (b_i)^2\right)\left(\frac{\pi a^2}{6}\right)}{N\pi a^2}$$

$$= \frac{4}{6}\left(\frac{ka^2}{2R^3}\right)^2 \left(\frac{\sum_{i=1}^{N} [\Delta b_i]^2 (b_i)^2}{N}\right)$$

$$\left(\overline{\Delta W}\right)^2 = \left[\frac{\sum_{i=1}^{N} \iint da_i \, \Delta w_i}{N\pi a^2}\right]^2$$

$$= \left[\frac{2\sum_{i=1}^{N} \iint da_i \, (\Delta b_i)\left(\dot{c}_{22_i}\right)\left(\rho^2 \cos 2\theta\right)}{N\pi a^2}\right]^2$$

$$= 0$$

$$\sigma_{WF}^2 \triangleq \overline{\Delta W^2} - \left(\overline{\Delta W}\right)^2$$

$$= \frac{4}{6}\left(\frac{ka^2}{2R^3}\right)^2 \left(\frac{\sum_{i=1}^{N} [\Delta b_i]^2 (b_i)^2}{N} \right) \text{ (Monte Carlo)} \qquad [A.22]$$

To further simplify Eqn. [A.22], we note:

$$\sigma_{WF}^2 = \frac{4}{6}\left(\frac{ka^2}{2R^3}\right)^2 \left(\frac{\sum_{i=1}^{N} [\Delta b_i]^2 (b_i)^2}{N} \right)$$

$$= \frac{4}{6}\left(\frac{ka^2}{2R^3}\right)^2 \left(\frac{1}{N}\right) \left(n_1 b_1^2 \frac{\sum_{i=1}^{n_1} [\Delta b_i]^2}{n_1} + n_2 b_2^2 \frac{\sum_{i=1}^{n_2} [\Delta b_i]^2}{n_2} + \ldots + n_{last\_ring} b_{last\_ring}^2 \frac{\sum_{i=1}^{n_{last\_ring}} [\Delta b_i]^2}{n_{last\_ring}} \right)$$

$$= \frac{4}{6}\left(\frac{ka^2}{2R^3}\right)^2 \left(\frac{\sigma_{\Delta b}^2}{N}\right) \left[n_1 b_1^2 + n_2 b_2^2 + \ldots + n_{last\_ring} b_{last\_ring}^2 \right]$$

$$= \frac{4}{6}\left(\frac{ka^2}{2R^3}\right)^2 \left(\frac{\sigma_{\Delta b}^2}{N}\right) \sum_{j=1}^{M} (6j) \left(\frac{\sqrt{3}a}{2} 2j\right)^2$$

$$= \frac{3}{4}\left(\frac{k^2 M^2 (M+1)^2}{N}\right)\left(\frac{a}{R}\right)^6 \sigma_{\Delta b}^2$$

or

$$\sigma_{WF}^2 = \frac{3}{4}\left(\frac{k^2 M^2 (M+1)^2}{N}\right)\left(\frac{a}{R}\right)^6 \sigma_{\Delta b}^2 \qquad [A.23]$$

where

- k: conic constant of the primary mirror
- N: total number of segments
- M: number of rings in the primary
- R: radius of curvature of the parent mirror
- a: radius of the segment (point-to-point dimension for a hexagonal segment)
- $\sigma_{\Delta b}$: standard deviation Gaussian random variable Δb (zero mean)

Rotation Error:

Using earlier expression for the aspherical departure for each off-axis segments, we find the effect of rotation misalignment as the wavefront error::

$$\Delta w_i = \left[\frac{\partial}{\partial\theta}\left(C_{40}(b,\theta) + C_{31}(b,\theta) + C_{22}(b,\theta) + C_{33}(b,\theta) + C_{44}(b,\theta)\right)\right]\Delta\theta_i \qquad \text{[A.24]}$$

where

$$C_{40}(\rho) := \left(\frac{K}{8\cdot R^3}\right)\cdot\rho^4$$

$$C_{31}(\rho,\theta) := \left(4\cdot b_i\cdot\frac{K}{8\cdot R^3}\right)\cdot\rho^3\cdot\cos(\theta)$$

$$C_{22}(\rho,\theta) := \left(2\cdot b_i^2\cdot\frac{K}{8\cdot R^3}\right)\cdot\rho^2\cdot\cos(2\cdot\theta)$$

$$C_{33}(\rho,\theta) := \left[2\cdot b_i^3\cdot\frac{\left[(K+1)^2 - 1\right]}{16\cdot R^5}\right]\cdot\rho^3\cdot\cos(3\cdot\theta)$$

$$C_{44}(\rho,\theta) := \left[10\cdot b_i^4\cdot\frac{\left[(K+1)^3 - 1\right]}{128\cdot R^7}\right]\cdot\rho^4\cdot\cos(4\cdot\theta)$$

and

- Δb_i: translation error [mm] of the ith segment. Drawn from a zero-mean Gaussian random variable with standard deviation of $\sigma_{\Delta b}$.
- b_i: off-axis distance of the ith segment
- (ρ,θ): local coordinates of the segment
- R: radius of curvature of the parent mirror
- N: total number of segments
- a: radius of the segment (point-to-point dimension for a hexagonal segment)
- k: conic constant of the primary mirror

To simplify Eqn.[A.24], we first evaluate the derivative:

$$\Delta w_i = \left[\tilde{C}_{40}(b,\theta) + \tilde{C}_{31}(b,\theta) + \tilde{C}_{22}(b,\theta) + \tilde{C}_{33}(b,\theta) + \tilde{C}_{44}(b,\theta)\right]\Delta\theta_i$$

where

$$\tilde{C}_{40(b,\theta)} = 0 \qquad [A.25]$$

$$\tilde{C}_{31(b,\theta)} = \left(\frac{k}{2}\right)\left(\frac{b_i}{R^3}\right)\left\{-\rho^3 \sin(\theta)\right\} \qquad [A.26]$$

$$\tilde{C}_{22(b,\theta)} = \left(\frac{k}{2}\right)\left(\frac{b_i^2}{R^3}\right)\left\{-2\rho^2 \sin(2\theta)\right\}$$

$$= (-k)\left(\frac{b_i^2}{R^3}\right)\left\{\rho^2 \sin(2\theta)\right\} \qquad [A.27]$$

$$\tilde{C}_{33(b,\theta)} = \left(\frac{1}{8}\right)\left(\frac{(k+1)^2-1}{R^5}\right) b_i^3 \left\{-3\rho^3 \sin(3\theta)\right\}$$

$$= \left\{\left(-\frac{3\left[(k+1)^2-1\right]}{8}\right)\left(\frac{b_i^2}{R^3}\right)\left(\frac{b_i}{R^2}\right)\right\}\left\{\rho^3 \sin(3\theta)\right\} \qquad [A.28]$$

$$\tilde{C}_{44(b,\theta)} = \left(\frac{5}{64}\right)\left(\frac{(k+1)^2-1}{R^7}\right) b_i^4 \left\{-4\rho^4 \sin(4\theta)\right\}$$

$$= \left\{\left(\frac{-5\left((k+1)^3-1\right)}{16}\right)\left(\frac{b_i^2}{R^3}\right)\left(\frac{b_i}{R^2}\right)^2\right\}\left\{\rho^4 \sin(4\theta)\right\} \qquad [A.29]$$

The following magnitude-comparisons show that the dominating term is the astigmatism-like $\check{C}_{22}(b,\theta)$:

$\check{C}_{31}(b,\theta)$ & $\check{C}_{22}(b,\theta)$: $\check{C}_{22}(b,\theta)$ dominates for any segments with off-axis distance $b_i \geq 1$m. For a primary mirror with segment size of 2-m, this means all segments and for segment size of ~ 1-m, this means for all segments but the 1st ring. The 1st ring of segments is most probably removed anyway due to the obscuration (from the secondary mirror).

$\check{C}_{33}(b,\theta)$ & $\check{C}_{22}(b,\theta)$: $\check{C}_{22}(b,\theta)$ dominates since the magnitude of $\check{C}_{33}(b,\theta)$ has a factor (b_i/R^2). For a 30-m f/1 primary, this amounts to ~4E-3 or $\check{C}_{33}(b,\theta)$ is more than three magnitude smaller than $\check{C}_{22}(b,\theta)$

$\check{C}_{44}(b,\theta)$ & $\check{C}_{22}(b,\theta)$: $\check{C}_{22}(b,\theta)$ dominates since the magnitude of $\check{C}_{44}(b,\theta)$ has a factor $(b_i/R^2)^2$. For a 30-m f/1 primary, this amounts to ~1.7E-5 or $\check{C}_{44}(b,\theta)$ is about five magnitude smaller than $\check{C}_{22}(b,\theta)$

Rotation Error (cont.):

Following above simplification, we can now have

$$\Delta w_i = 2\Delta\theta_i \left(\frac{\partial\left(c_{22_i}\rho^2\cos 2\theta\right)}{\partial\Delta\theta} \right) \qquad [A.30]$$

$$= 2\Delta\theta_i \left(\frac{kb_i^2 a^2}{4R^3} \right) 2\rho^2\cos 2\theta$$

$$\triangleq 4\Delta\theta_i \left(c_{22_i}\right)\rho^2\cos 2\theta$$

where

- $\Delta\theta_i$: rotation error [rad] of the ith segment. Drawn from a zero-mean Gaussian random variable with standard deviation of $\sigma_{\Delta\theta}$. All others in [m].
- b_i: off-axis distance of the ith segment
- (ρ,θ): local coordinates of the segment
- R: radius of curvature of the parent mirror
- N: total number of segments
- a: diameter of the segment (point-to-point dimension for a hexagonal segment)
- k: conic constant of the primary mirror

$$\overline{\Delta W^2} = \frac{\sum_{i=1}^{N} \iint da_i (\Delta w_i)^2}{N\pi a^2}$$

$$= \frac{4^2 \sum_{i=1}^{N} \iint da_i \left[\Delta\theta_i c_{22_i} \rho^2 \cos 2\theta\right]^2}{N\pi a^2}$$

$$= \frac{4^2 \left(\sum_{i=1}^{N} \left[\Delta\theta_i c_{22_i}\right]^2\right)\left(\frac{\pi a^2}{6}\right)}{N\pi a^2}$$

$$= \frac{4^2 \left(\frac{ka^2}{4R^3}\right)^2 \left(\sum_{i=1}^{N} [\Delta\theta_i]^2 (b_i)^4\right)\left(\frac{\pi a^2}{6}\right)}{N\pi a^2}$$

$$= \frac{4^2}{6}\left(\frac{ka^2}{4R^3}\right)^2 \left(\frac{\sum_{i=1}^{N} [\Delta\theta_i]^2 (b_i)^4}{N}\right)$$

$$\left(\overline{\Delta W}\right)^2 = \left[\frac{\sum_{i=1}^{N} \iint da_i \, \Delta w_i}{N\pi a^2}\right]^2$$

$$= \left[\frac{2\sum_{i=1}^{N} \iint da_i \, (\Delta b_i)\left(\dot{c}_{22_i}\right)\left(\rho^2 \cos 2\theta\right)}{N\pi a^2}\right]^2$$

$$= 0$$

$$\sigma_{WF}^2 \triangleq \overline{\Delta W^2} - \left(\overline{\Delta W}\right)^2$$

$$= \frac{4^2}{6}\left(\frac{ka^2}{4R^3}\right)^2 \left(\frac{\sum_{i=1}^{N} [\Delta\theta_i]^2 (b_i)^4}{N}\right) \text{ (Monte Carlo)} \qquad [A.31]$$

To further simplify Eqn.[A.31], we note:

$$\sigma_{WF}^2 \triangleq \overline{\Delta W^2} - \left(\overline{\Delta W}\right)^2$$

$$= \overline{\Delta W^2}$$

$$= \frac{4^2}{6}\left(\frac{ka^2}{4R^3}\right)^2 \left(\frac{\sum_{i=1}^{N}[\Delta\theta_i]^2 (b_i)^4}{N}\right)$$

$$= \frac{4^2}{6}\left(\frac{ka^2}{4R^3}\right)^2 \left(\frac{1}{N}\right)\left(n_1 b_1^4 \frac{\sum_{i=1}^{n_1}[\Delta\theta_i]^2}{n_1} + n_2 b_2^4 \frac{\sum_{i=1}^{n_2}[\Delta\theta_i]^2}{n_2} + \ldots + n_{last\_ring} b_{last\_ring}^4 \frac{\sum_{i=1}^{n_{last\_ring}}[\Delta\theta_i]^2}{n_{last\_ring}}\right)$$

$$= \frac{4^2}{6}\left(\frac{ka^2}{4R^3}\right)^2 \left(\frac{\sigma_{\Delta\theta}^2}{N}\right)\left[n_1 b_1^4 + n_2 b_2^4 + \ldots + n_{last\_ring} b_{last\_ring}^4\right]$$

$$= \frac{4^2}{6}\left(\frac{ka^2}{4R^3}\right)^2 \left(\frac{\sigma_{\Delta\theta}^2}{N}\right)\sum_{j=1}^{M}(6j)\left(\frac{\sqrt{3}a}{2}2j\right)^4$$

$$= \left\{\left(\frac{9}{N}\right)\left(\frac{a}{R}\right)^6 (ka)^2 \sum_{j=1}^{M} j^5\right\}\sigma_{\Delta\theta}^2$$

or

$$\sigma_{WF}^2 = \left\{\left(\frac{9}{N}\right)\left(\frac{a}{R}\right)^6 (ka)^2 \sum_{j=1}^{M} j^5\right\}\sigma_{\Delta\theta}^2 \qquad \text{[A.32]}$$

where

- k: conic constant of the primary mirror
- N: total number of segments
- M: number of rings in the primary
- R: radius of curvature of the parent mirror
- a: radius of the segment (point-to-point dimension for a hexagonal segment)
- $\sigma_{\Delta\theta}$: standard deviation Gaussian random variable $\Delta\theta$ (zero mean)

APPENDIX B

The IDL Algorithm For Selecting The Optimum Radius Of Curvature (ROC) For The Reference Surface

```
;*************************************************************************
;*
;* roc_selection
;*
 ;*Written by Feenix Y. Pan  01/17/01
;* Last Update: 07/23/02
;*
;* roc_selection is an IDL algorithm that computes the optimal radius of curvature for
;* testing  smaller mirror segments from a larger primary mirror.
;*
;*************************************************************************


PRO roc_selection

        CD, 'c:\documents and settings\feenix\my documents\adm res\idl'; Set working directory
        !P.MULTI=[0,2,1,1]
        ;WINDOW, 0, XSIZE=410, YSIZE=950;FOR 3 PLOTS ON LAPTOP
        WINDOW, 0, XSIZE=1800/1.3, YSIZE=700/1.3; FOR 2 PLOTS ON MONITOR

        DEVICE, DECOMPOSED = 0
        LOADCT, 0
        !P.BACKGROUND=255B
        !P.COLOR=0

;*****************************************************
;* OPTICAL SYSTEM SETUP
;*****************************************************

        COMMON SHARE1, index, sz, sag, ex, ey,z, XMIN, XMAX
        XMIN=-25E-3
        XMAX=25E-3
        pixel=3; NUMBER OF PIXELS PER SAGMENT OF RADIUS 1M
        sz=pixel*2+1

        PARENT=15.279210; RADIUS OF PARENT MIRROR IN [M]
        OFF_AXIS_STEP=15;[M]
        ;OFF-AXIS DISTANCE --PARAMETER B
```

```
OFF_AXIS=INDGEN(ROUND(PARENT/OFF_AXIS_STEP)+
(ROUND(PARENT/OFF_AXIS_STEP) EQ 1))*OFF_AXIS_STEP; 2ND PART IS IF ONLY
ONE OFF_AXIS PIECE

; for plot generation only
off_axis=DOUBLE([0,15.279210])
n_off_axis=N_ELEMENTS(off_axis);NUMBER OF DIFFERENT ROC_SPHERE
dr=0.02; in [meters]
n_roc_sphere=500


DRMIN=n_roc_sphere/2*(-dr);for plotting
DRMAX=n_roc_sphere/2*dr+1*dr

;DR_RANGE=6
;n_roc_sphere=ROUND(DR_range/dr)

;delta_r_axis=rotate(LINDGEN(2*n_roc_sphere+1,2*n_roc_sphere+1)/(2*n_roc_sphere+1)-
n_roc_sphere,3)

        ;delta_r_axis=1.0*delta_r_axis[*,0]*dr
        ;PRINT, delta_r_axis
        ;stop
        ;FOR PLOTTING PURPOSE
        ;DRMIN=MIN(delta_r_axis)
        ;DRMAX=MAX(delta_r_axis)


;RADIUS OF THE SEGMENTS IN [M]
;SIZE_OF_SEGMENT=[0.5, 1.0, 2.0,3.0, 3.5, 4.0]
;size_of_segment=0.5*INDGEN(50)
;stop
SIZE_OF_SEGMENT=[1.340/2.];RADIUS IN [M]
;SIZE_OF_SEGMENT=0.5*INDGEN(10)
n_sz_of_segment=N_ELEMENTS(SIZE_OF_SEGMENT)

intersect_x=DBLARR(n_roc_sphere, n_off_axis)
intersect_y=DBLARR(n_roc_sphere, n_off_axis)
ref_sphere_radius=DBLARR(n_sz_of_segment, n_off_axis)
location=INTARR(n_off_axis)

FOR P=0,n_sz_of_segment-1 DO BEGIN

        segment_size=SIZE_OF_SEGMENT[p]
        ;segement_size=DOUBLE(1.890/2)



        ;ASPHERE PARAMETERS
        ;PARAMETERS=[DOUBLE(33.0),DOUBLE(-1.002250),DOUBLE(0.0),
        DOUBLE(0.0) ,DOUBLE(0.0),DOUBLE(0.0)]
        PARAMETERS=[DOUBLE(60.0),  DOUBLE(-1.0),  DOUBLE(0.0),  DOUBLE(0.0)
        ,DOUBLE(0.0),DOUBLE(0.0)]
```

```
;*******************
;*DEFIND SPHERE
;*******************
K_SPHERE=0.0
;OPTIM=DOUBLE(33.205)
OPTIM=DOUBLE(60.9503)
ROC_SPHERE=OPTIM


;*************************
;* COORDINATE SYSTEM:ALL UNITS ARE IN METERS
;*************************
;CREAT THE CIRCULAR PUPIL IN POLAR AND CARTESIAN
x=rotate(LINDGEN(2*pixel+1,2*pixel+1)/(2*pixel+1)-pixel,3)
x=DOUBLE(1.0)*x/pixel; NORMALIZED
x=x*DOUBLE(segment_size);  IN REAL COORDINATE SYSTEM

y=pixel-LINDGEN(2*pixel+1,2*pixel+1)/(2*pixel+1)
y=DOUBLE(1.0)*y/pixel
y=y*DOUBLE(segment_size); IN REAL COORDINATE SYSTEM

r=SQRT(x^2+y^2)
index=WHERE(r GT segment_size)

r0=r
x0=x
y0=y
index0=index

;*******************
;*DEFINE THE ASPHERE
;*******************
ROC=DOUBLE(PARAMETERS[0])
K=DOUBLE(PARAMETERS[1])
A=DOUBLE(PARAMETERS[2])
B=DOUBLE(PARAMETERS[3])
C=DOUBLE(PARAMETERS[4])
D=DOUBLE(PARAMETERS[5])

;*******************
;
;* FIND epsilon_max for each fixed ROC_SPHERE
;
;*******************

;DECLEAR VARIABLES -- m=number of segments and n_roc_sphere=number of
ROC_SPHERE choices
xdata=DBLARR(n_roc_sphere,  n_off_axis)  ;for  each  segments  and  for  each
ROC_SPHERE choices
ydata=DBLARR(n_roc_sphere, n_off_axis)

;VARIABLE DECLARIATIONS FOR SEGMENTATION LOOP
x_new=DBLARR(sz,sz)
```

```
temp=DBLARR(sz,sz)
sag=DBLARR(sz,n_off_axis*sz)
sag_new=DBLARR(sz, n_off_axis*sz)
slope=DBLARR(sz, n_off_axis*sz)
tilt=DBLARR(sz, n_off_axis*sz)

w=DBLARR(sz,n_off_axis*sz)
ex=DBLARR(sz,n_off_axis*sz)
ey=DBLARR(sz,n_off_axis*sz)
z=DBLARR(sz,n_off_axis*sz)
ex_max=DBLARR(n_off_axis)
ey_max=DBLARR(n_off_axis)
ex_min=DBLARR(n_off_axis)
ey_min=DBLARR(n_off_axis)
mech_ctr_slope=DBLARR(n_off_axis)
delta_r_axis=DBLARR(n_roc_sphere)

FOR j=0, n_roc_sphere-1 DO BEGIN

        ;ZERO TO THE CENTER COORD FOR THE J-LOOP
        x=x0
         y=y0
        r=SQRT(x^2+y^2)
        index=index0

        ;TAKE delta_r ON BOTH SIDES OF OPTIM VALUE
        ;ROC_SPHERE=optim+delta_r_axis[j]
        ROC_SPHERE=OPTIM+dr*(j-(n_roc_sphere/2))
        ;PRINT, 'CURRENT ROC_SPHERE IS', ROC_SPHERE

        delta_r_axis[j]=dr*(j-(n_roc_sphere/2))
        ;TILT TO SEPERATE THE ORDERS
        OFFSET=0.0

        sphere=OFFSET+((r^2/ROC_SPHERE))/(DOUBLE(1.0)$
          +SQRT(1.0-(K_SPHERE+1.0)*(1./ROC_SPHERE)^2.*r^2.))

        ;PRINT, 'J IS THIS...',J, 'SPHRE IS'
        ;PRINT, SPHERE


        ;*************************************************************
        ;* FIND epsilon_max for each sagment with one fixed ROC_SPHERE
        ;*************************************************************

        ;NUMBER OF COLOUMS
        sz=2*pixel+1

        ;FOR EACH OFF-AXIS PIECE DO THIS
        ;TEST_SLOPE=DOUBLE([0.0, 2.816,5.639, 8.475, 4.881, 7.468,7.468])

        FOR i=0, n_off_axis-1 DO BEGIN
```

```
;ZERO TO THE CENTER COORD.
x=x0
 x=x + off_axis[i]
y=y0
r=SQRT(x^2+y^2)
index=index0

;SETTING UP COUNTING VAR'S FOR ROWS
row_s =sz*i
row_e= sz*i+(sz-1)
center=pixel+sz*i
;VAR NEEDED TO ZERO OUT-RADIUS PUPIL DATA
index=index0+i*(sz*sz)
;PRINT, 'index is ', index


;DEFINITIONS
                                        sag[*,
row_s:row_e]=((x^2+y^2)/ROC)/(DOUBLE(1.0)+SQRT(1.0-
(K+1.0)*(1./ROC)^2.*(x^2+y^2)))$

 +A*(x^2+y^2)^2.+B*(x^2+y^2)^3.+C*(x^2+y^2)^4.+D*(x^2+y^2)^5

;ADD TILT TO MIN. RMS SPOT SIZE-- SEE PG 57 OF THE
NOTEBOOK
slope[*,row_s:row_e]=DERIV(x,sag[*, row_s:row_e])
;TILT IS ADDED WRT EACH PART'S MECHANICAL CTR
mech_ctr_slope[i]=slope[pixel,center ]
;mech_ctr_slope[i]=TEST_SLOPE[I]*!PI/180.
;y=kx+b with b=sag[m_ctr]-slope[m_ctr]*x[m_ctr]
 tilt[*,row_s:row_e]=mech_ctr_slope[i]*x $
            + (sag[pixel, center]-mech_ctr_slope[i]*x[pixel,pixel])
;PRINT, 'the cente is at'
;PRINT, x[pixel, pixel]
sag[*,row_s:row_e]=sag[*,row_s:row_e]-tilt[*,row_s:row_e]
;PRINT, 'TILT IS '
;PRINT, TILT[*,ROW_S: ROW_E]
;PRINT, 'AFTER TILT SAG IS'
;PRINT, sag[*,row_s:row_e]

;PERFORMING COORD. TRANFORMATION (ROTATION)-- SEE
PG58 OF NOTEBOOK
x_new=x0/COS(ATAN(slope[pixel,
center]))+sag[*,row_s:row_e]*SIN(ATAN(slope[pixel, center]))
;sag[*,row_s:row_e]=sag[*,row_s:row_e]*COS(ATAN(slope[pixel,
center]))

sag_new[*,row_s:row_e]=sag[*,row_s:row_e]*COS(ATAN(slope[pix
el, center]))
;PRINT, 'x-new is '
;PRINT, x_new
;PRINT, 'sag_new is'
;PRINT, sag_new[*,row_s:row_e]
```

```
;CALL ROUTINE TO FIT sag_new TO x0
temp=sag_new[*,row_s:row_e]
sagTRans,sz,temp, x_new, x0,y0,data
;PRINT, 'DATA IS'
;PRINT, DATA

;PUT NEW SAG INTO SAG MATRIX
sag[*,row_s:row_e]=data
;PRINT, 'IN SIDE LOOP....DATA IS '
;PRINT, DATA

;PRINT, 'TRANSFROMED SAG IS ',sag_new[*,row_s:row_e]

;FIND RAY FAN BY DIFF WRT DIFFERENT X-AXES
;ex[*,row_s:row_e]=ROC_SPHERE*(DERIV(x0,sphere)-
DERIV(x_new,sag[*,row_s:row_e]) )
;PRINT, 'INSDIE LOOP AND SPHERE IS'
;PRINT, SPHERE
ex[*,row_s:row_e]=ROC_SPHERE*(DERIV(x0,(data-sphere)) )
;PRINT, 'INSIDE LOOP AND EX IS'
;PRINT, EX


ey[*,row_s:row_e]=ROC_SPHERE*(DERIV(ROTATE(y0,3),ROTAT
E((data-sphere),3)))

;ZERO ELEMENTS OUTSIDE OF THE PUPIL
ex(index)=0.0
ey(index)=0.0

;FIND THE MAX
ex_max[i]=MAX(ex[0:sz-1,row_s:row_e])
ey_max[i]=MAX(ey[0:sz-1,row_s:row_e])
ex_min[i]=MIN(ex[0:sz-1,row_s:row_e])
ey_min[i]=MIN(ey[0:sz-1,row_s:row_e])

;SPOT DIAGRAM
z[*,row_s:row_e]=SQRT(ex[*,row_s:row_e]^2+ey[*,row_s:row_e]^2)
;SET Z VALUES OUTSIDE OF THE RADIUS RANGE TO ZERO
z(index)=0.0
;PRINT, 'CURRENT I,j IS', I,j
;PRINT, 'CURRENT EX IS', EX_MIN[I]

;STORING EVERYTING INTO MATRIX-- colum is delta_r and row
is each segment piece
xdata[J,I]=ex_max[I]-ex_min[I]
ydata[J,I]=ey_max[I]-ey_min[I]

intersect_x[j,i]=ABS(xdata[j,i]-xdata[j,0])
```

```
                intersect_Y[j,i]=ABS(Ydata[j,i]-Ydata[j,0])

        ENDFOR; I-loop: number of segments loop


 ENDFOR; j-loop:ROC_sphere loop
 ;PRINT, XDATA
 ;PRINT, 'DELTA R IS'
 ;PRINT, delta_r_axis

 ;plot into a meta file for visio to convert
 mydevice=!D.NAME
 set_plot, 'METAFILE'
 DEVICE, FILE='Optimal_ROC071002.emf'


 TEXT=['S1_x', 'S14_x']
 @PLOT01
 N1=N_ELEMENTS(DELTA_R_AXIS) - 1
 PLOT,delta_r_axis+optim,xdata[*,0]*1E3/ROC_sphere,$
        XRANGE=[DRMIN+optim, (DRMAX)+optim+1], $
        YRANGE=[-MIN(XDATA)*1E3/ROC_sphere,
MAX(XDATA)*1E3/ROC_sphere],XTITLE='Test Plate ROC [M]',$; for plot!! unit IS
right 060602
        YTITLE='Slope Error [mrad]', PSYM=0

FOR Q=1,n_off_axis-1 DO

        OPLOT,delta_r_axis+optim,xdata[*,Q]*1E3/ROC_sphere,PSYM=0
FOR Q=0,n_off_axis-1 DO XYOUTS,

        DRmax+optim,XDATA[N1,Q]*1E3/ROC_sphere,TEXT[Q]
;PLOT FOR Y-DIRECTION
TEXT=['S1_y', 'S14_y']
@PLOT01
N1=N_ELEMENTS(DELTA_R_AXIS) - 2
PLOT,delta_r_axis+optim,ydata[*,0]*1e3/ROC_sphere,$
        XRANGE=[DRMIN+optim, (DRMAX)+optim+1], $
        YRANGE=[-MIN(yDATA)*1e3/ROC_sphere,
        MAX(yDATA)*1e3/ROC_sphere],XTITLE='Test Plate ROC [M]',$
  YTITLE='Slope Error [mrad]', PSYM=0
FOR Q=1,n_off_axis-1 DO
        OPLOT,delta_r_axis+optim,ydata[*,Q]*1E3/ROC_sphere,PSYM=0
FOR Q=0,n_off_axis-1 DO

        XYOUTS, DRmax+optim,XDATA[N1,Q]*1E3/ROC_sphere,TEXT[Q]

DEVICE, /CLOSE
SET_plot, mydevice
```

```
;*********************************************************
;FINDOUT THE LOCATION OF THE INTERSECTION
;*********************************************************
;same col has the same segment size 'a=const'
;same row has same "off-axis segment number': s0, s1, s2, etc
;PRINT, 'CURRENT INTERSECT_X'
;PRINT, INTERSECT_X

location_X=INTARR(n_off_axis)
location_Y=INTARR(n_off_axis)
;PRINT, 'CURRENT SEGMENT SIZE IS', size_of_segment[p]
FOR q=0, n_off_axis-1 DO begin
        ;print, 'for off-axis segment', q
        ;TEST=IS MATRIX INTERSECT_X EQUAL TO THE MIN VALUE ONLY
        AT ONE LOCATION?
        TEST_X=(N_elements(WHERE(       intersect_x[0:n_roc_sphere-1,q]       eq
        (MIN(intersect_x[0:n_roc_sphere-1,q])) )) eq 1)
        TEST_y=(N_elements(WHERE(       intersect_y[0:n_roc_sphere-1,q]       eq
        (MIN(intersect_y[0:n_roc_sphere-1,q])) )) eq 1)
        ;PRINT, 'TEST IS', TEST
        CASE TEST_x of
                0:
        location_x[q]=where(deriv(delta_r_axis,deriv(delta_r_axis,xdata[*,0]))       eq
        min(deriv(delta_r_axis,deriv(delta_r_axis,xdata[*,0]))))  ;IF 'TEST' IS FALSE
                1:
       location_x[q]=WHERE(DERIV(delta_r_axis,
        (DERIV(delta_r_axis,intersect_x[0:n_roc_sphere-1,q])))                  EQ
        MAX(DERIV(delta_r_axis,  (DERIV(delta_r_axis,intersect_x[0:n_roc_sphere-
        1,q]))))     )
        ENDCASE
                CASE TEST_y of
                0:
        location_y[q]=where(deriv(delta_r_axis,deriv(delta_r_axis,ydata[*,0]))       eq
        min(deriv(delta_r_axis,deriv(delta_r_axis,ydata[*,0]))))  ;IF 'TEST' IS FALSE
                1:      location_y[q]=WHERE(       DERIV(delta_r_axis,
        (DERIV(delta_r_axis,intersect_y[0:n_roc_sphere-1,q])))                  EQ
        MAX(DERIV(delta_r_axis,  (DERIV(delta_r_axis,intersect_y[0:n_roc_sphere-
        1,q]))))     )
       ENDCASE


ENDFOR; q-LOOP:LOCATION SEARCH


;PRINT,  'CURRENT  LOCATION  FOR  THIS  SEG  SIZE  OF  ',
SIZE_OF_SEGMENT[P],' IS'
;PRINT, LOCATION

PRINT, 'ASPHERE DATA IS'
PRINT, 'K IS', K
PRINT, 'RADIUS OF CURVATURE IN [M] IS', ROC
PRINT, 'PARENT SIZE IN [M] IS', PARENT
PRINT, 'SEGMENT RADIUS IN [M] IS', SIZE_OF_SEGMENT
```

```
                PRINT, 'OFF-AXIS DISTANCES IN [M] FOR S0 AND S14 ARE', OFF_AXIS

                ref_sphere_radius[p,0:n_off_axis-1]=(TRANSPOSE(delta_r_axis[location_x])+OPTIM)
                PRINT, 'ALONG X-DIRECTION: REF_SPHERE_RADIUS IN [M] WHERE S0
                INTERSECT S13 IS'
                PRINT, optim, '+', delta_r_axis[location_x[1]],'=',ref_sphere_radius[1]
                PRINT, 'EPISILON X IN [M] AT THAT POINT IS'
                PRINT, XDATA[LOCATION_X[1],*]
                ref_sphere_radius[p,0:n_off_axis-1]=(TRANSPOSE(delta_r_axis[location_y])+OPTIM)
                PRINT, 'ALONG X-DIRECTION: REF_SPHERE_RADIUS IN [M] WHERE S0
                INTERSECT S4 IS'
                PRINT, optim, '+', delta_r_axis[location_y[1]],'=',ref_sphere_radius[1]
                PRINT, 'EPISILON Y IN [M] AT THAT POINT IS'
                PRINT, YDATA[LOCATION_Y[1], *]
                stop

        ENDFOR; p_loop: SEGMENT SIZE LOOP
        ;plot_roc_sphere,OFF_AXIS,SIZE_OF_SEGMENT,ref_sphere_radius, ROC, OPTIM
        ;SURFACE, ref_sphere_radius, SIZE_of_segment/ROC, off_axis/ROC


        STOP
END;MAIN

;TO PRODUCE THE CONTOUR PLOT OF PARAMETERS A (SIZE OF SEGMENTS), B (OFF AXIS
DISTANCE) AND
;OPTIM=REFERENCE SPHERE RADIUS -- ALL NORMALIZED BY THE ROC OF THE ASPHERE
PRO plot_roc_sphere,OFF_AXIS,SIZE_OF_SEGMENT,ref_sphere_radius, ROC, OPTIM

        PRINT, 'OFF AXIS ARE'
        PRINT, TRANSPOSE(OFF_AXIS)
        PRINT, 'SEGMENT SIZES ARE'
        PRINT, SIZE_OF_SEGMENT
        PRINT, 'RAW DELTA ROC_SPHERE DATA ARE'
        PRINT, ref_sphere_radius+OPTIM


        ;GENERATING AXES FOR THE PLOTTING
        M=N_ELEMENTS(OFF_AXIS)
        N=N_ELEMENTS(SIZE_OF_SEGMENT)

        x=MAKE_ARRAY(M,N); X-AXIS=OFF_AXIS DISTANCE (PARMETER B)
        FOR I=0, N-1 DO x[*,i]=OFF_AXIS
        y=MAKE_ARRAY(M,N); Y-AXIS=SIZE OF SEGMENT (PARAMETER A)
        FOR J=0, M-1 DO Y[j,*]=TRANSPOSE(SIZE_OF_SEGMENT)
        STOP
        ;PLOT_3DBOX, (ref_sphere_radius+OPTIM)/ROC, off_axis/ROC, size_of_segment/ROC

END
```

```
;*************************************
;*SUBROUTINES
;*************************************
PRO sagTrans,sz,temp, x_new, x0,y0,data

        data=DBLARR(sz, sz)
        SIGMA=0.0001
        FOR i=0,sz-1 DO BEGIN
                data[*,i]=SPLINE(X_NEW[*,i],TEMP[*,i], X0[*,i],SIGMA)
        ENDFOR

END

PRO sagment0,sag0,ex0, ey0,z0,w,w0
COMMON SHARE1, index, sz, sag, ex, ey,z, XMIN, XMAX
        sag0=sag(*,sz*0:sz*0+sz-1)
        w0=w(*,sz*0:sz*0+sz-1)
        ex0=ex(*,sz*0:sz*0+sz-1)
        ey0=ROTATE(ey(*,sz*0:sz*0+sz-1),3)
        ex0(index)=0.0
        ey0(index)=0.0
        z0=z(*,sz*0:sz*0+sz-1)

        ;CONTOUR, z0, TITLE='sag0'
        PLOT,   ex0,ey0,PSYM=1,TITLE='Spot   diagram   for   sag0',XRANGE=[XMIN,XMAX],
YRANGE=[XMIN, XMAX]
        WAIT, 5
END

PRO sagment1,sag1,ex1, ey1,z1,w,w1
COMMON SHARE1, index, sz, sag, ex, ey,z, XMIN, XMAX
        sag1=sag(*,sz*1:sz*1+sz-1)
        w1=w(*,sz*1:sz*1+sz-1)
        ex1=ex(*,sz*1:sz*1+sz-1)
        ey1=ROTATE(ey(*,sz*1:sz*1+sz-1),3)
        z1=z(*,sz*1:sz*1+sz-1)
        ;CONTOUR, z1, TITLE='sag1'
        PLOT,   ex1,ey1,PSYM=1,TITLE='spot   diagram   for   sag1',XRANGE=[XMIN,XMAX],
YRANGE=[XMIN, XMAX]
        WAIT, 5
END
PRO sagment2,sag2,ex2, ey2,z2,w,w2
COMMON SHARE1, index, sz, sag, ex, ey,z, XMIN, XMAX
        sag2=sag(*,sz*2:sz*2+sz-1)
        w2=w(*,sz*2:sz*2+sz-1)
        ex2=ex(*,sz*2:sz*2+sz-1)
        ey2=ROTATE(ey(*,sz*2:sz*2+sz-1),3)
        z2=z(*,sz*2:sz*2+sz-1)
        ;CONTOUR, z2,  TITLE='sag2'
        PLOT,   ex2,ey2,PSYM=1,TITLE='Spot   Diagram   for   sag2',XRANGE=[XMIN,XMAX],
YRANGE=[XMIN, XMAX]
        STOP
END
```

```
PRO sagment3,sag3,ex3, ey3,z3,w,w3
COMMON SHARE1, index, sz, sag, ex, ey,z, XMIN, XMAX
        sag3=sag(*,sz*3:sz*3+sz-1)
        w3=w(*,sz*3:sz*3+sz-1)
        ex3=ex(*,sz*3:sz*3+sz-1)
        ey3=ROTATE(ey(*,sz*3:sz*3+sz-1),3)
        z3=z(*,sz*3:sz*3+sz-1)
        ;CONTOUR, z3, TITLE='sag3'
        PLOT,  ex3,ey3,PSYM=1,TITLE='Spot  Diagram  for  sag3',XRANGE=[XMIN,XMAX],
YRANGE=[XMIN, XMAX]
        STOP

END
PRO sagment4,sag4,ex4, ey4,z4,w,w4
COMMON SHARE1, index, sz, sag, ex, ey,z, XMIN, XMAX
        sag4=sag(*,sz*4:sz*4+sz-1)
        w4=w(*,sz*4:sz*4+sz-1)
        ex4=ex(*,sz*4:sz*4+sz-1)
        ey4=ROTATE(ey(*,sz*4:sz*4+sz-1),3)
        z4=z(*,sz*4:sz*4+sz-1)
        ;CONTOUR, z4,  TITLE='sag4'
        PLOT,  ex4,ey4,PSYM=1,TITLE='Spot  Diagram  for  sag4',XRANGE=[XMIN,XMAX],
YRANGE=[XMIN, XMAX]
        STOP

END
PRO sagment5,sag5,ex5, ey5,z5,w,w5
COMMON SHARE1, index, sz, sag, ex, ey,z, XMIN, XMAX
        sag5=sag(*,sz*5:sz*5+sz-1)
        w5=w(*,sz*5:sz*5+sz-1)
        ex5=ex(*,sz*5:sz*5+sz-1)
        ey5=ROTATE(ey(*,sz*5:sz*5+sz-1),3)
        z5=z(*,sz*5:sz*5+sz-1)
        ;CONTOUR, z5,  TITLE='sag5'
        PLOT,  ex5,ey5,PSYM=1,TITLE='Spot  Diagram  for  sag5',XRANGE=[XMIN,XMAX],
YRANGE=[XMIN, XMAX]
        STOP

END
PRO sagment6,sag6,ex6, ey6,z6,w,w6
COMMON SHARE1, index, sz, sag, ex, ey,z, XMIN, XMAX
        sag6=sag(*,sz*6:sz*6+sz-1)
        w6=w(*,sz*6:sz*6+sz-1)
        ex6=ex(*,sz*6:sz*6+sz-1)
        ey6=ROTATE(ey(*,sz*6:sz*6+sz-1),3)
        z6=z(*,sz*6:sz*6+sz-1)
        ;CONTOUR, z6,  TITLE='sag6'
        PLOT,  ex6,ey6,PSYM=1,TITLE='Spot  Diagram  for  sag6',XRANGE=[XMIN,XMAX],
YRANGE=[XMIN, XMAX]
        STOP

END
```

APPENDIX C

Zemax Macro For Checking The Hologram Phase

```
! check_CGH_phase.zpl
!
! Written by Feenix Y. Pan 04/30/01
! Modified by FYP 05/21/01
! modified by FYP 06/25/01
!
! To varify the phase value at user specified pupil points
!
!************************************************************

TODAY_FILE$="\CGHphase071101_z.txt"

OUTPUT SCREEN
PRINT "Calculating phase...."
PRINT "STORED IN ", today_file$

z$="C:\Documents and Settings\feenix\My Documents\Research\Thesis Project\CGH
Phase"

FILTER$=z$+TODAY_FILE$
print filter$

!write the output to a file located at FILTER$
OUTPUT FILTER$



!-------------------------------------------------------------
PRINT "TRACING THE RAY AT THE PRIMARY WAVELENGTH"
!/*PRIMARY WAVELENTH (#0) IN MICRO*/

FORMAT .14
WAVL(1)=.6328000000000000

!get all the defined surfaces
```

```
n=NSUR()
!PRINT "NUMBER OF DEFINED SURF IS", N

!this number should be the same as in c-code...gives the location of (x,y)
rcgh=10.0

!final_v1_052101
!rcgh=4.69404026000


dx=5.0000
dy=dx
FOR x=-rcgh,rcgh, dx

        ymax=sqrt(rcgh*rcgh-x*x)
        !print "ymax is", ymax
        FOR y=-rcgh,rcgh,dy

        IF ((y>=-ymax) & (y<=ymax) )
        !print "y is", y

                !*TRace the ray at hx, hy, px, py

                RAYTRACE 0,0, x/rcgh,y/rcgh

                !print "phase at (x,y) = (", x, ",",y," ) is:    " (opth(5)-
opth(4))/.6328000000e-3
                PRINT "(",x ,",", y,") ",(opth(5)-opth(4))/.6328000000e-3
        ELSE
        ENDIF
        NEXT
NEXT

PRINT "IF NOT THE SAME, MOVE THE STOP TO CGH SURFACE!!"


OUTPUT SCREEN
PRINT "done!"
```

APPENDIX D

Zemax Code for Selection of the Illumination Radius of Curvature (ROC)

System/Prescription Data

File : C:\Documents and Settings\feenix\My Documents\Research\NOAO Project\CGH design\labsetup_sphere040802.ZMX
Title: Lens has no title.
Date : FRI SEP 20 2002

GENERAL LENS DATA:

Surfaces : 4
Stop : 1
System Aperture : Entrance Pupil Diameter = 1340
Glass Catalogs : Schott MISC
Ray Aiming : Off
Apodization :Uniform, factor = 0.00000E+000
Effective Focal Length : 12089.76 (in air at system temperature and pressure)
Effective Focal Length : 12089.76 (in image space)
Back Focal Length : 12068.7
Total Track : 12105
Image Space F/# : 9.022206
Paraxial Working F/# : 9.022206
Working F/# : 8.974774
Image Space NA : 0.05533391
Object Space NA : 0
Stop Radius : 670
Paraxial Image Height : 0
Paraxial Magnification : 0
Entrance Pupil Diameter : 1340
Entrance Pupil Position : 0
Exit Pupil Diameter : 1.#INF
Exit Pupil Position : 1e+010
Field Type : Angle in degrees
Maximum Field : 0
Primary Wave : 0.6328
Lens Units : Millimeters
Angular Magnification : 0

Fields : 1
Field Type: Angle in degrees

#	X-Value	Y-Value	Weight
1	0.000000	0.000000	1.000000

Vignetting Factors

#	VDX	VDY	VCX	VCY	VAN
1	0.000000	0.000000	0.000000	0.000000	0.000000

Wavelengths : 1
Units: Microns

#	Value	Weight
1	0.632800	1.000000

Table 1. Zemax prescription of the system used to optimize the illumiation radius of curvature.

Surf	Type	Comment	Radius	Thickness	Glass	Diameter	Conic
OBJ	STANDARD	collimated light	Infinity	Infinity	0.000000, 0	0	0
STO	STANDARD	GAP	60000	5		1340	0
2	STANDARD		60955.39	100	SILICA	1340	0
3	STANDARD		-7791.868	12000		1340	0
IMA	STANDARD		Infinity			3.984838	0

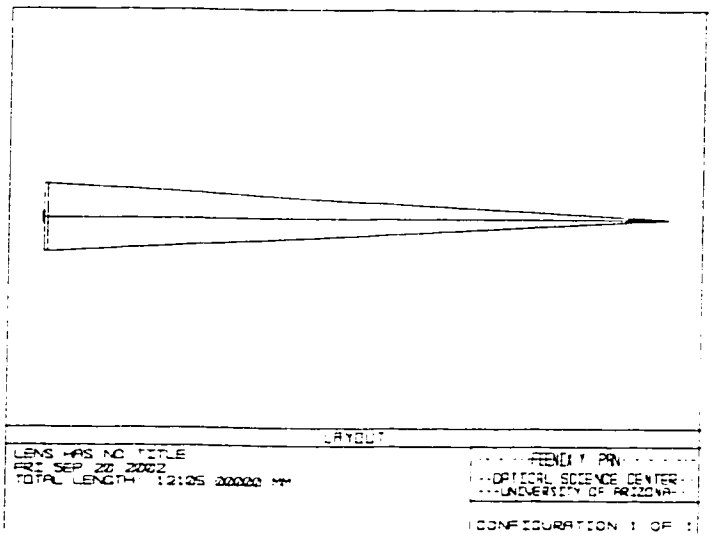

Figure 1 Zemax layout of the system described in Table 1

APPENDIX E

Summary Of The Holograms Designed For Testing An F/1 30-M Primary With 618 Segments With 1.33-M Point-To-Point Dimension

T1 CGH design

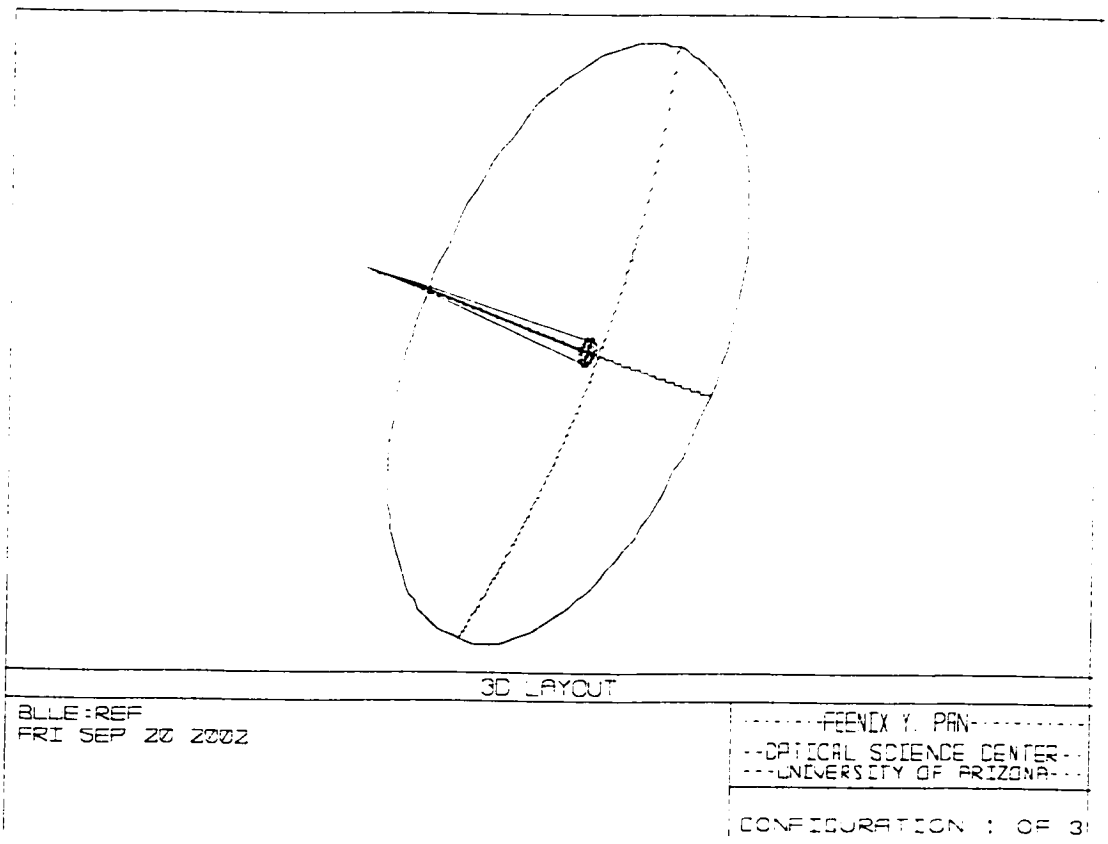

Figure 1 Layout of T1 test, showing parent primary.

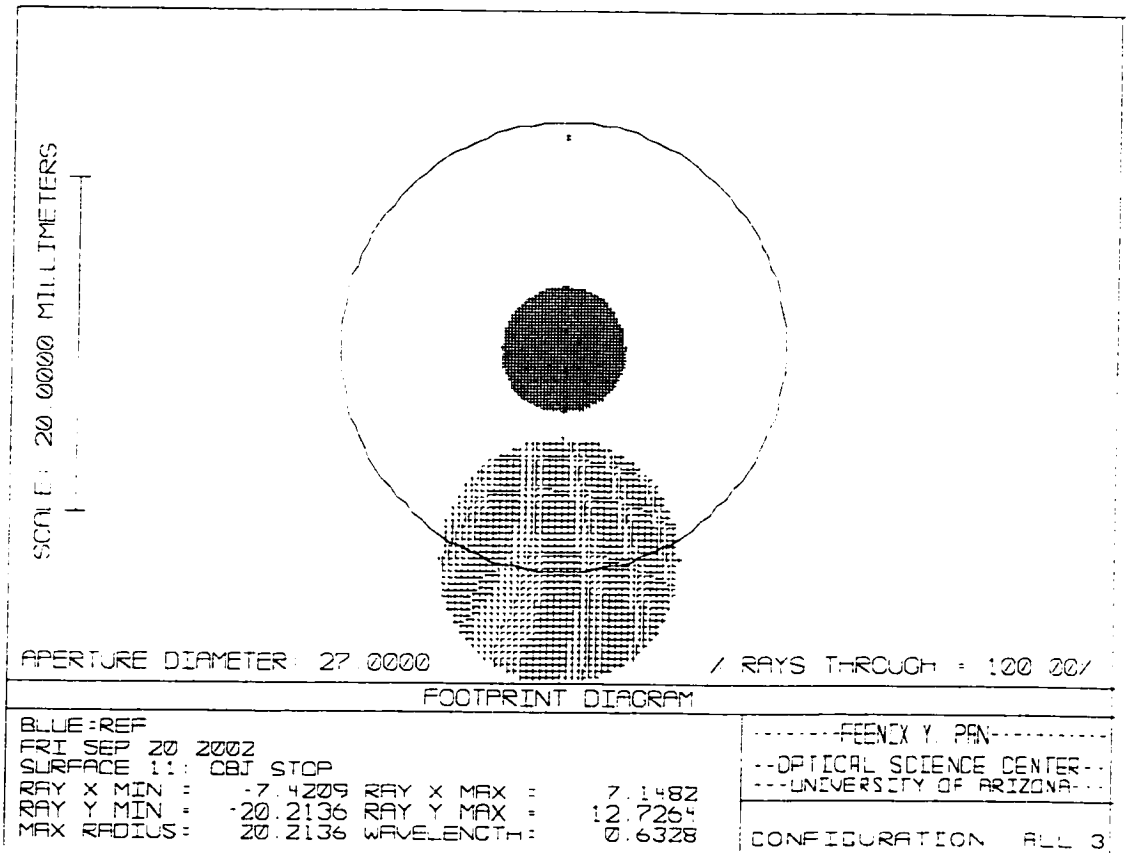

Figure 2 Appearance at the intermediate focus of the projection lens for the T1 hologram. The 2nd order is isolated from the 1st, but must be blocked. All orders other then 0 and 1 are blocked by the 50-mm aperture of the projection lens.

Table 1. The Zernike coefficients specifying the CGH for testing T1.

STORED IN \S1_zerns.txt
stored in\S1_zerns.txt
MAX TERM OF ZERN USED IS 37

NORMAL RADIUS IS 17.20

Zernike # 1 = 0.0000000000
Zernike # 2 = -0.9177405923
Zernike # 3 = -573.5882320367
Zernike # 4 = 55.496986117s5
Zernike # 5 = -0.0000387115
Zernike # 6 = -0.9346763574
Zernike # 7 = -0.9026334317
Zernike # 8 = -0.3269647982
Zernike # 9 = 0.0029013343
Zernike #10 = 0.0000315173
Zernike #11 = 0.1716170178
Zernike #12 = -0.0089349554
Zernike #13 = -0.0000283137
Zernike #14 = -0.0018793480
Zernike #15 = -0.0000023131
Zernike #16 = -0.0015687856
Zernike #17 = -0.0011964692
Zernike #18 = -0.0000210333
Zernike #19 = 0.0003314996
Zernike #20 = -0.0000321551
Zernike #21 = 0.0006761080
Zernike #22 = -0.0018532925
Zernike #23 = -0.0000091385
Zernike #24 = 0.0003076835
Zernike #25 = 0.0000014417
Zernike #26 = -0.0005445395
Zernike #27 = -0.0000362967
Zernike #28 = -0.0000154181
Zernike #29 = 0.0051634621
Zernike #30 = -0.0000477750
Zernike #31 = -0.0003776462
Zernike #32 = -0.0000175046
Zernike #33 = 0.0006661852
Zernike #34 = -0.0000165006
Zernike #35 = -0.0002280410
Zernike #36 = -0.0000208988
Zernike #37 = 0.0000348657

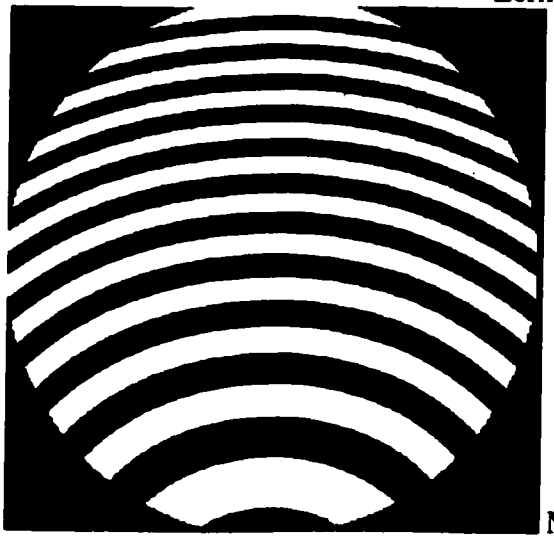

M=100x

T5 CGH design

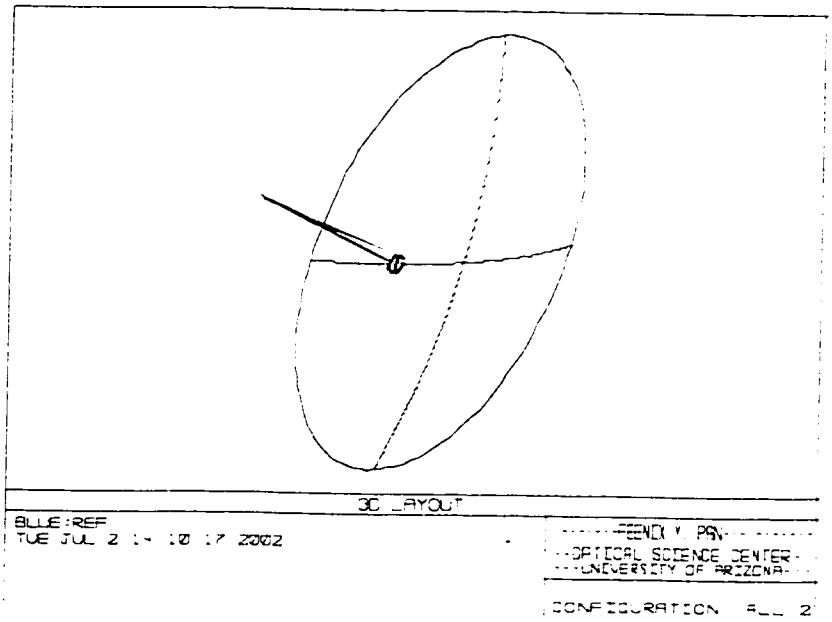

Figure 0-3 Layout of T5 test, showing parent primary.

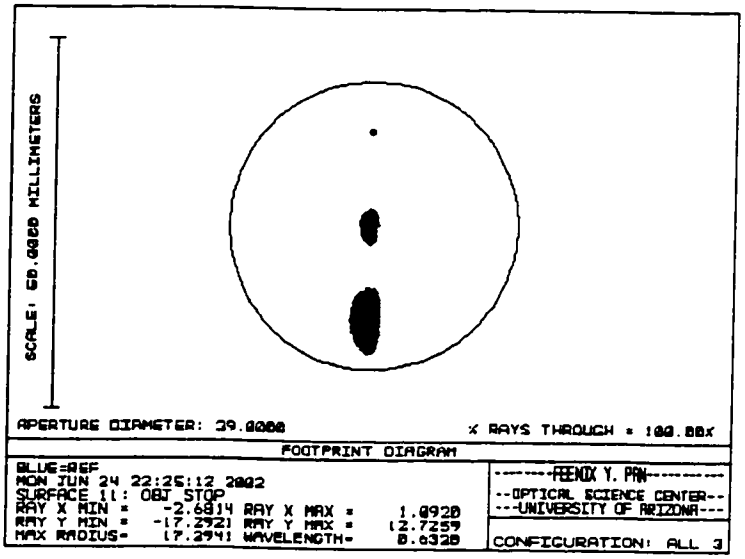

Figure 0-4 Appearance at the intermediate focus of the projection lens for the T5 hologram. The 2nd order is isolated from the 1st, but must be blocked. All orders other then 0 and 1 are blocked by the 50-mm aperture of the projection lens.

Table 2. The Zernike coefficients specifying the CGH for testing T5.

STORED IN \S5_zerns.txt
stored in\S5_zerns.txt
MAX TERM OF ZERN USED IS 37
NORMAL RADIUS IS 17.20

Zernike # 1 = 0.0000000000
Zernike # 2 = -5.3465889440
Zernike # 3 = -574.1664401950
Zernike # 4 = 9.2682298068
Zernike # 5 = -0.0022212161
Zernike # 6 = -33.3974920525
Zernike # 7 = -0.9052961428
Zernike # 8 = -1.9075895317
Zernike # 9 = 0.0010739350
Zernike #10 = 0.0131931135
Zernike #11 = 0.0162956187
Zernike #12 = -0.0918786794
Zernike #13 = -0.0001688691
Zernike #14 = -0.0028580720
Zernike #15 = 0.0000154444
Zernike #16 = -0.0093717972
Zernike #17 = -0.0011065403
Zernike #18 = -0.0001231728
Zernike #19 = 0.0003241494
Zernike #20 = 0.0000142404
Zernike #21 = 0.0006574374
Zernike #22 = -0.0010833622
Zernike #23 = 0.0000021019
Zernike #24 = 0.0004616137
Zernike #25 = 0.0000587124
Zernike #26 = -0.0005503913
Zernike #27 = 0.0000087255
Zernike #28 = 0.0000490709
Zernike #29 = 0.0052201008
Zernike #30 = -0.0000330061
Zernike #31 = -0.0003345798
Zernike #32 = -0.0000593920
Zernike #33 = 0.0006437138
Zernike #34 = 0.0000000000
Zernike #35 = 0.0000000000
Zernike #36 = 0.0000000000
Zernike #37 = 0.0000000000

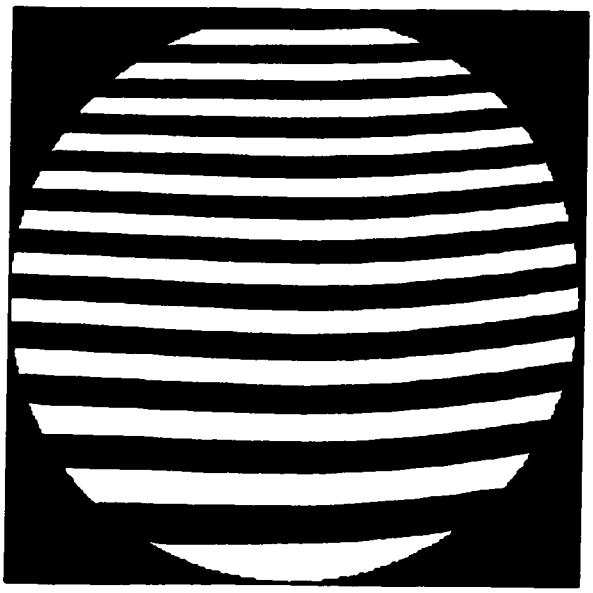

M=100x

T8 CGH design

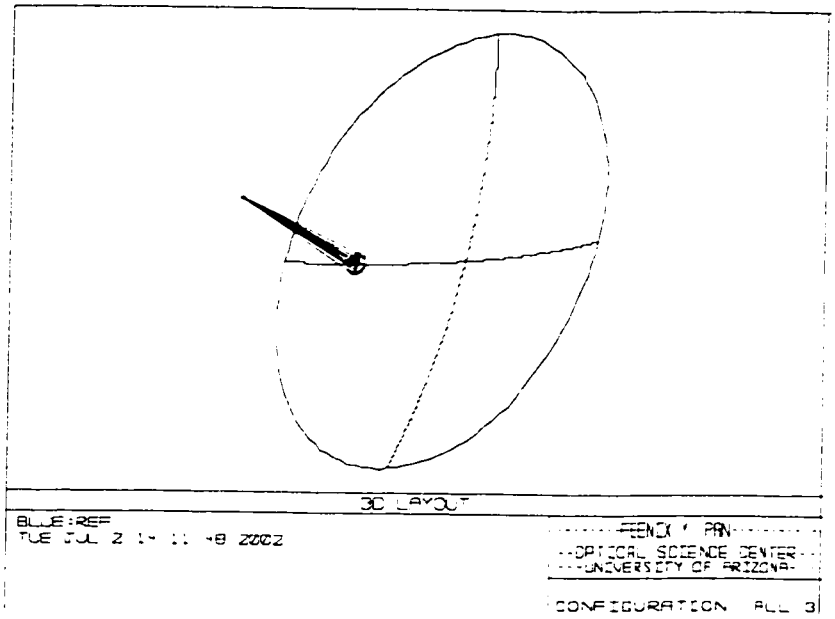

Figure 0-5 Layout of T8 test, showing parent primary.

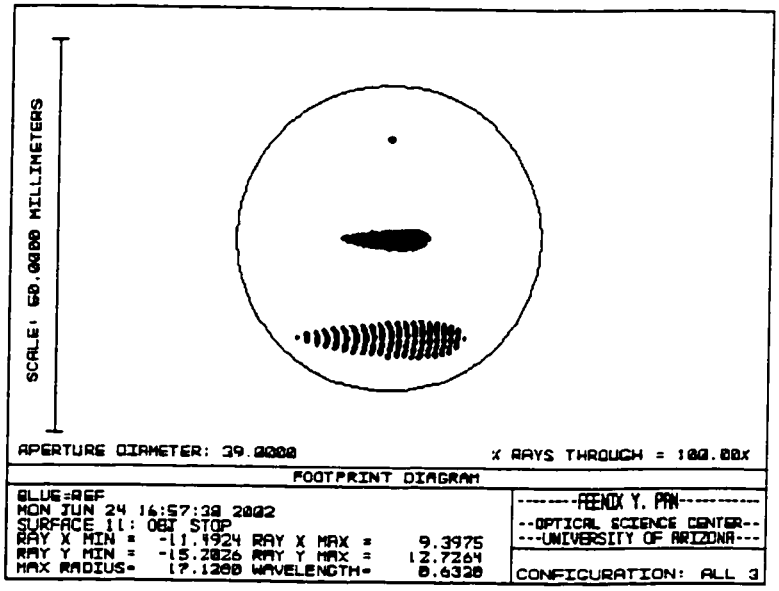

Figure 0-6 Appearance at the intermediate focus of the projection lens for the T8 hologram. The 2nd order is isolated from the 1st, but must be blocked. All orders other then 0 and 1 are blocked by the 50-mm aperture of the projection lens.

Table 3. The Zernike coefficients specifying the CGH for testing T8.
STORED IN \S8_zerns.txt
stored in\S8_zerns.txt
MAX TERM OF ZERN USED IS 37
NORMAL RADIUS IS 17.20

Zernike # 1 = 0.0000000000
Zernike # 2 = 0.0158158369
Zernike # 3 = -572.3489054128
Zernike # 4 = -26.9071510131
Zernike # 5 = -0.0045921578
Zernike # 6 = -58.6408320612
Zernike # 7 = -0.9050036473
Zernike # 8 = -2.4757460359
Zernike # 9 = -0.0001927577
Zernike #10 = 0.0317411032
Zernike #11 = -0.1075150359
Zernike #12 = -0.1577585797
Zernike #13 = -0.0002136560
Zernike #14 = -0.0038288406
Zernike #15 = 0.0000194760
Zernike #16 = -0.0119024688
Zernike #17 = -0.0017857955
Zernike #18 = 0.0001943988
Zernike #19 = 0.0003481587
Zernike #20 = 0.0002230864
Zernike #21 = 0.0006069800
Zernike #22 = -0.0015740254
Zernike #23 = 0.0000258095
Zernike #24 = -0.0001550209
Zernike #25 = 0.0000174877
Zernike #26 = -0.0008449205
Zernike #27 = 0.0000073887
Zernike #28 = 0.0001090043
Zernike #29 = 0.0060862131
Zernike #30 = 0.0000000000
Zernike #31 = 0.0000000000
Zernike #32 = 0.0000000000
Zernike #33 = 0.0000000000
Zernike #34 = 0.0000000000
Zernike #35 = 0.0000000000
Zernike #36 = 0.0000000000
Zernike #37 = 0.0000000000

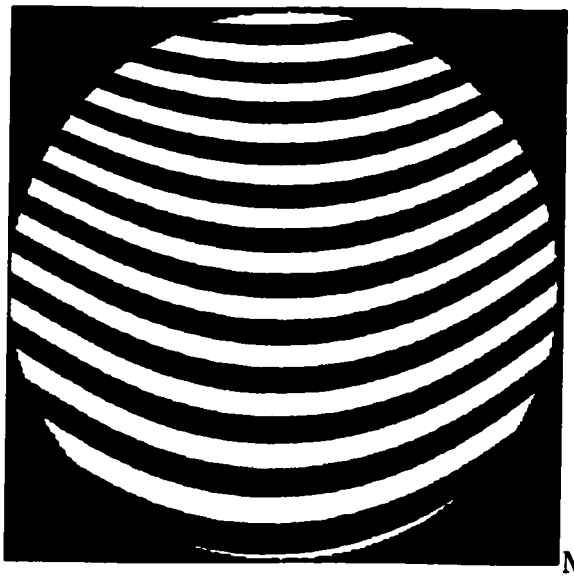

M=100x

T10 CGH design

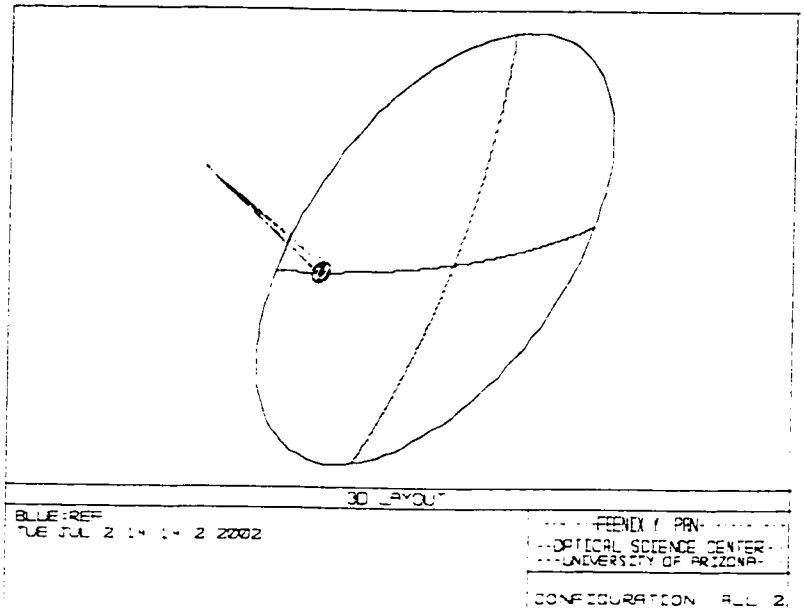

Figure 0-7 Layout of T10 test, showing parent primary.

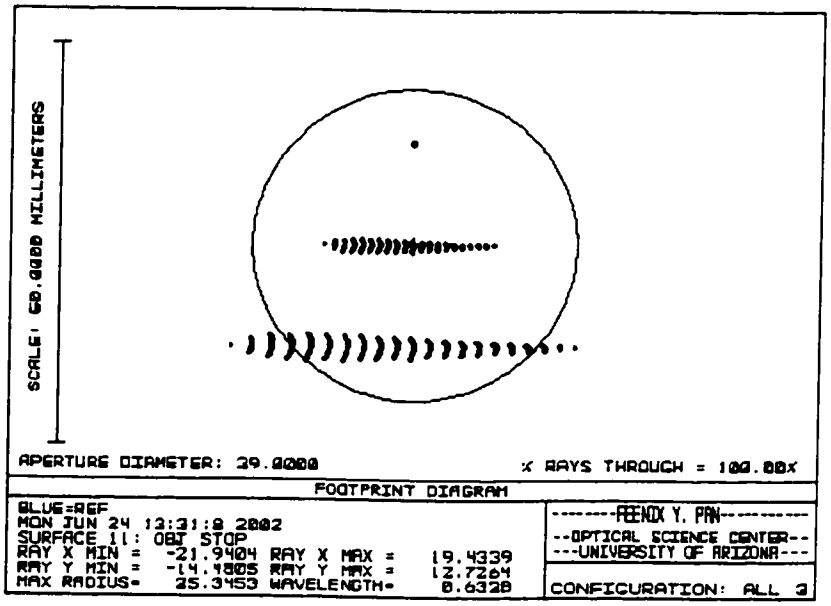

Figure 0-8 Appearance at the intermediate focus of the projection lens for the T10 hologram. The 2nd order is isolated from the 1st, but must be blocked. All orders other then 0 and 1 are blocked by the 50-mm aperture of the projection lens.

Table 4. The Zernike coefficients specifying the CGH for testing T10.

STORED IN \S10_zerns.txt
MAX TERM OF ZERN
USED IS 37
NORMAL RADIUS IS 17.20

Zernike # 1 = 0.0000000000
Zernike # 2 = 0.0000000000
Zernike # 3 = -572.3393204300
Zernike # 4 = -72.3699726529
Zernike # 5 = -0.0087756252
Zernike # 6 = -90.1426875166
Zernike # 7 = -0.8957849325
Zernike # 8 = -3.0029231187
Zernike # 9 = -0.0001660526
Zernike #10 = 0.0642469432
Zernike #11 = -0.2561638185
Zernike #12 = -0.2305721258
Zernike #13 = -0.0001873379
Zernike #14 = 0.0047491707
Zernike #15 = 0.0001298846
Zernike #16 = -0.0132831798
Zernike #17 = -0.0015854617
Zernike #18 = 0.0014838778
Zernike #19 = 0.0012774214
Zernike #20 = 0.0009526985
Zernike #21 = 0.0000761497
Zernike #22 = -0.0038170966
Zernike #23 = 0.0000257814
Zernike #24 = -0.0006626338
Zernike #25 = 0.0000168936
Zernike #26 = 0.0000000000
Zernike #27 = 0.0000000000
Zernike #28 = 0.0000000000
Zernike #29 = 0.0000000000
Zernike #30 = 0.0000000000
Zernike #31 = 0.0000000000
Zernike #32 = 0.0000000000
Zernike #33 = 0.0000000000
Zernike #34 = 0.0000000000
Zernike #35 = 0.0000000000
Zernike #36 = 0.0000000000
Zernike #37 = 0.0000000000

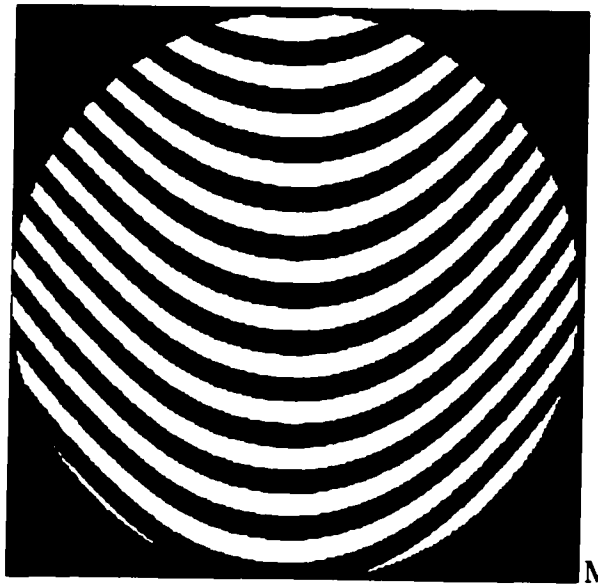

M=100x

APPENDIX F

Calibration Procedure[2]

1. Set up an interferometer to measure the concave reference sphere while it is in the same support as it will be for step #9 below. The interferometer will need to be 33 meters from the part so this is not trivial.
2. Fiducialize the concave reference sphere. Use appropriate fiducials to ultimately compare with the segment measurements.
3. Measure the reference sphere. Make multiple measurements using phase shifting interferometry to reduce noise in average to less than 0.001 λ rms.
4. Measure the absolute radius of curvature of the concave reference optic. This should be done to < 2 mm using a calibrated steel tape. Align to have less than 1 wave of power in the interferogram
5. Without changing the interferometer, measure a good sphere or a ball to determine errors in the reference sphere. Here again, use averaging to get the error down to 0.001 λ rms.
6. Determine surface of concave reference = map from #3 – map from #5.
7. Apply fiducials on the test plate that match those on the reference sphere.
8. Align the test plate and the top end optics as shown above to measure the convex test plate against the concave reference sphere. Line up fiducial marks on the reference circle on the test plate. Make a mechanical reference from the alignment marks.
9. Install the reference sphere (RS) and align it by mechanical reference and to get the return beam into the imager to see fringes.
10. Measure the test plate using phase shifting interferometry. Average maps together to reduce the noise to < 0.001 λ rms.
11. Using the fiducials, determine the surface figure of the test plate = map from #10 – map from #6.
12. With the fringes nulled, measure the gap between the test plate and the reference sphere to 0.05 mm absolute accuracy. Determine the absolute radius of the convex test plate as the radius from #4 minus the measured gap.
13. If necessary, you can repeat steps 1-11 with the reference sphere at several orientations. The error analysis does not assume that you do this, so you will improve on the absolute accuracy by making multiple measurements. Also, you reduce the chances of a mistake by making multiple measurements.

---

[2] developed by J. Burge

14. To calibrate the test plate refractive index errors, measure the reference sphere with CGH RSy and RSxy. This involves only changing the holograms, and changing the tilt on the reference sphere.
15. Remove the reference sphere and set the system up with the correct spacing for the segment measurements. Align the reference beam from the CGH into the stop.
16. Install a segment and its hologram and align it to match the reference beam, first using the return spot, then using the interference fringes.
17. Using phase shift interferometry, measure the segment. Average multiple maps to reduce the noise in the average to $< 0.001\ \lambda$ rms.
18. With the fringes nulled, measure the gap between the test plate and the segment to 0.05 mm. Determine the absolute radius of curvature of the segment = Design radius + TP radius offset + departure of the gap from nominal. For example, if the test plate is measured to be 33201 mm (1 mm too long) and the gap is measured at the edge to be 4.1 mm (0.5 mm to small), then the segment radius error would be 0.1 mm.
19. With the fringed nulled, measure the position of the segment relative to the mechanical reference that were set up in #8.
20. Using the fiducials on the test plate, determine the absolute figure in the segment = map from #17 – map from #11.

REFERENCES

CHAPTER 1

1. J. Neslon, T. Mast, G. Chanan, R. Dekany, "CELT conceptual Design Plan," http://celt.ucolick.org/reports_notes.html
2. T. Mast and J. Nelson, "The optical quality of the W.M. Keck Telescope," ESO conference on Progress in Telescope and Instrumentation Technologies, Ulrich Editor, April 1992
3. R. W. Sinnott and K. Nyren, "S & T's guide to the world largest telescopes," Sky and Telescopes, **86** (1), p27-32 (1993).
4. H. C. King, *The History of the Telescope*, Dover, New York (1955)
5. Dimitroff and Baker, *Telescope and Accessories*, Blakiston Co. Philadelphia (1945)
6. Kuiper and Middlehurst Editors, *Telescope*, University of Chicago Press, Chicago (1960)
7. Anderson et. al, "Stressed-lap polishing of 3.5-m f/1.5 and 1.8-m f/1.0 mirrors," Advanced Optical Manufacturing and Testing II, V. Doherty, editor, Proc. SPIE **1531**, p260-269 (1991)
8. J. Nelson, et. al, "California Extremely Large Telescope – conceptual design for a thirty meter telescope," CELT report No.34 (2002)
9. J. Nelson and et. al, "Conceptual Design for a 30-m telescope," CELT Report No. 34, (2002)
10. R. Gilmozzi, B. Delabre, P. Dierickx, N. Hubin, F. Koch, G. Monnet, M. Quattri, F. Rigaut, and R. Wilson, "The future of filled aperture telescopes: is a 100-m feasible?" Proc. SPIE **3352**, p778, (1998)
11. J. E. Nelson, "Design Concepts for the California Extremely Large Telescope (CELT)," Telescope Structures, Enclosures, Controls, Assembly and Commissioning, T. Sebring and T. Andersen editors, Proc. SPIE **4004** p282-289 (2000)
12. J. H. Burge, "Efficient testing of off-axis aspheres with test plate and computer-generated holograms," *Optical Manufacturing and Testing III*, H. Stahl Ed., Proc. SPIE **3782**, p348-357 (1999)
13. J. H. Burge and D. Anderson, "System and method for interferometric measurement of aspheric surfaces utilizing test plate and computer generated holograms," US patent 5,737,079

REFERENCES--CONTINUED

CHAPTER 2

14. G. A. Chanan and M. Troy, "Strehl Ratio and modulation transfer function for segmented mirror telescope as functions of segmented phase error, " App. Opt. **38**, p6642-6647 (1999)

15. G. A. Chanan and et al, "Phasing the mirror segments of the KECK telescopes: the broadband phasing algorithm," App. Opt. **37**, p140-155

16. G. Chanan, M. Troy and E. Sirko, "Phasing discontinuity senescing: a method for phasing segmented mirrors in the infrared," App. Opt. **38**, p704-713 (1999)

17. G. Chanan, M. Troy and C. Ohara, "Phasing the primary mirror segments for the Keck telescopes: A comparison of different techniques," *in Optical Design, Materials, Fabrication and Maintenance*, P. Dierickx, ed., Vol. **4003**, SPIE (2000)

18. G. Chanan, M. Troy and C. Ohara, "Phasing the primary mirror segments for the Keck telescopes: A comparison of different techniques," *in Optical Design, Materials, Fabrication and Maintenance*, P. Dierickx, ed., Vol. **4003**, SPIE (2000)

19. R. Shannon, J. Wyant (editors), *Applied Optics and Optical Engineering* Vol XI, (Academic Press, New York, 1992)

CHAPTER 3

20. http://www.diffraction.com

21. Goodman, "Introduction to Fourier Optics," McGraw-Hill, New York 1996

22. Burge, "Design study for measuring the GRANTECAN primary mirror segments using a test plate with computer generated holograms," private consulting report, October 1998

23. Sommargren, "Phasing shifting diffraction interferometry for measuring extreme ultraviolet optics," OSA Trend in Optics and Photonics Vol.4, Extreme Ultraviolet Lithography, Kubiak and Kania, Eds. (Optical Society of America, Washington, DC, 1996), pp108-112

REFERENCES--CONTINUED

24. Sommargren, Phillion and Campbell, "Sub-nanometer interferometry for aspheric mirror fabrication," Precision Science and Technology for Perfect Surfaces, " Proc. of 9th International Conference on Production Engineering, Y. Furukawa and t. Tori, eds., pp329-335 (1999)

CHAPTER 4

25. D. Baiocchi and J. H. Burge, "Radius of Curvature metrology for segmented mirrors," pre-prints
26. Goodman, *Introduction to Fourier Optics*, McGraw-Hill, New York, 1968

27. J. H. Burge, "Applications computer generated holograms for interferometric measurement of large aspheric optics, " Proc. SPIE 2576 (1995)
28. J. H. Burge, "Fizeau Interferometry for large convex surfaces, " Proc. SPIE 2536 (1995)

CHAPTER 5

CHAPTER 6

29. E. Hanson of NOAO [Ref: 4_51.doc from E. Hansen]
30. J. H. Burge, "Design study for measuring the GRANTECAN primary mirror segments using a test plate with computer-generated holograms, " Private consulting report, October 1998
31. R. Robles from NOAO supplied the SolidWorks Drawing data.

CHAPTER 7

32. J. H. Burge, "Efficient Testing of off-axis aspheres with test plate and computer-generated holograms," Optical Manufacturing and Testing III, H. Stahl Editor, Proc. SPIE **3782**, p348 (1999)
33. J. Burge, "Design study for measuring the GRANTECAN primary mirror segments using a test plate with computer-generated holograms," Private consulting report, October 1998